UNIVERSIDAD COMPLUTENSE DE MADRID
FACULTAD DE CIENCIAS FÍSICAS

TESIS DOCTORAL

Spin-orbit interaction and topological phases at correlated oxide interfaces

Interacción espín-órbita y fases topológicas en interfases de óxidos correlacionados

MEMORIA PARA OPTAR AL GRADO DE DOCTOR

PRESENTADA POR

Andrea Peralta Somoza

Director

Jacobo Santamaría Sánchez-Barriga

Madrid

UNIVERSIDAD COMPLUTENSE DE MADRID
FACULTAD DE CIENCIAS FÍSICAS

TESIS DOCTORAL

Spin-orbit interaction and topological phases at correlated oxide interfaces
Interacción espín-órbita y fases topológicas en interfases de óxidos correlacionados

MEMORIA PARA OPTAR AL GRADO DE DOCTORA

PRESENTADA POR

Andrea Peralta Somoza

DIRECTOR

Jacobo Santamaría Sánchez-Barriga

UNIVERSIDAD COMPLUTENSE DE MADRID

Facultad de Ciencias Físicas

Doctorado en Física

Spin-orbit interaction and topological phases at correlated oxide interfaces

Interacción espín-órbita y fases topológicas en interfases de óxidos correlacionados

Andrea Peralta Somoza

Memoria presentada para optar al título de doctora

Director: **Jacobo Santamaría Sánchez-Barriga**

Madrid 2023

A mi madre Sara

Coeur de pirate

Agradecimientos

Para mí, hacer la tesis es como ver una prensa hidráulica haciendo un cubo de chatarra, pero tú no eres la prensa, tú eres la chatarra. Piensas que será un desafío científico, pero en realidad es un viaje tremendamente solitario y personal, que te enfrenta a ti mismo. Justamente por eso, las personas que pasan por tu vida en estos años tan turbulentos, dejan una huella muy especial. Ha llegado el momento de agradecérselo a todas ellas.

Muchas gracias a Jacobo Santamaría, mi director de tesis, y a Carlos León por esta oportunidad, por toda la confianza que habéis depositado en mí y para hacer las cosas con libertad y por todo lo que he aprendido. Vosotros lo hicisteis posible. Gracias Alberto Rivera por siempre ser tan amable y ayudarme con cualquier asunto científico. Gracias a Zouhair Sefrioui, por todo el tiempo y el esfuerzo que echamos en el experimento de las uniones. Por supuesto, gracias a María Varela, Norbert Nemes, Rainer Schmidt y Neven Biskup por mostraros siempre accesibles y cercanos.

Las personas que han estado día a día conmigo en el laboratorio forman parte intrínseca de esta tesis. Gracias a Javi Tornos, mi mentor en el laboratorio, por enseñarme la importancia de ser una científica resolutiva y pensar de manera independiente, y por ponerle el nombre al Pintoyo. No conseguiste que abrazase a la Pachamama pero sí que hiciese la ciencia con amor. Gracias a Fer por enseñarme que la ciencia se puede tomar con humor, aunque a veces se volviese un poco ácido. Pero sobre todo gracias por darme una de las cosas que más feliz me hace en la vida, mis gatitas Kira y Lula, gracias tronco. A David, otro grande del humor, gracias por ser tan máquina. Tu pasión por la siensia es realmente contagiosa. Gracias por todos tus buenos consejos. Gracias a Fabián, por siempre estar ahí para resolver cualquier problema. Gracias por las cervezas en el Pato. Pero sobre todo gracias esos desayunos en la cafetería de Biología durante el

año de pandemia. Recuerdo con cariño esos tiempos en los que solo éramos el illo, tú y yo en el laboratorio, estábamos muy solos pero comíamos muchas magdalenas. No me puedo ni imaginar esta tesis sin todo el apoyo que ha recibido de tu parte. Gracias a Alex, mi compi de despacho más duradero, no sé ni cómo me aguantaste tanto tiempo. Gracias por mantener la alegría y el chill de ese despacho, aunque estuvieras tan jodido como yo. Gracias a Emanuel, por tus juegos de palabras y tus referencias a los Simpson, sabes sacar una risa de la manera más insospechada. Gracias a Victor Rouco, por ser el putoooo (amo del laboratorio). A veces, cuando me sentía una inútil total, tú sabias hacerme cambiar de opinión, porque de ti sí que me fiaba. A Gabi, gracias por las charlas a deshora y los buenos consejos. A Isa Tenreiro, mi choco-compi de cursos, escuelas de verano, congresos y festivales, gracias por todos esos momentos de pasarlo increíble, eres LA fiesta. Y gracias por ser una amiga y dejarme llorar en tu hombro de vez en cuando, sobre todo en ese 2021 post pandemia tan raro. A Sandra, gracias por ser tan pendeja y hacerme más llevadera la recta final, he disfrutado mucho enseñándote bebesita. Nunca olvidare esa bofetada que me soltaste mientras iba conduciendo por no haber desayunado. Allá donde vayas, que nada te quite esa manera de hacerte temida y querida por todos. A Isa Barbero, gracias por tus post-it de colores, por traer una energía nueva al laboratorio y tu propia manera de hacer las cosas. A Sara, gracias por las charlas de despacho, cuando te venias por aburrimiento y nos contábamos las penas. A Víctor Zamora, gracias por ser el mejor compañero de sincrotrón. Esa fiesta que nos pegamos en el bar de la residencia de Berlín, en mitad de un experimento, está en mi top 5 de momentos de la tesis. A Rafa, gracias por devolverme la fe en que se puede hacer ciencia y ser una persona balanceada, me has inspirado más de lo que imaginas. Ojala nunca cambies.

Fuera de las puertas del GFMC, los laboratorios continuaban y no puede dejar de agradecer a todo equipo del 2-D Foundry toda la ayuda que me han prestado. A Mar García y Federico Mompean por la incalculable ayuda que nos han dado para medir en el PPMS, siempre tenía la tranquilidad de poder contar con vosotros. A Carmen Munuera y Juanjo Riquelme, gracias por ayudarme a sacar los mejores resultados de la tesis

y subir el experimento a otro nivel. Carmen, gracias por ser todo un referente de que se puede ser buena científica y tener una mecha incombustible para salir de fiesta cuando la situación lo requiere. Juanjo, mil gracias por todo el esfuerzo que pusiste en el experimento de MFM y por todos tus consejos para disfrutar de mi estancia en UK. To Sean Giblin, thank you for welcoming me into your lab and showing me other ways of working in science.

Fuera del laboratorio, los amigos que me han acompañado en todo este viaje realmente me han salvado de la locura. Gracias a Vanesa y Carmela por esas reuniones vecinales en el mercado. Con vosotras he podido compartirlo todo. Carmela, gracias por estar siempre ahí, por ser la niñera de las gatillas cuando lo necesitaba y por las videollamadas desde Bristol. A Rocio, Dani, Sandra, Carlos y Pepelu, gracias redescubrirme Madrid y hacerme disfrutar como nunca en mi vida. Gracias por las cervezas, los scape room, las noches en el Delirio y tantos otros buenos momentos. A Andres, mi compi de piso y de carrera, gracias por las canciones de Disney que tocabas en el piano mientras yo cantaba, por los podcast y por los experimentos de ciencia con el microondas. A Ana, mi confidente del amor y compi de festivales, gracias por tu grandísimo corazón y acompañarme todo el camino.

A Hono, gracias por recordarme día a día todo lo que soy más allá de este doctorado. Por estar ahí para romper mis esquemas y cambiar mi perspectiva. He crecido como persona a tu lado.

Mi familia, que me lleva apoyando toda la vida, no puede faltar. Gracias mama, por todo el amor que me has dado que aunque pasemos temporadas sin vernos, yo lo siento ahí cada día. Gracias por estar ahí aunque a veces no fuera fácil. A mis tíos Pablo y Álvaro, que son dos padres para mí gracias por hacerme sentir tan querida. A mi tía María, gracias por toda la ayuda que me ha dado para convertirme en la persona que soy ahora. No hay palabras para agradecerte todo lo que has hecho. A Maribel, gracias por tus preguntas de ciencia y tu cariño. A Ivana y Marco, que completáis una familia increíble. No podría haber hecho esto sin vosotros.

A todos vosotros, gracias.

Contents

Motivation

Quantum materials have become a focal point of solid-state physics research, offering a fascinating platform to observe and manipulate emergent phenomena [1]. Prominent phenomena observed in these materials are driven by spin-orbit coupling, a fundamental quantum interaction that ties the orbital motion of electrons with their spin [2]. This complex interaction between electron's spin and orbital motion often gives rise to unique physical phenomena, including unusual electronic phases and unconventional magnetic behaviours [1]–[3]. The manipulation of spin-orbit coupling using relatively minor external influences allows us to tailor profound modifications in material properties [4]. More specifically, at surfaces and interfaces of these materials where the interplay between symmetry breaking and spin-orbit coupling kicks in, remarkable effects such as spin currents, chiral magnetization, and the emergence of topologically protected states have been observed [2]–[4]. These phenomena not only enrich our understanding of quantum materials but also hint at their vast potential for applications in next-generation electronic and spintronic devices [4], [5].

Within the intriguing world of quantum materials, $SrIrO_3$, a 5d transition metal oxide, has garnered particular interest. $SrIrO_3$ features a delicate balance between electronic correlations and spin-orbit coupling which are at the bottom of intriguing quantum states [6]. This balance crafts an stimulating benchmark to modulate its physical properties and thereby nucleate novel electronic phases [6]. Recognized for its unique properties, $SrIrO_3$ is sensitive to even weak external perturbations, leading to significant changes in its material characteristics. This exceptional responsiveness establishes $SrIrO_3$ as an excellent candidate for studying the effects of external influences on quantum materials.

Employing external perturbations to manipulate the properties of quantum materials is an ambitious project. Our focus rests primarily on

two promising ´knobs´: epitaxial strain and ionic liquid gating. Epitaxial strain has proven to be an effective mean of modifying material properties, with the ability to dictate the electronic behaviour of correlated oxides such as $SrIrO_3$. By the judicious choice of substrate, strain can be selected between compressive and expansive, providing crucial insights into the effect of structural modifications on electronic states. On the other hand, ionic liquid gating is a powerful technique to induce strong electric fields in a material. This tool will give us the opportunity to study the interrelation between symmetry breaking, and the band structure of quantum materials enabled by spin-orbit coupling. These investigations aim not only to explore the rich behaviour of $SrIrO_3$ under external perturbations but also to offer insights into the potential of controlling emergent properties towards future device concepts in oxide electronics.

The combination of 5d oxides with strong spin-orbit coupling and ferromagnetic 3d oxides also offers a fertile platform to examine the interplay between topology and correlations enabling the study of a variety of interesting new phenomena, such chiral spin textures or exotic proximity interactions at interfaces resulting from the Dzyaloshinskii-Moriya interaction and broken symmetry. We will realize these heterostructures combining $SrIrO_3$ and $La_{0.7}Sr_{0.3}MnO_3$. The peculiar characteristics of these bilayers offer a vast playground to investigate phenomena like the anomalous Hall effect (AHE) and the topological Hall effect (THE) driven by the topological properties of electronic states in momentum and real space respectively. The emergence of THE and its relationship with the nucleation of chiral spin textures is a fascinating scenario allowing insights into the fundamental mechanisms underlying the THE.

These investigations are not only intended to delve into the fundamental understanding of the role of spin-orbit coupling in quantum materials but also pave the way towards the design of new spintronic devices. The development of such devices could leverage the fine control over chiral magnetic domains and other emergent properties that these rich heterostructures might offer.

Objectives

The main objectives of this thesis are to:

- Control the electronic states of $SrIrO_3$ through external perturbations. This objective will be accomplished by two different routes: epitaxial strain and ionic liquid gating. Both techniques will give us information about the relationship between symmetry breaking with electronic structure enabled by spin orbit coupling.

- Study the interplay between topology and correlations. We will characterise heterostructures combining $SrIrO_3$ with a ferromagnetic 3d oxide such as $La_{0.7}Sr_{0.3}MnO_3$. We will examine proximity-induced magnetism at these interfaces as well as the emergence of chiral magnetic textures.

These objectives will be accomplished through the growth of thin films and heterostructures via high-pressure sputtering. Their structural, electrical, and magnetic properties will be explored using a wide variety of experimental techniques. The results will be contrasted by first principles simulations.

Thesis outline

- **Chapter 1:** We review general ideas of complex oxides and provide a brief introduction to key materials such as $La_{0.7}Sr_{0.3}MnO_3$ and $SrIrO_3$. We go over fundamental physics concepts like epitaxial strain, the Hall effect, magnetic textures, and field effect and ionic liquid gating.

- **Chapter 2: Introduction.** We provide a comprehensive overview of the experimental methods employed throughout this thesis. We first delve into growth techniques, specifically focusing on the high-pressure sputtering system. Next, we describe the nanofabrication methods used, including optical lithography and reactive ion etching. We then examine structural characterization techniques, such as X-ray and Transmission Electron Microscopy. This is followed by a description of magnetotransport methods, particularly the Physical Property Measurement System, and magnetic characterization techniques such as the superconducting quantum interference device, magnetic circular dichroism, polarized neutron reflectometry, and magnetic force microscopy. The chapter concludes with a brief description of scanning tunnelling microscopy. For completeness, we provide a brief description of the first principles simulations using the density functional theory which are used in this thesis through collaborations with theory groups.

- **Chapter 3: Effect of epitaxial strain.** We study the structural and electronic properties of $SrIrO_3$ under different epitaxial strains. We show that substrates may impose symmetry constrains triggering profound modifications of the electronic properties. In particular we describe how the non-symmorphic structure of $DyScO_3$ substrate yields a highly anomalous monoclinic phase exhibiting a Dirac cone 30 mV above the Fermi level.

- **Chapter 4: Electric field effects.** We use ionic liquid gating to study the interplay between the symmetry breaking, the spin orbit coupling, and the electronic structure of the ultrathin layer of $SrIrO_3$. Magnetotransport characterization is used to study the metal-insulator transition and the emergence of anomalous Hall effects in the insulator state. First-principles density functional theory simulations are performed to acquire insight into the electric field-driven alteration of $SrIrO_3$ electronic states.

- **Chapter 5: Anomalous Hall Effect (AHE)**. Intrinsic anomalous Hall Effect (AHE) was detected in the $La_{0.7}Sr_{0.3}MnO_3/SrIrO_3$ bilayers which we ascribe to a magnetic state induced in the $SrIrO_3$ by proximity. This effect depends on the layer sequence at the interface: while anomalous Hall Effect (AHE) was detected in the $La_{0.7}Sr_{0.3}MnO_3/SrIrO_3$ bilayers, it was absent in $SrIrO_3$/ $La_{0.7}Sr_{0.3}MnO_3$ bilayers. We correlate this AHE with the magnetic state of the interface and the proximity-induced magnetism within the initial 2 nm of $SrIrO_3$ at the interface.

- **Chapter 6: Topological Hall effect (THE).** We study the emergence of topological Hall effect (THE) in $La_{0.7}Sr_{0.3}MnO_3/SrIrO_3$ bilayers. THE unusual features are carefully studied by magnetotransport measurements. Imaging of the magnetic texture with magnetic force microscopy revealed the presence of a granular magnetic textures akin to skyrmions and spin spirals. The correlation of these magnetic textures with the emergence of THE provide insight into the role of the Dzyaloshinskii-Moriya interaction and magnetic anisotropy as mechanisms underlying THE.

- **Chapter 7: Conclusions**. The final chapter summarizes the main conclusions of this thesis.

References

[1] Y. Tokura, M. Kawasaki, y N. Nagaosa, «Emergent functions of quantum materials», *Nature Phys*, vol. 13, n.º 11, pp. 1056-1068, nov. 2017, doi: 10.1038/nphys4274.

[2] A. Soumyanarayanan, N. Reyren, A. Fert, y C. Panagopoulos, «Emergent phenomena induced by spin–orbit coupling at surfaces and interfaces», *Nature*, vol. 539, n.º 7630, pp. 509-517, nov. 2016, doi: 10.1038/nature19820.

[3] S. Gariglio, A. D. Caviglia, J.-M. Triscone, y M. Gabay, «A spin–orbit playground: surfaces and interfaces of transition metal oxides»,

Rep. Prog. Phys., vol. 82, n.º 1, p. 012501, ene. 2019, doi: 10.1088/1361-6633/aad6ab.

[4] M. Bibes, J. E. Villegas, y A. Barthélémy, «Ultrathin oxide films and interfaces for electronics and spintronics», *Advances in Physics*, vol. 60, n.º 1, pp. 5-84, feb. 2011, doi: 10.1080/00018732.2010.534865.

[5] R. Ramesh y D. G. Schlom, «Creating emergent phenomena in oxide superlattices», *Nat Rev Mater*, vol. 4, n.º 4, pp. 257-268, mar. 2019, doi: 10.1038/s41578-019-0095-2.

[6] S. J. Moon *et al.*, «Dimensionality-Controlled Insulator-Metal Transition and Correlated Metallic State in 5 d Transition Metal Oxides Sr n + 1 Ir n O 3 n + 1 (n = 1 , 2, and ∞)», *Phys. Rev. Lett.*, vol. 101, n.º 22, p. 226402, nov. 2008, doi: 10.1103/PhysRevLett.101.226402.

Chapter 1

Introduction

1. Transition-Metal Oxides

Transition metal oxides (TMOs) are one of the material families with a lot of potential for use in novel electronics. Due to the intricate interplay between their spin, charge, and orbital degrees of freedom, these materials exhibit a an exceptionally rich palette of electronic groundstates. In this section, we will review the basic characteristics of these materials, the interactions that shape their electrical properties, and the primary phenomena that make them a fascinating topic of research.

TMOs are compounds arising from the bonding of oxygen with transition metals, whose valence electrons are in unfilled d-shells. Although atoms TMOs can be organised in a variety of crystalline forms, we shall concentrate on the perovskite structure because it is common to many material families allowing their epitaxial growth in heterostructures. In this structure, with the generic formula of ABO_3, the transition metal ions are surrounded by six oxygen ions (O^{-2}), forming an octahedron. This octahedra give rise to the crystal field potential, hinder the free rotation of the electrons and quenches the orbital angular momentum by introducing the crystal field splitting of the d orbitals. The former wave functions, $d(x^2\text{-}y^2)$ and $d(3z^2\text{-}r^2)$, are called e_g orbitals, whereas the latter, d(xy), d(yz), and d(zx), are called t_{2g} orbitals. As shown in Figure 1.1, wave functions pointing toward O^{-2} ions have higher cohesive energy in comparison with those pointing between them. The splitting between e_g and t_{2g} orbitals is written as 10 Dq. The value of this splitting is about 2-3 eV [1]–[3].

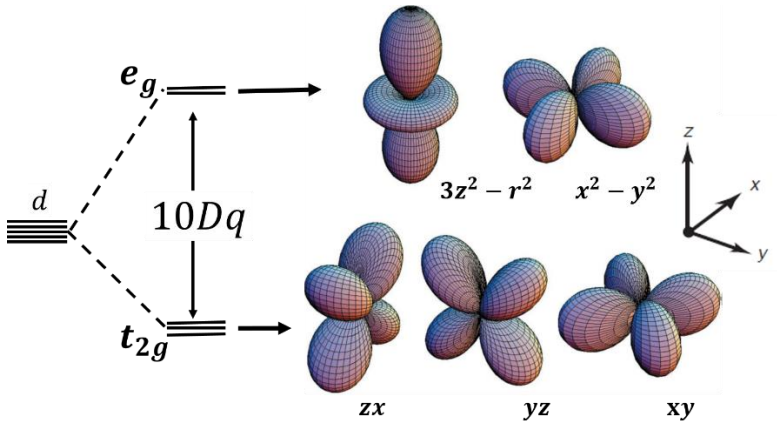

Figure 1.1. Schematic of the d-orbital splitting into the e_g and the t_{2g} orbitals and their spatial representation.

1.1. Electronic correlations

Inside the TMOs, 3d and 4d oxides have been deeply studied in relation to the metal-insulator transitions, high-Tc superconductivity, and Mott insulating states. Underlying these phenomena, we find strong electronic correlations—the electronic repulsion between electrons on neighbouring sites. This interaction, arising from the overlap between contiguous orbitals, prevents the electrons to be described as non-interacting particles.

The Mott transition, a metal-insulator transition (MIT) that occurs in correlated systems, is the most essential property of correlated materials. In the one-electron approximation, these systems with one electron per site are expected to be metals, but electrostatic repulsions localizes the electrons at their atomic sites. This opens a Mott gap at the Fermi energy level. The interaction between repulsive energy (U) and electronic bandwidth (W) moderates the formation of different electronic states.

The simplest way to take these correlations into account is to use the Hubbard model, an extension of the tight-binding model whose Hamiltonian comprises two terms. The first term refers to the hopping energy, t, the energy that electrons need to hop to the nearest-neighbour lattice sites. The second term measures the energy penalty U for a pair of

electrons occupying the same site due to Coulomb repulsion. Following this, the Hubbard expression is given as [4]:

$$H = -t \sum_{i,j,\sigma} c_{j\sigma}^{\dagger} c_{i\sigma} + \sum_{i} U_i n_{i\uparrow} n_{i\downarrow}$$

where the first part is the kinetic energy t, which describes the removal of a fermion with spin σ on site i and its formation on close site j (or vice versa). The interaction energy, which adds an energy U if a site is twice occupied, is the second part. Figure 1.2 represents pictorially both energies.

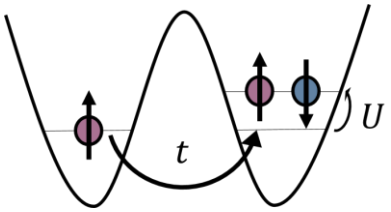

Figure 1.2. Hubbard model. Intersite hopping energy t, and double occupancy energy U.

The Hubbard model accurately predicts the Mott insulating state, while traditional band theory predicts a metallic state for a half-filled band. High-temperature superconductivity and the superfluid-Mott insulator transition in cold-atom investigations rely on the Hubbard model. Dynamical mean-field theory, employed extensively in the calculation of the electronic structure of highly correlated materials, was inspired by this model.

1.2. Spin-orbit coupling

Belonging to the, the 5d TMOs have received less attention than 3d and 4d oxides because of the difficulties encountered in their chemical synthesis. Aside from high correlations, the electrons in these materials exhibit an important property known as strong spin-orbit coupling (SOC), which is a relativistic interaction that couples the spin and orbital degrees of freedom. This characteristic is especially relevant in combination with the strong correlations for applications because it may serve as a platform

for spintronics (devices that rely on spin currents rather than charge currents) and enable data processing with little energy dissipation.

The spin-orbit interaction is given by $H_{spin-orbit} = \lambda \vec{L} \cdot \vec{S}$, where $\vec{L}$ is the orbital angular momentum and $\vec{S}$ is the spin angular momentum. This interaction plays an important role in some cases, especially for t_{2g} electrons where the orbital sector may become relevant. In solids, SOC causes the splitting of otherwise degenerate electronic bands. When these bands are near to the Fermi level and the splitting is big enough, the electrical properties may be significantly modified.

As a consequence, in 5d TMOs we may include the SOC as a relevant interaction determining the interplay between U and W. As we will see in the following section, in materials such as $SrIrO_3$, the balance of these three energy scales is critical for the stabilization of novel electronic groundstates with exciting electrical characteristics.

2. Materials

In this section, we are going to give a brief review of the TMOs that had an important role in this thesis: the 5d $SrIrO_3$, as the main character; and the 3d $La_{0.7}Sr_{0.3}MnO_3$ as the secondary one.

2.1. $SrIrO_3$

$SrIrO_3$ (SIO) has attracted much attention in the last decade. This is due to the extraordinary nature of this material, which has a plethora of interactions that compete with each other and place it in a delicate equilibrium, enabling small external perturbations to cause large changes in the system. As a result, it is considered a promising quantum oxide material.

In order to understand the SIO, first of all, we should describe its electronic band structure. SIO is a 5d oxide. In contrast to 3d oxides, which yield strongly correlated narrow bands with a large Coulomb repulsion, U, and a small band width, W, the 5d orbitals states are

spatially more extended, and U is expected to be further reduced [3]. Given this, one might expect 5d oxides with a partially filled wide t_{2g} band to become metals, as shown in Figure 1.3a. However, in the strong SOC limit, the t_{2g} band splits into effective total angular momentum J_{eff}= 1/2 doublet and J_{eff}=3/2 quartet bands, shown in Figure 1.3b. As a result, the system is effectively reduced to a half-filled J_{eff}=1/2 single-band system with the filled J_{eff}=3/2 band. Figure 1.3c shows that the J_{eff}=1/2 spin-orbit integrated states make a narrow band where even a small U can open a Mott gap, making a J_{eff}=1/2 Mott insulator [5].

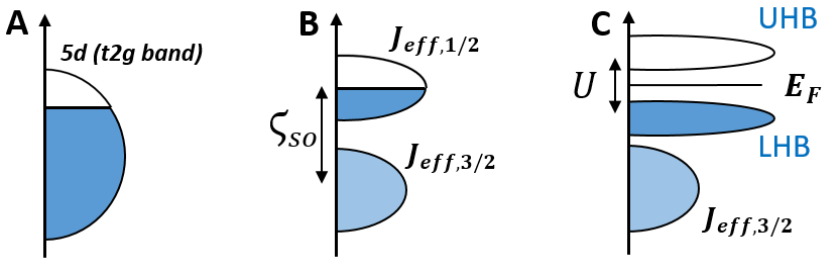

Figure 1.3. Schematic energy diagrams for the 5d (t_{2g}) configuration (a) without SO and U, (c) with SO but no U, and (d) with SO and U. This figure was adapted from Ref. [5].

This is the case for the insulator Sr_2IrO_4, which in contrast with $SrIrO_3$ is a correlated metal. The difference between both compounds lies in the W, which is directly proportional to the number of neighbouring Ir atoms, z. Among the Ruddlesden-Popper series $Sr_{n+1}Ir_nO_{3n+1}$ compounds, the z values increased with each successive compound: Sr_2IrO_4 (n = 1) has a z value of 4, $Sr_3Ir_2O_7$ (n = 2) has 5, and $SrIrO_3$ (n = ∞) has 6. As the z values increased, the W in the 5d bands increased, producing an MIT between $Sr_3Ir_2O_7$ and $SrIrO_3$ (Figure 1.4) [6].

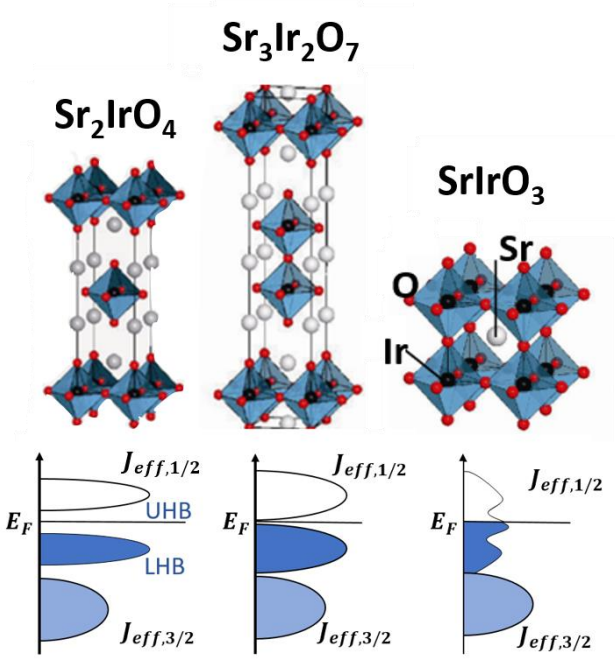

Figure 1.4. Schematic band diagrams of 5d $Sr_{n+1}Ir_nO_{3n+1}$ compounds, which are well described by the effective total angular moment Jeff states due to strong spin-orbit coupling: (left) Mott insulator Sr_2IrO_4, (centre) barely insulator $Sr_3Ir_2O_7$, and (right) correlated metal $SrIrO_3$. EF represents the Fermi level and the arrow indicates the direction for the bandwidth W increase. This figure was adapted from Ref.[6].

$SrIrO_3$ is thus a correlated metal on the edge of an MIT, with the SOC, U, and W competing on the same energy scale. The degree of connectivity dictates the degree of ionic vs covalent bonding, which in turn indicates the degree of metallicity. Given the connectivity of the IrO_6 octahedra, we could place the $SrIrO_3$ halfway between the completely metallic rutile IrO_2 and the Mott insulator Sr_2IrO_4. Kawasaki et al. confirmed this in 2016 using ARPES data, as shown in Figure 1.5 [7].

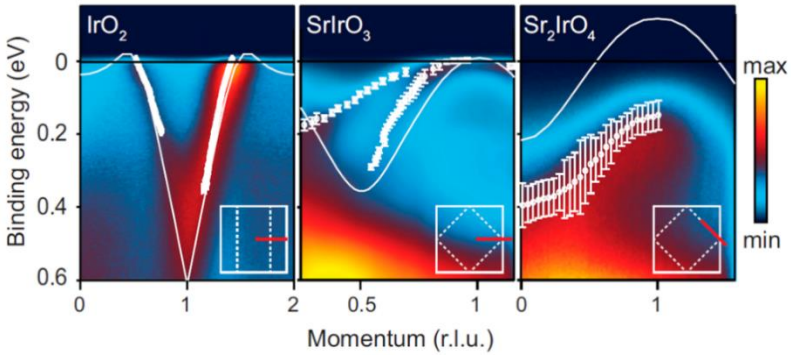

Figure 1.5. ARPES intensity (color scale), extracted dispersions (white circles), and DFT+SO (white lines) showing increasing renormalizations from IrO_2 to $SrIrO_3$ and Sr_2IrO_4. Momenta are expressed in units of $\pi/2d110$, π/a, and $\sqrt{2}\pi/a$, respectively. $SrIrO_3$ and Sr_2IrO_4 data adapted from Ref. [7].

Contrary to predictions, we find that enhanced coordination results in narrower bands in $SrIrO_3$, with bandwidths of around 0.3 eV. Surprisingly, they are even narrower than in the Mott-like insulating state of Sr_2IrO_4, where the bandwidths range from 0.3 to 0.8 eV [8], [9]. This is attributed to the cooperative interaction of the SOC, dimensionality, and complex octahedral rotation patterns. Both in- and, crucially, out-of-plane octahedral rotations $a^-b^+a^-$, lead to the array of narrow intersecting bands in $SrIrO_3$, as shown experimentally by Nie et al. in 2015 using ARPES (see Figure 1.6). These ARPES measurements also revealed an unusual coexistence of heavy holelike and light electronlike bands [8] crossing the Fermi level.

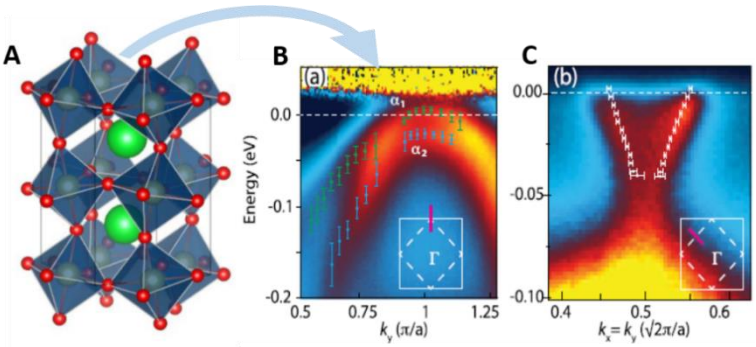

Figure 1.6. (a) orthorhombic unit cell of SrIrO3. This figure was adapted from Ref. [10]. ARPES measurements (adapted from Ref. [8]) of (b) two massive holelike bands at (0,π), and (c) a light, almost linearly dispersive electron band at (-π/2, π/2) along the cuts shown by red lines in the insets.

The carrier densities and mobilities were estimated in 2018 by Manca et al., combining thermoelectric and magnetotransport measurements with first-principles calculations. Table 1.1 summarizes the findings, which show that electrons and holes have comparable densities and mobilities, indicating that $SrIrO_3$ is a compensated semimetal. Although electrons and holes have comparable concentrations and mobilities, the electron channel dominates the Hall transport due to its larger mobility [11].

t (uc)	n_e $(10^{20}/cm^3)$	n_h $(10^{20}/cm^3)$	μ_e $(cm^2V^{-1}s^{-1})$	μ_h $(cm^2V^{-1}s^{-1})$
20	$1.6\ x\ 10^6$	$2.5\ x\ 10^6$	18	13.5
6	$1.8\ x\ 10^6$	$2.6\ x\ 10^6$	27	22

Table 1.1. Charge-carrier characteristics extracted from the sampling analysis with the experimental constraints. This table was adapted from Ref [11].

$SrIrO_3$ can be driven into a correlated insulating state in the 2D limit. In 2017, Groenendijk et al. found that an MIT occurs at a film thickness of 4 unit cells (u.c.), as shown in Figure 1.7 [12]. First principles show a concomitant enhancement of anti-ferromagnetic order [11]. However, at the moment, it is not clear whether the MIT transition is driven by enhanced correlations in two dimensions or by the emergent magnetic state at the transition. The origin of the MIT remains still elusive.

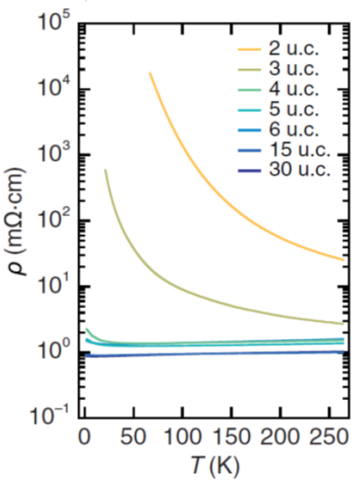

Figure 1.7. Resistivity as a function of temperature curves for films of different thicknesses. This figure was adapted from Ref. [12].

It becomes clear, thus, that $SrIrO_3$ is a very promising material for stabilize exotic quantum states of matter and will be the central player of this thesis.

2.2. $La_{0.7}Sr_{0.3}MnO_3$

Lanthanum strontium manganite $La_{0.7}Sr_{0.3}MnO_3$ (LSMO) is a 3d ferromagnetic oxide characterized for been a half-metal what means it provides a 100% spin polarized current at a wide range of temperature.

The LSMO used in this thesis is the optimally doped manganite of the $La_{1-x}Sr_xMnO_3$ family. This system presents an interesting phase diagram as a function of Sr concentration, featuring both metal-insulator and magnetic transitions. The un-doped manganite $LaMnO_3$ is an insulator with antiferromagnetic order. The insulating gap corresponds to a charge transfer excitation from the oxygen 2p orbitals to the manganese 3d orbitals. Due to the valence of manganese being Mn^{3+}, it possesses four d-electrons: three of these are in t_{2g} states, while one electron is in an e_g state. Among these electrons, the t_{2g} electrons have relatively poor hybridization (interaction) with the oxygen 2p states. On the other hand, the e_g states, which are strongly hybridized with the oxygen 2p states, can either be itinerant (mobile) or localized (confined to specific regions) depending on the specific circumstances. The exchange interaction between the Mn ions results in an (ferromagnetic) orbital ordering within the xy plane and antiferromagnetic coupling along the z direction, shown in Figure 1.8.

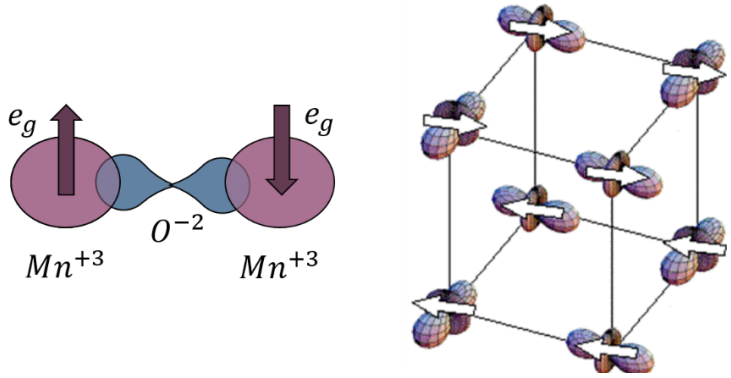

Figure 1.8. (left) Orbital hybridation between the e_g Mn orbital and the oxygen 2p orbital. (right) Orbtial and magnetic ordering in $LaMnO_3$

The substitution of divalent Sr^{2+} for La^{3+} in LaMnO3 causes an equal number of Mn^{3+} to convert to Mn4+ and proportionally induces itinerant holes with carrier delocalization. As shown in Figure 1.9 the increasing Sr concentration is followed by a ferromagnetic ordering and metallic behaviour [13].

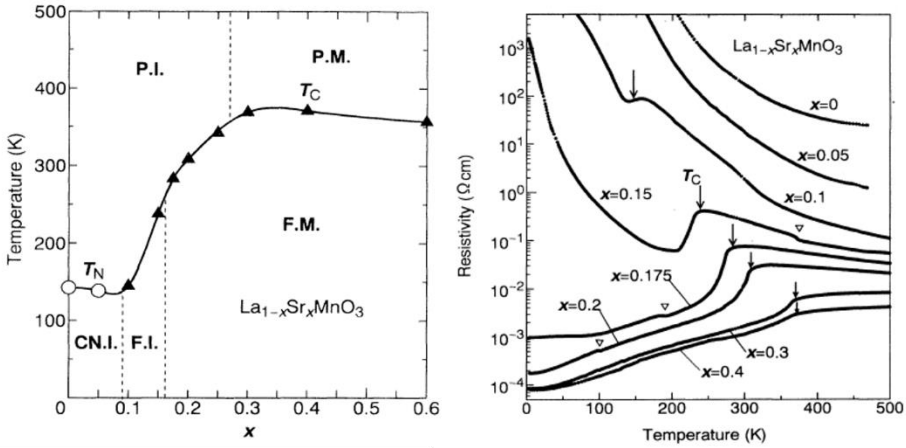

Figure 1.9. (left) Phase diagram of $La_{1-x}Sr_xMnO_3$. The letters P, F, I and M denote paramagnet, ferromagnet, insulator and metal, respectively. (right) Resistivity as a function of temperature for different Sr concentration in the family $La_{1-x}Sr_xMnO_3$. Figures adapted from [13].

The metallic behavior observed in this system was explained by Zener's model of double exchange. Zener's model considers the exchange interaction between Mn^{3+} and Mn^{4+} ions mediated by an oxygen ion [14]. In this model, simultaneous electron transfers occur from Mn^{3+} to oxygen and from oxygen to the neighboring Mn^{4+}. Due to the strong intra-atomic Hund coupling, which favors parallel spins, the simultaneous hopping of electrons results in a ferromagnetic interaction between the Mn ions. This ferromagnetic interaction is responsible for the observed ferromagnetic and metallic behavior in the material.

Observing Figure 1.9, it becomes clear why we chose $La_{0.7}Sr_{0.3}MnO_3$ (which corresponds to x=3) as our study material. It exhibits metallic properties and a ferromagnetic order with the highest Curie temperature, T_C= 354 K. For this stoichiometry, the saturation magnetization is 3.7 μ_B/Mn_{atom}.

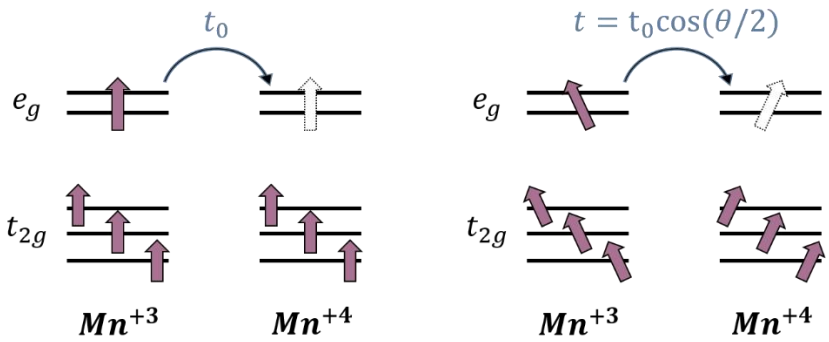

Figure 1.10. (left) Schematic illustrating the double exchange mechanism. (right) Hopping integral t depends on the relative angle between spins.

The Hund coupling favours parallel spins for all involved electrons during simultaneous hopping. The hopping energy t is influenced by the relative angle between spins as $t = t_0 \cos\left(\frac{\theta}{2}\right)$. If the localized spins are polarized in one direction, such as "up," the conduction electrons with "up" spin can move easily, while the conduction electrons with "down" spin face difficulties in hopping. As a result, the conduction electrons near the Fermi level become 100% polarized at low temperatures, with all spins aligned in one direction, giving the LSMO the half-metallic character. The hopping angle is not only determined by the fraction of Mn^{4+} and Mn^{3+} ions in the sample but also by temperature. Above the Curie temperature (T_C), spins become dynamically disordered, resulting in a paramagnetic insulator state. However, below T_C and close to it, spins can easily align when a magnetic field is applied. This alignment of spins serves as one of the contributing factors for the occurrence of so called colossal magnetoresistance (CMR) in manganites, the huge change in the resistance due to the application of a magnetic field.

It is worth noting in LSMO thin films the existence of the so-called "dead layer" or critical thickness, which can be defined as the thinnest layer for which metallic as well as ferromagnetic behaviours are observed. In different studies, this dead-layer thickness for thin films was estimated to be 3–4 nm, depending on the substrate chosen. For thin films grown on STO, the LSMO dead layer thickness is estimated to be 8 u.c [15]. The mechanism behind the dead layer problem is still controversial. This dead layer will play a crucial role in the following experiments.

3. Epitaxial engineering

Epitaxial growth is a method in which a thin film of material grows atom-by-atom with nearly the same lattice parameter and crystalline orientation as the substrate crystal. Its potential for controlling and engineering novel responses in transition metal oxide (TMO) heterostructures has generated significant interest in research in recent decades. This technique is especially useful in perovskites, such as ABO_3, in which the B-site cation is surrounded by six O anions in a corner-shared BO_6 octahedron. The physical properties of these materials are largely determined by their octahedral structure, as electron hopping between the d-orbitals relies heavily on the shape, size, and position of the octahedra. The application of epitaxial strain in TMO offers not only a mechanism for tuning thin film functionalities but also opens up possibilities for the generation of novel correlated phenomena [16].

The enormous progress achieved in the study of TMOs by epitaxial engineering was due to the development of modern deposition techniques such as pulsed laser deposition (PLD), molecular beam epitaxy (MBE), or sputtering. These techniques enable the growth of ultrathin layers with epitaxial relationships to the bottom substrates.

The choice of substrate is essentially the basis of strain engineering. Choosing an appropriate metal oxide substrate is critical for producing high-quality epitaxial thin films. The structure and properties of a thin film depend on the underlying substrate and the interfacial interaction between the substrate and film. For this reason, the lattice match between the substrate and the film is an important factor to consider when choosing a metal oxide substrate for the development of epitaxial films since it has a substantial influence on structural compatibility. Most ABO_3 perovskites have lattice constants ranging from 3.80 to 4.00 Å. Several commercially available perovskite substrates have lattice constants ranging from 3.70 to 4.20 Å. Among a variety of perovskite substrates, the insulating $SrTiO_3$ is notably the most commonly used due to its cubic structure and lattice constant of approximately 3.905 Å. However, as seen

in Figure 1.11, there is also a wide range of substrates with structures similar to $SrTiO_3$ but varied in lattice constants and crystal orientations.

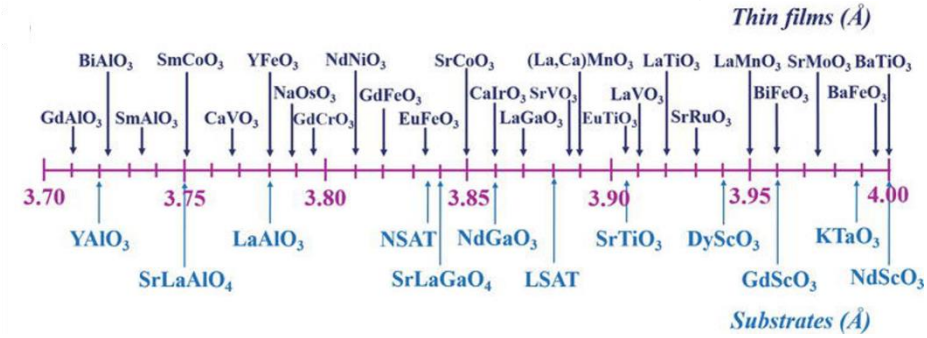

Figure 1.11. List of cubic (pseudo-cubic) substrates and thin films within the lattice constant range from 3.70 to 4.00 Å. Adapted from [17]

The mismatch between the lattice constant of the substrate (a_S) and the growing material (a_F) provokes strain in the thin film. When the growing material has a larger lattice parameter than the substrate ($a_F > a_S$), we talk about compressive strain, and when the material's lattice parameter is shorter ($a_F < a_S$), we talk about tensile strain. While it is widely assumed that the strain acts by imposing a new in-plane lattice constant on the film, the exact mechanism of that change in lattice constant is unknown and difficult to determine experimentally. As shown in Figures 1.12a and 1.12b, one possibility is that the change in in-plane lattice parameter is entirely accommodated by a change in in-plane metal-oxygen bond lengths. The other limit is shown in Figures 1.12c and 1.12d, where the lattice mismatch is accommodated by a change in magnitude (or type) of the tilt patterns caused by rigid rotations of the oxygen octahedra, while the B-O distances remain unchanged. Clearly, the two responses will have vastly different effects on the film's functionality. Changes in the length of the B-O bond, for example, affect the magnitude and symmetry of the crystal field splitting, whereas changes in the angles of the B-O-B bond determine the strength and sign of magnetic superexchange interactions [18].

Changes in the tilt pattern and octahedral deformations can affect the hopping between d-orbitals, potentially changing the bandwidth of the thin film. Changes in bandwidth affect the effective correlation, as changes in these energy scales cause the appearance of novel functionalities in oxide heterostructures under strain in general.

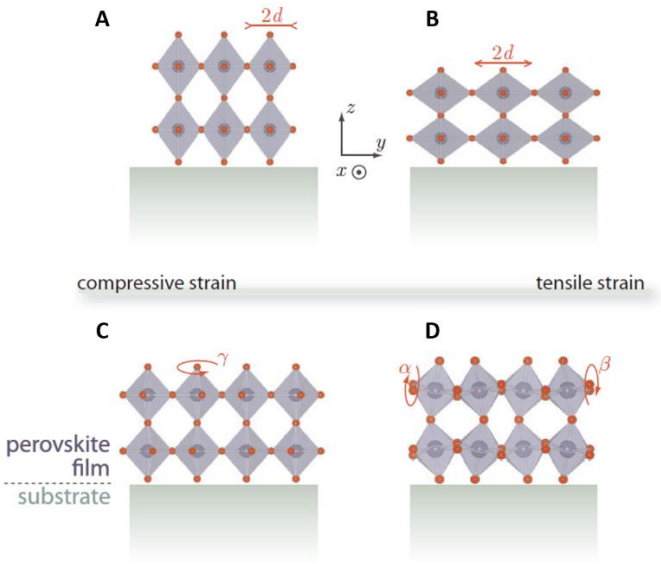

Figure 1.12. In coherently strained perovskite films, the BO_6 octahedra can distort through contraction (a) or elongation (b) of the equatorial B-O bond lengths d are due to compressive or tensile strain, respectively. Simultaneously/ alternatively, the octahedra can accommodate the substrate-induced change of the in-plane lattice parameters by rotation perpendicular to the substrate as in (c) and/or about an axis parallel to the substrate plane (d). Adapted from [18].

4. Ionic liquid gating

One of the most common ways to change a system's resistance and control its MIT is through modifications of the carrier density by electrostatic doping [19]. As shown in Figure 1.13, changing the carrier concentration induces new states of matter in complex oxides, changing not only the conductivity but also the intrinsic properties and electronic groundstates. Looking into the numbers; typically, a sheet carrier density of 10^{15} carriers/cm^2 is needed to explore the phase diagram of correlated oxides, such as manganites or cuprates.

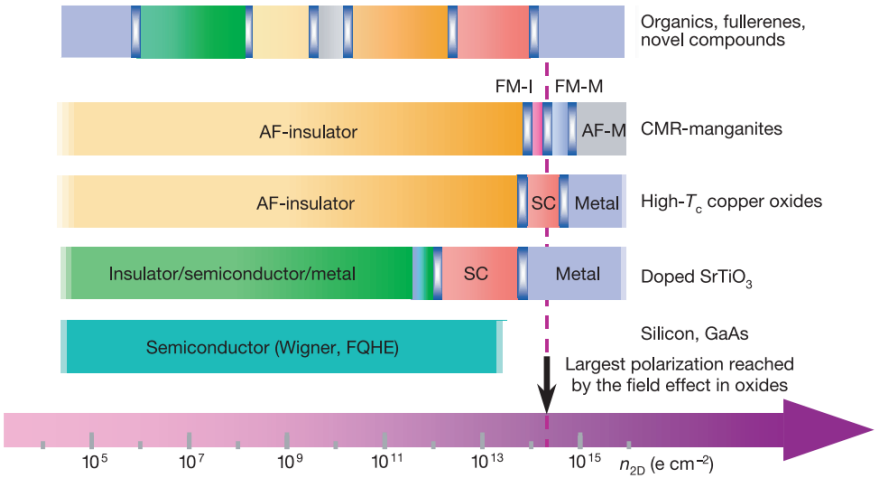

Figure 1.13. Illustration of various correlated material at T= 0 K as a function of sheet charge density. Adapted from [20].

In order to achieve electrostatic doping (much more desirable than chemical doping), the field effect transistor (FET) is the most common option[20]. This device, long used in semiconductor technology, uses an electric field at a gate to induce a carrier density by accumulation or depletion of charges at the surface of the material underneath the gate (see Figure 1.14).

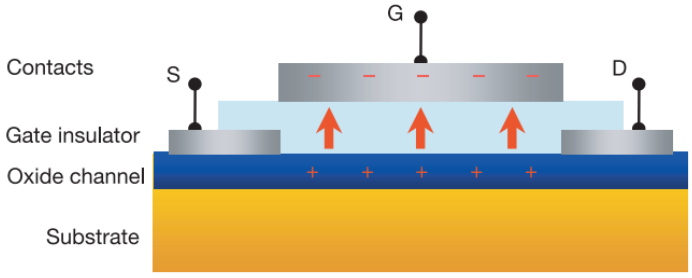

Figure 1.14. Transistor scheme. S, D and G correspond to Source, Drain and Gate.

However, FET structures are limited to inducing a carrier concentration of 10^{13} carriers/cm^2, which is enough to induce large changes to the electronic structures of intrinsic or weakly doped semiconductors. However, as shown in Figure 1.13, is not enough to modulate the intrinsic properties of a correlated oxide. In order to attain larger modifications of

the carrier density, ferroelectric oxides can be used as gate electrodes. As an advantage, the ferroelectric polarization is remnant, so it is not necessary to maintain the voltage applied once the polarization is set. Oxides such as $BiFeO_3$ or $BaTiO_3$ present spontaneous polarization values of 0.25 C/m^2, achieving charge transfers of 10^{14} carriers/cm^2. However, these carrier densities are still not enough to explore the phase diagrams of the complex oxides.

The Electronic Double Layer Transistor (EDLT) overcomes the doping limitations of the FET, achieving carrier densities of 10^{15} carriers/cm^2, enabling the exploration of complex oxide transitions. This system uses a dielectric liquid for the gate instead of a solid dielectric, which makes it possible to achieve such high carrier densities.

The dielectric liquid used in EDLT and in this study is an ionic liquid (IL), which is a molten salt typically composed of an organic cation and an inorganic anion. The electronic conductivity of an IL is negligible because the electrons are entirely bonded to the organic molecules. The cation is highly asymmetric, making the combined structure difficult to pack in a symmetric lattice, resulting in unusually low melting temperatures compared to normal salts like NaCl (800°C). Most ILs form glasses at low temperatures and are typically in the liquid state at room temperature, exhibiting a large ionic conductivity. Due to the long-range Coulomb interactions between ions, ILs have unique properties, such as very low vapor pressures. The ionic liquid mostly used in the gating of EDLT and consequently used in this work is the N,N-diethyl-N-methyl-N- (2-methoxyethyl)-ammonium bis- (trifluoromethanesulfonyl)imide ([DEME] [TFSI]), specified in Figure 1.15.

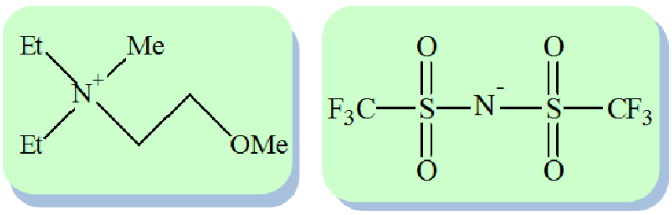

Figure 1.15. Molecular structure of ionic liquid, DEME-TFSI. DEME is positively charged while TFSI is negatively charged.

In EDLT devices, the three terminals (source, drain, and gate) and the surface of the material are submerged in an IL, as shown in Figure 1.16. When a positive voltage is applied between the material/source and the gate, anions accumulate at the gate interface, and cations distribute over the surface of the material, doping the channel with electrons to screen the electric field of the cations and form the Electric Double Layer (EDL) of the device. The name "Electric Double Layer" refers to the two layers of charge that form at the interface between the ionic liquid and the material. The first layer is a layer of anions that accumulates at the gate interface, and the second layer is a layer of cations that distributes over the surface of the conducting channel. The combined effect of these two layers of charge forms the EDL of the device. However, as in conventional FETs with solid dielectrics, it is impossible to operate EDLTs with an unlimited value of the gate bias. Increasing the voltage beyond a specific value determined by the electrochemical stability window of the IL leads to electrochemical reactions. The redox potential between the ionic liquid and the material defines a range of gate doping of several volts, limiting the maximum gate voltage and, therefore, the maximum carrier tunability in the device.

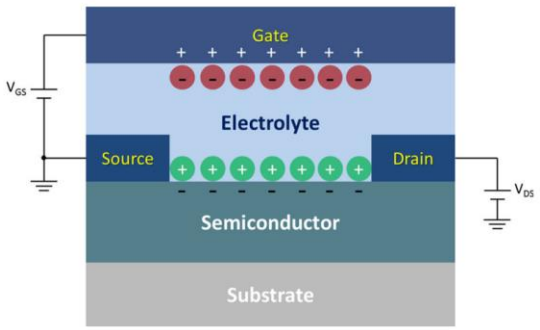

Figure 1.16. Configuration of the electric double-layer transistor

5. Non-collinear spin textures

Non-collinear spin structures have attracted renewed attention in recent years, both in the oxide world and in metal-based systems, for their potential utility as information carriers in computer devices.

Spin textures like spin spirals, magnetic skyrmions, and skyrmion bubbles occur from the competition between the Heisenberg exchange (which causes spins to align parallel or anti-parallel, $S_i \cdot S_j$) and other (non collinear) magnetic interactions. In most cases, the SOC is an essential element that, when combined with a symmetry breaking, results in the Dzyaloshinskii-Moriya Interaction (DMI). Broken inversion symmetry can arise intrinsically in low-symmetry crystals, but there is also extrinsic inversion-symmetry breaking at thin-film interfaces. The DMI is an antisymmetric exchange interaction caused by superexchange between two spins through a third atom with large spin-orbit coupling. Spins are canted to one another as a result of this interaction. The energy contribution is written as $D_{ij} \cdot (S_i \times S_j)$, where D_{ij} is a vector with a direction normal to the plane formed by the three atoms, the magnitude of this vector relies on the symmetry and the spin-orbit coupling. According to the previous expersion, when all of the vectors are perpendicular, the energy term is minimized. This energy factor is usually small in comparison to symmetric Heisenberg exchange, but in some cases, the DMI can result in considerable spin canting. When competing with the Heisenberg exchange, DMI yields a spin-spirals phase. The spiral competes with ferromagnetism in the presence of an external magnetic field or an easy-plane anisotropy, and a skyrmion phase arises at intermediate field strengths [21].

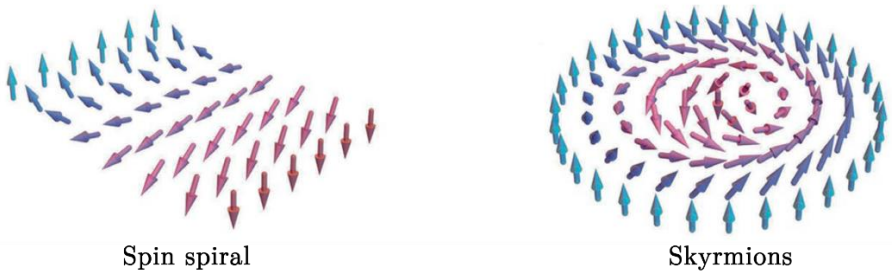

Figure 1.17. Schematic illustration of a spin spiral phase (left) and a skyrmion phase (right).

A slightly distinct particle-like magnetic texture known as the skyrmion bubble has been observed in centrosymmetric magnets [22], [23]. The magnetic bubble is primarily stabilized by the magnetic dipolar interaction, in contrast to the Dzyaloshinskii-Moriya Interaction (DMI).

While skyrmions and chiral magnetic bubbles exhibit varying magnetization profiles within their core regions, they share common characteristics in terms of dynamical response and impact on the Hall signal, which we will discuss further in the following section. These shared properties can be quantified using the skyrmion number (N), a common topological invariant defined as the number of spheres encased by the constituent spins. As a result, a magnetic bubble can be perceived as a type of skyrmion in general and is thus referred to as a "skyrmionic bubble".

Though the study of skyrmion bubbles has a long history, it has recently re-emerged as a hot topic, owing to the emergence of more intricate skyrmion textures caused by the underlying helicity degree of freedom. Furthermore, skyrmion bubbles can form not only in single-phase bulk crystals but also in thin-film multilayers, sometimes in conjunction with the DMI.

Skyrmions and magnetic bubbles can be categorized as topological when they have a non-zero topological charge. This charge is represented by the quantity $\int dr^2 \boldsymbol{m} \cdot (\partial_x \boldsymbol{m} \times \partial_y \boldsymbol{m})$, where 'm' represents the magnetization vector. The in-plane component of the magnetization acquires a Néel-type configuration when it is influenced by an interface-driven Dzyaloshinskii–Moriya interaction (DMI). Conversely, Bloch-type configurations are favored when induced by bulk DMI, dipolar interactions, or a combination of both [24].

Mixed Néel-Bloch states can emerge in the presence of competing interactions. Non-topological bubbles, on the other hand, are distinguished by a combination of opposite chiralities, as shown in Figure 1.18. When DMI shows dominance over dipolar interactions, skyrmion states become preferred. They are distinguished by a compact core with a peak-like

variation in the magnetization's polar angle (θ),that operates as a function of the radial distance 'r' from the core center.

When the dipolar interaction is dominant, magnetic bubbles are preferred, and they are distinguished by a smooth plateau in (r) at their center. Skyrmions are always homochiral, whereas bubbles have varying chirality. They can be homochiral if the DMI is large enough, or heterochiral or achiral if the DMI is small or non-existent. The chirality of the spin textures and their relationship with the topological Hall effect (commented in the following section) will play an essential role in our experiments [24].

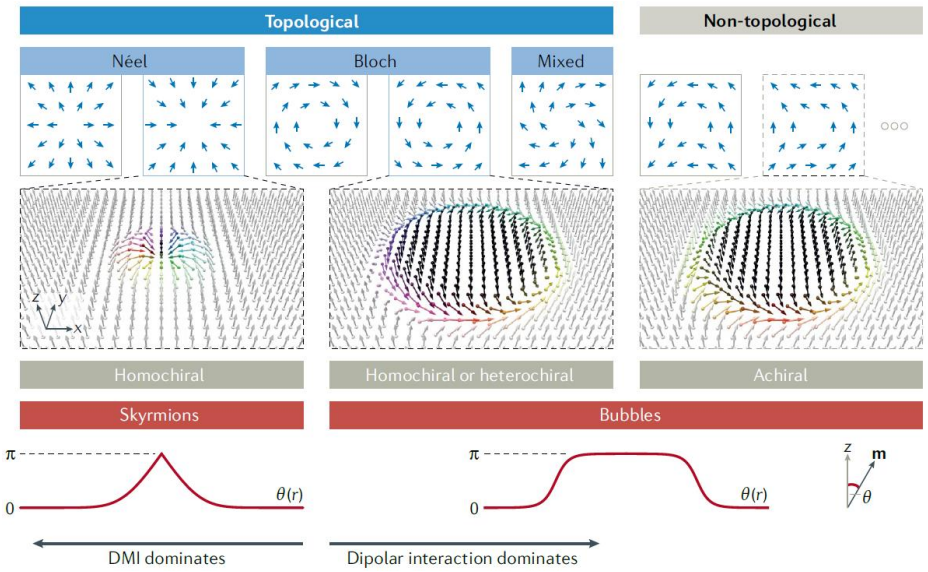

Figure 1.18. Diagram of the various skyrmionic bubble configurations. Topological properties are either Neel-type (where the spin progression occurs in the same plane) or Bloch-type (where the spin progression occurs out-of-plane), but mixed types can generate non-topological spin textures. Adapted from [24].

6. Hall effect

The Hall effect refers to the emergent transversal electric field E_x, generated by an electric current density J_y, under the effect of a perpendicular magnetic field. This relationship can be mathematically expressed using conventional tensor notation as $E_x = \rho_{xy} \cdot J_y$, where ρ_{xy} signifies the Hall resistivity.

The Hall resistivity is recognized as the off-diagonal element of the resistivity tensor, ρ, which stands as the inverse of the conductivity tensor, σ. The connection between Hall resistivity and Hall conductivity is given by $\rho_{xy} = \frac{-\sigma_{xy}}{\sigma_{xx}^2 + \sigma_{xy}^2}$. For smaller Hall angles, when σ_{xy} is much less than σ_{xx}, this relation can be approximated as $\rho_{xy} = \frac{-\sigma_{xy}}{\sigma_{xx}^2}$.

The Hall effect is a powerful tool for the characterization of ferromagnetic materials. It involves different contributions, as illustrated in Figure 1.19, that are associated with diverse material properties: the ordinary Hall effect, OHE, due to the Lorentz force; the anomalous Hall effect, AHE, caused by broken time-reversal symmetry, spin–orbit coupling and intrinsic Berry curvature in momentum space (which can also be non-vanishing in anti-ferromagnets [25], [26]); and the topological Hall effect, THE, which commonly results of Berry curvature effects in real space arising from chiral spin textures. For small Hall angles, the sum of individual contributions gives the total Hall resistivity:

$$\rho_{xy}^{TOTAL} = \rho_{xy}^{OHE} + \rho_{xy}^{AHE} + \rho_{xy}^{THE}$$

The analysis and study of the Hall effect constitute an important part of the research carried out on this thesis. For this reason, in the following subsections, we will discuss in detail these three different components.

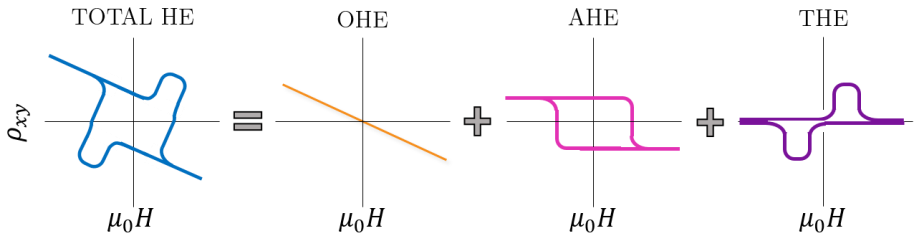

Figure 1.19. Diagram of the three different contributions that make up the Hall effect: the ordinary Hall effect (OHE), the anomalous Hall effect (AHE), and the topological Hall effect (THE). (AHE). As the slope was negative, the OHE was depicted as being dominated by electrons. The AHE was modelled as a ferromagnetic material, with the easy axes oriented perpendicular to the transport measurement direction.

6.1. Ordinary Hall effect

The ordinary Hall effect (OHE) corresponds to the transversal electric field (E_x) generated by an electric current density (J_y) under the application of a perpendicular magnetic field (B_z). It was discovered by Erwin H. Hall in 1879 [27] when he observed that the Lorentz force "presses" its electrons against one side of the conductor.

The Lorenz force (F) follows the equation $F = q(E + v \times B)$, where **F** is the force on charge carriers, q is the charge, **E** is electric field, **v** is the velocity of charge carriers and **B** is an applied magnetic field. In this sense, the steady state is reached when generated the electric field (E_x) compensates the Lorentz force, that is when $E_x = -v_y B_z$. Since the current density can be written as $J_y = v_y nq$, where n is the number density of charge carriers:

$$E_x = -\frac{J_y}{nq} \cdot B_z \quad \rightarrow \quad \frac{E_x}{J_y} = -\frac{1}{nq} \cdot B_z \quad \rightarrow \quad \rho_{xy}^{OHE} = R_0 B_z$$

The ordinary Hall contribution is linear with field with a gradient of $R_0 = -1/nq$, so the carrier density can calculated by measuring ρ_{xy} as a function of the magnetic field. This finding gave a simple and intuitive technique for measuring carrier concentrations in nonmagnetic conductors

and contributed to the birth of semiconductor physics and solid-state electronics in the late 1940s.

This, however, presupposes that only one kind of charge carrier contributes to the OHE; if more than one band is examined, the OHE could differ significantly from linearity. This is significant when the mobility and carrier density of electrons and holes in a material are comparable. The two-band OHE has been used to explain non-linear and non-monotonic Hall effects.

6.2. Anomalous Hall effect

The anomalous Hall effect (AHE) corresponds to the transversal electric field generated by an electric current under the effect of the material magnetization perpendicular to the current (M_z). It was also discovered by Hall in 1881, as he reported that the Hall effect was ten times stronger in ferromagnetic iron than in nonmagnetic conductors [28].

The experiments of Pugh (1930) [29] and Pugh and Lippert (1932) [30] established that an empirical relation for the AHE:

$$\rho_{xy}^{AHE} = R_s M_z$$

This term scales with the magnetization M_z and is characterized by the anomalous Hall coefficient R_s.

The AHE has been an enigmatic problem that has resisted theoretical and experimental assaults for almost a century. The main reason seems to be that, at its core, the AHE problem involves concepts based on topology and geometry that have been formulated only in recent times. It has since been established that the AHE is the result of three mechanisms: one intrinsic contribution and two extrinsic contributions, skew-scattering and side-jump.

Intrinsic contribution

In 1954, Karplus and Luttinger (KL) [31] proposed a theory for the AHE, which was a significant step towards understanding the AHE problem. The KL theory showed that, when an external electric field is applied to a solid, electrons acquire an "anomalous velocity" perpendicular to the electric field. This anomalous velocity contributes to the Hall effects, especially in ferromagnetic conductors. This intrinsic contribution to the AHE depends only on the band structure and is largely independent of scattering, making it proportional to the square of the conductivity tensor, $\rho_{xy}^{int} \approx \sigma_{xy}^{int} \cdot \rho_{xx}^{2}$. This contribution can be related to changes in the phase of Bloch state wave packets in crystal momentum space. The KL theory anticipated modern interest in the Berry phase and the Berry curvature effects, particularly in momentum space.

Skew scattering

The primary criticism of the KL theory is based on the absence of scattering from disorder in the derived Hall response contribution. The semiclassical AHE theories of Smit and Berger, on the other hand, focused on the influence of disorder scattering in imperfect crystals [32], [33]. Smit argued that skew scattering from impurities due to the spin-orbit interaction was what caused the AHE currents, giving the anomalous contribution a linear relationship with the longitudinal resistivity $\rho_{xy}^{sk} \approx \sigma_{xy}^{sk} \cdot \rho_{xx}$.

In ferromagnets the skew scattering (extrinsic) component of the AHE is caused by the spin-dependent scattering of electrons from spin-orbit coupled impurities. The skew-scattering contribution has been more recently understood to result from the spin orbit interaction (either from impurities or from the lattice) and in fact dominates with long scattering times, however in these systems the OHE is expected to be much larger than the AHE, making experimental observation of this contribution difficult. Introducing inelastic scattering (by impurities or phonons) quickly destroys the skew scattering contribution, and in most real materials this effect is negligible.

Side jump

Berger [34] proposed the side-jump mechanism, where quasiparticles experience a side jump upon scattering from spin-orbit coupled impurities. The side-jump mechanism is a discontinuous sideways displacement of quasiparticles scattering from spin-orbit coupled impurities. For the side-jump mechanism the transverse resistivity was predicted to have the same resistivity squared dependence as the intrinsic mechanism, and thus it is very difficult to separate the two experimentally. The side jump mechanism can also be viewed as a result of the intrinsic mechanism acting under a local electric field due to an impurity, rather than due to the applied electric field.

To summarise, Figure 1.20 depicts the three processes underlying the AHE: two extrinsic mechanisms that are influenced by the scattering rate of the system, and one intrinsic mechanism that is connected to the topological properties of the system.

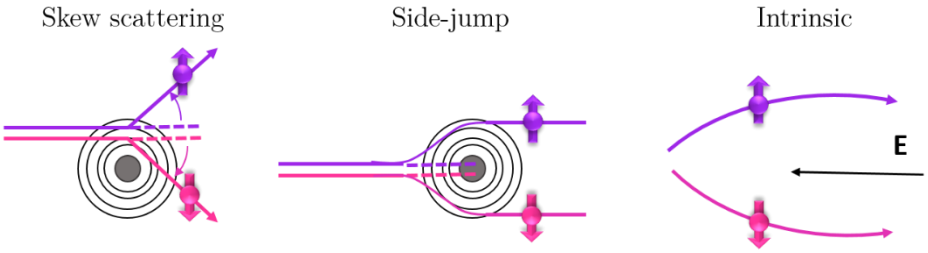

Figure 1.20. Illustration of the three main mechanisms that can give rise to an AHE. (left) Skew scattering: Asymmetric scattering due to the effective spin-orbit coupling of the electron or the impurity. (center) Side jump: The electron velocity is deflected in opposite directions by the opposite electric fields experienced upon approaching and leaving an impurity. (rigth) Intrinsic contribution: Electrons have an anomalous velocity perpendicular to the electric field related to their Berry's phase curvature. In any real material, all of these mechanisms act to influence electron motion.

6.2.1. AHE in manganites

Since part of our research focuses on the anomalous Hall effect in $La_{0.3}Sr_{0.7}MnO_3$ (LSMO) and $SrIrO_3$ (SIO) heterostructures, in this section we are going to analyse the special characteristics of the AHE in manganites as the LSMO. Manganites, as stated in this chapter, are double exchange systems in which itinerant e_g electron spins are coupled to localised t_{2g} spins through the Hund interaction.

AHE in manganites is attributed to non-coplanar spin configurations of the localised t_{2g} manifolds, which acquire a scalar spin chirality (real space Berry phase) and operate as a virtual magnetic field in real space, resulting in an intrinsic (real space) contribution to the AHE [35], [36]. This unusual AHE is responsible for the AHE distinctive temperature dependence. It is negligibly small at low temperatures, developing only when the temperature reaches approximately $T_C/2$ and peaking near T_C [37]–[39], and in the case of LSMO, it is approximately 300 K.

Illustrating this temperature dependence, we can see Hall measurements of a 16-nm LSMO layer in Figure 1.21: (a) shows the total Hall effect (Total HE) at temperatures ranging from 2 K to 280 K, and (b) shows the AHE derived from the OHE subtraction. It is essential to note that the applied magnetic field was out of plane. This explains the absence of hysteresis in the Hall measurements, as out of the easy axis magnetization switching occurs by rotation of spins which produces no hysteresis.

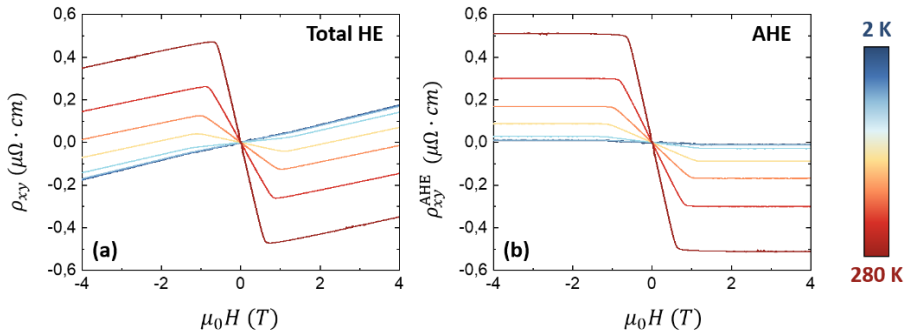

Figure 1.21. Transverse Hall resistivity vs magnetic field applied perpendicularly to the surface at temperatures from 2 K to 280 K. The sample is a 16-nm LSMO monolayer. (a) Total Hall Effect (Total HE), and (b) Anomalous Hall Effect (AHE), arising from the substration of the Ordinary Hall Effect (OHE).

6.3. Topological Hall effect

Contrary to the intrinsic AHE, which relies on the Berry curvature in k-space, the topological Hall effect (THE) is associated with the accumulation of Berry-phase in real space [40] due to chiral spin textures. When an electron is subjected to a slowly changing exchange field in a ferromagnet, its spin follows the direction of the magnetization in the adiabatic limit (or strong-coupling limit). If the magnetization varies in a closed loop, the electron experiences a cycle in parameter space, acquiring a geometrical phase. In this scenario, the phase is proportional to the solid angle subtended by the exchange field, generating an additional emergent magnetic field experienced by the electrons, which contributes to the Hall effect.

Chiral spin structures, as skyrmion bubbles described before, can exhibit spin chirality. Spin chirality can also arise from magnetic frustration or thermally activated spin chirality fluctuations [36], [38], [41]. Typically, spin chirality is stabilized within a limited field range, causing the THE to manifest as a peak in the Hall effect versus field. The magnitude of this peak is commonly approximated as[40]:

$$\rho_{xy}^{THE} = PR_0B_{eff} = PR_0n_{SK}\Phi_0$$

where P represents the transport spin polarization of the ferromagnet, R_0 is the effective charge density contributing to the THE (usually taken as the ordinary Hall coefficient [42]), and B_{eff} is the effective magnetic flux density generated by the skyrmions [43]. This effective magnetic flux density is defined as $B_{eff} = n_{SK}\Phi_0$, where n_{SK} denotes the skyrmion density and Φ_0 is the magnetic flux quantum.

The term "topological Hall effect" (THE) may cause confusion as it doesn't necessarily require a topologically non-trivial spin texture. THE arises from an effective magnetic flux generated by electrons passing through a chiral spin texture or from a real-space Berry curvature. Chiral spin textures without integer topological charge can still contribute to the Hall effect due to Berry phase, and these effects are sometimes called THE. A more general term like "spin chirality Hall effect" might be more

appropriate, but for consistency, we continue to use "topological Hall effect." Intrinsic Anomalous Hall Effect (AHE) is related to Berry curvature in k-space and includes topological aspects of the band structure. Both intrinsic and topological Hall effects can be viewed as Berry curvature in real or momentum space [44]. The distinction between AHE and THE is helpful from an experimental perspective. Intrinsic AHE is due to Berry curvature commensurate with the crystal lattice, while THE results from chiral spin textures not necessarily commensurate with the lattice, leading to spatially non-uniform emergent fields [45].

6.3.1. THE and chiral spin textures in thin films

The Hall effect arising from real-space spin chirality was first discussed in the context of colossal magnetoresistance manganites [36], [38], pyrochlore ferromagnets [46], and non-coplanar antiferromagnets [47]. This phenomenon was attributed to spin chirality at the microscopic level, stemming from thermally excited chiral fluctuations or magnetic frustration, rather than skyrmions.

The topological Hall effect (THE) caused by skyrmions was first reported in single-crystal MnSi [43] and polycrystalline MnGe [48] bulk samples. However, difficulties often arise in correlating THE with skyrmions measured by real-space imaging. The stability of different skyrmion phases is strongly dependent on sample dimensions and material quality [49]. Additionally, correlating transmission electron microscopy (TEM) measurements with Hall effects is challenging due to the requirement to mill samples into thin cross-section layers.

The detection of THE in thin films remains controversial, primarily due to discrepancies between THE and real-space imaging. Although there have been reports of THE in Ir/Fe/Co/Pt heterostructures [50], subsequent studies using Hall measurements and real-space skyrmion imaging found that the change in the Hall signal cannot be solely attributed to THE [42], [51], [52]. This discrepancy has been ascribed to changes in the anomalous Hall effect (AHE) due to skyrmions altering the net magnetization value [51]. Moreover, the assumptions used in the related equation have been called into question, such as the use of the

ordinary Hall coefficient R_0 [18] and the applicability of the adiabatic approximation in thin films with significant spin-flip scattering.

In addition to metallic heterostructures such as Co/Pt [42], [50]–[52], topological Hall effects (THEs) have been reported in various thin films, including intermetallics [53]–[55], Heusler compounds [56], topological insulator heterostructures [57], [58], and diverse oxide thin-film systems. A giant THE, significantly larger than those observed in other single-crystal and thin-film systems, has been recently detected in Ce-doped calcium manganite [59].

Many studies abandon real-space imaging of skyrmions, relying instead on non-monotonic Hall signals or discrepancies between magnetic and Hall hysteresis loops as evidence of chirality. Real-space imaging, when employed, often yields results that are challenging to interpret, with the number of bubble-like features frequently being lower than the expected skyrmion count based on Hall effect and theoretical predictions. The practice of ascribing Hall effect anomalies to chiral spin textures has been questioned [60], as topological Hall signals could potentially be interpreted as multiple anomalous Hall effects (AHEs) arising from various inhomogeneities, as it is sketched in Figure 1.22.

The ambiguity between differing interpretations of the same Hall data has been further explored using $SrRuO_3$ as a model system. The AHE of the $SrRuO_3$ change as a function of various parameters such as magnetisation [61], temperature [62], strain [63], film thickness [64] and doping [65].

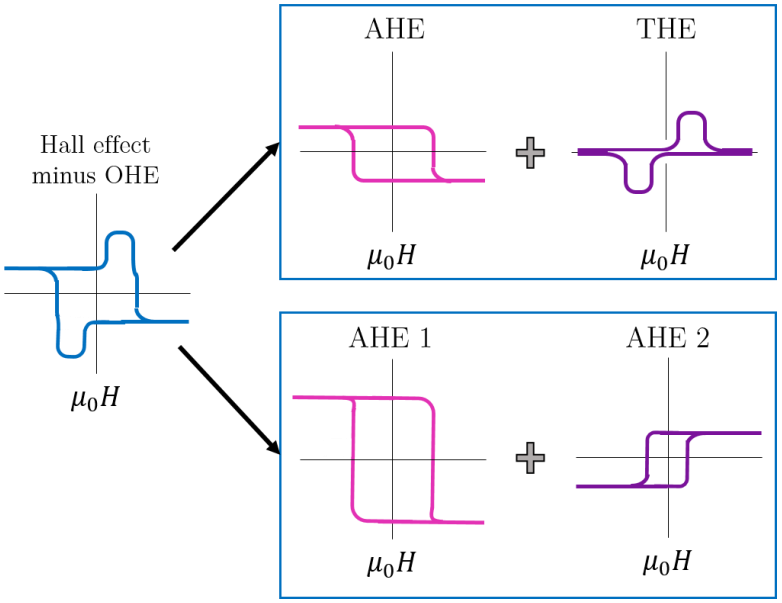

Figure 1.22. The analysis of different non-monotonic Hall signals can vary between being attributed to various types of AHE or a combination of AHE and THE. Figure adapted from [66].

7. References

[1] S. Maekawa, T. Tohyama, S. E. Barnes, S. Ishihara, W. Koshibae, y G. Khaliullin, *Physics of transition metal oxides*, vol. 144. Springer Science & Business Media, 2004.

[2] Y. Tokura y N. Nagaosa, «Orbital Physics in Transition-Metal Oxides», *Science*, vol. 288, n.º 5465, pp. 462-468, abr. 2000, doi: 10.1126/science.288.5465.462.

[3] M. Imada, A. Fujimori, y Y. Tokura, «Metal-insulator transitions», *Rev. Mod. Phys.*, vol. 70, n.º 4, 1998.

[4] J. Hubbard, «Electron correlations in narrow energy bands III. An improved solution», *Proceedings of the Royal Society of London. Series A. Mathematical and Physical Sciences*, vol. 281, n.º 1386, pp. 401-419, 1964.

[5] B. J. Kim *et al.*, «Novel J eff = 1 / 2 Mott State Induced by Relativistic Spin-Orbit Coupling in Sr 2 IrO 4», *Phys. Rev. Lett.*, vol. 101, n.º 7, Art. n.º 7, ago. 2008, doi: 10.1103/PhysRevLett.101.076402.

[6] S. J. Moon *et al.*, «Dimensionality-Controlled Insulator-Metal Transition and Correlated Metallic State in 5 d Transition Metal Oxides Sr n + 1 Ir n O 3 n + 1 (n = 1 , 2, and ∞)», *Phys. Rev. Lett.*, vol. 101, n.º 22, Art. n.º 22, nov. 2008, doi: 10.1103/PhysRevLett.101.226402.

[7] J. K. Kawasaki, M. Uchida, H. Paik, D. G. Schlom, y K. M. Shen, «Evolution of electronic correlations across the rutile, perovskite, and Ruddelsden-Popper iridates with octahedral connectivity», *Phys. Rev. B*, vol. 94, n.º 12, Art. n.º 12, sep. 2016, doi: 10.1103/PhysRevB.94.121104.

[8] Y. F. Nie *et al.*, «Interplay of Spin-Orbit Interactions, Dimensionality, and Octahedral Rotations in Semimetallic SrIrO 3», *Phys. Rev. Lett.*, vol. 114, n.º 1, Art. n.º 1, ene. 2015, doi: 10.1103/PhysRevLett.114.016401.

[9] B. Kim, P. Liu, y C. Franchini, «Dimensionality-strain phase diagram of strontium iridates», *Phys. Rev. B*, vol. 95, n.º 11, Art. n.º 11, mar. 2017, doi: 10.1103/PhysRevB.95.115111.

[10] J. Liu *et al.*, «Tuning the electronic properties of J_eff=1/2 correlated semimetal in epitaxial perovskite SrIrO3», n.º arXiv:1305.1732. arXiv, 8 de mayo de 2013. Accedido: 23 de enero de 2023. [En línea]. Disponible en: http://arxiv.org/abs/1305.1732

[11] N. Manca *et al.*, «Balanced electron-hole transport in spin-orbit semimetal SrIrO3 heterostructures», *Phys. Rev. B*, vol. 97, n.º 8, Art. n.º 8, feb. 2018, doi: 10.1103/PhysRevB.97.081105.

[12] D. J. Groenendijk *et al.*, «Spin-Orbit Semimetal SrIrO 3 in the Two-Dimensional Limit», *Phys. Rev. Lett.*, vol. 119, n.º 25, Art. n.º 25, dic. 2017, doi: 10.1103/PhysRevLett.119.256403.

[13] A. Urushibara, Y. Moritomo, T. Arima, A. Asamitsu, G. Kido, y Y. Tokura, «Insulator-metal transition and giant magnetoresistance in La 1- x Sr x MnO 3», *Physical Review B*, vol. 51, n.º 20, p. 14103, 1995.

[14] C. Zener, «Interaction between the d-Shells in the Transition Metals. II. Ferromagnetic Compounds of Manganese with Perovskite Structure», *Phys. Rev.*, vol. 82, n.º 3, pp. 403-405, may 1951, doi: 10.1103/PhysRev.82.403.

[15] M. Huijben *et al.*, «Critical thickness and orbital ordering in ultrathin La0.7Sr0.3MnO3 films», *Phys. Rev. B*, vol. 78, n.º 9, p. 094413, sep. 2008, doi: 10.1103/PhysRevB.78.094413.

[16] D. G. Schlom, L.-Q. Chen, X. Pan, A. Schmehl, y M. A. Zurbuchen, «A thin film approach to engineering functionality into oxides», *Journal of the American Ceramic Society*, vol. 91, n.º 8, pp. 2429-2454, 2008.

[17] A. Biswas, Y. H. Jeong, A. Biswas, y Y. H. Jeong, «Strain Effect in Epitaxial Oxide Heterostructures», en *Epitaxy*, IntechOpen, 2017. doi: 10.5772/intechopen.70125.

[18] J. M. Rondinelli y N. A. Spaldin, «Structure and properties of functional oxide thin films: insights from electronic-structure calculations», *Advanced materials*, vol. 23, n.º 30, pp. 3363-3381, 2011.

[19] Greve D.W., «Field effect devices and applications», Guide books. Accedido: 24 de febrero de 2023. [En línea]. Disponible en: https://dl.acm.org/doi/abs/10.5555/290018

[20] C. H. Ahn, J.-M. Triscone, y J. Mannhart, «Electric field effect in correlated oxide systems», *Nature*, vol. 424, n.º 6952, Art. n.º 6952, ago. 2003, doi: 10.1038/nature01878.

[21] X. Li, W. V. Liu, y L. Balents, «Spirals and skyrmions in two dimensional oxide heterostructures», *Physical review letters*, vol. 112, n.º 6, p. 067202, 2014.

[22] S. Mühlbauer *et al.*, «Skyrmion lattice in a chiral magnet», *Science*, vol. 323, n.º 5916, Art. n.º 5916, 2009.

[23] M. Ezawa, «Compact merons and skyrmions in thin chiral magnetic films», *Physical Review B*, vol. 83, n.º 10, p. 100408, 2011.

[24] F. Trier, P. Noël, J.-V. Kim, J.-P. Attané, L. Vila, y M. Bibes, «Oxide spin-orbitronics: spin–charge interconversion and topological spin textures», *Nat Rev Mater*, vol. 7, n.º 4, pp. 258-274, nov. 2021, doi: 10.1038/s41578-021-00395-9.

[25] L. Šmejkal, R. González-Hernández, T. Jungwirth, y J. Sinova, «Crystal time-reversal symmetry breaking and spontaneous Hall effect in collinear antiferromagnets», *Science advances*, vol. 6, n.º 23, p. eaaz8809, 2020.

[26] M. Asa *et al.*, «Anomalous Hall effect in antiferromagnetic/nonmagnetic interfaces», *Physical Review Research*, vol. 2, n.º 4, p. 043394, 2020.

[27] E. H. Hall, «On a New Action of the Magnet on Electric Currents», *American Journal of Mathematics*, vol. 2, n.º 3, pp. 287-292, 1879, doi: 10.2307/2369245.

[28] E. H. Hall, «XVIII. On the "Rotational Coefficient" in nickel and cobalt», *The London, Edinburgh, and Dublin Philosophical Magazine and Journal of Science*, vol. 12, n.º 74, pp. 157-172, sep. 1881, doi: 10.1080/14786448108627086.

[29] E. M. Pugh, «Hall Effect and the Magnetic Properties of Some Ferromagnetic Materials», *Phys. Rev.*, vol. 36, n.º 9, pp. 1503-1511, nov. 1930, doi: 10.1103/PhysRev.36.1503.

[30] E. M. Pugh y T. W. Lippert, «Hall e.m.f. and Intensity of Magnetization», *Phys. Rev.*, vol. 42, n.º 5, pp. 709-713, dic. 1932, doi: 10.1103/PhysRev.42.709.

[31] R. Karplus y J. M. Luttinger, «Hall Effect in Ferromagnetics», *Phys. Rev.*, vol. 95, n.º 5, pp. 1154-1160, sep. 1954, doi: 10.1103/PhysRev.95.1154.

[32] J. Smit, «The spontaneous hall effect in ferromagnetics I», *Physica*, vol. 21, n.º 6, pp. 877-887, ene. 1955, doi: 10.1016/S0031-8914(55)92596-9.

[33] J. Smit, «The spontaneous hall effect in ferromagnetics II», *Physica*, vol. 24, n.º 1, pp. 39-51, ene. 1958, doi: 10.1016/S0031-8914(58)93541-9.

[34] L. Berger, «Side-Jump Mechanism for the Hall Effect of Ferromagnets», *Phys. Rev. B*, vol. 2, n.º 11, pp. 4559-4566, dic. 1970, doi: 10.1103/PhysRevB.2.4559.

[35] Y. Lyanda-Geller *et al.*, «Charge transport in manganites: Hopping conduction, the anomalous Hall effect, and universal scaling», *Phys. Rev. B*, vol. 63, n.º 18, p. 184426, abr. 2001, doi: 10.1103/PhysRevB.63.184426.

[36] J. Ye, Y. B. Kim, A. J. Millis, B. I. Shraiman, P. Majumdar, y Z. Tešanović, «Berry Phase Theory of the Anomalous Hall Effect: Application to Colossal Magnetoresistance Manganites», *Phys. Rev. Lett.*, vol. 83, n.º 18, pp. 3737-3740, nov. 1999, doi: 10.1103/PhysRevLett.83.3737.

[37] M. Bibes *et al.*, «Anisotropic magnetoresistance and anomalous Hall effect in manganite thin films», *Journal of Physics Condensed Matter*, vol. 17, n.º 17, pp. 2733-2740, may 2005.

[38] P. Matl *et al.*, «Hall effect of the colossal magnetoresistance manganite La1-xCaxMnO3», *Phys. Rev. B*, vol. 57, n.º 17, pp. 10248-10251, may 1998, doi: 10.1103/PhysRevB.57.10248.

[39] G. Jakob, F. Martin, W. Westerburg, y H. Adrian, «Evidence of charge-carrier compensation effects in La0.67Ca0.33MnO3», *Phys. Rev. B*, vol. 57, n.º 17, pp. 10252-10255, may 1998, doi: 10.1103/PhysRevB.57.10252.

[40] P. Bruno, V. K. Dugaev, y M. Taillefumier, «Topological Hall Effect and Berry Phase in Magnetic Nanostructures», *Phys. Rev. Lett.*, vol. 93, n.º 9, p. 096806, ago. 2004, doi: 10.1103/PhysRevLett.93.096806.

[41] W. Wang *et al.*, «Spin chirality fluctuation in two-dimensional ferromagnets with perpendicular magnetic anisotropy», *Nature materials*, vol. 18, n.º 10, pp. 1054-1059, 2019.

[42] M. Raju *et al.*, «The evolution of skyrmions in Ir/Fe/Co/Pt multilayers and their topological Hall signature», *Nature communications*, vol. 10, n.º 1, p. 696, 2019.

[43] A. Neubauer *et al.*, «Topological Hall Effect in the A Phase of MnSi», *Phys. Rev. Lett.*, vol. 102, n.º 18, p. 186602, may 2009, doi: 10.1103/PhysRevLett.102.186602.

[44] O. Busch, B. Göbel, y I. Mertig, «Microscopic origin of the anomalous Hall effect in noncollinear kagome magnets», *Physical Review Research*, vol. 2, n.º 3, p. 033112, 2020.

[45] P. Nikolić, «Quantum field theory of topological spin dynamics», *Physical Review B*, vol. 102, n.º 7, p. 075131, 2020.

[46] Y. Taguchi, Y. Oohara, H. Yoshizawa, N. Nagaosa, y Y. Tokura, «Spin chirality, Berry phase, and anomalous Hall effect in a frustrated ferromagnet», *Science*, vol. 291, n.º 5513, pp. 2573-2576, 2001.

[47] R. Shindou y N. Nagaosa, «Orbital ferromagnetism and anomalous Hall effect in antiferromagnets on the distorted fcc lattice», *Physical Review Letters*, vol. 87, n.º 11, p. 116801, 2001.

[48] N. Kanazawa *et al.*, «Large topological Hall effect in a short-period helimagnet MnGe», *Physical review letters*, vol. 106, n.º 15, p. 156603, 2011.

[49] S. Wang *et al.*, «Giant topological Hall effect and superstable spontaneous skyrmions below 330 K in a centrosymmetric complex noncollinear ferromagnet NdMn2Ge2», *ACS applied materials & interfaces*, vol. 12, n.º 21, pp. 24125-24132, 2020.

[50] A. Soumyanarayanan, «Tunable Room Temperature Skyrmions in Ir/Fe/Co/Pt Multilayers», en *APS March Meeting Abstracts*, 2017, pp. F50-001.

[51] D. Maccariello *et al.*, «Electrical detection of single magnetic skyrmions in metallic multilayers at room temperature», *Nature nanotechnology*, vol. 13, n.º 3, pp. 233-237, 2018.

[52] K. Zeissler *et al.*, «Discrete Hall resistivity contribution from Néel skyrmions in multilayer nanodiscs», *Nature Nanotechnology*, vol. 13, n.º 12, pp. 1161-1166, 2018.

[53] N. Kanazawa *et al.*, «Discretized topological Hall effect emerging from skyrmions in constricted geometry», *Physical Review B*, vol. 91, n.º 4, p. 041122, 2015.

[54] K. K. Meng *et al.*, «Robust emergence of a topological Hall effect in MnGa/heavy metal bilayers», *Physical Review B*, vol. 97, n.º 6, p. 060407, 2018.

[55] B. M. Ludbrook, G. Dubuis, A.-H. Puichaud, B. J. Ruck, y S. Granville, «Nucleation and annihilation of skyrmions in Mn2CoAl observed through the topological Hall effect», *Scientific reports*, vol. 7, n.º 1, p. 13620, 2017.

[56] P. K. Sivakumar *et al.*, «Topological Hall signatures of two chiral spin textures hosted in a single tetragonal inverse Heusler thin film», *ACS nano*, vol. 14, n.º 10, pp. 13463-13469, 2020.

[57] K. Yasuda *et al.*, «Geometric Hall effects in topological insulator heterostructures», *Nature Physics*, vol. 12, n.º 6, pp. 555-559, 2016.

[58] Q. L. He *et al.*, «Exchange-biasing topological charges by antiferromagnetism», *Nature communications*, vol. 9, n.º 1, p. 2767, 2018.

[59] L. Vistoli *et al.*, «Giant topological Hall effect in correlated oxide thin films», *Nature Physics*, vol. 15, n.º 1, pp. 67-72, 2019.

[60] A. Gerber, «Interpretation of experimental evidence of the topological Hall effect», *Physical Review B*, vol. 98, n.º 21, p. 214440, 2018.

[61] Z. Fang *et al.*, «The anomalous Hall effect and magnetic monopoles in momentum space», *Science*, vol. 302, n.º 5642, pp. 92-95, oct. 2003, doi: 10.1126/science.1089408.

[62] L. Klein, J. R. Reiner, T. H. Geballe, M. R. Beasley, y A. Kapitulnik, «Extraordinary Hall Effect in SrRuO 3», *Physical Review B*, vol. 61, n.º 12, p. R7842, 2000.

[63] D. Tian *et al.*, «Manipulating Berry curvature of SrRuO3 thin films via epitaxial strain», *Proceedings of the National Academy of Sciences*, vol. 118, n.º 18, p. e2101946118, 2021.

[64] L. Wang, Q. Feng, H. G. Lee, E. K. Ko, Q. Lu, y T. W. Noh, «Controllable thickness inhomogeneity and Berry curvature engineering of anomalous Hall effect in SrRuO3 ultrathin films», *Nano letters*, vol. 20, n.º 4, pp. 2468-2477, 2020.

[65] R. Mathieu *et al.*, «Scaling of the Anomalous Hall Effect in S r 1- x C a x R u O 3», *Physical review letters*, vol. 93, n.º 1, p. 016602, 2004.

[66] G. Kimbell, C. Kim, W. Wu, M. Cuoco, y J. W. Robinson, «Challenges in identifying chiral spin textures via the topological Hall effect», *Communications Materials*, vol. 3, n.º 1, p. 19, 2022.

Chapter 2

Experimental Methods

1. Sample growth by high pressure sputtering

The samples used in this thesis have been grown by high oxygen pressure sputtering from a target stoichiometrically identical to the samples being grown. Targets used during this thesis include $SrIrO_3$, $La_{0.7}Sr_{0.3}MnO_3$, and $BaTiO_3$. The targets, located inside a vacuum chamber, are connected to an RF signal, and, as a result, self-polarize to a negative DC voltage. Energetic electrons and positive ions are formed in the ionization of the sputtering gas (oxygen) which is excited into a plasma state. Positive ions diffuse towards the target feel its electric field and are accelerated collisioning with its surface, from which atoms are extracted. The RF power depends on the substrate's size; targets with a 35 mm diameter are connected to 45-55 W, while targets with a 50 mm diameter receive 100-120 W.

The O ions impact the target surface provoking the ejection of atomic and binary oxides species[1]. The particles are deposited on a substrate below the target. The substrates are oxide single crystals, for example, $SrTiO_3$, cut along crystalline directions. The choice of substrate depends on its lattice parameter, as well as on its electronic and magnetic properties. This substrate is placed on a heater plate with a temperature between 650 and 900°C. High temperatures are necessary to ensure high mobility of the deposited particles, what enables layer-by-layer growth instead of three-dimensional growth.

The growth takes place in a vacuum chamber, as observed in Figure 2.1. Prior to the growth, a base pressure of about 3×10^{-5} mBar is achieved

using a turbo-molecular pump baked by a membrane pump. During the growth, a constant O_2 flow is injected into the chamber, and the pressure is controlled by a system of needle valves. To enable good thermalization of the sputtered particles and to avoid back-sputtering phenomena, the growth must take place in a high-pressure atmosphere of 2.8 – 3.4 mBar. This pressure level is considered high compared to typical sputtering growth which is performed at pressures of the order of 10^{-2} mBar.

The sputtering process depends on several parameters, such as the substrate temperature, chamber pressure, power applied to the target, and distance between the target and substrate. For this reason, for each target material it is necessary to determine the optimum growth conditions.

After the growth, a (typically) 1-hour annealing at temperatures between 650 and 800°C is necessary to ensure the correct oxygen content in the sample. Following this method, a very slow rate of deposition (about 0.3 nm/min) is achieved, which is necessary for growing uniform and epitaxial samples with high crystal quality. The deposition rate and thickness uniformity are analyzed after the growth process using XRD, XRR, and STM, as detailed in the following sections.

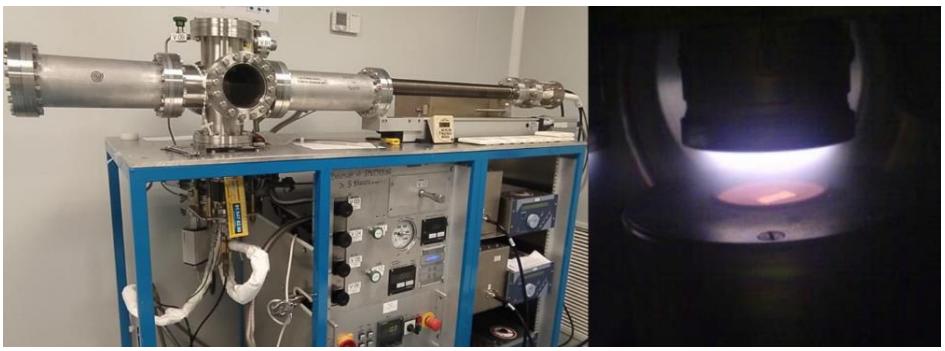

Figure 2.1. (left) Sputtering chamber (right) oxygen plasma formed at the sputtering target.

2. Nanofabrication techniques

To perform accurate magnetotransport characterization, the thin film must be patterned into a Hall bar with well-defined dimensions using optical lithography and reactive ion etching. Hall bar devices are commonly used for this objective due to their good geometry for measuring resistance.

2.1. Optical lithography

Optical lithography is a widely used technique for generating two-dimensional patterns at the micron scale. This process essentially involves transferring a pattern from a mask to our thin film [2]. The pattern we want to fabricate is designed and replicated on a photomask made of glass or quartz. The pattern is printed on the photomask with a thin chromium or ferrite layer using high-resolution electron beam lithography. Once the pattern is on the photomask, a photoresist sensitive to UV light is applied over the thin-film surface to transfer the pattern to the sample. The photoresist used will be detailed in the following section. By applying UV light through the mask, parts of the surface will be exposed. The exposed part will undergo polymeric reactions that will either harden or soften the exposed resist, depending on the resist type.

There are two different resist types: positive and negative. The positive resist reproduces the exact same mask pattern, as the exposed resist undergoes scission of its polymeric chains and is later removed by a developer. On the other hand, the negative photoresist will reproduce the opposite pattern, as the exposed resist undergoes repolymerization, becoming chemically inert. In this case, the unexposed part will be removed [3]. In order to achieve high lateral resolution—about a few microns—the resist layer applied must be considerably thinned. For this reason, the resist is applied using a spinner system that reaches 7000 rpm (see Figure 2.2 right).

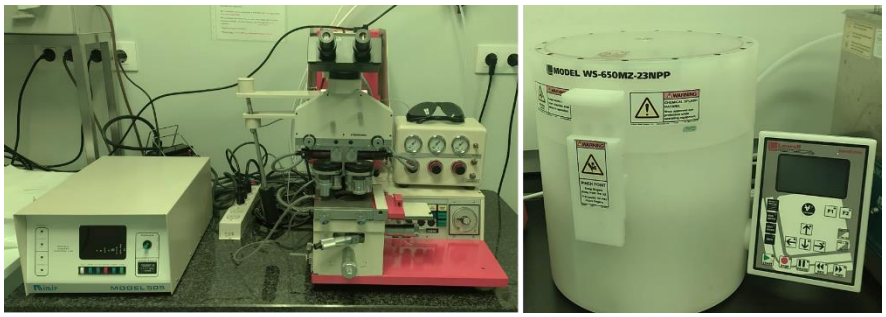

Figure 2.2. (left) Photography of the alignment and exposure system. (right) Photography of spinner system

The most critical part of the photolithography process is mask alignment and exposure, which are carried out using a Karl Suss MJB 3 mask aligner system, as seen in Figure 2.2 left. This system consists of a lens set to collimate the UV light generated by the Hg lamp, an optical microscope, a mask holder, and an alignment system with different micrometer screws. After development, the thin-film part not protected by the resist will be removed. This process can be carried out using two different methods: wet etching, with chemical etchants like HCl, KCl, phosphoric acid, etc., or dry etching, using ion milling. The etching process used in the experiment will be described in the following section. Finally, the resist will be completely removed, leaving the pattern on our sample. Figure 2.3 illustrates the entire process.

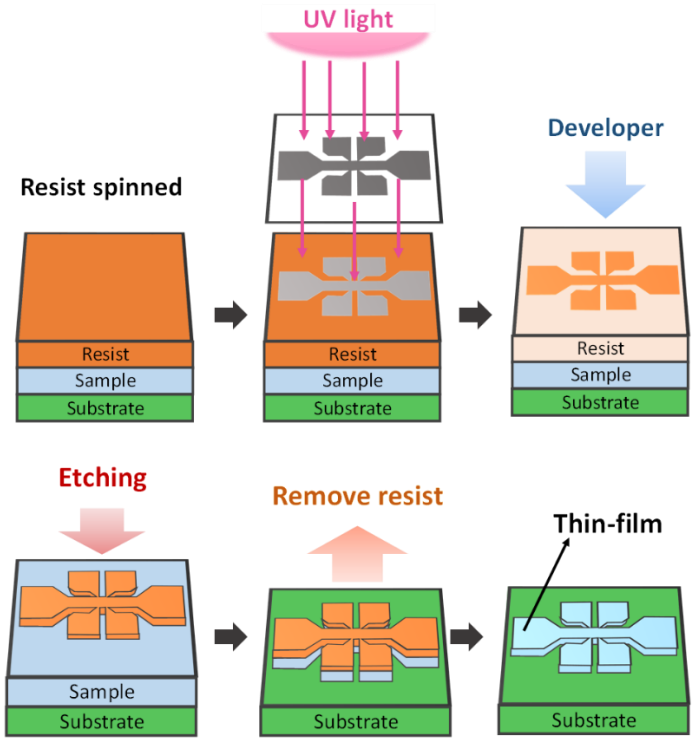

Figure 2.3. Scheme of the whole photolithography process

2.2. Reactive ion etching (RIE)

Reactive ion etching (RIE) is an etching technology used in microfabrication. RIE is a type of dry etching where reactive plasma is used to remove material from a sample. In this thesis, all the dry etching processes have been carried out using a South Bay Reactive Ion Etcher 2000, as shown in Figure 2.4. The ion etching process is basically a sputtering process, where our sample is the sputtered target. The sample is placed on an isolated holder from the rest of the vacuum chamber. By applying an RF power of 13.56 MHz and some hundreds of watts, the oscillating electric field will rip electrons from the gas molecules, ionizing them and forming plasma. The electrons deposited on the sample holder will build up a charge due to its isolation. The charge will generate a negative voltage that drifts the positive ions towards the sample, etching the sample [4]–[6]. This process will be developed at a considerably high

pressure of about 200 mTorr in order to ensure an isotropic and low-ratio etching. As in other sputtering systems, the RIE process strongly depends on many parameters, such as pressure, RF power, gas used, and sample sputtered. In our case using Ar plasma, the etch oxide ratios are low compared with the resist ratio; however, the resist thickness is three orders of magnitude larger than the thin-film thickness. Thanks to this, the film etching can be finished before the resist is completely removed. To minimize the sample heating, which can degrade the resist and deoxygenate the sample, the sample holder is water cooled. Despite this, the Ar etching frequently forms a degraded resist layer that is not soluble in acetone. In order to remove this resist, O_2 plasma etching has been demonstrated to be a valid solution.

Figure 2.4. Photography of RIE system

2.3. Hall bar fabrication process

The Hall bar fabrication process can be divided into four distinct steps, as sketched in Figure 2.5:

1- Gold sputtering: After growing the thin film by high-pressure sputtering, a metal layer of gold is deposited on the entire sample surface. This gold layer will serve as the future contacts of the Hall Bar. The sputtering is carried out in a sputtering system, which operates using the same physical principles as the high-pressure sputtering described in the Sample Growth section. In

this case, Ar ions are used as the sputtering agent, and a low pressure of about 10^{-3} mBar is employed to increase the deposition rate.

2- Hall Bar optical lithography: This first lithography process defines the shape of the entire Hall Bar. Positive resist (SPR-700) and a clear mask with the Hall Bar patterns in chromium are used for this purpose, as shown in Figure 2.5. After alignment and exposure, the developer MF-319 is used to remove the softened resist.

3- Reactive ion etching: Both the gold layer and the thin film not protected by resist are removed by Ar ion milling. As this process may burn the resist, an additional O_2 ion etching is performed to remove it. As a result, a gold Hall Bar is formed.

4- Contacts definition by optical lithography: In the second lithography step, a mask similar to the first one is used, but with the contacts shape, allowing the gold deposited on the contacts to remain and removing the gold deposited on the bar. An example of the resulting Hall Bar can be observed in Figure 2.5 (bottom left).

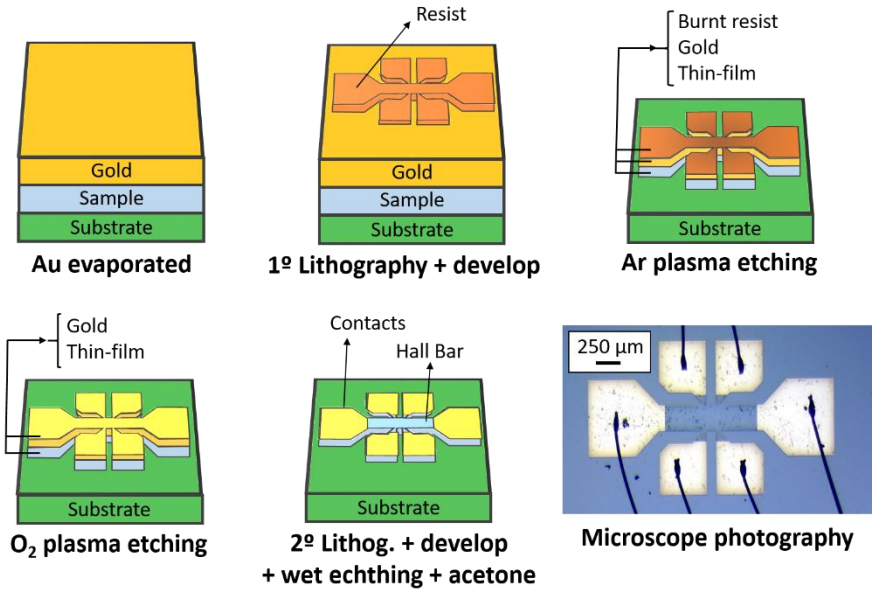

Figure 2.5. Sketch illustrating the Hall Bar fabrication process

3. Structural characterization

3.1. X-ray characterization

The patterns observed in X-ray reflectivity (XRR) and diffraction (XRD) provide information about the thickness, crystalline structure, and roughness of a sample. The XRR and XRD measurements were conducted using a Philips X'pert Pro MRD diffractometer with a Cu tube as the X-ray source ($\lambda_x = 0{,}15418\ nm$). These patterns are obtained by measuring the reflected or refracted X-ray intensity as a function of the radiation incident angle (θ), which is detected by a detector positioned at 2θ respect the source, as shown in Figure 2.6.

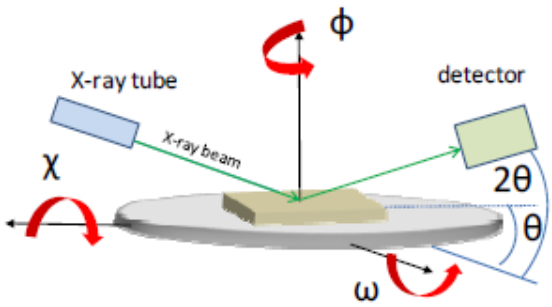

Figure 2.6. Schematic diagram of the θ-2θ measuring geometry

3.1.1. X-ray reflectivity (XRR)

When collimated and coherent Cu k_α radiation impinges onto the sample, reflections occur both at the material surface and at the sample-substrate interface. These reflections depend on the refractive index of the sample, which is given by the formula:

$$n = 1 - \frac{\rho_n r_e \lambda_x}{2\pi}(f_0 + \Delta f' - i\Delta f'') = 1 - \delta + i\beta \qquad (2.1)$$

where ρ_n is the electron density, r_e is the electron radius, f_0 is the atomic dispersion factor and $\Delta f'$, $\Delta f''$ are corrections to the anomalous dispersion [7]. Reflections at different interfaces produce differences in the

X-ray path length, resulting in constructive or destructive interference (see Figure 2.7).

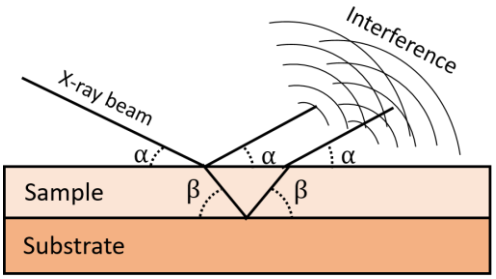

Figure 2.7. Scheme of the interference process

As a result, interference creates oscillations in the reflective pattern. The period of these finite-size oscillations scale inversely with the thickness (d) of the sample. By indexing the position of the maximum or minimum peaks, the thickness can be calculated using the formula:

$$\sin^2\theta = \left[\frac{(m-k)\lambda_x}{2d}\right] + 2\delta \tag{2.2}$$

where k = 0 in a minimum, k = 1/2 in a maximum, and 1 - δ corresponds to the real part of the refractive index [8]. This method is routinely used to determine film thickness and, consequently, the deposition rate. The reflective pattern is usually measured up to $2\theta \approx 8°$, as finite-size oscillations are only observable for $2\theta < 6°$. In Figure 2.8, a typical reflectivity pattern of a thin film is shown.

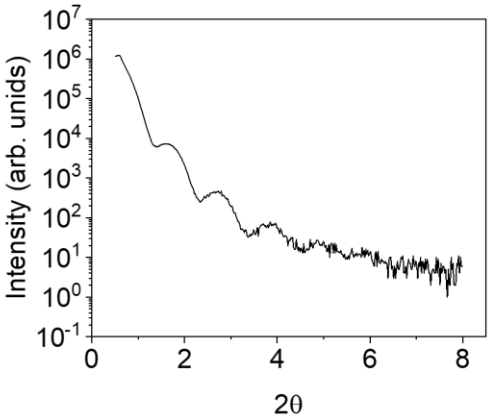

Figure 2.8. XRR measurement of a SIO monolayer of 8 nm

3.1.2. X-ray diffraction (XRD)

This method is used to obtain both the interatomic spacing (c) and the average thickness of the sample (d), which should be in good agreement with the thickness (d) calculated in the previous section.

X-rays specularly reflected at different parallel lattice planes will travel different optical paths due to the separation of layers, resulting in interference that will be constructive if the difference in path is an integer multiple of the X-ray wavelength λ_x. The diffraction condition is given by Bragg's law:

$$2d_{hkl} \sin\theta = n\lambda_x \tag{2.3}$$

where d_{hkl} represents the lattice spacing between crystallographic planes with [hkl] vector. By measuring the diffraction pattern in θ-2θ geometry and optimizing around one of the (00l) diffraction peaks of the substrate, we will observe the Bragg peaks of the same (00*l*) family. Using this, we can determine our sample lattice parameter (c). In Figure 2.9, we see, as an example, a diffraction pattern of a $SrIrO_3$ (SIO) thin film grown on a $SrTiO_3$ (STO) substrate where both diffraction peaks are labeled. By calculating c and comparing it with the bulk value, we can determine the amount of the epitaxial strain stored in our sample.

As the samples we work with are thin films, the film thickness (comparable to lattice spacing) will cause new diffraction peaks to appear around the sample Bragg peak. By indexing these peaks, we can determine the average thickness (d) using the formula:

$$2\frac{\sin\theta}{\lambda_x} = \frac{1}{\bar{d}}(1 \pm m) \tag{2.4}$$

where m is an integer number [9]. In Figure 2.9., the satellite peaks of an SIO sample are shown, which appear at both sides of the principal Bragg peak.

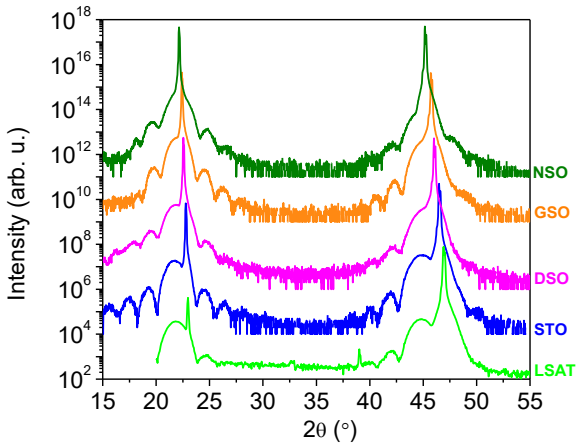

Figure 2.9. XRD measurements of $SrIrO_3$ grown at different substrates.

3.2. Scanning Transmission Electron Microscopy (STEM)

To examine structure and composition of our complex oxides layers with atomic resolution, we have performed imaging and spectroscopy using scanning transmission electron microscopy (STEM). The measurements were acquired using a JEOL JEM ARM200cF operated at 200 kV (see Figure 2.10, right) located at the ICTS National Center of Electron Microscopy at the Universidad Complutense Campus.

In a STEM, field emission electrons are designed to form a small electron probe through the strong electromagnetic lenses integrated into the STEM column. As the probe is scanned over the specimen's surface pixel-by-

pixel, the scattered electrons are collected in multiple imaging and analytical detectors [10], [11] (see Figure 2.10, left). The ability to detect multiple signals simultaneously makes STEM a powerful technique for characterization.

On one hand, a high angle annular dark field (HAADF) detector is used for Z-contrast imaging. In HAADF images, a ring-shaped (annular) detector measures the transmitted electrons through relatively high angles. The use of a high-angle detector reduces the detection of coherent Bragg reflection and increases that of the incoherent thermal diffuse scattering (TDS). As a result, incoherent images exhibit strong intensity dependence on atomic number, providing a directly interpretable Z-contrast [11], [12] (see Figure 2.11a). The ability to obtain Z-contrast images makes the HAADF technique a powerful tool. However, to increase collection efficiency, a lower angle (ADF) detector can be used, reducing the signal-to-noise ratio.

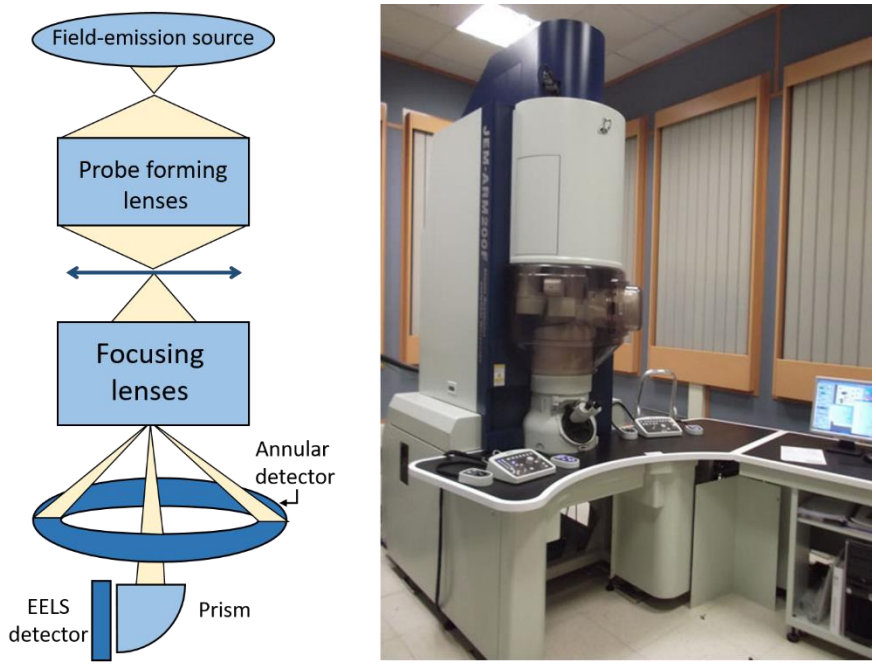

Figure 2.10. (left) Scheme of a scanning transmission electron microscope column. (right) Photography of the JEOL JEM ARM200cF

In addition, electron energy-loss spectra (EELS) are simultaneously acquired at each position (pixel) [13]. The scanning transmission electron microscope (STEM) geometry can provide atomic column resolution EELS [10], [14]. In some ways, EELS is equivalent to X-ray absorption spectrometry because the scattered electrons at low angles allow us to study the fine structure and the absorption edges of the specimen´s elements. Electrons scattered through smaller angles enter a single prism spectrometer, producing an energy-loss spectrum (EEL spectrum) for any given position of the probe on the specimen [10]. With modern microscopes, it is possible to obtain an EEL spectrum from each atomic column (Figure 2.11b), making this technique a powerful tool for investigating the chemical composition of interfaces, mapping terminations, and studying interdiffusion between different interfaces in oxide thin films or multilayers. EELS edges result from the excitations of inner shell electrons into occupied levels above the Fermi level. Using this technique, we can estimate the oxidation state of each atom column by measuring the NEXAFS absorption at edges of the transition metal and oxygen [15]. The high energy resolution of this technique (0.3 eV for a cold field emission gun) also allows the study of the fine structure of the absorption edges, enabling the investigation of electronic properties. The EELS fine structure arises from the material's unoccupied density of states and can be used to probe electronic properties [15]–[17].

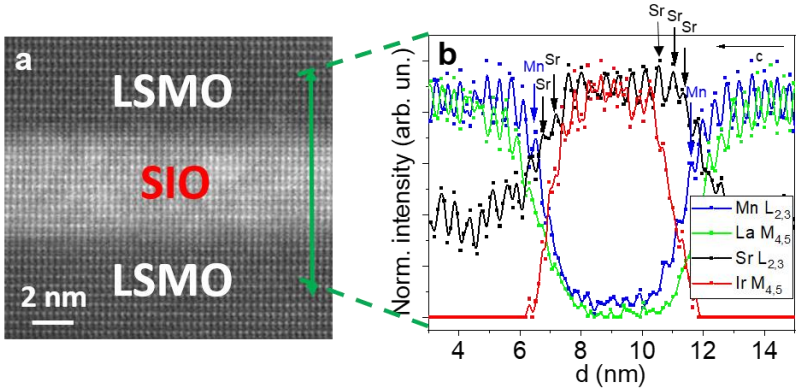

Figure 2.11. HAADF image of an LSMO (15 nm)/SIO (4.4 nm)/LSMO (15 nm) sample. (b) Electron energy loss spectroscopy (EELS) acquired across the LSMO/SIO/STO interfaces following the green line.

4. Magnetotransport characterization: PPMS

A Quantum Design PPMS was used to measure longitudinal and transverse resistivity as a function of temperature and magnetic field. The equipment, depicted in Figure 2.12, utilizes a combination of a He flow refrigerator and a superconductor magnet to achieve the required temperature and magnetic field ranges. The PPMS can apply up to 14 T and has a temperature operating range of 1.8 K to 320 K. The PPMS system used in this thesis is located at the Material Science Institute of Madrid (ICMM CSIC) which we can access on a routine basis thanks to being Unidad Asociada (Laboratorio de Estructuras y Dispositivos de Espintrónica)

The samples were measured in the DC resistivity mode using a standard puck, shown in Figure 2.13 right. The samples, which were measured using either the 4-point technique or a Hall bar, were connected to one of the three probe head channels. We used an external switching box, which is shown in Figure 2.13 left, to simultaneously measure both the longitudinal resistivity (in the direction of the current) and the transverse resistivity (perpendicular to the current direction) of the samples. This box allows us to change the direction of the applied current and voltage without the need to reposition the probe head.

Figure 2.12. Image of the PPMS located at the Materials Science Institute ICMM CSIC

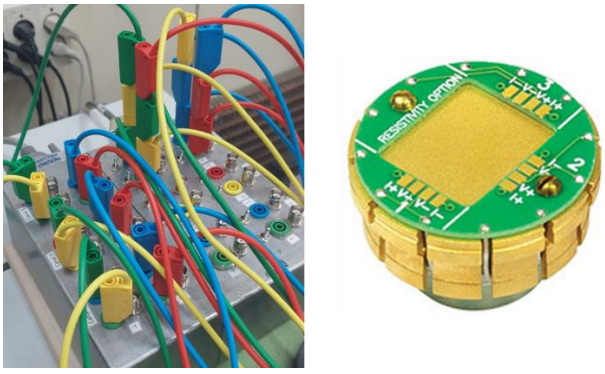

Figure 2.13 (left) Image of the switching box. (right) Image of the of a standard puck for resistivity measurements

5. Magnetic characterization

5.1. SQUID magnetometry

In this study, SQUID measurements were conducted using a Physical Property Measurement System (PPMS) described in the previous section. The SQUID detection hardware comprises superconducting detection coils

configured as a second-order gradiometer with counter-wound outer loops, making them non-responsive to uniform magnetic fields and linear gradients. The coils generate a current in response to local magnetic field disturbances, and their current is a function of the sample position.

SQUID feedback nulls the current in the detection coils, with the feedback current providing the actual SQUID voltage for analysis. The SQUID measurement technique vibrates the sample at frequency ω, generating a SQUID signal, V(t), based on sample position z and time t. Scaling factor A relates to the magnetic moment of the sample, while amplitude B corresponds to the sample vibration.

$$V(t) = AB^2 \sin^2(wt)$$

Lock-in amplifier techniques isolate and quantify the signal at frequency 2ω, which is exclusive to the sample when the vibration frequency is correctly selected. This is achieved by multiplying the measured signal with a phase-corrected reference signal at 2ω and then extracting the DC component of the result. This DC component is proportional to the 2ω component of the measured signal, efficiently isolating the sample signal from other noise sources, such as drifting SQUID signals and synchronized mechanical noise sources.

5.2. X-ray magnetic circular dichroism (XMCD)

X-ray magnetic circular dichroism (XMCD) has become an important experimental technique in the investigation of magnetic properties. As the name suggests, an XMCD experiment consists of measuring the difference in absorption of left- and right-handed circularly polarized X-rays. The difference, the magnetic dichroic signal, can then be used to estimate the (spin and orbital) magnetization in the material. In comparison with other techniques, XMCD has several attractive features. The first is that XMCD experiments provide information on the spin and orbital magnetizations separately: most other methods (bulk magnetization, neutron scattering, etc.) are sensitive to the total magnetization only. Second, by studying the dichroism around absorption edges, as is in fact usual practice, the

technique is element specific. Lastly, XMCD is very sensitive, which allows it to be used to determine extremely small magnetic moments and to study small quantities of materials. For all these reasons, one of the most important applications of XMCD is in the study of nano-scale structures, such as multilayers and thin films. In fact, the sensitivity of XMCD is such that magnetic moments of 0.001 μ_B per atom can be detected.

To understand the origin of the XMCD signal, a description of the circularly polarized waves is a good starting point. By definition, a right circularly polarized (RCP) electromagnetic wave has an electric field that rotates in a clockwise sense as viewed along k, while for a left circularly polarized (LCP) electromagnetic wave, the sense of rotation is counterclockwise, as shown in Figure 2.14. A circularly polarized electromagnetic wave in a quantum mechanical description is still composed of photons, but in this case, the photon is a definite eigenstate of the angular momentum operator, J_z, where z is the direction of propagation k. For RCP (LCP) photons, the eigenvalue of J_z is $+\hbar$ ($-\hbar$). This fact makes the selection rules for the conservation of angular momentum in electronic transitions easy to understand. The probability of electronic transitions is controlled by selection rules for the change in the quantum numbers describing the initial and final states. As the parity of the initial and final states is given by their respective orbital quantum numbers l, by the dipole transition electron rule, the non-vanishing matrix elements are obtained if:

$$\Delta l = \pm 1$$

On the other hand, since the photon is annihilated in the absorption process, the angular momentum Jz must be transferred to the sample, so for circularly polarized photons one has

$$\Delta m = +1\ (-1)\ \text{, for RCP (LCP) photons}$$

Following this, illuminating our sample with RCP (LCP) radiation, an electron from the core 1s, $|0,0\rangle$, will transit to the state $|-1,1\rangle$ ($|-1,-1\rangle$) [18]–[20]. Depending on the occupation of these states, the transition will occur or not. In the case of ferromagnetic transition metals, the valence band d

is spin-splitted, giving different densities of unoccupied states at the Fermi level, as shown in Figure 2.14 [21], [22]. The magnetization of the element is closely related to d-band occupation and will affect the number of transitions. The selection rules together with unoccupied d estates will cause the differences in the abortion RCP and LCP spectra, as shown in figure 2.15.

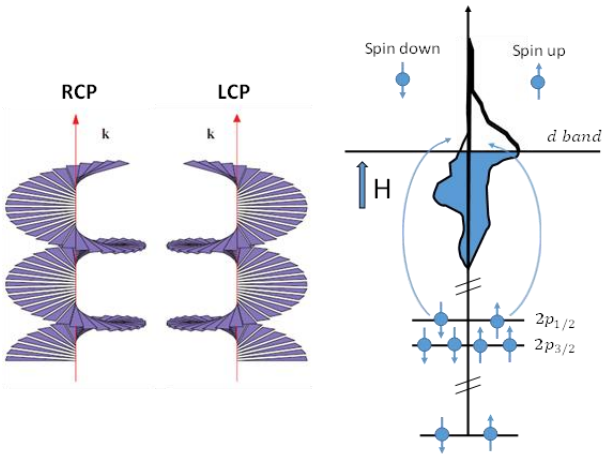

Figure 2.14. (left) helicity of the polarized radiation (right) diagram of the band structure spin-spitted

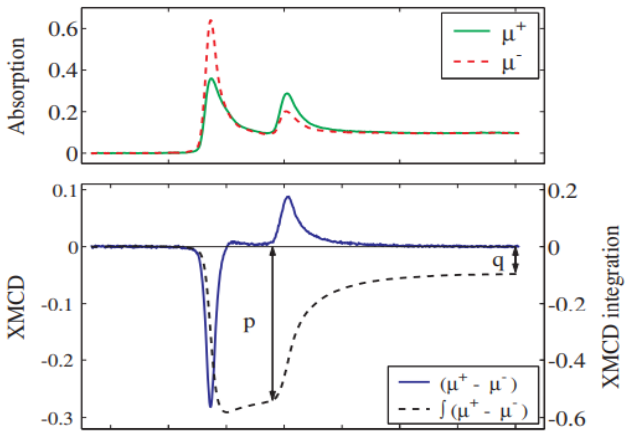

Figure 2.15. X-ray absorption spectra from iron in the vicinity of the L edges. Circularly polarized light was used, and the spectra were recorded with the spin of the incident photon parallel (I+, solid curve) and antiparallel (I−, dashed curve) to the spin of the Fe 3d electrons.(up) the X-ray absorption spectra calculated from the transmission data ; (down) the XMCD spectra. Figure adapted from [18].

5.3. Polarized Neutron Reflectometry (PNR)

Polarized Neutron Reflectometry (PNR) is a widely used technique [23], [24], that measures the reflection of a neutron beam on a sample as a function of the perpendicular component of the wave vector transfer. Polarized neutrons are intrinsically sensitive to the difference between the magnetic and nuclear components of the refractive index across interfaces. PNR provides quantitative information about the magnetization depth profile and structural details of thin films, heterostructures, and multilayers. In reflectivity geometry, the incidence angle θ_i is the same as the reflection angle θ_r and typically starts from a region of total reflection, in the range 0.5^o-5^o. The reflected neutrons are related to the depth dependence of the index of refraction averaged over the lateral dimensions of the interface. With an extremely high depth resolution of a fraction of a nanometer, PNR can analyze films that are several hundred nanometers thick. Due to their high penetration into the sample without causing structural damage and their ability to interact with magnetic moments, neutrons are ideal for investigating magnetic thin films. During PNR experiments, a magnetic field H is applied to the sample as a reference (see Figure 2.16). As H is usually much smaller than M in the relation $B=\mu_0 H+M$, the neutron spin interacts only with the magnetic induction inside the sample and cannot differentiate between spin and orbital moments. The magnetic contribution to the scattering potential is given by $V_m=-\mu_n \cdot B$, where μ_n is the neutron magnetic moment.

Neutrons can be polarized parallel or antiparallel to the applied field using suitable devices. The guiding field, incident beam polarization axis, and detector field are typically collinear, establishing a quantization axis for the neutron spin. If the magnetic induction B inside the sample forms an angle with the applied field H, the in-plane component of B, perpendicular to H, causes spin-flip scattering and the neutron spin to precess around B. Conventionally, R^{++} and R^{--} represent non-spin-flip reflectivities, where + and - indicate spin parallel or antiparallel to H, respectively. Neutrons are reflected by potential gradients across interfaces, and since $\nabla B=0$, perpendicular components of B stay constant across a reflecting interface, not producing specularly reflected intensity.

PNR measurements of this thesis were conducted in collaboration with Dr. Suzanne te Velthuis of Argonne National Laboratory, who conducted measurements at the Spallation Neutron Source, SNS at Oak Ridge National Laboratory.

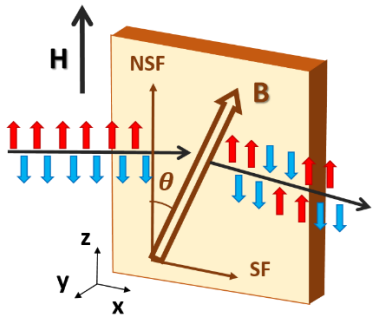

Figure 2.16. Sketch of the magnetization components responsible for the spin flip (SF) or the non-spin flip (NSF) scattering in relation to the neutron polarisation.

6. Magnetic force microscopy (MFM)

Magnetic force microscopy (MFM) [25], [26] is a commonly used characterization technique to study the magnetic structure of the sample surface. In this functional technique, the measurement of the long-range magnetostatic force between the magnetic sample and a magnetically coated probe is recorded as a magnetic image. The image provides qualitative information by showing magnetic textures near the surface of the sample.

The MFM procedure used in these experiments involves two vertically shifted scans for the sake of separating long-range and short-range interactions.

In the first scan, we acquire the topography of the surface (by controlling the amplitude of cantilever [27], probing the effects of the short-range forces as the van der Walls force.

In the second one, the probe is lifted away from the sample to get rid of the short-range forces. The tip follows the topography acquired during the first scan with a lift-off value between about 100 nm and 200 nanometers, as shown in Figure 2.17. During this second scan, the long-range magnetic forces generate a phase shift ($\Delta\phi$) in the movement of the cantilever regarding the excitation signal.

$$\Delta\phi = \frac{Q}{k}\frac{\partial F_{ts}}{\partial z}$$

Where Q is the quality factor, k is the spring constant and F_{ts} is the force tip-sample STM.

A NanoMagnetics commercial microscope located at the Institute for Materials Sciences of Madrid ICMM CSIC was used to acquire the images shown in this thesis. MFM work was conducted by Dr. Juan José Riquelme and Dr. Carmen Munuera of the Material Science Institute of Madrid (ICMM CSIC). It uses an interferometer to track the movement of the cantilever [28] and operates from 2K to 300 K in a He blown cryostat with a vector magnet providing 5:1:1 T or in a PPMS with fields of up to 5 T.

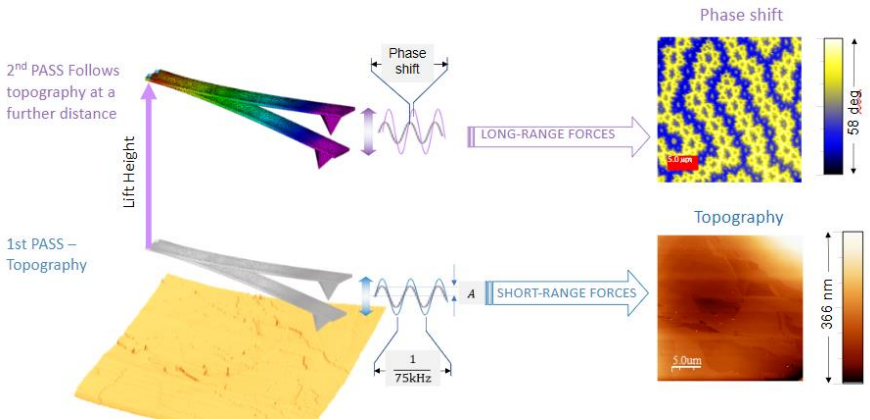

Figure. 2.17. Sketch of the scan that the magnetic probe follows to measure the long-range magnetic forces, taking into account the topography of the surface.

7. Scanning tunneling microscopy (STM)

Scanning tunneling microscopy (STM) is a powerful technique in surface science [29], [30], offering unique atomic-resolution real-space maps of the electronic density of states (DOS). STM is also particularly well-suited for studying new layered superconducting materials, which may initially only be available as small single crystals [31]. The STM apparatus used in this thesis was located at the Characterization Facility at the University of Minnesota (thanks to the collaboration of Dr. Javier Garcia Barriocanal).

An STM features a sharp metallic tip that scans over an electrically conductive sample surface with minimal separation, typically a few angstroms. The piezoelectric scanner enables precise control of the tip-sample separation and lateral position with sub-angstrom accuracy (refer to Fig. 1). When a negative bias voltage is applied to the sample, electrons in the sample's occupied states tunnel through the vacuum barrier to the tip's empty states, generating a detectable tunneling current. Conversely, applying a positive bias voltage causes electrons to tunnel from the tip to the sample. The tunneling current (I) is exponentially dependent on the tip-sample distance (d) [32] as per the following equation:

$$I \propto e^{-2\kappa d} \;\; ; \;\; \kappa = \frac{\sqrt{2m\phi}}{h}$$

Where ϕ is the average work function of tip and sample. Typically, the work function measured by STM in metals is around 3 eV. The materials frequently used for STM tips, selected for their featureless DOS near the Fermi energy (E_F), include platinum (Pt), platinum-iridium (PtIr) alloys, and tungsten (W).

By maintaining a constant tunneling current as the STM tip scans the sample surface, a contour of constant integrated DOS is traced. This method is known as constant-current mode. In the case of homogeneous elemental metals, the constant DOS contour corresponds to the sample surface's topography. When the local DOS exhibits spatial variation, the resulting image blends DOS and topographic information. However, with suitable tunneling parameters, topography primarily influences the image.

Apart from depicting the sample's geometrical surface structure, STM can also evaluate the sample DOS as an energy function, spanning several eV from the Fermi level in both occupied and unoccupied states. This is typically achieved by varying the bias voltage (V) and measuring the tunneling current (I) while keeping the tip-sample separation (d) constant. Conductance (dI/dV) can be obtained through numerical differentiation of I(V). To minimize noise, a lock-in technique is employed, in which a small AC modulation is combined with the bias voltage, and the tunneling current is demodulated to yield dI/dV. Although interpreting dI/dV spectra can be challenging, under ideal circumstances, dI/dV serves as a reliable indicator of the sample DOS.

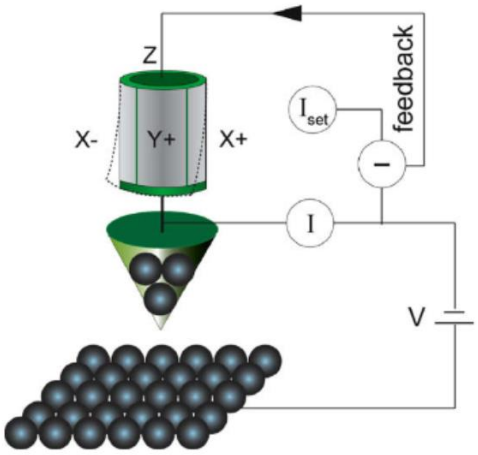

Figure 2.18. Sketch of an STM

8. Density Functional Theory (DFT)

Density Functional Theory (DFT) is currently the most successful and promising approach for calculating the electronic structure of matter. Its applicability ranges from atoms, molecules and solids to nuclei and quantum and classical fluids. However the Schrödinger equation is the simplest expression that compiles all the interactions of this systems, the solution become complex when a large number of atoms are considered. For this reason, Hohenberg and Kohn postulated a successful solution of

the Schrödinger equation which constitute the basis of the Density Functional Theory (DFT) [33], [34].

The Schrödinger equation is represented as $H\Psi = E\Psi$, where $\Psi = \Psi(x_1, \dots x_n; R_1, \dots R_n)$ is the wave function that depends on the coordinates of N electrons and M ions, and E represents the system energy [35]. The Hamiltonian (H) encompasses both electronic and ionic terms. Born and Oppenheimer's approximation simplifies the many-body problem by considering a stationary nucleus and concentrating on electronic states [36]. Consequently, the Schrödinger equation is rewritten to focus on electronic components, employing T and U as universal operators for kinetic energy and electron-electron interaction, respectively, and V as the system-dependent non-universal term:

$$H\Psi = [T + U + V]\Psi = -\frac{1}{2}\sum_{i=1}^{N}\nabla_i^2 + \sum_{i=1}^{N}V(r_i) + \sum_{i=1}^{N}\sum_{i=1}^{N}U(r_i, r_j) = E\Psi$$

DFT provides a way to convert the many-body problem, characterized by electron-electron interaction (U), into a single-body problem without U through the introduction of the density variable (n). Hohenberg and Kohn's first DFT theorem, enables expressing the wave function (Ψ) as a functional of electronic density, which means any observable becomes a functional of n.

$$n = |\Psi * \Psi^*| = N\int d^3r_2 \int d^3r_3 \int d^3r_N \ \Psi(x_1, \dots x_n) * \Psi^*(x_1, \dots x_n)$$

Their second theorem posits that the total energy of an electronic system is a universal functional of density, with the global energy minimum corresponding to the ground state charge density. The Kohn-Sham equation, a density functional expression, delivers the same solutions as the Schrödinger equation when energy is minimized. This equation includes the effective potential (V_S), composed of the nucleus-electron potential (V), the classical Coulomb term of electron-electron interaction (U), and the exchange-correlation (XC) term (V_{XC}). The XC term covers all unknown terms and is generally treated with approximations, producing exact results only in simpler systems, such as the free electron gas case.

$$[T_S + V_S]\Psi = E\Psi = T + U + V_{XC}$$

The exchange-correlation (XC) energy density per electron is defined mathematically, enabling the representation of total XC energy.

$$E_{XC} = \int \varepsilon_{XC}[n_-, n_+]d^3r$$

Utilizing free electron gas values, we implement the local (spin) density approximation (L(S)DA) for the XC term. L(S)DA posits a constant electron density, hence XC effects are primarily proximal. Our L(S)DA-based calculations draw on precise many-body models. By considering L(S)DA as an initial step in energy density expansion, we can refine the XC approximation via inclusion of density gradient corrections, an approach termed generalized gradient approximation (GGA), which accommodates electron density variability.

First principles simulations using the Density Functional Theory described in this thesis were conducted by Dr. Juan Beltrán (member of our research group and Maria Carmen Muñoz of the Material Science Institute of Madrid (ICMM CSIC).

9. References

[1] U. Poppe *et al.*, «Low-resistivity epitaxial YBa2Cu3O7 thin films with improved microstructure and reduced microwave losses», *Journal of Applied Physics*, vol. 71, n.º 11, pp. 5572-5578, jun. 1992, doi: 10.1063/1.350535.

[2] I. Brodie y J. J. Muray, *The physics of micro/nano-fabrication*. Springer Science & Business Media, 2013.

[3] M. Ohring, *Materials Science of Thin Films: Depositon and Structure*. Elsevier, 2001.

[4] J. A. Bondur, «Dry process technology (reactive ion etching)», *Journal of Vacuum Science and Technology*, vol. 13, n.º 5, pp. 1023-1029, 1976.

[5] S. M. Rossnagel, J. J. Cuomo, y W. D. Westwood, «Handbook of Plasma Processing Technology Noyes», *Park Ridge, NJ*, p. 285, 1990.

[6] «Fundamentals of Semiconductor Fabrication | Wiley», *Wiley.com*. https://www.wiley.com/en-us/Fundamentals+of+Semiconductor+Fabrication-p-9780471232797.

[7] D. M. Kelly, E. E. Fullerton, J. Santa-Maria, y I. K. Schuller, «A simple closed-form expression for the X-ray reflectivity from multilayers with cumulative roughness», *Scripta Metallurgica et Materialia*, vol. 33, n.º 10, pp. 1603-1608, dic. 1995, doi: 10.1016/0956-716X(95)00391-8.

[8] M. Varela, D. Arias, Z. Sefrioui, C. León, C. Ballesteros, y J. Santamaria, «Epitaxial mismatch strain in YBa2 Cu3O7-δ/PrBa2Cu3O7 superlattices», *Physical Review B*, vol. 62, n.º 18, p. 12509, 2000.

[9] E. E. Fullerton, I. K. Schuller, H. Vanderstraeten, y Y. Bruynseraede, «Structural refinement of superlattices from x-ray diffraction», *Physical Review B*, vol. 45, n.º 16, p. 9292, 1992.

[10] N. D. Browning, D. J. Wallis, P. D. Nellist, y S. J. Pennycook, «EELS in the STEM: Determination of materials properties on the atomic scale», *Micron*, vol. 28, n.º 5, pp. 333-348, 1997.

[11] R. F. Egerton, *Electron energy-loss spectroscopy in the electron microscope*. Springer Science & Business Media, 2011.

[12] K. Watanabe, T. Yamazaki, I. Hashimoto, y M. Shiojiri, «Atomic-resolution annular dark-field STEM image calculations», *Physical Review B*, vol. 64, n.º 11, p. 115432, 2001.

[13] C. Jeanguillaume y C. Colliex, «Spectrum-image: the next step in EELS digital acquisition and processing», *Ultramicroscopy*, vol. 28, n.º 1-4, pp. 252-257, 1989.

[14] P. E. Batson, «Simultaneous STEM imaging and electron energy-loss spectroscopy with atomic-column sensitivity», *Nature*, vol. 366, n.º 6457, pp. 727-728, 1993.

[15] J. H. Rask, B. A. Miner, y P. R. Buseck, «Determination of manganese oxidation states in solids by electron energy-loss spectroscopy», *Ultramicroscopy*, vol. 21, n.º 4, pp. 321-326, 1987.

[16] O. L. Krivanek y J. H. Paterson, «ELNES of 3d transition-metal oxides: I. Variations across the periodic table», *Ultramicroscopy*, vol. 32, n.º 4, pp. 313-318, 1990.

[17] H. Kurata y C. Colliex, «Electron-energy-loss core-edge structures in manganese oxides», *Physical Review B*, vol. 48, n.º 4, p. 2102, 1993.

[18] J. Als-Nielsen y D. McMorrow, *Elements of modern X-ray physics*. John Wiley & Sons, 2011.

[19] B. T. Thole, P. Carra, F. Sette, y G. van der Laan, «X-ray circular dichroism as a probe of orbital magnetization», *Physical review letters*, vol. 68, n.º 12, p. 1943, 1992.

[20] C. Kao, J. B. Hastings, E. D. Johnson, D. P. Siddons, G. C. Smith, y G. A. Prinz, «Magnetic-resonance exchange scattering at the iron L II and L III edges», *Physical review letters*, vol. 65, n.º 3, p. 373, 1990.

[21] W. Grange y J. P. Kappler, «M. Maret in Magnetism: Molecule to Materials, Models and experiments, edited by JS Miller, M. Drillon». Wiley-VCH, 2001.

[22] T. Burnus *et al.*, «Local electronic structure and magnetic properties of La Mn 0.5 Co 0.5 O 3 studied by X-ray absorption and magnetic circular dichroism spectroscopy», *Physical Review B*, vol. 77, n.º 12, p. 125124, 2008.

[23] G. P. Felcher, R. O. Hilleke, R. K. Crawford, J. Haumann, R. Kleb, y G. Ostrowski, «Polarized neutron reflectometer: A new instrument to measure magnetic depth profiles», *Review of scientific instruments*, vol. 58, n.º 4, pp. 609-619, 1987.

[24] V. F. Sears, «Neutron scattering lengths and cross sections», *Neutron news*, vol. 3, n.º 3, pp. 26-37, 1992.

[25] Y. Martin y H. K. Wickramasinghe, «Magnetic imaging by ‘‘force microscopy’’ with 1000 Å resolution», *Applied Physics Letters*, vol. 50, n.º 20, pp. 1455-1457, may 1987, doi: 10.1063/1.97800.

[26] J. J. Sáenz *et al.*, «Observation of magnetic forces by the atomic force microscope», *Journal of Applied Physics*, vol. 62, n.º 10, pp. 4293-4295, nov. 1987, doi: 10.1063/1.339105.

[27] Q. Zhong, D. Inniss, K. Kjoller, y V. B. Elings, «Fractured polymer/silica fiber surface studied by tapping mode atomic force microscopy», *Surface Science Letters*, vol. 290, n.º 1-2, pp. L688-L692, 1993.

[28] Ö. Karcı, «Design of a self-aligned, high resolution, low temperature (30 mk - 300 k) magnetic force microscope».

[29] G. Binnig, H. Rohrer, C. Gerber, y E. Weibel, «Tunneling through a controllable vacuum gap», *Applied Physics Letters*, vol. 40, n.º 2, pp. 178-180, 1982.

[30] G. Binnig y H. Rohrer, «Scanning tunneling microscopy», *Surface science*, vol. 126, n.º 1-3, pp. 236-244, 1983.

[31] Y. Yin, M. Zech, T. L. Williams, y J. E. Hoffman, «Scanning tunneling microscopy and spectroscopy on iron-pnictides», *Physica C: Superconductivity*, vol. 469, n.º 9-12, pp. 535-544, 2009.

[32] J. G. Simmons, «Generalized Formula for the Electric Tunnel Effect between Similar Electrodes Separated by a Thin Insulating Film», *Journal of Applied Physics*, vol. 34, n.º 6, pp. 1793-1803, jun. 2004, doi: 10.1063/1.1702682.

[33] P. Hohenberg y W. Kohn, «Inhomogeneous electron gas phys. rev. 136», *B864*, 1964.

[34] «Density functional theory», *Wikipedia*. 3 de abril de 2023. Accedido: 13 de mayo de 2023. [En línea]. Disponible en: https://en.wikipedia.org/w/index.php?title=Density_functional_theory&oldid=1148003979

[35] C. C. Tannoudji, B. Diu, y F. Laloë, *Quantum Mechanics: Vol. Two*. John Wiley and Sons, 2002.

[36] «Born M, Oppenheimer R (1927) Ann Phys 84: 457».

Chapter 3

Strain effects on the structural and transport properties of $SrIrO_3$ ultrathin films

1. Introduction

Epitaxial growth is a process in which a thin film of material is grown atom-by-atom on a single crystalline substrate, preserving its crystalline structure. I.e., the layer grows with nearly the same lattice parameter and crystalline orientation as the substrate crystal. This technique has long been used by researchers to study the properties of materials with a high degree of control over their structure.

Especially 5d oxides are highly susceptible to small changes in the bond lengths and bond angles [1]–[3], driven partly by their strong spin orbit interaction, which couples the lattice details to the electronic structure. In this context, strain engineering constitutes a good approach for tuning the electronic structure, the conductivity, and the magnetic properties of the iridate family [4]–[9].

In this chapter, we will analyse how the structural and transport properties of $SrIrO_3$ (SIO) are modified by epitaxial strain, and through this, we will gain insight into the fundamental physics of the material. This information can be useful in the fabrication of materials with properties by design. This is a natural way to start the experimental part

of this dissertation, which aims at describing functional properties of SIO thin films.

As a good example of the high crystalline quality of our SIO thin films grown by high-pressure sputtering, figures 3.1 (left) and (right) show aberration-corrected high-resolution electron microscopy images taken in bright field and dark field of an epitaxial $SrIrO_3$ thin film, grown on a $SrTiO_3$ (STO) substrate and capped with $La_{0.7}Sr_{0.3}MnO_3$ (LSMO).

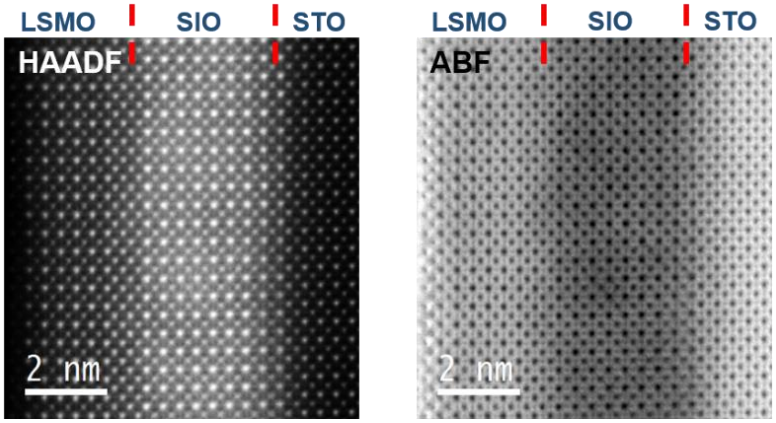

Figure 3.1. HR-TEM image at bright field (left) and dark field (right) of SIO on STO and capped with LSMO. These measurements were taken by Gabriel Sanchez Santolino in collaboration with Prof. Ikuhara's group at the University of Tokyo.

The images show highly ordered cube-on-cube growth of the SIO on the STO (001) surface, evidencing that our high-pressure pure oxygen sputtering technique at high temperature is a very adequate technique for the epitaxial growth of the 5*d* SIO oxide.

2. SIO growth on different substrates. Effects of epitaxial strain.

$SrIrO_3$ (SIO) has a lattice parameter a = 3.94 Å, allowing us to grow epitaxial samples with substantial degrees of both tensile and compressive strain with the right substrate choice. In order to study the effect of this strain, we have characterized a set of samples grown on: $NdGaO_3$ (110), NGO; $(LaAlO_3)_{0.3}(Sr_2TaAlO_6)_{0.7}$ (100), LSAT; $SrTiO_3$ (100), STO; $DyScO_3$ (110), DSO; $GdScO_3$ (110), GSO; $NdScO_3$ (110), NSO. SIO samples were grown at the Complutense University of Madrid by the high pressure sputtering technique at 650 °C and 2.8 mbar (see the Experimental Methods chapter 2).

Figure 3.2 depicts the XRD results of these various samples with a nominal 5 nm thickness measured in a Phillips X'pert Pro MRD diffractometer. The finite-size (thickness) fringes indicate epitaxial growth with thicknesses between 4.6 nm and 5.4 nm.

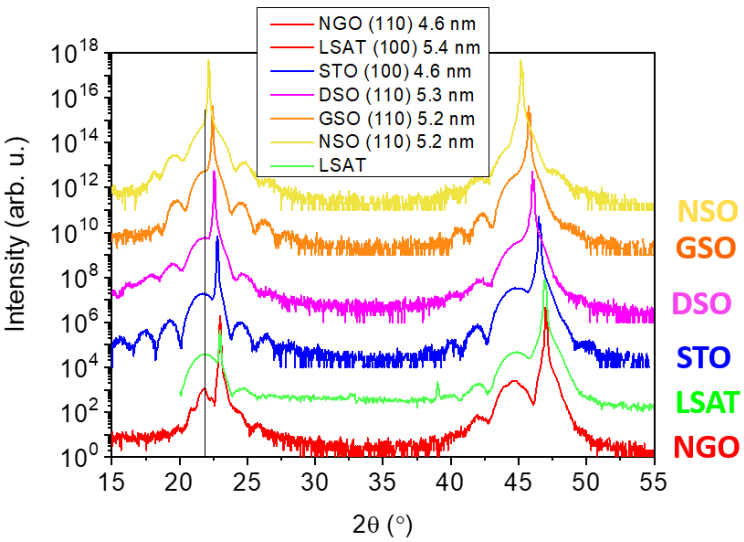

Figure 3.2. XRD of SIO over different substrates: NdGaO3 (110), NGO; $(LaAlO_3)0.3(Sr_2TaAlO_6)0.7$ (100), LSAT; SrTiO3 (100), STO; DyScO3 (110), DSO; GdScO3 (110), GSO; NdScO3 (110), NSO.

The lattice parameter c of the SIO can be estimated from the angular position of the main (00l) peaks of the perovskite structure, which is widened by the size effect associated with the small layer thickness. As it is observed in Figure 3.3, substrates with a lattice parameter smaller than SIO's—that occurs in NGO, LSAT, STO, and DSO—produce a compressive strain that forces the SIO unit cell to increase its c lattice parameter. On the other hand, substrates with a lattice parameter larger than that of SIO—GSO and NSO—generate a tensile strain, reducing the c out of plane parameter.

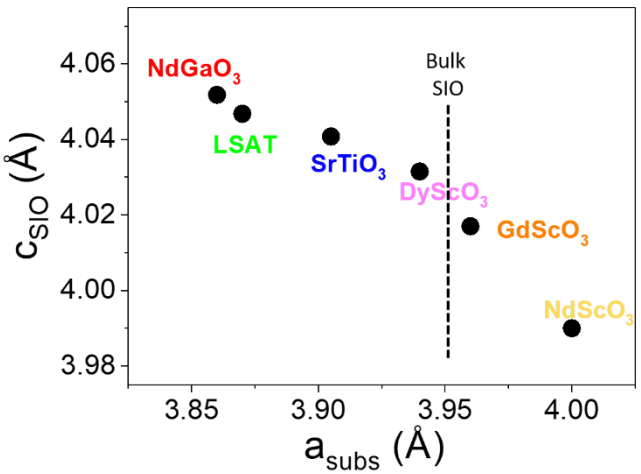

Figure 3.3. Lattice parameter c in SIO depending on the substrate strain.

The strain effect visible in the deformation of the lattice also manifests in the transport properties. As shown in the resistivity vs. temperature curves in Figure 3.4, there is a strain-driven metal-insulator transition. At a given SIO thickness of 4 nm, compressive strain results in metallic behaviour, whereas tensile strain results in insulator behaviour.

The dependence of the resistivity on strain inferred from measurements of the temperature dependence of the resistivity for SIO films of similar thickness grown on different substrates is fully unexpected. Notice (see Figure 3.4) that compressive plane strains yield the lowest resistivity

values and metallic behaviour. On the other hand, increasing the in-plane substrate's lattice parameter yields larger resistivity and eventually insulating behaviour. In the simple scenario of transport dominated by the in-plane overlap of the orbitals, this is a fully unexpected result since in-plane compressive strain should decrease the overlap between orbitals and thus bandwidth, resulting in depressed screening properties. It follows, then, that the observed dependence of the resistivity on strain may be explained in terms of the out-of-plane overlap between orbitals.

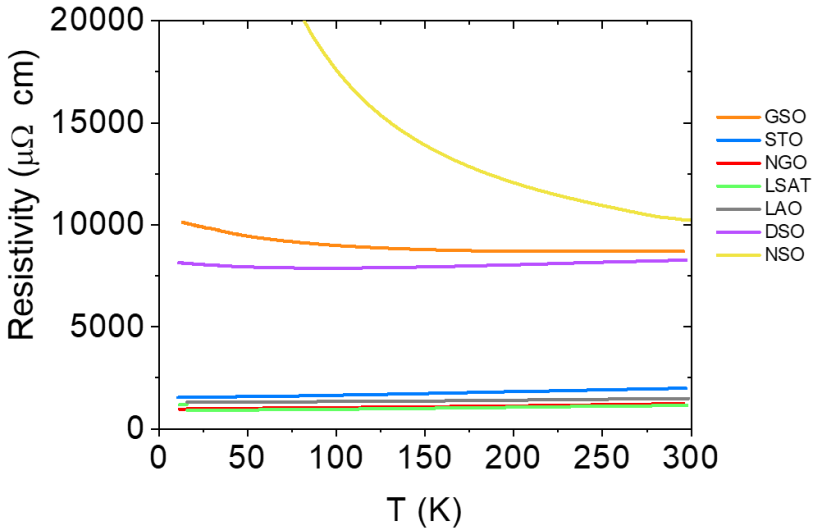

Figure 3.4. Resistivity vs Temperature graph of SIO samples of the same 4 nm thickness grown at different substrate.

This behaviour may be understood by taking into account the characteristics of the t_{2g} orbitals as well as the interplay of the interactions that govern the bandwidth of the SIO.

Following the model of the bulk electronic structure of a cubic perovskite, ABO_3, the bonding networks of the three t_{2g} bands are decoupled. For example, a xy orbital on one B site can hop only along the y or x direction through an intermediate p_x or p_y orbital to a xy orbital on the B site of a neighbouring cubic cell [10], [11]. However, in materials like SIO, the spin-orbit coupling hybridizes the three t_{2g} orbitals, opening new hopping channels.

The bonding angle between the t_{2g} orbitals, θ, plays a significant role in the hopping amplitude. The hopping amplitude is proportional to $\cos\theta$, therefore it will maximum at 180^0 and cancel at 90^0. On the other hand, there is a geometrical quantity called the tolerance factor, Γ, which is defined as:

$$\Gamma = \frac{d_{A-O}}{\sqrt{2}d_{B-O}} \qquad [1]$$

Where d_{A-O} is the distance between the A-ion (Sr in our case) to the nearest oxygen and d_{B-O} is the same for the B-ion (Ir). For and undistorted perovskite $\Gamma = 1$. However, sometimes the A ions are too small to fill the space in the cube centers and for this reason the oxygens tend to move toward that center, reducing d_{A-O}. In general d_{B-O} also changes at the same time. For these reasons, the tolerance factor becomes less than unity, $\Gamma < 1$, as the radius of the A-site element is reduced, and the Ir-O-Ir angle becomes smaller than 180^0 [12], thus reducing the hopping rate in the SIO.

As explained in the introduction chapter, the bandwidth, *W*, in SIO is given by a balance between the spin-orbit coupling, SOC, the Coulomb energy, U, the coordination between the oxygen octahedron, *m*, and the oxygen octahedra rotations. This puts the hopping, which is directly connected to the bandwidth, in a delicate equilibrium and makes it highly susceptible to small changes in the interaction parameters.

The effect of strain is manifested by a change of the structural distortions within the octahedral network, specifically on the planar and apical Ir-O-Ir angles (α_{IP} and α_{OP}) and Ir-O bond length (d_{IP} and d_{OP}). Like many other perovskite-type oxides, upon compressive strain d_{IP} decreases and d_{OP} increases, whereas the octahedral rotation angle α_{IP} decreases and α_{OP} increases, as shown in figure 3.5. This promotes vertical hopping while increasing *W* such that the system turns to the metallic side. However, tensile strain narrows the t_{2g} orbitals (smaller W) and increases U, which is understandable in terms of a reduction of the hopping amplitude [13].

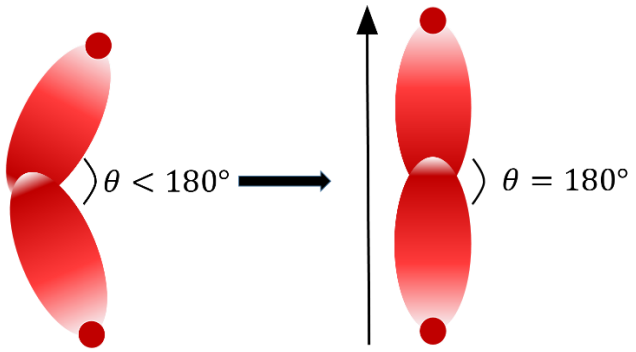

Figure 3.5: Out-of-plane orbitals and the effect of increasing the c lattice parameter.

Out-of-plane hopping plays a decisive role in the connectivity of the network of oxygen octahedra. For reduced out-of-plane bond angles happening under tensile strain, the reduced out-of-plane hopping decouples perovskite blocks in the c-direction, which reduces the 3D connectivity of the oxygen sublattice. On this limit, decoupled IrO planes make the sample shift to the 2D limit and become akin to the Sr_2IrO_4 compound, where the SrO rocksalt blocks break the 3D connectivity [14]. The insulating antiferromagnetic groundstate of the 214 compound emerges from increased correlations and reduced bandwidth of the 2D IrO planes. On the other hand, more compressive strain results in elongated out-of-plane bonds (to preserve cell volume), and the increased out-of-plane hopping restores the 3D connectivity of the oxygen sublattice, promoting the 3D semimetallic (paramagnetic) ground state.

We can notice that, although the DSO substrate provides weak compressive strain and a metallic behaviour, there is a remarkable difference in the resistivity values between this sample and the rest of the samples with compressive strain. As we will show in the following section, the DSO substrate has a non-symmorphic symmetry driven by the surface geometry of oxygen octahedra, which induces profound structural changes and also leads to significant modifications of the electronic structure that depart from the 3D semimetallic paramagnetic ground state.

For each substrate, there is also a metal-insulator transition driven by the thickness. The critical thickness, as shown in Figure 3.6, depends on the

substrate, probably through the degree of epitaxial strain. In substrates with compressive strain, a larger reduction in thickness is required to find the transition and enter the insulating state. In a STO substrate, the metal insulator transition takes place for thicknesses below 2 nm, whereas in an LSAT substrate, the thickness has to be reduced even further. On the other hand, in substrates (of the scandates family) imposing tensile strain, we find the metal insulator transition for larger layer thicknesses, around 5.5 nm.

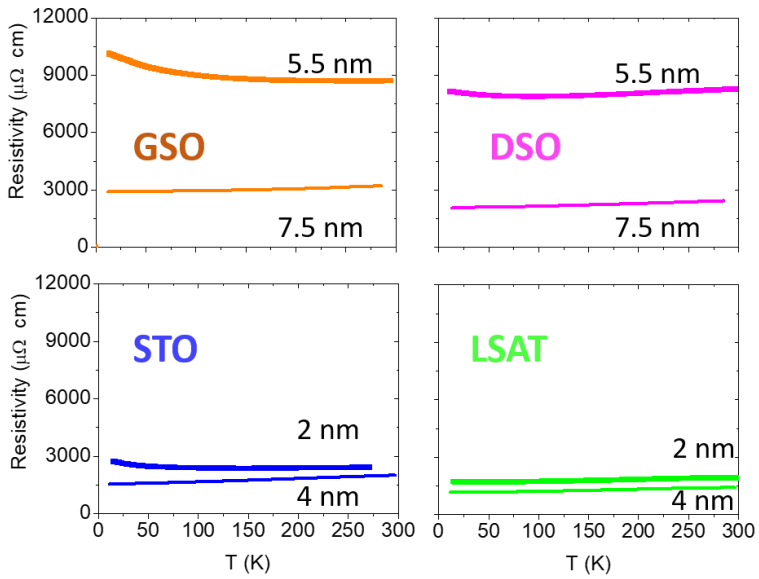

Figure 3.6. Resistivity vs temperature of sample with different thickness grown on (a) GSO (b) DSO (c) STO and (d) LSAT.

3. Growth of ultrathin SIO on (110) DSO. A 3D Dirac semimetal.

For the rest of the chapter, we will focus on the growth of SIO thin films on $DyScO_3$ (110), DSO. As previously discussed, this substrate has an in-plane lattice parameter of 3.95 Å, which corresponds to the side of the blue square painted on the surface of the DSO (Figure 3.7a).

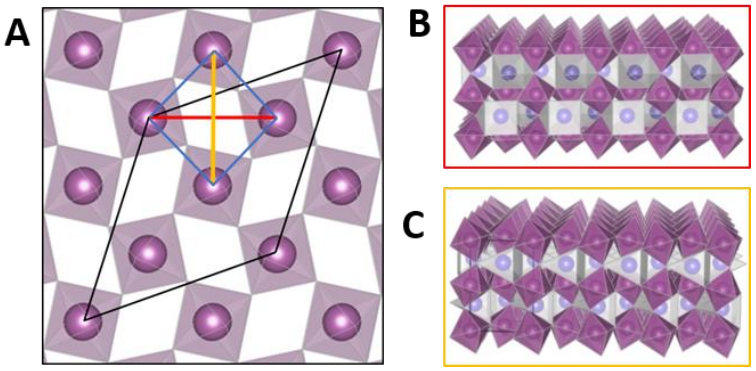

Figure 3.7. DSO (110)-orientated substrate crystal structure schematics (A–C). (a) Plane view: Blue lines indicate the pseudo-square ScO6 octahedron network, red and yellow lines illustrate the varied major diagonal lengths owing to rhombohedral distortion. Black lines show the substrate's rebuilt unit cell. (b), (c) Side views from the pseudocubic structure's red (b) and yellow (b) diagonals.

Due to a rhombohedral distortion of the lattice, the surface of the crystal is non-symmorphic. The angles of the oxygen bonds between the Sc atoms are 93° and 87°, which correspond to 5.44 and 5.73 diagonal distances in the unit cell (red and yellow lines, respectively, in Figure 3.7a). The non-symmorphism is highlighted in Figures 3.7b and 3.7c, which show DSO structure side projections along the red and yellow diagonals. Note that the red and yellow lines match the frame lines of figures 3.7b and 3.7c. The tilting of the oxygen octahedron alters its modulation for the two side perspectives, resulting in differing apical oxygen periodicities. This reconstructs the substrate's unit cell, lowering its symmetry to a 4 x 2 times larger unit cell.

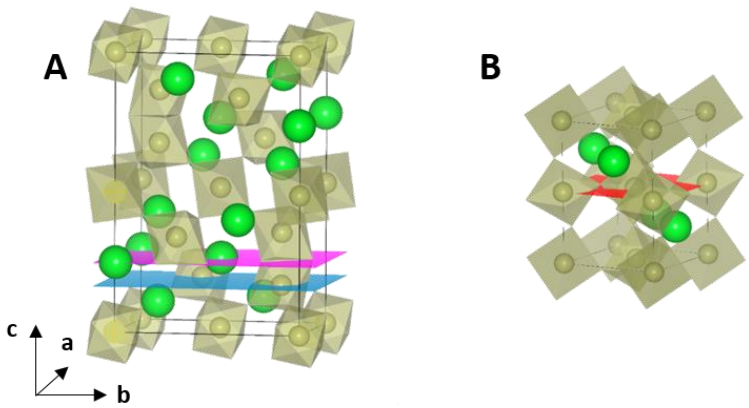

Figure 3.8. Crystallographic structure of the (a) orthorhombic and (b) monoclinic structures.

The non-symmorphic character of the DSO substrate has an inprint on the structure of the SIO thin films. As explained in the introduction, two different structures have been reported for SIO, depending on the growth conditions (Figure 3.8). On the one hand, there is monoclinic structure with lattice parameters: a = 5.57 Å, b=9.67 Å and c = 14.26 Å, as well as an angle $\beta = 93.23°$ (respect the plane). This is a non-symmorphic structure with crystal symmetries C2/c (Figure 3.8a). On the other hand, there is an orthorhombic structure with lattice parameters: a=5.58 Å, b=5.6 Å and c=7.75 Å. This is a symmorphic structure with crystal symmetries Pnma (Figure 3.8b). Focusing on the XRD, the C2/c symmetry is essentially invisible for θ-2θ XRD scans because its structural factor along the out-of-plane coordinate does not generate any intensity for this (0 0 L) family of planes, save for the (0 0 4) reflection, which has 1.35% intensity. But the Pnma symmetry will show the (0 0 2) and (0 0 4) reflections with an intensity of 10.28% and 12.76%, respectively. This will cause film Bragg peaks and thickness fringes in specular XRD [15].

Using this information, we can analyse the XRD data to determine which structures are growing on the DSO substrate. Figure 3.9a shows the specular XRD data of SIO thin films with thicknesses from 3.5 to 9.5 nm. The 45° Bragg diffraction peak indicates that the SIO grows with an

orthorhombic-like structure. The orthorhombic SIO (0 0 4) reflection decreases in strength between 5 and 7.5 nm, and the 8 nm film nearly totally loses its (0 0 4) intensity. Thickness fringes of the finite thick film feature a flat SIO film, yet an orthorhombic symmetry is doubtful. The samples stabilized in the orthorhombic phase after growing to 9.5 nm thick films, as shown by the full intensity recovery of the (0 0 4) Bragg peak, which curiously maintains a stable maximum location at 2θ=45° (d=4.03 A).

Figure 3.9b shows the sheet resistance vs. temperature curves of the same sample set and an 8 nm orthorhombic SIO grown on $SrTiO_3$ (STO) as a counter experiment. The counter sample has an order of magnitude lower resistance than the DSO-grown samples. The series goes from metallic to insulating behaviour as thickness decreases, with the resistance of the 5 nm-thick SIO film being impressively independent of temperature at a resistance value of 6.62 k ohms per square when normalized to its nominal thickness. This is near to quantum pair sheet resistance (6.45 kΩ), what constitutes a fascinating hint that the 5 nm-thick film may be at the verge of a quantum phase transition. From now on, we will focus the characterization on the 5 nm sample.

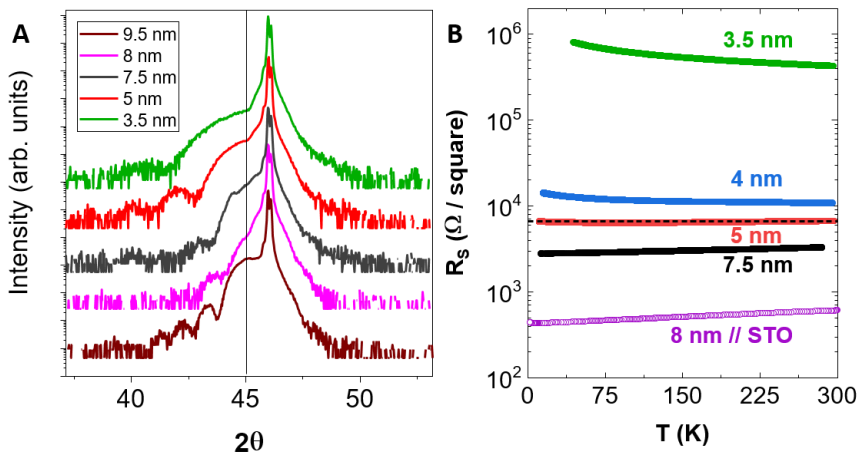

Figure 3.9. (a) Specular XRD of films with thicknesses (from top to bottom): 9.5 nm, 8 nm, 7.5 nm, 5 nm, and 3.5 nm. (b) Sheet resistance of the same samples.

4. Structure characterization: X-ray diffraction reciprocal space maps.

In order to get insights into the strain impact in the SIO structure on the 5 nm-thick SIO film, we measured the Reciprocal Space Maps (RSM). These maps have been measured at the Characterization Facility at the University of Minesotta in collaboration with Dr. Javier García Barriocanal. Figure 3.10 illustrates the reciprocal space (a) HL and (b) KL projection maps. Each map is the projection of 191 detector images collected as a function of incident angle, where each detector pixel is converted to reciprocal space units of the pseudocubic DSO substrate notation (used from now) and the intensity of scattered X-rays is represented using a temperature colour scale. Image processing techniques are used to filter the resulting maps so that the Bragg diffraction peaks of the substrate are less noticeable and the weaker scattering of the film has more contrast.

The map for the HL projection shows a large reconstruction of the unit cell of the film, including components that are both out of plane and in plane. It is interesting to note that when the sample is rotated in plane by 90 degrees, the KL projection does not display any superstructure peaks on the film. This is a solid indication of the non-symmorphic symmetry imposed by the substrate.

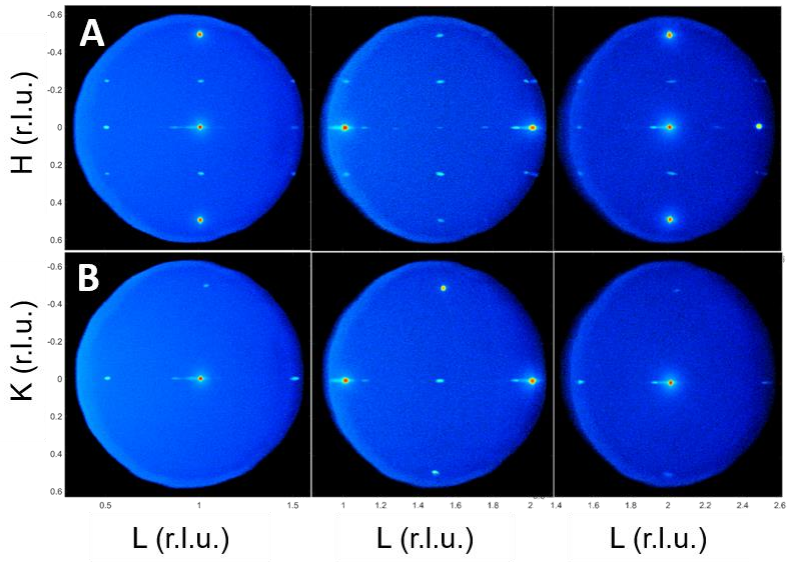

Figure 3.10. Reciprocal space (a) HL and (b) KL maps of the 5 nm DSO sample. The units correspond to the reciprocal space of the pseudocubic substrate.

In order to provide a more clear explanation of the layered projections along HL, HL and KL projections are combined into the three-dimensional reconstruction of the reciprocal space shown in Figure 3.11. The temperature-coloured scale is proportional to the intensity fitting.

The discussion of the x-ray diffraction experiments can be summarized in four observations:

1- The SIO film grows epitaxially in a distorted orthorhombic structure with an interplanar lattice distance of 4.03 Å. This is evidenced in the (0 0 L) specular rod (black dotted line in Figure 3.9), with the highest intensity peaks at smaller L values than the substrate (0 0 1) and (0 0 2) Bragg peaks.

2- A periodicity of two unit cells that can be given to both the substrate and the film. This is revealed in the (0 0 L) direction by the superstructure scattering for half-order reflections (0 0 0.5), (0 0 1.5), and (0 0 2.5).

3- A triple or six-fold periodicity in the c crystallographic direction linked with film scattering corresponding to 0.66 L units along the (0 0 L) rod.
4- In addition, there are crystal truncation rods (0.25 0 L), (0 0.25 L), (-0.25 0 L), and (0 -0.25 L) that are indicated in blue with dashed lines in Figure 3.9. The (0.25 0 L) and (0 0.25 L) peaks rotate 90 degrees in-plane every 0.25 L reciprocal space units. When compared to the data from the substrate, they can only be assigned to the epitaxial film.

In view of the elongated diffraction rods, an important caveat is that at the present stage we cannot distinguish the structural information of the film from a structural reconstruction of the substrate occurring over a thin layer at its surface. Resonant diffraction techniques at synchrotron light sources would be necessary to this end. The reciprocal space analysis suggests that the substrate's rhombohedral structure is inprinted into the SIO film during the early stages of growth. The interfacial SIO has a reduced symmetry superstructure that is four times bigger along the sample's c axis than the pseudocubic orthorhombic unit cell. It also contains a third-order periodicity characteristic of the monoclinic structure, as highlighted by the blue plane of the monoclinic structure in Figure 3.8a, suggesting that nucleation of the monoclinic phase may be taking place.

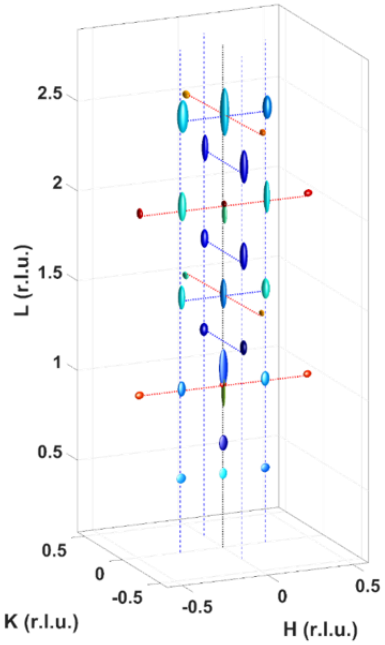

Figure 3.11. Representation reciprocal space in 3D. The findings correspond to the film's (0 0.25 L), (0.25 0 L), (0 -0.25 L), and (-0.25 0 L) crystal truncation rods (blue dashed lines), the substrate's (0 0.5 L), (0.5 0 L), (0 -0.5 L), and (0 0 L) specular rod (black line). The intensity of the crystal truncation and specular rod scattering peaks is shown by the ellipsoids' temperature-coloured scale. The dynamic range of measurements spans five orders of magnitude from red to dark blue. Using a Gaussian fit of the observed scattering peaks in both the HL and KL projections, the ellipsoids' size and intensity are calculated.

In order to gain a deeper understanding of the structural changes taking place in ultrathin SIO layers we have measured Scanning Tunneling Microscopy and Spectroscopy in the 5 nm-thick SIO film.

5. STM measurements. Evidence for the growth of the SIO monoclinic phase

Scanning tunneling microscopy and spectroscopy of the 5 nm film was performed in an ultra-high vacuum STM at the Characterization Facility of the University of Minesotta in collaboration with Dr. Javier García Barriocanal. Figure 3.12a shows a sample region (450 x 450 nm^2 area) with a 100 nm scale bar.

The vast majority of the picture corresponds to a single 3.6 ± 0.05 Å terrace with very irregular terrace edges and adislands of comparable relative thickness as the terraces themselves. A first indication of the formation of the monoclinic-like SIO phase at the surface of the 5 nm thick film is evidenced by the terrace height. The anticipated terrace height of the bulk orthorhombic SIO phase is 3.88 Å, while the monoclinic equivalent is 3.57 Å. This value is equal to one-quarter of the whole unit cell of the monoclinic crystal (see the magenta plane in figure 3.7a), which is very close to what the STM results showed.

To emphasize the different growth process between the orthorhombic and the monoclinic phases, in Figure 3.12b we show a typical 500 × 500 nm^2 region of a 5 nm thick SIO film grown on a cubic (0 0 1) oriented $SrTiO_3$ (STO) substrate. The two surfaces are markedly different. Figure 3.12b shows the terrace height and average terrace width as h=4.2 ± 0.05 Å and w=85 nm respectively, while the SIO (DSO) film has h=3.6 Å and w=350 nm. The SIO (STO) film lacks adislands and irregular edge geometry. The distinct surface morphology of the two samples clearly suggests that while SIO films formed on STO substrates show orthorhombic symmetry a deep structural change occurs when SIO is grown on DSO.

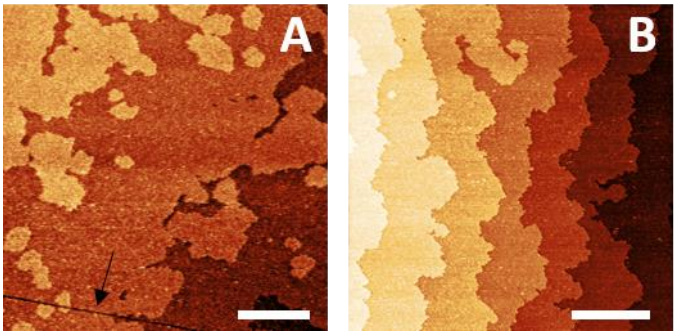

Figure 3.12. 450 nm^2 x 450 nm^2 STM low magnification images of the DSO (A) and STO (B) 5 nm thick films, the two images share the same 100 nm scale bar.

Further evidence can be obtained from high resolution images measured with atomic resolution after conditioning the surface by "tip brushing" to remove adsorbates. Figures 3.13a and 3.13b, respectively, provide a 5x5 nm^2 topographic map of the 5 nm film acquired at a sample bias of V=-500 mV and its associated Fourier transformation. Notice that negative voltages are probing occupied electronic state with an electron tunnelling current to the tip. White dots and lines on top of STM picture 3.13a indicate the presence of a rhombohedral-like surface structure that fits the basal plane of the monoclinic SIO unit cell, a= 5.6 ± 0.1 Å and b= 9.8 ± 0.1 Å, as well as the deformed hexagonal pattern seen in figure 3.13b.

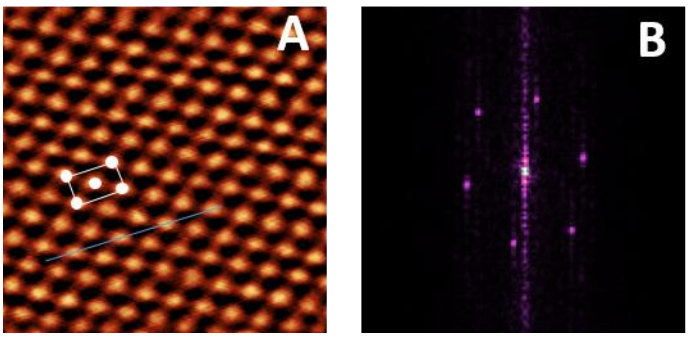

Figure 3.13. (a) 5 nm x 5 nm high resolution STM images obtained at tip bias: V= -500 mV. (b) 11 nm x 11 nm Fourier transform of the image.

Figure 3.14(a and c) shows the 5x5 nm^2 topographic maps of the same region collected at sample biases of -370 mV, 340 mV together with their corresponding Fourier transforms (b and d). Similar to that seen in Figure 3.13a, the sample surface in Figure 3.14a displays a relatively uniform triangular/rhombohedral lattice structure. It's interesting to notice that a second topographic feature appears between two Ir surface atoms when the negative bias is decreased. This characteristic is more visible in figure 3.14c (at 340 mV), where a honeycomb-like pattern with inter-atomic lengths of 2.2 ± 0.1 Å appears. The surface's atomic contrast changes with the bias sign, so the rhombohedral lattice observed when probing occupied states (at negative voltages) becomes a buckled honeycomb lattice when adding the signal from unoccupied states (at positive tip voltages).

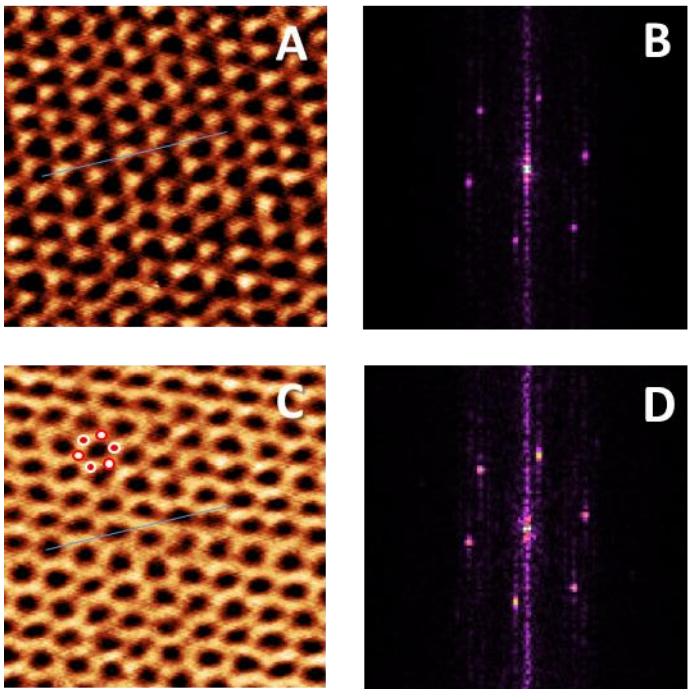

Figure 3.14. (a) and (c) high-resolution STM pictures of 5 nm x 5 nm that were taken with a tip bias/current of -370 mV/ 216 pA and 340 mV/ 216 pA, respectively. (b) and (d) 11 nm x 11 nm Fourier transformation of the images of (a) and (c). The white and red circles in (c) correspond to Ir1 and Ir2 atoms respectively.

Figure 3.15 shows a line profile over the blue lines in figures 3.12a and 3.13a and c, respectively. In this picture, we can see a change in the heights of atoms next to each other. This change corresponds to the heights of the white and red dots in Figure 3.13c. The two Ir triangular lattices correspond to the two adjacent Ir planes of phase sharing oxygen octahedral of the monoclinic structure (see Figure 3.8 a) and constitute a direct evidence of a monoclinic phase at the SIO surface. The alternating heights and lateral contrast show that the unoccupied states being probed are highly confined to the individual Ir octahedrons.

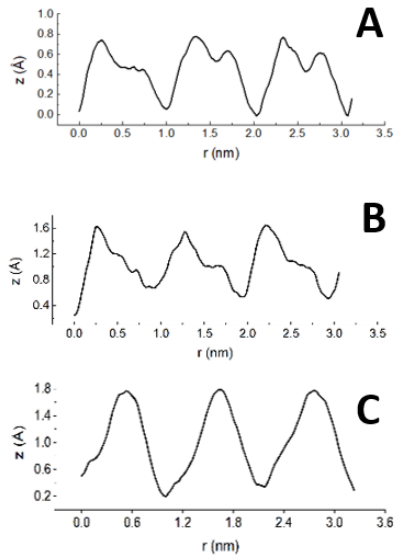

Figure 3.15. (a), (b) and (c) line profile along the blue lines in figures 3.13a and 3.14a and c, respectively.

We gain access to the momentum space of the sample by imaging the surface with scanning tunneling spectroscopy (STS). Figure 3.16 depicts a 128 x 128 matrix over a 3 nm x 3 nm map of the SIO/DSO film. This figure was reconstructed from current-distance curves using the Shockley surface state approximation, as well as the work function value obtained using ultraviolet photoelectron spectroscopy (4.8 eV). The effective mass of surface electrons on the film is found to be surprisingly homogeneous,

with a value of roughly 0.21 ± 0.05 m*. This homogeneity in effective mass is consistent with extremely delocalized surface charge transport.

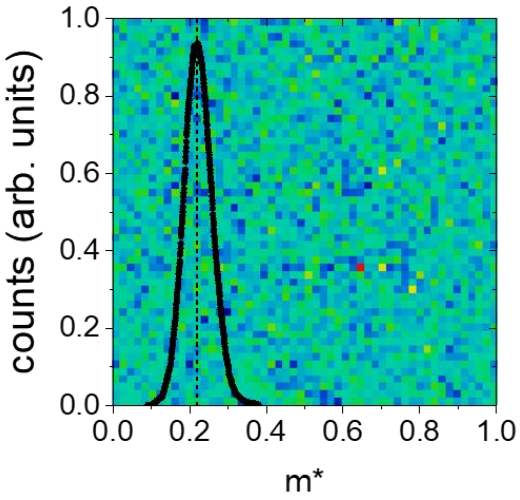

Figure 3.16. STS image of the effective mass of charge carriers in the 5 nm DSO sample at 500 nm x 500 nm. The spectrum distribution of effective electron masses is displayed above the image.

Differential current spectroscopy curves (dI/dV) are presented in Figure 3.17, at 295 K (red) and 77 K (blue). Both curves demonstrate a linear, symmetric change in the conductance, centered at 30 mV, with a gap-like appearance. The 77 K curve shows a narrowing of the gap as well as the emergence of two distinct states from the sample's conductance and valence bands separated by 500 meV, which is approximately the value of the spin-orbit splitting predicted in Ir. For reference, a curve of an 8 nm thick SIO/STO sample collected at 77 K is given, which shows a wide conductance feature with a non-zero DOS at the Fermi level, which is consistent with expected semi-metal behaviour. Three key observations can be inferred from the STS results on the 5nm SIO sample on DSO:

1. There is a linear change in the DOS as a function of bias above and below the Fermi level with occupancy approaching zero as the temperature decreases. The temperature independent DOS at the Fermi level would be consistent with the low conductance value shown in Figure 1, which is mostly unaffected by temperature.

2. The linear relationship between DOS and bias is compatible with a narrow Dirac cone with a Dirac crossing point 30 meV above the Fermi level.
3. The valence and conduction bands begin to localize as the temperature drops. There are two broad (quasiparticle-like) bands at room temperature, but as the temperature drops, the bands get into multiple, narrow states.

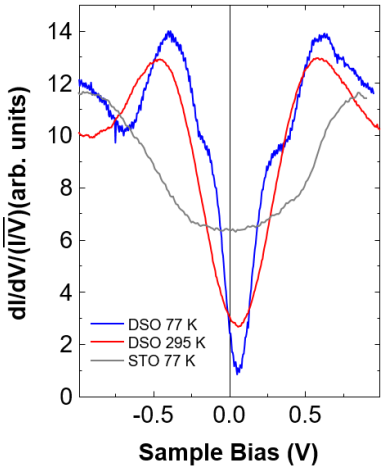

Figure 3.17. Normalized differential conductance as a function of tip bias for the DSO sample at room temperature (red line) and 77 K (blue line) and the STO sample at 77 K (grey line).

These findings are in great agreement with the first principles simulations of the electronic structure presented by Takayama and colleagues [16]. These simulations take into account the strong SOC of t_{2g} Ir electrons in the SIO bulk monoclinic structure. It shows that monoclinic $SrIrO_3$ is a semimetal made up of two protective gapless Dirac bands at the A and M points of the Brillouin zone, close to the Fermi energy.

In fact, the topographic contrast practically disappears when the tunnelling signal is evaluated at 5 mV, close to the minimum of the DOS (see Figure 3.18a). Yet, the Fourier transform shows very weak spots evidencing hexagonal structural features, as indicated by the white arrows

in Figure 3.18b. This is consistent with the minimal amount of charge carriers expected near the Dirac point.

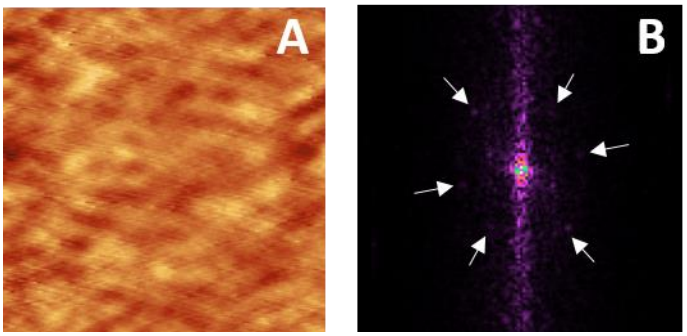

Figure 3.18. (a) 5 nm x 5 nm high resolution STM images obtained at tip bias/current: 5 mV/104 pA. (b) The corresponding 11 nm x 11 nm Fourier transformed data.

The observed features can be discussed in the light of the electronic structure proposed by Daniel Khomskii and collaborators for transition-metal compounds in the case of the face-sharing MO6 octahedra. Transition -metal (Ir) ions in presence of the strong spin orbit interaction show double degenerate ($e_{\sigma g}$) or triple degenerate (t_{2g}) orbitals. The trigonal distortions typical of the structures with face-sharing octahedra lead to splitting of t_{2g} orbitals into an a_{1g} singlet and $e_{\pi g}$ doublet. It is proposed that for both doublets ($e_{\sigma g}$ and $e_{\pi g}$), in the case of one electron or hole per site, we arrive at a Kugel-Khomskii like symmetric model for the orbital and spin interactions. The alternating heights in the Ir and the highly localized states in the specific Ir octahedrons can be understood by looking at the orbital configurations of the two forms of crystallographic Ir in the monoclinic SIO. Figure 3.19 shows the differences in coordination between the two types of octahedrons. Ir1 octahedron creates a network by coordination between vertices, in which the SOC lifts the degeneracy of the t_{2g} electrons into two lower levels with J = 3/2 and one higher level with J = 1/2 respectively (see Figure 3.19b). In the case of Ir2 octahedrons, this distribution of energy levels shifts as a result of face sharing coordination splitting t_{2g} orbitals into an a_{1g} singlet

and $e_{\pi g}$ doublet. This occurs as a consequence of the linear combination of the remaining t2g states [17], [18]. As can be seen in figure 3.13c and the line profiles in figure 3.15, in the scenario of Ir2, the anti-bonding e_g and a1g states open up a channel for tunnelling from the tip to the empty states thus explaining the observed STS features in positive voltages.

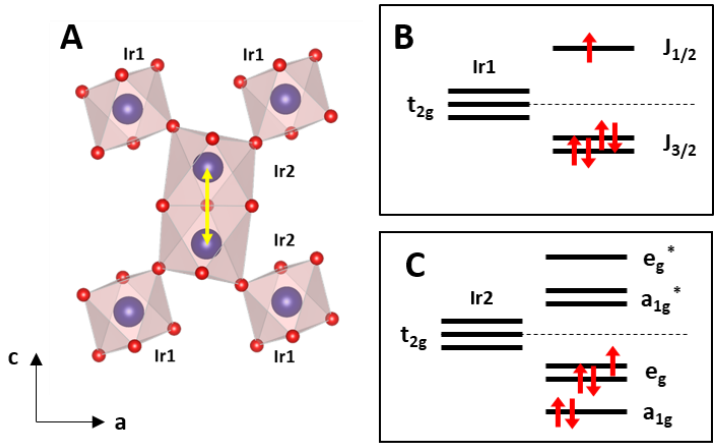

Figure 3.19. Schematic illustration of the coordination of IrO polyhedron along the ac plane, noticed the two different Ir crystallographic positions.

6. Conclusions

We have grown SIO thin films on different substrates with the objective of understanding the impact of epitaxial strain on the structural and transport properties. Our experiments revealed that compressive in-plane strains yield the lowest resistivity values and metallic behaviour, indicating that the overlap between out-of-plane orbitals plays a crucial role in the transport properties of the SIO thin films. Particularly when grown on DSO substrates, SIO thin films exhibit a phase transition to the monoclinic phase over a narrow thickness range (5 to 8 nm). Interestingly, the monoclinic SIO has a Dirac crossing point in the DOS that is centered 30 meV above the Fermi level. These results demonstrate a clear influence

of strain and thickness on the transport and structural properties of SIO thin films, offering valuable insights into the modulation of these properties. Furthermore, our findings suggest a significant interaction between the substrate material and film growth dynamics, resulting in distinct phase transitions. In conclusion, strain and film thickness are key factors that can be manipulated to tune the properties of SIO thin films. This understanding can potentially open new avenues for the fabrication of thin-film materials with properties *by-design*.

7. References

[1] J. K. Kawasaki, M. Uchida, H. Paik, D. G. Schlom, y K. M. Shen, «Evolution of electronic correlations across the rutile, perovskite, and Ruddelsden-Popper iridates with octahedral connectivity», *Phys. Rev. B*, vol. 94, n.º 12, p. 121104, sep. 2016, doi: 10.1103/PhysRevB.94.121104.

[2] G. Jackeli y G. Khaliullin, «Mott Insulators in the Strong Spin-Orbit Coupling Limit: From Heisenberg to a Quantum Compass and Kitaev Models», *Phys. Rev. Lett.*, vol. 102, n.º 1, p. 017205, ene. 2009, doi: 10.1103/PhysRevLett.102.017205.

[3] G. Cao, J. Bolivar, S. McCall, J. E. Crow, y R. P. Guertin, «Weak ferromagnetism, metal-to-nonmetal transition, and negative differential resistivity in single-crystal Sr2IrO4», *Phys. Rev. B*, vol. 57, n.º 18, pp. R11039-R11042, may 1998, doi: 10.1103/PhysRevB.57.R11039.

[4] B. Kim, P. Liu, y C. Franchini, «Magnetic properties of bilayer Sr3Ir2O7: Role of epitaxial strain and oxygen vacancies», *Phys. Rev. B*, vol. 95, n.º 2, p. 024406, ene. 2017, doi: 10.1103/PhysRevB.95.024406.

[5] J. Liu *et al.*, «Strain-induced nonsymmorphic symmetry breaking and removal of Dirac semimetallic nodal line in an orthoperovskite iridate», *Phys. Rev. B*, vol. 93, n.º 8, p. 085118, feb. 2016, doi: 10.1103/PhysRevB.93.085118.

[6] B. Kim, B. H. Kim, K. Kim, y B. I. Min, «Substrate-tuning of correlated spin-orbit oxides revealed by optical conductivity

calculations», *Sci. Rep.*, vol. 6, n.º 1, Art. n.º 1, jun. 2016, doi: 10.1038/srep27095.

[7] J. Nichols *et al.*, «Tuning electronic structure via epitaxial strain in Sr2IrO4 thin films», *Appl. Phys. Lett.*, vol. 102, n.º 14, p. 141908, abr. 2013, doi: 10.1063/1.4801877.

[8] A. Lupascu *et al.*, «Tuning Magnetic Coupling in Sr2IrO4 Thin Films with Epitaxial Strain», *Phys. Rev. Lett.*, vol. 112, n.º 14, p. 147201, abr. 2014, doi: 10.1103/PhysRevLett.112.147201.

[9] J. Liu *et al.*, «Tuning the electronic properties of J_eff=1/2 correlated semimetal in epitaxial perovskite SrIrO3». arXiv, 8 de mayo de 2013. Accedido: 23 de enero de 2023. [En línea]. Disponible en: http://arxiv.org/abs/1305.1732

[10] L. F. Mattheiss, «Energy Bands for KNiF3 , SrTiO3 , KMoO3 , and KTaO3», *Phys. Rev. B*, vol. 6, n.º 12, pp. 4718-4740, dic. 1972, doi: 10.1103/PhysRevB.6.4718.

[11] G. Khalsa, B. Lee, y A. H. MacDonald, «Theory of t 2 g electron-gas Rashba interactions», *Phys. Rev. B*, vol. 88, n.º 4, p. 041302, jul. 2013, doi: 10.1103/PhysRevB.88.041302.

[12] E. Dagotto, T. Hotta, y A. Moreo, «Colossal magnetoresistant materials: the key role of phase separation», *Phys. Rep.*, vol. 344, n.º 1-3, pp. 1-153, abr. 2001, doi: 10.1016/S0370-1573(00)00121-6.

[13] B. Kim, P. Liu, y C. Franchini, «Dimensionality-strain phase diagram of strontium iridates», *Phys. Rev. B*, vol. 95, n.º 11, p. 115111, mar. 2017, doi: 10.1103/PhysRevB.95.115111.

[14] J. K. Kawasaki, M. Uchida, H. Paik, D. G. Schlom, y K. M. Shen, «Evolution of electronic correlations across the rutile, perovskite, and Ruddelsden-Popper iridates with octahedral connectivity», *Phys. Rev. B*, vol. 94, n.º 12, p. 121104, sep. 2016, doi: 10.1103/PhysRevB.94.121104.

[15] A. Biswas y Y. H. Jeong, «Growth and engineering of perovskite SrIrO 3 thin films», *Curr. Appl. Phys.*, vol. 17, n.º 5, pp. 605-614, may 2017, doi: 10.1016/j.cap.2016.09.020.

[16] Y. S. Lee *et al.*, «Systematic trends in the electronic structure parameters of the 4 d transition-metal oxides SrMO3 (M=Zr, Mo, Ru, and Rh)», *Phys. Rev. B*, vol. 67, n.º 11, p. 113101, mar. 2003, doi: 10.1103/PhysRevB.67.113101.

[17] K. I. Kugel, D. I. Khomskii, A. O. Sboychakov, y S. V. Streltsov, «Spin-orbital interaction for face-sharing octahedra: Realization of a highly symmetric SU(4) model», *Phys. Rev. B*, vol. 91, n.º 15, p. 155125, abr. 2015, doi: 10.1103/PhysRevB.91.155125.

[18] S. V. Streltsov, G. Cao, y D. I. Khomskii, «Suppression of magnetism in Ba5 AlIr2O11 : Interplay of Hund's coupling, molecular orbitals, and spin-orbit interaction», *Phys. Rev. B*, vol. 96, n.º 1, p. 014434, jul. 2017, doi: 10.1103/PhysRevB.96.014434.

Chapter 4

Manipulation of the metal-insulator transition in $SrIrO_3$ ultrathin layers through field effect

1. Introduction

5d oxides with strong spin-orbit coupling can host a wide range of novel quantum states due to the interplay between Coulomb repulsion, U, and spin orbit coupling, SOC, energy scales [1], [2]. $SrIrO_3$ (SIO) is in the vicinity of a metal-insulator transition, MIT, triggered, as explained in the introduction, by this interplay in a system where U, SOC, and bandwidth, W (mediated by the octahedron coordination and rotations), share nearly the same energy scale (0.3–0.4 eV) [3]–[10]. Naively speaking, the narrow bands driven by the reduced hopping rate in distorted oxygen bonds are split by the SO interaction in a way that the moderate Coulomb repulsion of the 5d electrons is enough to induce an insulating state. In this way, tiny external perturbations can deeply alter this balance and modify transport and magnetic properties.

In transition metal oxides ultrathin films, the multiorbital nature of d electrons together with the interplay between spin orbit interaction and symmetry breaking opens interesting new avenues to control the electronic structure [11]–[13]. Spin-orbit interaction mixes t_{2g} bands (corresponding to d_{xy}, d_{xz}, and d_{yz} orbitals) with different spin and orbital symmetry, causing spin-orbit splitting and narrow bands where Coulomb interaction

kicks in [2], [14], [15]. Inversion symmetry breaking, occurring naturally at surfaces or interfaces, opens new hopping channels, influences orbital mixing, band width, and spin splitting [11]–[13], [16]. The strong electric fields developing in field effect experiments with ionic liquids can conspire to modulate symmetry-breaking fields of ultrathin layers in the 2D limit. As a result, the electronic structure, which is highly connected to the electric field by the strong spin-orbit coupling, may be substantially modified.

In the previous chapter, we used the epitaxial strain as a knob to modulate the transport properties of SIO. In this chapter, we will use ionic liquid gating [17]–[24] in ultrathin films of SIO to modify the electronic structure in a way that the MIT can be controlled. Typically, the large electric field generated at the interface between the ionic liquid and the oxide is screened over the Thomas Fermi length, λ_{TF}, whose value is [25]:

$$\lambda_{TF}^2 = \left(\frac{\pi}{6}\right)^{1/3} \frac{\varepsilon a_0}{4n^{1/3}m^*}$$

Where ε is the dielectric constant, a_0 is the Bohr radius, n is the density of the electrons responsible of the screening of the electric field and m^* is the effective mass . Because of the reduced charge density in SIO triggered by the high degree of carrier (electron-hole) compensation, its screening length becomes nanometric, precisely matching the thickness range where SIO thin films become insulating. The incomplete screening of the electric field by the small carrier density of SIO, which is further decreased at MIT, is essential for observing effects of the electric field apart from just electrostatic doping.

2. Epitaxial SIO ultrathin layers deposited on (001) STO

Ultrathin films of SIO grown on (001) $SrTiO_3$ (STO) with thicknesses ranging from 1-3 nm showed a metal-insulator transition when the thickness was below 2 nm. As depicted in Figure 4.1, specular X-ray diffraction experiments revealed that the out-of-plane lattice parameter increased as the film thickness decreased. This is indicated by a shift of diffraction peaks to lower angles, as seen by the inclined line connecting the (002) diffraction peaks in Figure 4.1. These structural modifications appear to be connected to the thickness-controlled metal-insulator transition observed in the films.

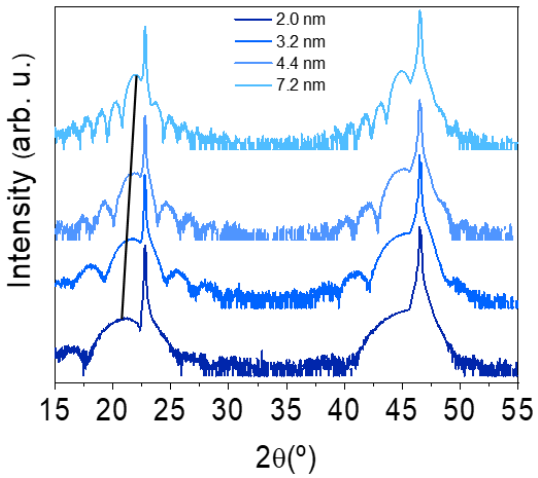

Figure 4.1. Specular x-ray diffraction of SIO ultrathin films grown on STO.

In order to study the impact of oxygen rotations on the reduced symmetry of the unit cell, we conducted three-dimensional X-ray reciprocal space imaging. The reciprocal space maps of the 5 nm sample, shown in Figure 4.2, are indexed using (H, K, L) triads that refer to the cubic unit cell of the $SrTiO_3$ substrate. Non-integer reflections can be seen in both the in-plane and out-of-plane axes, which indicates that the oxygen octahedra

are rotating around both axes, similar to what is observed in bulk SIO. The mixed {0, ±K/2, L/2}, {±H/2, 0, L/2}, and {±H/2, ±K/2, L/2} reflections indicate the presence of a $a^-a^-c^+$ pattern of oxygen octahedral [26]–[28], which is formed by the out-of-phase rotation of the octahedra within the plane of the film layers, combined with out-of-plane tilting and antipolar displacements of the A-site cations [27], [28]. This is an indication that antiferrodistortive in-plane rotations $a^0a^0c^-$ occur in SIO films with thicknesses below 1 nm [10]. When the thickness is increased to four unit cells, these rotations relax into the 3D rotation pattern of the Pbnm space group that is characteristic of bulk samples.

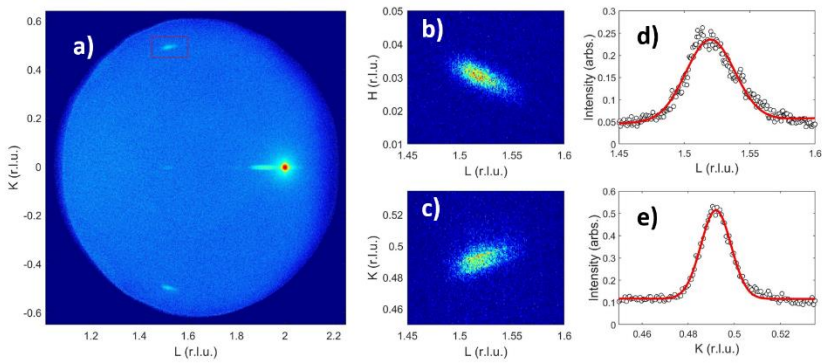

Figure 4.2. (a) Reciprocal space map of a 5 nm SIO ultrathin film grown on STO, showing the X-ray diffraction reflections projected on the KL plane. The contour plot uses a logarithmic false colour scale and shows half-integer reflections (0, -0.5, 1.5), (0, 0.5, 1.5) and (0, 0, 1.5) corresponding to the pseudocubic unit cell of the iridate, as well as the integer (0 0 2) reflections of both film and substrate. (b) and (c) Linear false colour scale contour plots of KL and HL projections of the (0, 0.5, 1.5) reflection highlighted with a red box in (a). (d) and (e) Intensity profiles of the map displayed in (b) along the horizontal and vertical axes, respectively.

This rotating pattern was observed repeatedly in a series of samples ranging in thickness from 2 to 10 nm; this is a thickness range in which the films are metallic, as can be seen in Figure 4.3.

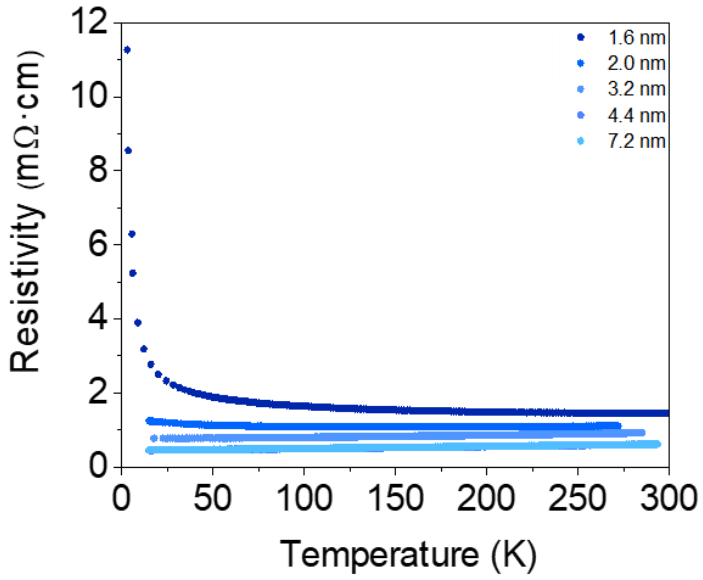

Figure 4.3. Resistivity as a function of temperature of SIO ultrathin films grown on STO.

3. *In-operando* transport measurement with ionic liquid gating

In order to perform the transport measurements, we first fabricate a Hall bar device in the manner that is explained in the Experimental Methods chapter. In this device, longitudinal (V_{XX}) and transverse voltages (V_{XY}) (Hall Effect) can be measured using the two different configurations shown in Figure 4.4.

Next to the Hall bar gate, electrodes were patterned to yield the gating geometry shown in Figure 4.5a. The ionic liquid drop is deposited on the sample, covering all its surface (Figure 4.5b). The Hall bar is connected to ground, and the gates are connected to the voltage source as indicated in figure 4.5c. Using this configuration, if we apply positive gate voltages, the sample will be doped with electrons, and negative gate voltages will dope it with holes.

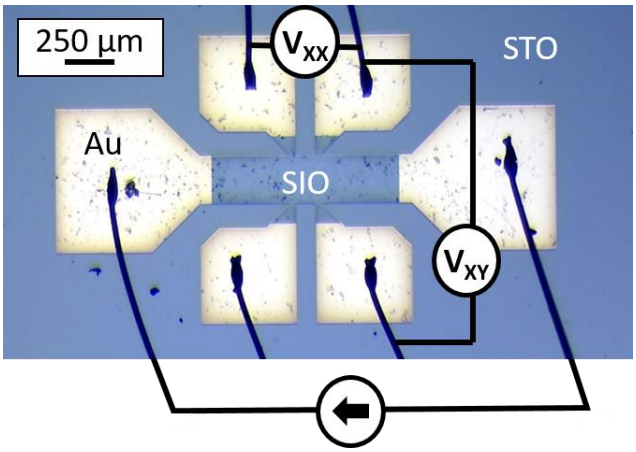

Figure 4.4. Scheme of the Hall bar configuration for measuring longitudinal and transverse resistivity

We chose sample thickness at the verge of the MIT on both the insulating (1.6 nm) and metallic (2.0 nm) sides of the transition and performed the ionic liquid gating experiments in these samples to cross the MIT from both sides. Longitudinal resistivity and Hall effect measurements were taken at the same time for each gate voltage. Ionic liquid gating turned the conducting state of the samples from metal to insulating, and vice versa. As we will discuss below, it is interesting that the effect of the gating was the opposite of what one would expect from electrostatic doping. When positive gate voltages (expected to produce electron doping) are applied to the metallic 2 nm sample (Figure 4.6a), it turns into an insulator. This is a surprising result in view of the semi-metallic band structure of SIO 113, where an increase in the number of electrons (the more mobile carriers) should increase conductivity, contrary to what is observed. Under negative gate voltages (expected to produce hole doping), the insulating 1.6 nm sample (Figure 4.6a) turns metallic. These anomalous changes are a first indication that the effect of the electric field in the gating experiment is not simply causing electrostatic doping.

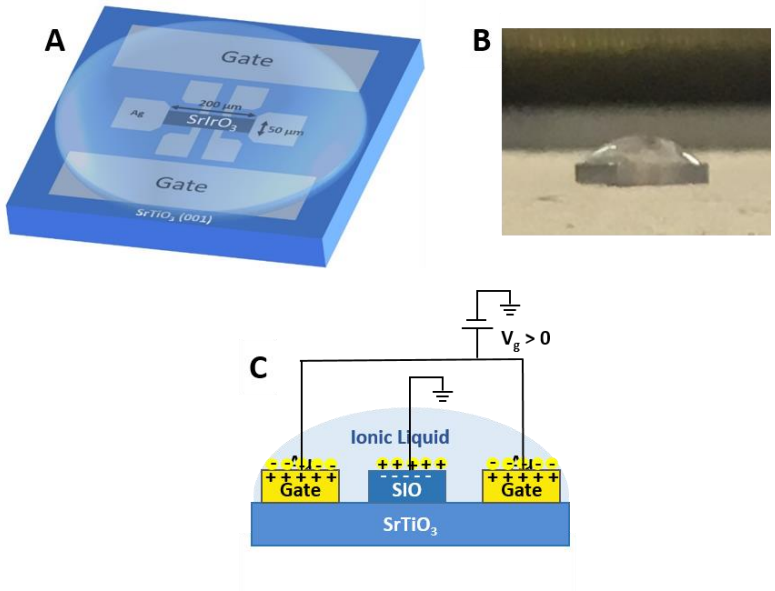

Figure 4.5. (a) Scheme of the gating geometry. (b) Image of the sample with the ionic liquid drop on top. (c) Scheme of the polarization configuration for a positive voltage applied.

We investigate the variations in carrier density caused by the gating process by measuring the Hall effect at 40 K for various gate voltages. This temperature is sufficiently high to avoid the effects of quantum corrections on the conductivity or magnetoresistance of magnetic phases, which appear at low temperatures, as detailed below. According to previous reports, transverse resistivity always had a negative slope, indicating that electrons have larger mobilities than holes [8], [28], [29]. When the metallic 2 nm sample is gated with positive voltages (expected to generate electron doping), an increase in Hall resistivity is induced, which might be explained in principle as a drop in hole density in a two-band picture. On the other hand, when the insulating 1.6 nm sample is gated with negative voltages, the Hall resistivity drops, which might be explained in terms of an increase in hole density in a two-band picture (Figures 4.6c y 4.6d).

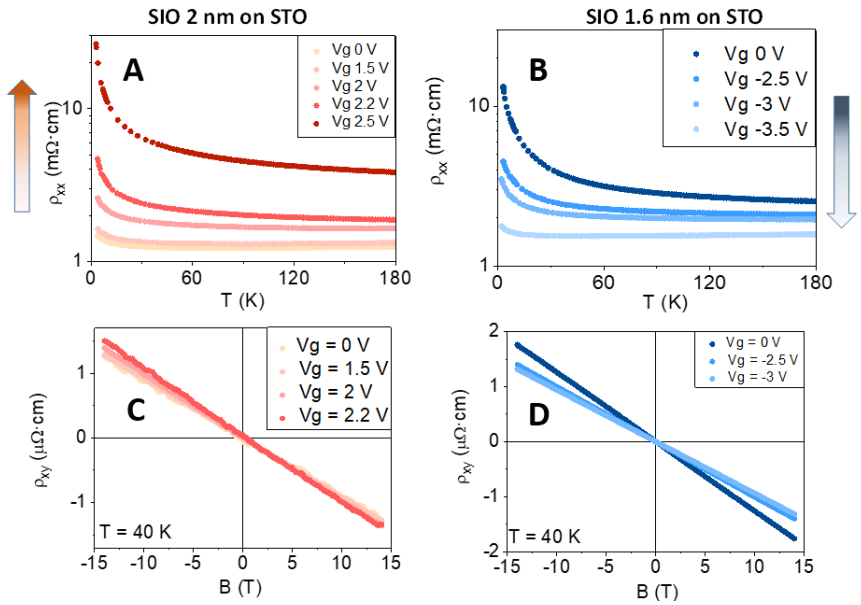

Figure 4.6. Longitudinal resistivity (a) and (b) and Hall effect (c) and (d) measured at 40 K at each gate voltage during an ionic liquid IL gating experiments of a 2 nm SIO 113 sample at the metallic side of the MIT (a) and (c) and of a 1.6 nm sample at the insulating side (b) and (d).

3.1. Reversibility of the gating process

The following sections address two critical issues in ionic liquid doping: the creation of oxygen vacancies by the strong electric field in the double layer and the chemical stability of the ionic liquid as a result of reaction with the sample. To avoid reactivity with the sample, the ionic liquid was deposited on the SIO in a precooled sample plate of a cryostat in an inert atmosphere. The temperature was quickly decreased and maintained below room temperature during the gating experiment. When the temperature is maintained below 240 K, no degradation by the ionic liquid is detected. The reversibility of the gating experiments demonstrated the absence of degradation. Positive gate voltages forced an insulating condition from a metallic sample, while negative gate voltages restored the metallic state (see Figure 4.7).

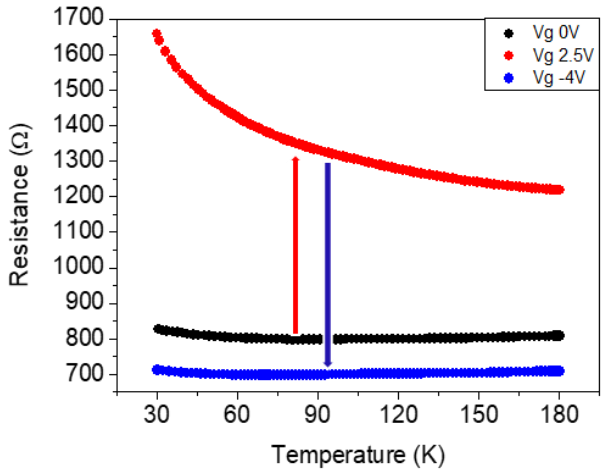

Figure 4.7. Gate reversibility. Resistance vs. temperature graph (black symbols) of a pristine metallic sample. Positive voltage doping (red curve) turns the sample insulating. Red arrow indicates direction of the changes. Negative voltages recover metal (blue symbols). The blue arrow indicates changing direction.

Regarding oxygen vacancies, as shown in the references [30], [31], oxygen vacancies might be created under positive gate voltages, where the strong electric field towards the SIO layer could attract oxygen anions to the ionic liquid. The reduction in electron density found at positive gate voltages, on the other hand, is incompatible with the electron doping induced by oxygen vacancies. Furthermore, we did not see the signal of ionic liquid deterioration by oxygen accumulation in capacitance versus frequency measurements taken concurrently with gating, as depicted in Figure 4.8. Finally, although oxygen vacancies have been proven in gating studies to occur in cuprates and other mixed valence compounds, the great chemical stability of Ir4+ towards reduction makes vacancy formation challenging.

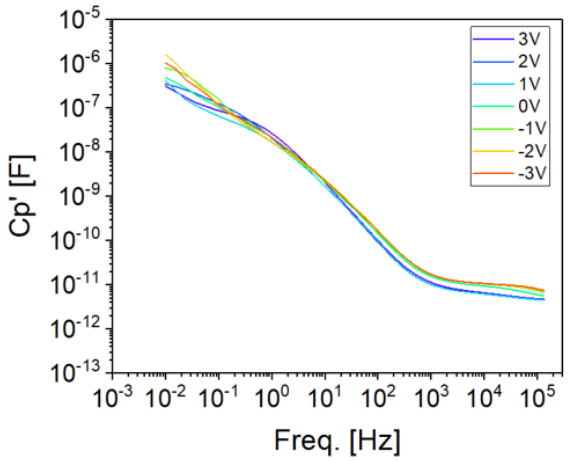

Figure 4.8. Ionic liquid capacitance reversibility. Ionic liquid capacitance between the SIO and side electrode at varying gate voltages. Reversibility suggests the ionic liquid has not deteriorated.

3.2. Evolution of charge densities and mobilities with IL gating

We analyzed the evolution of the transport properties during gating to extract the induced changes in charge densities and mobilities [8]. As the SIO has an electron and a hole band crossing the Fermi level, we analyzed the Hall effect using a two-bands model, as described in Eq. 1. As the Hall transport is dominated by electrons, this expression can be approximated with its low field limit to the Eq. 2

$$\rho_H = \frac{tR_{xy}}{B} = \frac{1}{e}\frac{n_h\mu_h^2 - n_e\mu_e^2 + (n_h - n_e)(\mu_h\mu_e B)^2}{\sigma_0^2/e^2 + (n_h - n_e)^2(\mu_h\mu_e B)^2} \qquad [1]$$

$$\rho_H = \frac{e}{\sigma_0^2}\left(n_h\mu_h^2 - n_e\mu_e^2\right) \qquad [2]$$

Where

$$\sigma_0 = \sigma_h + \sigma_e = e(n_h\mu_h + n_e\mu_e)$$

On the other hand, we can fit the cyclotron component of the magnetoresistance to the Eq. 3, which assuming low field and the same concentrations for electrons and holes, and thus that the term, MR can be written as Eq.4

$$MR = \frac{1}{e}\frac{n_h\mu_h - n_e\mu_e + (n_h\mu_h + n_e\mu_e)(\mu_h\mu_e B)^2}{\sigma_0^2/_{e^2} + (n_h - n_e)^2(\mu_h\mu_e B)^2} \qquad [3]$$

$$MR = \frac{e}{\sigma_0}\left(n_h\mu_h\mu_e^2 + n_e\mu_e\mu_h^2\right)B^2 \qquad [4]$$

Parabolic field dependence of magnetoresistance was experimentally verified at 40 K during the gating process. This temperature is enough to avoid quantum corrections and ensure a dominating parabolic shape [29], as shown in Figure 4.9. We used a sampling algorithm, assuming a constant ratio between electron and hole mobilities to determine carrier densities and mobilities consistent with equations [2] and [3].

Figure 4.10 shows carrier densities (a) and mobilities (b) for an insulating 1.6 nm-thick sample (blue symbols) turned conducting by gating with negative voltages (hole doping) and a conducting 2 nm-thick sample (red symbols) made insulating by gating with positive voltages (corresponding to electron doping). Solid figures represent electron concentrations and mobilities, whereas open symbols represent hole carrier mobilities. Notice that gating affects carrier density but not mobility.

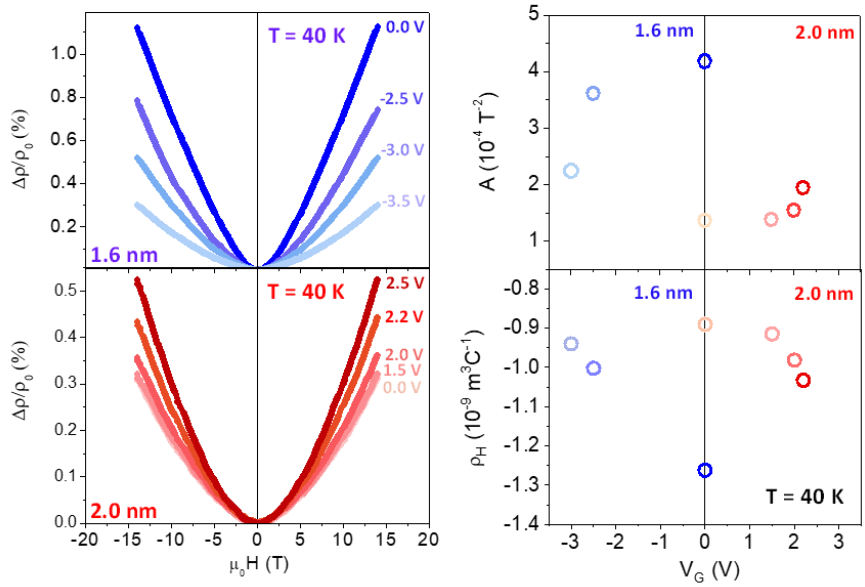

Figure 4.9. Left panels. Magnetic field dependence of the magnetoresistance upon gating for a 1.6-nm thick sample (upper panel) and a 2-nm thick sample (lower panel). Right panels. Coefficient of the parabolic magnetoresistance $MR = \frac{e}{\sigma_0}(n_h\mu_h\mu_e^2 + n_e\mu_e\mu_h^2)B^2 = AB^2$ (upper panel) and Hall resistivity (lower panel) for both samples (blue symbols correspond to the 1.6 nm sample and red symbols to the 2 nm sample).

When the 2 nm sample is doped with positive gate voltages (electron doping), electron density diminishes. Electron doping of a semimetal should increase hole concentration, however as well as the electron density, the hole density decreases too. The Hall resistivity increases with positive gate voltages because the electron-hole ratio increases. However, negative voltages (hole doping) increase the density of holes and electrons in the 1.6 nm thick sample. Due to double layer charge screening, the usual doping effect cannot explain this behavior. The sudden suppression in carrier density in the insulating state suggests the opening of a gap in a way controlled by the external electric field.

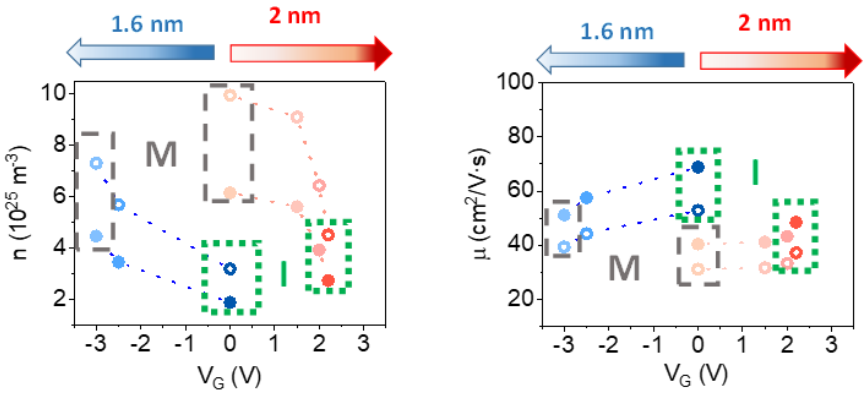

Figure 4.10. Carrier density (left panel) and mobility (right panel) as a function of gate voltage for a metallic 2 nm-thick sample (red symbols) and a 1.6 nm-thick sample (insulating). Electrons are solid and holes are open. Insulating states have green dotted squares while metallic states have grey ones.

The unusual decrease in electron and hole concentrations when the insulating state is approached suggests the opening of a charge gap. However, it is unclear why this phenomenon (if unrelated to doping) is affected by the direction of the electric field. It is expected that the applied electric field should modify the confining potential and spin-orbit interaction, but not the field direction, as in fact happens. The reduced carrier density reduces screening effects on charge density, especially in the insulating state where the Thomas Fermi screening length is comparable to sample thickness. In a system like ours with broken symmetry and high spin orbit interaction, the enormous partially screened electric field generated in the gating operation can deeply modify the electronic structure. This suggests that the surprising asymmetric electric field dependence is caused by the symmetry-breaking of the ultrathin samples controlled by the electric field generated during the gating process.

3.3. Anomalous Hall effect

The unexpected (ferro)magnetism shown by low-temperature measurements of the transverse resistivity in the insulating state is direct evidence of the correlated nature of the insulating state driven by an electric field. Figures 4.11 (a)-(f) clearly exhibit the anomalous Hall effect in the insulating state between 2 and 40 K. Subtraction of the normal Hall resistivity (linear component) from the high field slope results in an evident (inverted) hysteresis cycle. This hysteresis suggests not only an emergent ferromagnetism but also a negative anomalous Hall conductivity (Figure 4.11 (g)).

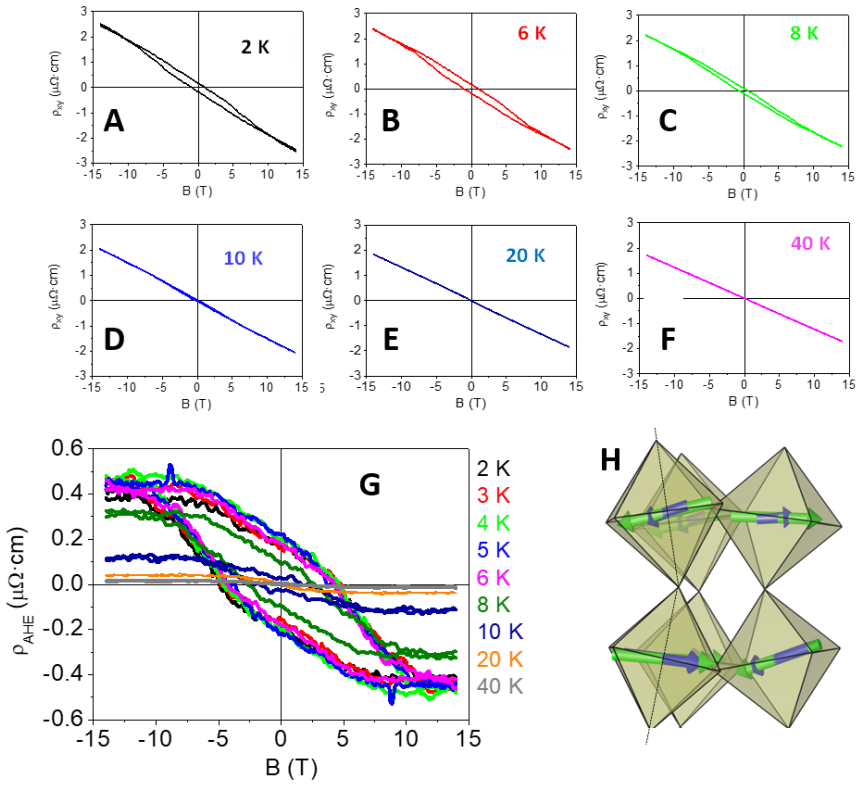

Figure 4.11. (a)-(f) Hysteretic Hall effect measured as a function of magnetic field at low temperatures; (g) anomalous Hall effect measured by subtracting the ordinary component from transverse resistivity. (h) Sketch showing that the out-of-plane canted moment is caused by bending Ir-O-Ir bonds or tilting octahedrons (Ir atoms are at the center and oxygens are at the vertexes).

4. DFT

The electric field modulation of the ground state of SIO ultra-thin films reveals an intriguing scenario of external control of symmetry breaking. We used first-principles density functional theory (DFT) simulations to acquire insight into the electric field-driven alteration of SIO electronic states. The DFT calculations were carried out by Juan Beltran (GFMC-UCM) and María del Carmen Muñoz (ICMM-CSIC). I did not directly participate in these calculations, but the results are described below as they are essential for the understanding of the gating effect.

4.1. Previous considerations

To model SIO films, asymmetric (001) SIOm/STO slabs with two SrO layers on the free surface and at the SIO/STO interface. The supercells had four formula units in the plane to account for the reduction in symmetry observed in X-ray reciprocal space maps. This reduction in symmetry is caused by anisotropic bond distortions caused by oxygen octahedron rotation and polar displacement of Sr atoms. A sawtooth-like potential is used to add the external electric field. We varied the number of unit cells in (001) SIOm/STO between m=1 and 6 and the slabs were structurally optimized to take into account the electrostatic screening effects (see Figure 4.12).

4.2. Band structure simulations

Films are insulators for m = 2 and a MIT occurs for m = 3. Figure 4.13 shows the band structure around the Fermi level of the SIO (m = 3)/STO slab (sketch in Figure 4.12). The metallic state has a band structure controlled by the tilting and rotation of the IrO_6 octahedra and the U Hubbard electron correlation (U=1.5 eV). This band structure matches the most stable $a^-a^-c^+$ crystal configuration observed in the x-ray measurements, although the STO substrate affects the rotation angles of the IrO_6 octahedra nearest the SIO-STO interface. Different colors indicate projections into the IrO_2 planes of the structure (green, red and blue correspond to the surface, middle, and interfacial planes). Figure 4.13

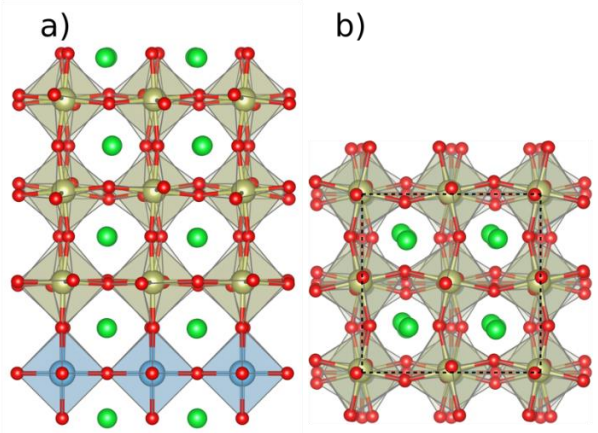

Figure 4.12. Atomic diagram of the [SIO]3/STO heterostructure for positive external electric field (E=0.1 eV) showing oxygen, titanium, strontium, and Iridium atoms as red, blue, green, and yellow circles with the atomic plane along the: a) [010], b) [001] direction.

also illustrates the band structures under electric fields of ±0.1 eV/Å perpendicular to the layers. Positive values indicate electric field from the SIO surface to the STO interface that corresponds to positive gate voltages in the experiment.

We observe that the electric field direction affects calculated ground state. Positive electric fields push the narrow J_{eff} = 1/2 t_{2g} bands above the Fermi level, driving an insulating state. For negative electric fields, wider bands cross the Fermi level and become metallic. Thus, positive and negative electric fields affect the band structure around the Fermi energy asymmetrically. These calculations reflect the above experiments: electric field has a symmetry breaking effect. Positive electric fields restore band degeneracy of the IrO_2 planes, which have already been lifted in the asymmetric SIO/STO slab, and increase the energy of the bands, which are primarily localized on the film surface (green coloured bands). In negative fields, however, the bands remain non-degenerate. As a result, even with zero applied electric field, electronic states that belong to different planes appear separated in the metallic state and mixed in the insulating state. Negative electric fields increase film asymmetry, whereas

positive electric fields decrease it, demonstrating that the intrinsic asymmetry of the film produced on STO can be compensated.

It is important to remark that the symmetry breaking comes from the differences in the confining potentials of STO and vacuum. Calculations (Figure 4.13 d, e and f) removing the STO layer, while keeping the structure unrelaxed to retain a certain degree of asymmetry, provide direct support for this statement. Removing the STO (and thus reducing band asymmetry) yields in an insulating state at E=0, that a negative electric field cannot restore into the metallic state, but it reduces the gap and increases band asymmetry. This implies the symmetry breaking of the STO is analogous to a negative electric field.

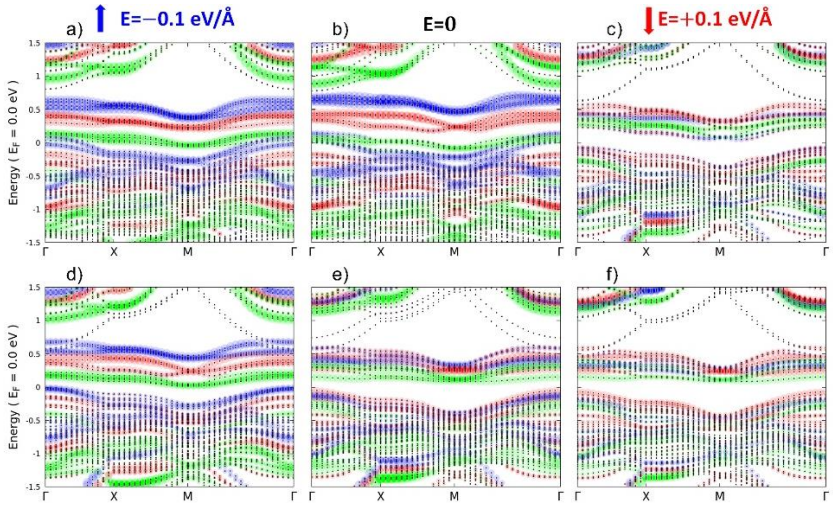

Figure 4.13. SIO supercell on STO band dispersion (panels a–c). The structure's IrO2 planes produce bands of varied hues (green, red, and blue correspond to the surface, middle and interfacial planes). Calculations are under external electric fields E = -0.1 eV/Å (a), E = 0 (b), and E = +0.1 eV/Å. (c). SIO supercell band dispersion without the STO layer (panels (d), (e), (f)).

In the same way, the spin-orbit interaction is essential for tuning the metal-insulator transition by using positive electric fields. As shown in Figure 4.14, not including the spin-orbit interaction, the film is metallic, and the electric field is screened by charge redistribution between the IrO_2 layers. The competition between the different asymmetries (STO and electric field-driven) is only active when spin-orbit coupling (SOC) is switched on.

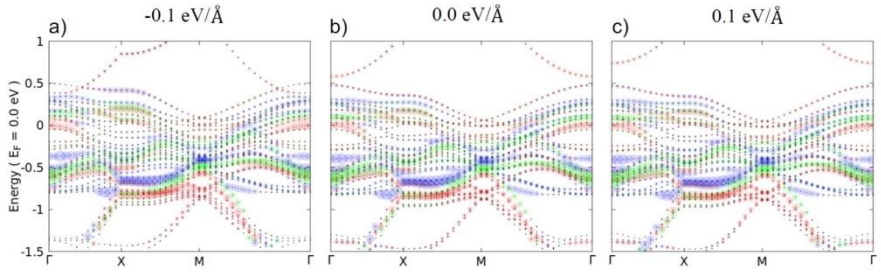

Figure 4.14. Band dispersion for the SIO supercell on STO, like figure 4.13, but without including the spin-orbit interaction.

4.3. Density of states

To investigate the role of the electric field in modulating the inversion asymmetry introduced by the STO substrate further, we examined the layer projected densities of states for three fields, E = 0 and E = 0.1 eV/Å, in structures with or without the STO substrate. The results, observed in Figure 4.15, indicates the SIO layers exhibit a metallic density of states in the presence of the STO base layer and in the absence of an external field (first row). When a positive field is applied, the energy distribution of the occupied bands changes and the energy gap opens. The negative field, on the other hand, induces a significant rearrangement of the electronic levels within the film while preserving the density of states at the Fermi level. The second row of Figure 4.15 shows the layer projected DOS of SIO slabs without the STO layer, but with no the atomic relaxation. In this case, the insulating state is found at E = 0 (rather than at E = 0.1 eV/Å as with STO), indicating that the effect of intrinsic

symmetry breaking is comparable to that of a negative electric field pointing from the STO to the SIO surface. The relaxed SIO slab without STO is shown in the three bottom panels of Figure 4.15, which produces an insulating state that, because the SIO slab is now fully symmetric, does not change when the direction of the electric field is reversed. This analysis shows that the interplay between the electric field and the asymmetry of the slab cause the inversion symmetry breaking and induce the metal to insulator transition in the system. This interplay is enhanced by the strong spin-orbit coupling, which makes the bands mainly localized at the surface always have smaller energy. The applied electric field has a larger spin-orbit-driven symmetry breaking effect at the surface than at the interface.

5. Discussion

The restoration of the orbital angular momentum degree of freedom in the t_{2g} manifold (effective L = 1) may couple the electronic structure to the electric field. Orbital angular momentum interacts to ultrathin oxide layers' inversion symmetry-breaking electric fields to produce Rashba-type surface band splitting, which can lead to interesting new phenomena [32]. Rashba-type splitting occurs when the electric field interacts with the dipolar charge distributions associated with orbital angular momentum states [33], [34]. However, this contradicts the "up-down" electric field asymmetry shown by gating experiments and first-principles calculations.

Alternatively, the multiorbital effects of Rashba spin-orbit interaction in the t_{2g} electron could be used to explain how spin-orbit interaction and inversion symmetry breaking interact [11]–[13]. SIO is a t_{2g} electron system because the strong crystal field splits the d orbitals, as mentioned in the Introduction chapter. In a cubic environment, parity symmetry prevents interorbital hopping, whereas inversion symmetry breaking opens additional hopping channels in the Ir-oxygen network.

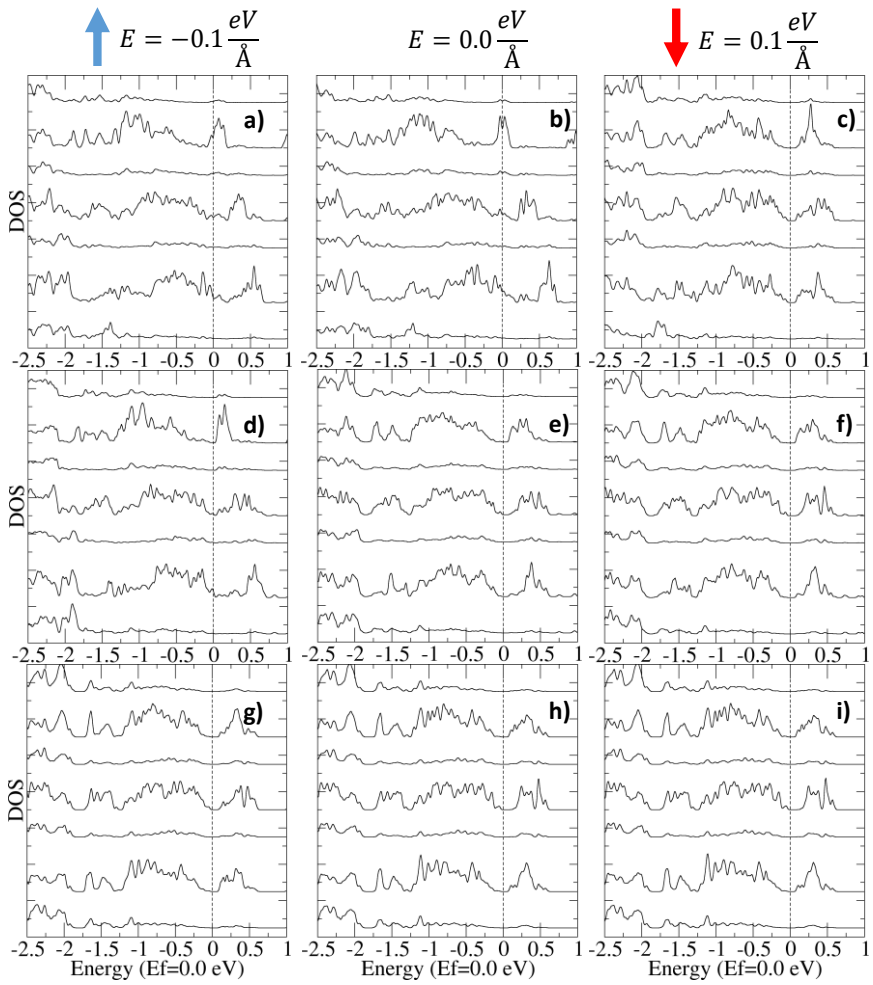

Figure 4.15. Density of states projected to SIO [001] lattice planes. The three columns represent applied electric fields of -0.1 eV/Å, 0 eV/Å, and +0.1 eV/Å. Three SIO atomic models are shown in the tree rows: SIO superstructure developed on STO, without the STO layer but without relaxation of the atomic positions, and without the STO layer permitting relaxation.

Thus, the external electric field modulates hopping processes, and when combined with the atomic-like spin-orbit interaction, the new hopping channels generate additional Rashba band splittings, which in multiorbital systems are much more complex than spin-splitting in 2D semiconductor quantum wells. The electric field breaks inversion symmetry, modulating the effect of other symmetry breaking on the polar deformations of the orbital lobes that create new hopping channels. The electric field cannot distinguish up from down, but other types of symmetry breaking can create different hopping energies at the surface and at the STO interface, which can be changed by the electric field. In this case, the oxygen rotations are asymmetric at the interface (where the titanate suppresses out-of-plane bond bending) and the surface (where the film relaxes towards the bulk's $a^-a^-c^+$ structure). Octahedral rotations allow antisymmetric interorbital hopping terms between xy and yz orbitals along the x direction, coming from surface layer orbital lobe deformation [12].The absent apical oxygen above the surface lowers the energy of the z^2 orbital, enabling additional coupling paths to the electric field. The modulation of the broken symmetry hopping channels by the strong external electric field is central to the observed effect and justifies the lower energy (larger hopping) of the IrO2 planes at the surface. Future work will establish the direct connection between the detailed mechanism and the broken symmetry channels.

According to the experimental data, the estimated insulator phase for the SIO/STO in a positive electric field has canted orbital (0.26 μ_B) and spin (0.17 μ_B) moments with out of plane components of 0.04 and 0.02 μ_B, respectively. Their ratio is 1.52, close to two, the ideal Jeff = 1/2 state. Orbital and spin moments in adjacent Ir atoms align antiferromagnetically both within and between layers, despite canting of magnetic moments generated by rotation and tilting of the IrO6 octahedron, providing a weak ferromagnetic component perpendicular to the film, see Figure 4.11h. On the contrary, in the metallic state reached with a negative electric field, the long-range magnetic order observed in the insulator does not occur, although smaller local orbital and spin moments may survive.

Dzyaloshinskii-Moriya interaction gerenates a canted antiferromagnetic state, that produces tiny out-of-plane moments [35]. Bertaut's law [36] dictates that out-of-plane Ir-O-Ir bonds bend to generate symmetry conditions for weak ferromagnetism [37]. This canted antiferromagnetic order is reflected in the anomalous Hall conductivity. Strong spin-orbit interaction causes non-collinearity, which breaks time reversal symmetry. This makes it possible to observe AHE [38], [39], which comes from the Berry flux at avoided crossings caused by symmetry breaking and spin-orbit interaction [40].

6. Conclusion

In conclusion, we have shown that the high electric fields produced in a field effect experiment with ionic liquids strongly couple to the electronic structure of ultrathin films of $SrIrO_3$, creating deep modifications beyond those expected from doping. Driven by the strong spin orbit interaction, the external electric field conspires with inversion symmetry breaking to yield anomalous band splitting which trigger the metal-to-insulator transition. Solid evidence for the main role played by electron correlations in producing the transition is provided by the emergent anomalous Hall effect and magnetism, which is related to the out-of-plane canted antiferromagnetic state discovered in the insulating phase. We have shown that the electric field-controlled inversion symmetry breaking is a useful knob for manipulating the effective strength of the correlations yielding the MIT transition [41].

7. References

[1] W. Witczak-Krempa, G. Chen, Y. B. Kim, y L. Balents, «Correlated Quantum Phenomena in the Strong Spin-Orbit Regime», *Annu. Rev. Condens. Matter Phys.*, vol. 5, n.º 1, pp. 57-82, 2014, doi: 10.1146/annurev-conmatphys-020911-125138.

[2] H. Watanabe, T. Shirakawa, y S. Yunoki, «Microscopic Study of a Spin-Orbit-Induced Mott Insulator in Ir Oxides», *Phys. Rev. Lett.*, vol. 105, n.º 21, p. 216410, nov. 2010, doi: 10.1103/PhysRevLett.105.216410.

[3] G. Cao, J. Bolivar, S. McCall, J. E. Crow, y R. P. Guertin, «Weak ferromagnetism, metal-to-nonmetal transition, and negative differential resistivity in single-crystal Sr2IrO4», *Phys. Rev. B*, vol. 57, n.º 18, pp. R11039-R11042, may 1998, doi: 10.1103/PhysRevB.57.R11039.

[4] S. J. Moon *et al.*, «Dimensionality-Controlled Insulator-Metal Transition and Correlated Metallic State in 5d Transition Metal Oxides Srn+1IrnO3n+1 (n=1, 2, and ∞)», *Phys. Rev. Lett.*, vol. 101, n.º 22, p. 226402, nov. 2008, doi: 10.1103/PhysRevLett.101.226402.

[5] A. Yamasaki *et al.*, «Three-dimensional electronic structures and the metal-insulator transition in Ruddlesden-Popper iridates», *Phys. Rev. B*, vol. 94, n.º 11, p. 115103, sep. 2016, doi: 10.1103/PhysRevB.94.115103.

[6] H. Zhang, K. Haule, y D. Vanderbilt, «Effective J=1/2 Insulating State in Ruddlesden-Popper Iridates: An LDA+DMFT Study», *Phys. Rev. Lett.*, vol. 111, n.º 24, p. 246402, dic. 2013, doi: 10.1103/PhysRevLett.111.246402.

[7] J. K. Kawasaki, M. Uchida, H. Paik, D. G. Schlom, y K. M. Shen, «Evolution of electronic correlations across the rutile, perovskite, and Ruddelsden-Popper iridates with octahedral connectivity», *Phys. Rev. B*, vol. 94, n.º 12, p. 121104, sep. 2016, doi: 10.1103/PhysRevB.94.121104.

[8] Y. F. Nie *et al.*, «Interplay of Spin-Orbit Interactions, Dimensionality, and Octahedral Rotations in Semimetallic SrIrO 3», *Phys. Rev. Lett.*, vol. 114, n.º 1, p. 016401, ene. 2015, doi: 10.1103/PhysRevLett.114.016401.

[9] D. J. Groenendijk *et al.*, «Spin-Orbit Semimetal SrIrO 3 in the Two-Dimensional Limit», *Phys. Rev. Lett.*, vol. 119, n.º 25, p. 256403, dic. 2017, doi: 10.1103/PhysRevLett.119.256403.

[10] P. Schütz *et al.*, «Dimensionality-Driven Metal-Insulator Transition in Spin-Orbit-Coupled SrIrO 3», *Phys. Rev. Lett.*, vol. 119, n.º 25, p. 256404, dic. 2017, doi: 10.1103/PhysRevLett.119.256404.

[11] G. Khalsa, B. Lee, y A. H. MacDonald, «Theory of t 2 g electron-gas Rashba interactions», *Phys. Rev. B*, vol. 88, n.º 4, p. 041302, jul. 2013, doi: 10.1103/PhysRevB.88.041302.

[12] Z. Zhong, A. Tóth, y K. Held, «Theory of spin-orbit coupling at LaAlO3/SrTiO3 interfaces and SrTiO3 surfaces», *Phys. Rev. B*, vol. 87, n.º 16, p. 161102, abr. 2013, doi: 10.1103/PhysRevB.87.161102.

[13] Y. Kim, R. M. Lutchyn, y C. Nayak, «Origin and transport signatures of spin-orbit interactions in one- and two-dimensional SrTiO${}_{3}$-based heterostructures», *Phys. Rev. B*, vol. 87, n.º 24, p. 245121, jun. 2013, doi: 10.1103/PhysRevB.87.245121.

[14] G. Dresselhaus, «Spin-Orbit Coupling Effects in Zinc Blende Structures», *Phys. Rev.*, vol. 100, n.º 2, pp. 580-586, oct. 1955, doi: 10.1103/PhysRev.100.580.

[15] Rashba, E. I. J. S. P., «Properties of semiconductors with an extremum loop. I. Cyclotron and combinational resonance in a magnetic field perpendicular to the plane of the loop», *Sov Phys-Solid State*, vol. 2, n.º 1109, 1960.

[16] K. V. Shanavas, Z. S. Popović, y S. Satpathy, «Theoretical model for Rashba spin-orbit interaction in d electrons», *Phys. Rev. B*, vol. 90, n.º 16, p. 165108, oct. 2014, doi: 10.1103/PhysRevB.90.165108.

[17] H. Shimotani, H. Asanuma, A. Tsukazaki, A. Ohtomo, M. Kawasaki, y Y. Iwasa, «Insulator-to-metal transition in ZnO by electric double layer gating», *Appl. Phys. Lett.*, vol. 91, n.º 8, p. 082106, ago. 2007, doi: 10.1063/1.2772781.

[18] K. Ueno *et al.*, «Electric-field-induced superconductivity in an insulator», *Nat. Mater.*, vol. 7, n.º 11, pp. 855-858, nov. 2008, doi: 10.1038/nmat2298.

[19] H. Yuan, H. Shimotani, A. Tsukazaki, A. Ohtomo, M. Kawasaki, y Y. Iwasa, «High-Density Carrier Accumulation in ZnO Field-Effect Transistors Gated by Electric Double Layers of Ionic Liquids», *Adv. Funct. Mater.*, vol. 19, n.º 7, pp. 1046-1053, 2009, doi: 10.1002/adfm.200801633.

[20] J. T. Ye *et al.*, «Liquid-gated interface superconductivity on an atomically flat film», *Nat. Mater.*, vol. 9, n.º 2, pp. 125-128, feb. 2010, doi: 10.1038/nmat2587.

[21] Y. Yamada *et al.*, «Electrically induced ferromagnetism at room temperature in cobalt-doped titanium dioxide», *Science*, vol. 332, n.º 6033, pp. 1065-1067, may 2011, doi: 10.1126/science.1202152.

[22] X. Leng, J. Garcia-Barriocanal, S. Bose, Y. Lee, y A. M. Goldman, «Electrostatic Control of the Evolution from a Superconducting Phase to an Insulating Phase in Ultrathin YBa2Cu3O7−x Films», *Phys. Rev. Lett.*, vol. 107, n.º 2, p. 027001, jul. 2011, doi: 10.1103/PhysRevLett.107.027001.

[23] A. T. Bollinger, G. Dubuis, J. Yoon, D. Pavuna, J. Misewich, y I. Božović, «Superconductor-insulator transition in La2-xSrxCuO4 at the pair quantum resistance», *Nature*, vol. 472, n.º 7344, pp. 458-460, abr. 2011, doi: 10.1038/nature09998.

[24] Y. Ohuchi *et al.*, «Electric-field control of anomalous and topological Hall effects in oxide bilayer thin films», *Nat. Commun.*, vol. 9, n.º 1, Art. n.º 1, ene. 2018, doi: 10.1038/s41467-017-02629-3.

[25] L. S, «Ashcroft And Mermin Solid State Physics».

[26] A. M. Glazer, «Simple ways of determining perovskite structures», *Acta Crystallogr. Sect. A*, vol. 31, n.º 6, pp. 756-762, 1975, doi: 10.1107/S0567739475001635.

[27] A. K. Choquette *et al.*, «Octahedral rotation patterns in strained EuFeO3 and other Pbnm perovskite films: Implications for hybrid improper ferroelectricity», *Phys. Rev. B*, vol. 94, n.º 2, p. 024105, jul. 2016, doi: 10.1103/PhysRevB.94.024105.

[28] J. Liu *et al.*, «Tuning the electronic properties of J_eff=1/2 correlated semimetal in epitaxial perovskite SrIrO3». arXiv, 8 de mayo de 2013. doi: 10.48550/arXiv.1305.1732.

[29] N. Manca *et al.*, «Balanced electron-hole transport in spin-orbit semimetal SrIrO3 heterostructures», *Phys. Rev. B*, vol. 97, n.º 8, p. 081105, feb. 2018, doi: 10.1103/PhysRevB.97.081105.

[30] J. Jeong, N. Aetukuri, T. Graf, T. D. Schladt, M. G. Samant, y S. S. P. Parkin, «Suppression of metal-insulator transition in VO2 by electric field-induced oxygen vacancy formation», *Science*, vol. 339, n.º 6126, pp. 1402-1405, mar. 2013, doi: 10.1126/science.1230512.

[31] A. M. Perez-Muñoz *et al.*, «In operando evidence of deoxygenation in ionic liquid gating of YBa2Cu3O7-X», *Proc. Natl. Acad. Sci. U. S. A.*, vol. 114, n.º 2, pp. 215-220, ene. 2017, doi: 10.1073/pnas.1613006114.

[32] V. Sunko *et al.*, «Maximal Rashba-like spin splitting via kinetic-energy-coupled inversion-symmetry breaking», *Nature*, vol. 549, n.º 7673, pp. 492-496, sep. 2017, doi: 10.1038/nature23898.

[33] S. R. Park, C. H. Kim, J. Yu, J. H. Han, y C. Kim, «Orbital-Angular-Momentum Based Origin of Rashba-Type Surface Band Splitting», *Phys. Rev. Lett.*, vol. 107, n.º 15, p. 156803, oct. 2011, doi: 10.1103/PhysRevLett.107.156803.

[34] S. Oh y H. J. Choi, «Orbital angular momentum analysis for giant spin splitting in solids and nanostructures», *Sci. Rep.*, vol. 7, n.º 1, Art. n.º 1, may 2017, doi: 10.1038/s41598-017-02032-4.

[35] D. I. Khomskii, *Transition Metal Compounds*. Cambridge: Cambridge University Press, 2014. doi: 10.1017/CBO9781139096782.

[36] E. F. Bertaut, «Symbols for space groups», en *International Tables for Crystallography*, Th. Hahn, Ed., 1.ª ed.en International Tables for Crystallography, vol. A. Chester, England: International Union of Crystallography, 2006, pp. 62-76. doi: 10.1107/97809553602060000509.

[37] E. Bousquet y A. Cano, «Non-collinear magnetism in multiferroic perovskites», *J. Phys. Condens. Matter Inst. Phys. J.*, vol. 28, n.º 12, p. 123001, mar. 2016, doi: 10.1088/0953-8984/28/12/123001.

[38] H. Chen, Q. Niu, y A. H. MacDonald, «Anomalous Hall Effect Arising from Noncollinear Antiferromagnetism», *Phys. Rev. Lett.*, vol. 112, n.º 1, p. 017205, ene. 2014, doi: 10.1103/PhysRevLett.112.017205.

[39] S. Nakatsuji, N. Kiyohara, y T. Higo, «Large anomalous Hall effect in a non-collinear antiferromagnet at room temperature», *Nature*, vol. 527, n.º 7577, pp. 212-215, nov. 2015, doi: 10.1038/nature15723.

[40] L. Šmejkal, Y. Mokrousov, B. Yan, y A. H. MacDonald, «Topological antiferromagnetic spintronics», *Nat. Phys.*, vol. 14, pp. 242-251, mar. 2018, doi: 10.1038/s41567-018-0064-5.

[41] S. Manipatruni *et al.*, «Scalable energy-efficient magnetoelectric spin-orbit logic», *Nature*, vol. 565, n.º 7737, pp. 35-42, ene. 2019, doi: 10.1038/s41586-018-0770-2.

Chapter 5

Interface dependent anomalous Hall effect in $SrIrO_3$ by magnetic proximity effect

1. Introduction

Traditionally, topological phenomena have been studied in materials with strong spin-orbit interaction, where electronic states are typically extended due to the large atomic numbers of these material families (for example, topological insulators). On the other hand, strongly correlated materials (such as high-Tc superconductors or colossal magnetoresistance manganites) owe their correlated electronic groundstates to highly localized early transition metal states [1]. As such, correlated and topological physics have long been considered to result from opposite research strands with little mixing. In recent years, there has been growing interest in the study of the interplay between topological phenomena and correlated physics [2], [3], as exciting electronic groundstates (like topological Mott insulators or Weyl semimetals) may emerge. Moreover, this competition may be the seed of new responses of interest in quantum technologies, where the correlated physics brings a wide manifold of tunable responses and the topological states their robustness against external perturbations and decoherence. In this sense, the 3d/5d oxide interface is a highly promising area of research as it combines the strong spin-orbit coupling of the 5d oxides with the strong electron correlations

and magnetism of the 3d oxides. In addition, the perovskite structure common to many of both 3d and 5d oxides allows to bring them in "intimate" electronic contact at epitaxial interfaces, which may constitute a unique playground to realize the interplay between topology and correlations and enable exciting opportunities to explore novel electronic and magnetic groundstates. In this chapter we will focus on the study of the interplay between correlations and topology in $La_{0.3}Sr_{0.7}MnO_3/SrIrO_3$ (LSMO/SIO) heterostructures. To probe the topological states, we will examine the intrinsic anomalous Hall effect, a transport phenomenon that is related to the topology of the electronic band structure [4], [5], and correlated physics will be probed through interfacial magnetism (SQUID magnetometry and x-ray absorption) and MIT in transport experiments.

In the following, we will investigate the AHE of LSMO/SIO interfaces, which constitutes an attractive playground for investigating unique contributions to the intrinsic Hall effect [6], [7] connected to the topological features of correlated electrons. Both layer sequences LSMO/SIO and SIO/LSMO will be examined as, as shown below, the different interface bonding causes markedly different forms of electronic reconstruction.

2. Sample growth and structural characterization

The bilayers were grown utilizing the high-pressure pure oxygen sputtering process detailed in the introductory chapter. Employing high oxygen pressures (2.8 mbar) and high temperatures (650 °C for SIO and 900°C for LSMO), epitaxial growth of the samples on (001) oriented $SrTiO_3$ substrates occurred in a pure oxygen environment. We fabricated two types of samples: LSMO/SIO bilayers with SIO at the bottom and SIO/LSMO bilayers with SIO at the top. To protect the SIO layer from deterioration, samples with SIO on top were capped with a 3-nm amorphous BTO layer.

Aberration-corrected scanning transmission electron microscopy (STEM) was used to examine the structure and chemistry of both sets of samples. However, to analyze both interfaces concurrently, Figure 5.1 displays the high angle annular dark-field (HAADF) and electron energy loss spectroscopy (EELS) results pertaining to a trilayer of LSMO (15 nm)/SIO (4.4 nm)/LSMO (15 nm). This trilayer structure allows examining both interface stackings in the same sample. These measurements were acquired at the "Centro Nacional de Microscopia Electrónica" (CNME) using a JEOL JEM ARM200cF operated at 200 kV.

Figure 5.1a features a HAADF image obtained from a cross-section sample thinned in the [100]/[001] plane, revealing flat and coherent interface growth over extensive lateral distances. Due to contrast scaling with atomic number, the heavier Ir atoms at the B site of the perovskite (IrO_2 planes) appear brighter in the SIO, while La/Sr (A site of the perovskite) exhibit less brightness in the LSMO.

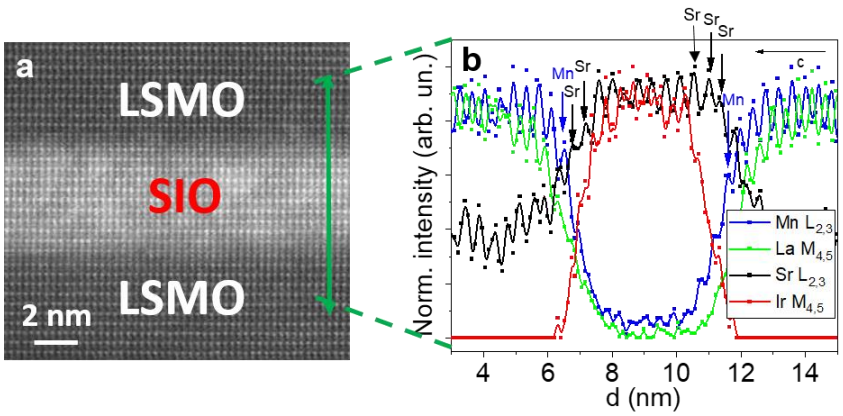

Figure 5.1. Structure and chemistry of the LSMO/SIO, SIO/LSMO interfaces. (a) Low magnification HAADF image of an LSMO (15 nm)/SIO (4.4 nm)/LSMO (15 nm) sample. (b) Electron energy loss spectroscopy (EELS) acquired across the LSMO/SIO/STO interfaces following the green line.

Figure 5.1b presents the Mn $L_{2,3}$, La $M_{4,5}$, Sr $L_{2,3}$, and Ir $M_{4,5}$ integrated signals from an EELS line scan perpendicular to the interface, as indicated by the green line in Figure 5.1a. By comparing the decay of the La $M_{4,5}$ and Mn $L_{2,3}$ signals towards the interfaces, it becomes evident that additional SrO planes exist at the interfaces. The LSMO/SIO interface

(LSMO at the top) contains an extra SrO plane, resulting in a LaSrO/SrO/SrO/IrO2 layer sequence (Sr planes marked with black arrows). Conversely, the SIO/LSMO interface (SIO at the top) possesses two additional SrO planes, yielding a LaSrO/SrO/SrO/SrO/IrO2 layer sequence.

Figure 5.2 displays a magnified HAADF view of the two distinct interfaces. The SrO planes between the La and Ir planes (marked with yellow arrows) are laterally displaced in relation to one another, as in the rock salt structure. A clear contrast anomaly observed at both interfaces highlights the differences between the LSMO/SIO and SIO/LSMO interfaces. Notice the increased interface width of the SIO/LSMO interface due to the extra SrO block with an extra SrO plane, which will confer an insulating character to the interface.

Such interface reconstructions have not been reported in other manganite iridate superlattices [8]–[10] grown by pulsed laser deposition (PLD). However, they are frequently observed at interfaces between perovskites involving members of the Ruddlesden-Popper series [11]–[13]. As demonstrated below, similar to other manganite-based heterostructures [13], the interfacial SrO planes will profoundly impact the transport and magnetic properties of the interface.

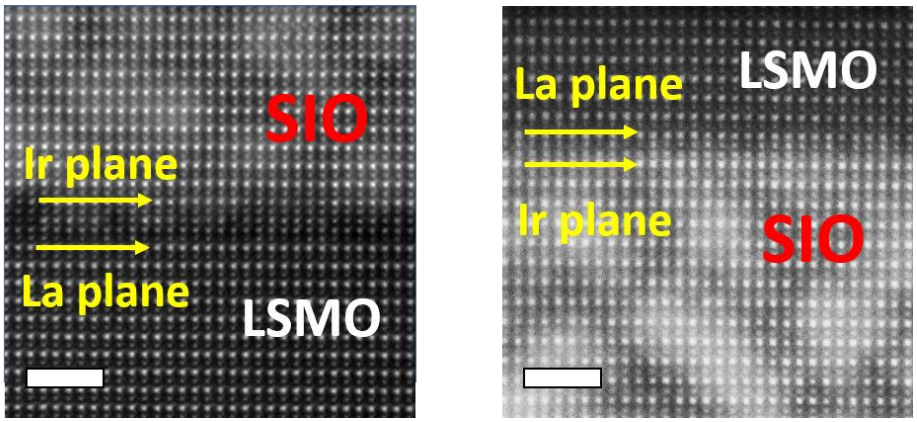

Figure 5.2. HAADF magnification of the (a) SIO/LSMO interface and the (b) LSMO/SIO interface. The scale bar corresponds to 2 nm. The La and Ir planes that delimit the interface are marked with yellow arrows.

3. Transport characterization

The longitudinal and transverse dc resistances, R_{xx} and R_{xy} , were measured as a function of the magnetic field H (applied perpendicular to the film plane) for different temperatures in the range 5–300 K using a Quantum Design PPMS apparatus equipped with a He flow refrigerator (see Methods chapter) and a superconducting magnet. The LSMO/SIO samples were measured at the CNRS Thales of Paris while the SIO/LSMO samples were measured at the "Instituto de Ciencia de Materiales de Madrid" (ICMM).

The resistances are defined as $R_{xx} = V_{xx}/I_{xx}$ (longitudinal resistance) and $R_{xy} = V_{xy}/I_{xx}$ (transverse resistance), with I_{xx} the injected dc current and V_{xx} and V_{xy} the voltages measured parallel and perpendicular to the injected current. The LSMO/SIO samples were measured using the 4-point technique, while the SIO/LSMO samples were measured using a Hall Bar of 250 µm width as shown in Figure 5.3. Voltage offsets were removed by inverting the current sign and averaging the measured voltage.

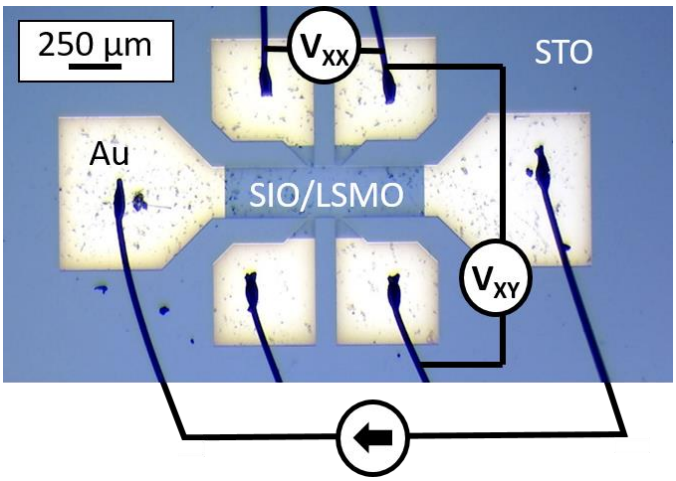

Figure 5.3. Microscopy image of the Hall Bar used in transport measurement of the SIO/LSMO samples.

The pure Hall signal, which is "odd" with respect to the applied field, was calculated as $\langle R_{xy}(H)\rangle = (R_{xy}(+H) - R_{xy}(-H))/2$. This allows removing

any spurious contribution to R_{xy} resulting from the electrodes' misalignment and the strong magnetoresistance of LSMO (which is "even" with respect to the applied field). In LSMO/SIO samples we calculated the resistivity ρ_{xx} and ρ_{xy} via the Van der Pauw method from the resistances obtained as described above, by considering the films' dimensions and thickness. In SIO/LSMO samples we calculated the resistivity ρ_{xx} and ρ_{xy} using the resistivity equation from the resistances obtained by also considering the films' dimensions and thickness.

In this study, we analyze two sets of samples, namely, LSMO/SIO bilayers and SIO/LSMO bilayers, as sketched in Figure 5.4. The LSMO/SIO samples, measured at CNRS Thales of Paris, have a constant LSMO thickness of 25 nm and the SIO thickness is varied between 0 and 15 nm. The SIO/LSMO samples, measured at the Instituto de Ciencia de Materiales de Madrid, have a constant LSMO thickness of 16 nm and the SIO thickness is varied between 0 and 15 nm.

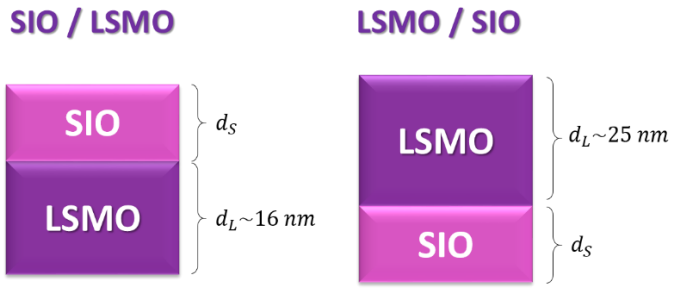

Figure 5.4. Sketch illustrating the two bilayers configuration: SIO/LSMO (left), LSMO/SIO (right).

The longitudinal resistivity of each sample was measured as a function of temperature. As illustrated in Figure 5.5a, both sample sets demonstrate consistent metallic behaviour across the entire temperature range, with the resistivity values being remarkable similar. Further analysis reveals that within each set of samples, the resistivity values are maintained, irrespective of the SIO thickness variations. This is clearly depicted in Figure 5.5b, which uses the SIO/LSMO interface as an example. The uniformity in resistivity values is predominantly attributed to the

substantial thickness of LSMO presented in all the samples. The relatively large LSMO thickness effectively enforces a characteristic metallic behaviour, thereby determining unaltered specific resistivity values.

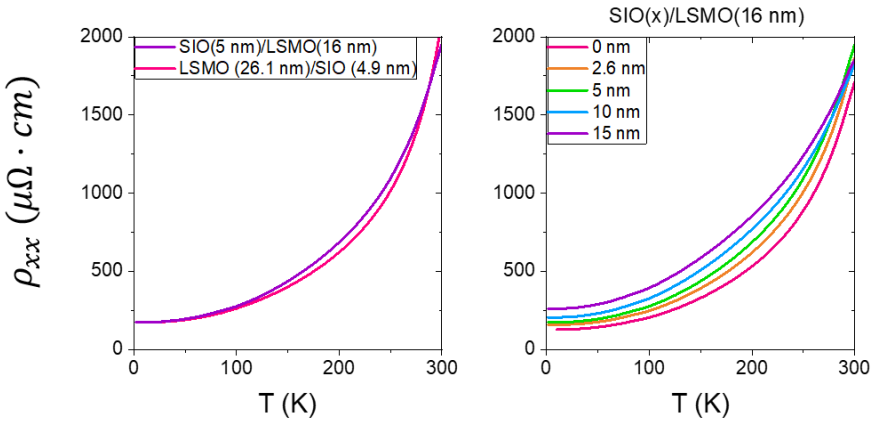

Figure 5.5. Longitudinal resistivity ρ_{xx} vs. temperature for (a) SIO (5 nm)/LSMO(16 nm) and LSMO(26.1 nm)/SIO (4.9 nm) and for (b) SIO(x)/LSMO(16 nm) with x between 0 and 15 nm.

Similar to previous observations, the magnetoresistance (MR) measurements exhibit remarkably consistent behaviour across all samples set, dominated by the presence of LSMO. Figure 5.6 serves as a representative example, showing the MR measurements at various temperatures for LSMO/SIO (on the left) and SIO/LSMO (on the right) bilayer samples with equivalent SIO thicknesses. Interestingly, the magnetoresistance takes a positive value under low magnetic fields, which we attribute to anisotropic magnetoresistance (AMR). Subsequently, upon saturation of magnetization, the MR transitions to a negative value, attributed to colossal magnetoresistance (CMR), a phenomenon widely reported in manganites, as explained in the introductory chapter.

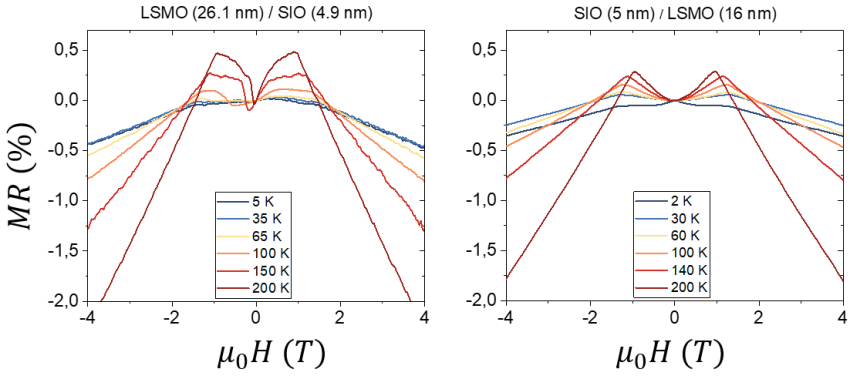

Figure 5.6. Magnetoresistance at temperatures from 2 to 200 K in (left) LSMO(26.1 nm)/SIO (4.9 nm) and (right) SIO(5 nm)/LSMO(16 nm).

On the other hand, we have carried out transverse resistivity measurements of all samples in a wide range of temperatures. As an example of the systematic work we have carried out, Figure 5.7 shows the transverse resistivity measurements taken between 20 and 100 K for LSMO/SIO and SIO/LSMO bilayers with varying SIO thicknesses.

We first study Hall effect in LSMO and SIO individual layers by measuring the Hall resistivity (ρ_{xy}) at low temperatures (T ≤ 100 K). The measured ρ_{xy} includes contributions from both the ordinary Hall effect (OHE) and the anomalous Hall effect (AHE), such that $\rho_{xy} = \rho_{xy}^{OHE} + \rho_{xy}^{AHE}$. The OHE is proportional to the magnetic field (H_z), while the AHE is proportional to the magnetization (M_z) perpendicular to the film plane.

It is crucial to note that the sign of the OHE in LSMO is opposite to that in SIO because carriers in manganites are holes, while transport in SIO is dominated by more mobile electrons.

Focusing on the AHE, we observe in the LSMO example of Figure 5.8a that, for plain LSMO films, ρ_{xy}^{AHE} becomes constant once M_z is saturated by the applied field H_z. This allows us to determine ρ_{xy}^{OHE} and ρ_{xy}^{AHE} from the measured ρ_{xy}.

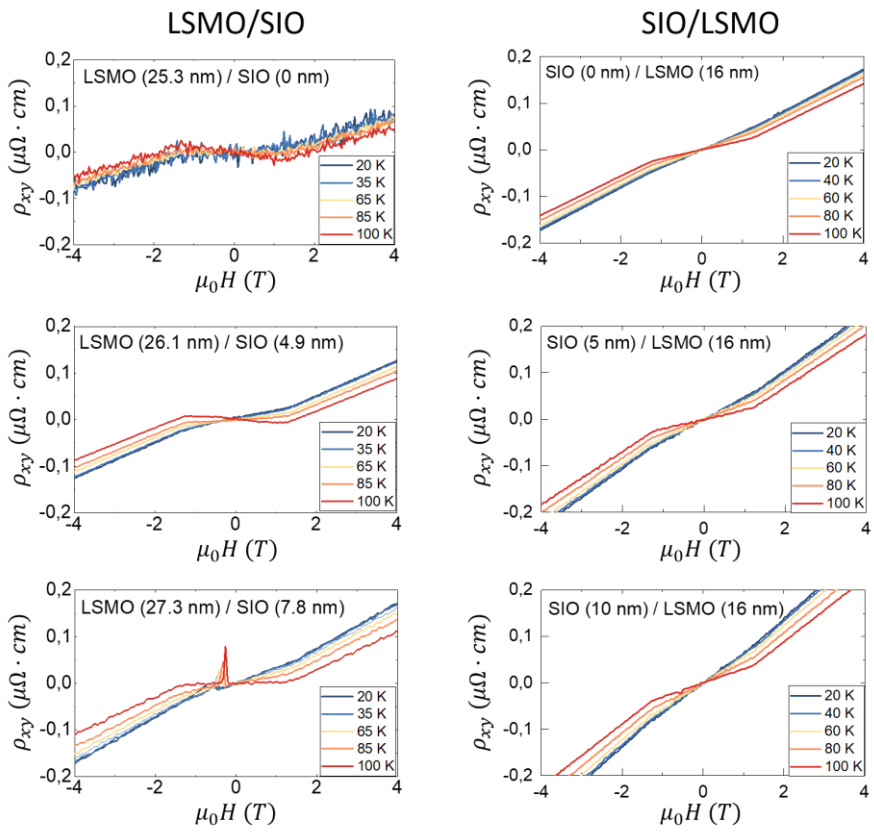

Figure 5.7. Transverse Hall resistivity ρ_{xy} vs. out of the plane magnetic field, H_z, at temperatures between 20 K and 100 K in bilayers LSMO/SIO (left side) and bilayers SIO/LSMO (right side) for thickness of SIO between 0 nm and 10nm.

Figure 5.8b reveals that ρ_{xy}^{AHE} (depicted by the red line) in SIO is zero, which is expected due to its paramagnetic (non-ferromagnetic) ground state. On the other hand, a finite ρ_{xy}^{AHE} can be observed in LSMO (red line in Figure 5.8) and LSMO/SIO bilayers (visible in Figure 5.8c and Figure 5.8d). We define $\Delta\rho_{xy}^{AHE}$ as the value of ρ_{xy}^{AHE} when M_z is saturated by H_z, as marked by the green arrows in Figure 5.8a.

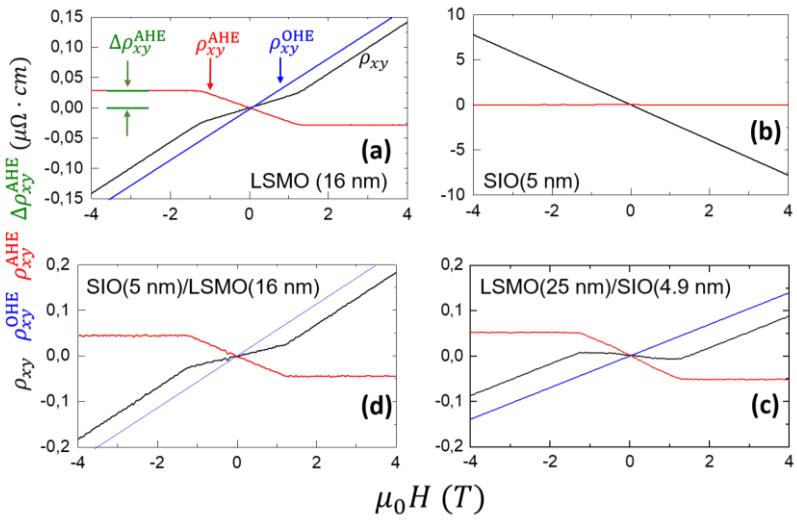

Figure 5.8. Transverse Hall resistivity ρ_{xy} vs. out of the plane magnetic field, H_z, (black lines) of LSMO 16 nm (a) and SIO 5 nm (b) thin films SIO (5 nm)/ LSMO (16 nm) bilayer (c) and an LSMO (25 nm)/ SIO (4.9 nm) bilayer (d) measured at T = 100 K. Ordinary Hall resistivity ρ_{xy}^{OHE} (blue lines) and anomalous Hall resistivity, $\Delta\rho_{xy}^{AHE}$ (red lines) have been separated. $\Delta\rho_{xy}^{AHE}$ indicates the value of ρ_{xy}^{AHE} at magnetic saturation (green arrow).

We assess the $\Delta\rho_{xy}^{AHE}$ changes for both sets of samples within a temperature range where magnetization remains essentially constant (occurring for T≤100 K). The measured $\Delta\rho_{xy}^{AHE}$ undergoes changes solely through its relationship with the longitudinal resistivity ρ_{xx}, given by the inversion of the conductivity tensor, as described:

$$\Delta\rho_{xy}^{AHE}(T) = \left|\sigma_{xy}^{AHE}\right| \cdot \rho_{xx}^{2}(T) \qquad (1)$$

We graph $\Delta\rho_{xy}^{AHE}(T)$ against $\rho_{xx}^{2}(T)$ for the two bilayer sets, SIO/LSMO (Figure 5.9a) and LSMO/SIO (Figure 5.9b). In each set we have kept a constant LSMO thickness (d_L= 16 nm in SIO/LSMO and d_L= 25 nm in LSMO/SIO) and varied the SIO thickness (d_S). For both sets, a linear scaling is observed throughout the entire range of d_S, including the sample

without SIO (d_S= 0). This finding suggests that the anomalous Hall conductivity is independent of the scattering rate, and thus, it is an intrinsic contribution of the AHE driven by the topological properties of Bloch states in reciprocal space.

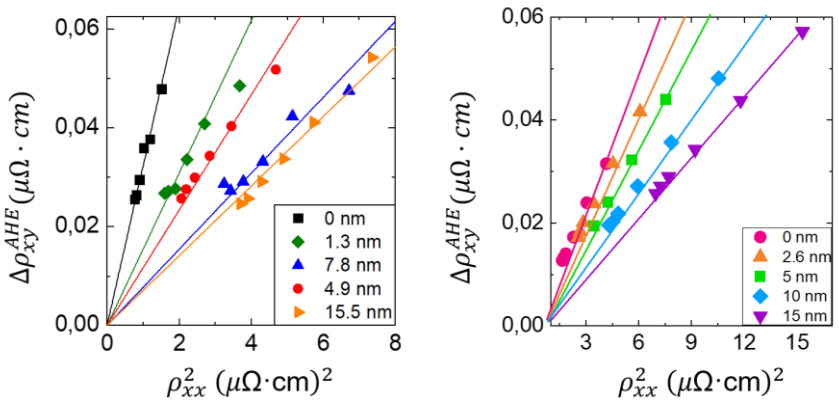

Figure 5.9. Evolution in temperature of the AHE at saturation, $\Delta\rho_{xy}^{AHE}$, vs. the longitudinal resistivity, ρ_{xx}^2, of LSMO/SIO bilayers (right) and SIO/LSMO bilayers (left) for different thicknesses of SIO.

Following the previous equation, the slope of $\Delta\rho_{xy}^{AHE}$ against ρ_{xx}^2 represents the AHE conductivity σ_{xy}^{AHE} for the bilayer system. Figure 5.10 displays the conductivity σ_{xy}^{AHE} for both the SIO/LSMO bilayers (purple points) and LSMO/SIO bilayers (pink points). We observe that the σ_{xy}^{AHE} for the SIO/LSMO bilayers exhibits a smooth decrease as the SIO thickness (d_S) increases, while the σ_{xy}^{AHE} for the LSMO/SIO bilayers experience an abrupt decrease when d_S increases, followed by saturation.

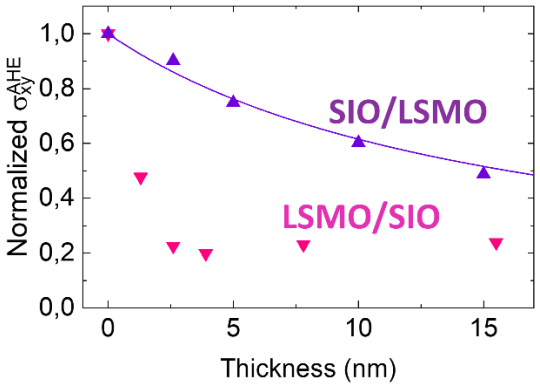

Figure 5.10. AHE conductivity, σ_{xy}^{AHE}, vs. thickness of the SIO layer, of the bilayer samples. The symbols are experimental values of the Hall conductivity obtained from linear fitting curves in Fig. 5.8. The purple dashed line indicates the calculated σ_{xy}^{AHE} using a bilayer model (Eq. 3). To calculate σ_{xy}^{AHE}, we use d_L= 27.3 nm which is the average value of dL of the different samples.

To understand the sudden decrease of the AHE in LSMO/SIO bilayers when a few layers of SIO come into contact with LSMO, we analyze the AHE data using a circuit model. This model facilitates the calculation of transverse ρ_{xy}^{AHE} and longitudinal ρ_{xx} resistivity of a multilayer based on the individual layers. The model generates an expression for the AHE conductivity. Assuming a relationship between the AHE and longitudinal resistivity in the form of Eq. 1, the model provides the following expression for the AHE conductivity:

$$\sigma_{xy}^{AHE} = \frac{\Delta\rho_{xy}^{AHE}}{\rho_{xx}^2} = \frac{\sum_{i=1}^{n} d_i \, \sigma_{xy,i}^{AHE}}{\sum_{i=1}^{n} d_i} \qquad (2)$$

Here, $\Delta\rho_{xy}^{AHE}$ and ρ_{xx} represent the anomalous Hall and longitudinal resistivity expected in measurements on a heterostructure composed of n different materials, with each material having a thickness d_i and anomalous Hall conductivity $\sigma_{xy,i}^{AHE} = \Delta\rho_{xy,i}^{AHE}/\rho_{xx,i}^2$. In our investigation, n = 2 (bilayers consist of LSMO and SIO as illustrated in the left panel of Fig. 5.6). If we assume that both materials (LSMO and SIO) retain their intrinsic AHE resistivity when combined in the heterostructures—

i.e., only LSMO displays a finite $\sigma_{xy,L}^{AHE}$ while the SIO layer has $\sigma_{xy,S}^{AHE} = 0$ as depicted in Fig. 5.7—then Eq. 2 yields:

$$\sigma_{xy}^{AHE} = \frac{d_L}{d_L + d_S}\sigma_{xy,L}^{AHE} \qquad (3)$$

For the SIO/LSMO bilayers, we find that they fit well the equation (line in Figure 5.10), indicating that these samples preserve their intrinsic AHE conductivity when assembled in a heterostructure. However, we observe that the LSMO/SIO bilayers do not follow the smooth decay. This observation reveals that the assumption that LSMO and SIO maintain their intrinsic AHE conductivity in the LSMO/SIO heterostructure is not valid.

Subsequently, we demonstrate that the sharp decline in AHE conductivity in LSMO/SIO bilayers can be attributed to the emergence of AHE in SIO, which has a sign opposite to that in LSMO. We show that the AHE in SIO originates from proximity-induced magnetism in its narrow bands. The AHE is discussed below (from theoretical arguments) to originate at an intrinsic contribution driven by the topological properties of Bloch states in reciprocal space.

4. Magnetic characterization

Polarized neutron reflectometry (PNR) and X-ray magnetic dichroism (XMCD) measurements were conducted in order to examine interface contributions to the sample magnetization in both LSMO/SIO and SIO/LSMO bilayers.

4.1. Polarized Neutron Reflectometry (PNR)

To investigate the evolution of the LSMO magnetic moment at the two interfaces, we carried out Polarized Neutron Reflectometry (PNR) measurements on two distinct samples: LSMO (5 nm)/SIO (4 nm) and SIO (4 nm)/LSMO (5 nm). These PNR measurements were performed by

Dr. Suzanne te Velthuis using a Magnetism Reflectometer BL-4A at the Spallation Neutron Source (SNS) at Oak Ridge National Laboratory.

Since magnetization is parallel to the applied field, spin-flip scattering should be absent. Therefore, we measured the reflectivity irrespective of the polarization of the reflected beam to obtain the nonspin-flip cross-sections R+ and R−, which are shown in Figure 5.11. as a function of momentum transfer q. PNR spectra were fit to obtain the scattering length density, which is proportional to layer magnetization.

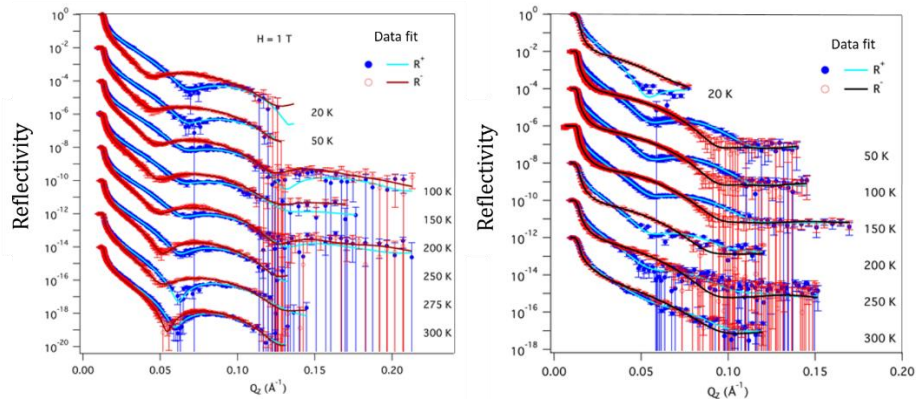

Figure 5.11. Polarized neutron reflectivity measurement (points) and the fitting realized (lines) in bilayer LSMO (5 nm)/SIO (4 nm) at the left, and bilayer SIO (4 nm)/LSMO (5 nm) at the right.

In order to obtain the magnetization depth profile in our sample we fit the data from Figure 5.11. using an iterative Parratt algorithm [14], [15]. The free parameters in this fitting procedure are for each layer their thickness, interface roughness, structural, and magnetic-scattering length densities. In order to constrain the fits further, we also measured the x-ray and fitted that data simultaneously with the polarized neutron reflectivity, as there is little contrast in the nuclear scattering length density for neutrons, but more contrast with the x-ray. Therefore, the x-rays were essential for determining the exact chemical structure, such as individual layer thickness and interfacial roughness.

Figure 5.12 presents the nuclear (dashed line) and magnetic (solid line) scattering length density profiles of the LSMO (5 nm)/SIO (4 nm) sample

at temperatures ranging from 20 K to 300 K. The interfacial LSMO exhibits a lower magnetization than the rest of the LSMO layer across all temperature range. However, this reduction in magnetization is relatively weaker compared to the decrease observed in the SIO (4 nm)/LSMO (5 nm) sample, as shown in the analogous measurements depicted in Figure 5.13.

Figure 5.14 displays the magnetic moment per Mn atom for both the LSMO layer and the LSMO interface at both interfaces. While the magnetization of the LSMO layer is similar at both interfaces, the LSMO magnetization at the interfaces exhibits a stark contrast.

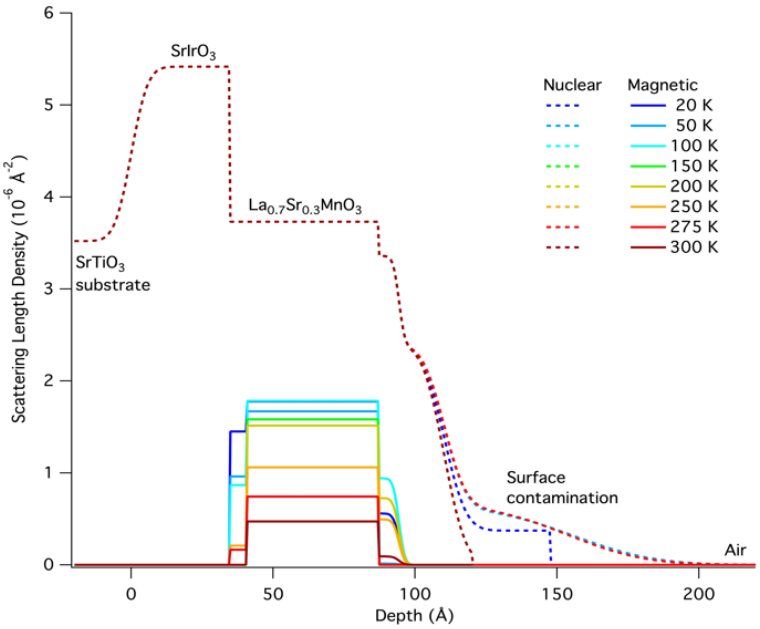

Figure 5.12. Scattering profile of the polarized neutron reflectivity measurement of a bilayer LSMO (5 nm)/SIO (4 nm)

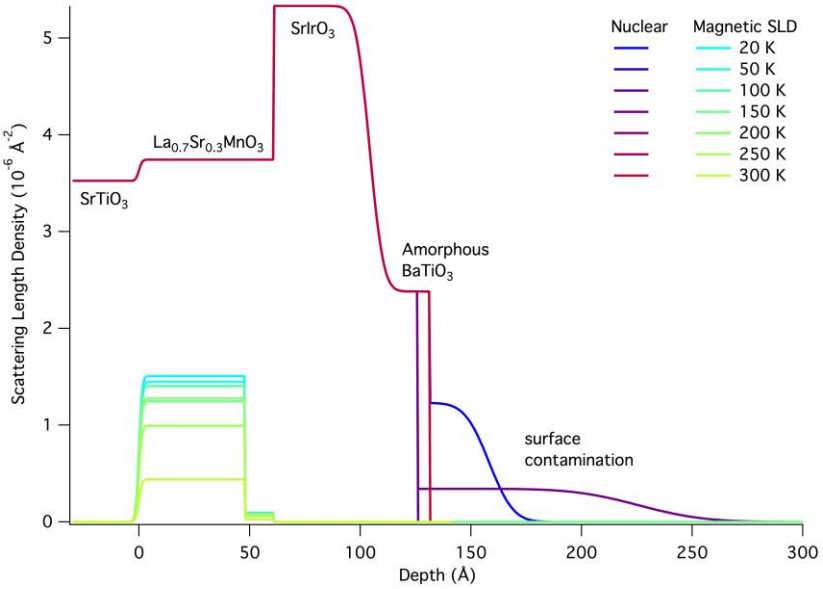

Figure 5.13. Scattering profile of the polarized neutron reflectivity measurement of a bilayer SIO (4 nm)/LSMO (5 nm).

When LSMO is the top layer of the bilayer (LSMO/SIO), at low temperatures there is only a weak reduction of the magnetization of the interface layer; conversely, when SIO is the top layer (SIO/LSMO), the magnetization at the interface is drastically suppressed. Notice also that although in LSMO/SIO samples the LSMO at the interface is strongly magnetic, the Curie temperature seems to be substantially depressed. As the most important structural difference between the two interfaces is the additional SrO plane—LSMO/SIO has two SrO planes while SIO/LSMO has three—it is reasonable to speculate that the suppression of LSMO magnetization at the SIO/LSMO interface may be related to the emergence of this extra SrO plane.

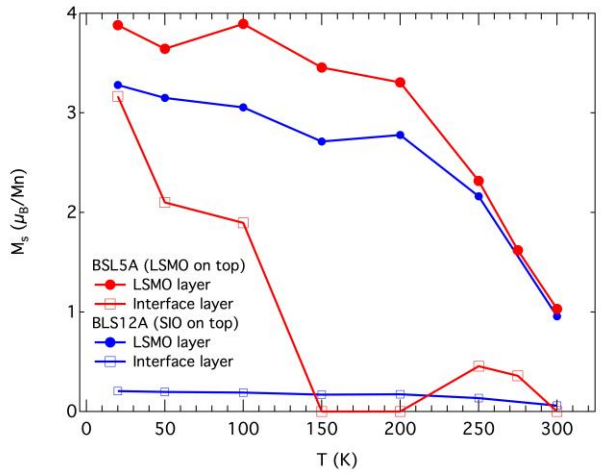

Figure 5.14. LSMO magnetization, as a function of temperature in the layer (solids points) and in the interface (empty squares) of both interfaces: LSMO/SIO (red) and SIO/LSMO (blue).

4.2. X-ray magnetic circular dichroism (XMCD)

The magnetism in LSMO and SIO was investigated through a combination of X-ray absorption spectroscopy (XAS) and X-ray magnetic circular dichroism (XMCD) at the Mn L2,3 and Ir L2,3 edges for LSMO/SIO and SIO/LSMO bilayers. XMCD measurements in total electron yield (TEY) mode revealed a robust magnetic moment of Mn at both interfaces, consistent with the magnetization observed in PNR. Conversely, XMCD spectra in partial fluorescence yield (PFY) mode displayed clear evidence of an Ir magnetic moment when LSMO is positioned atop the bilayer. Figure 5.15 illustrates the Ir L3 edge XAS (top) and XMCD (bottom) at 2 K and 0.5 T for an LSMO (5 nm)/SIO (4 nm) bilayer and an SIO (4 nm)/LSMO (5 nm) bilayer. In contrast to the bilayer with LSMO on top, the bilayer with SIO on top does not exhibit an Ir magnetic moment. The Ir magnetic state can be discussed in relation to the magnetic moment of the interfacial LSMO, which could also be connected to the atomic reconstruction of the interface uncovered by the STEM EELS experiment.

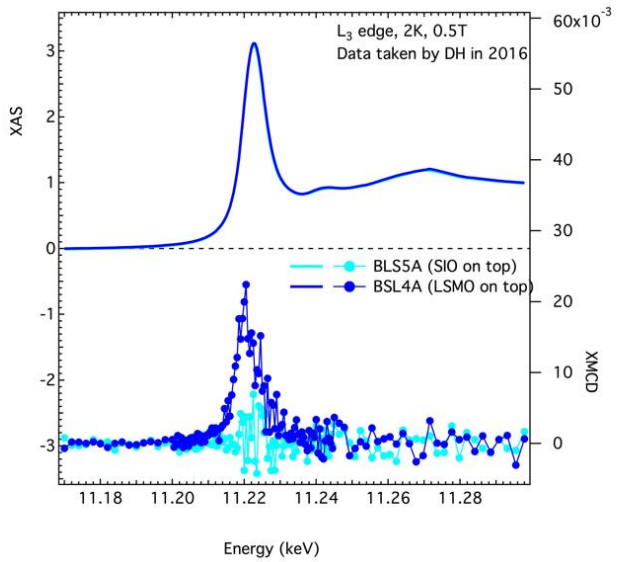

Figure 5.15. Ir L3 XAS (black lines) and XMCD (blue lines) PFY spectra measured at T= 20 K under a saturating magnetic field of 55.6 mT applied in the [100] direction of a sample of SIO (4 nm)/LSMO (5 nm) (light blue) and LSMO(5nm)/SIO(4nm).

The absence of induced moment at SIO in the SIO/LSMO (SIO on top) bilayers may be connected to the suppressed magnetism of the interface and possibly also to the additional SrO planes suppressing superexchange interactions across the interface (see below).

Previously, induced magnetism in iridates has been discovered in manganite/iridate superlattices with various interface reconstructions [8]–[10], although significant differences arise from our unique LSMO/SIO interface reconstruction, as discussed below. To obtain information on the depth length scale of the induced moment, X-ray absorption spectroscopy experiments were conducted at the Ir L_3 edge in a series of LSMO (5 nm)/SIO (d_S) bilayers, with d_S = 1.2 nm, 4 nm, and 7 nm. XMCD spectra did not display any measurable shift (see inset to Fig. 5.16c) as thickness varied, suggesting that the charge transfer mechanism observed in SrMnO3/SIO interfaces [16] is inhibited here, likely due to the two interfacial SrO rock salt blocks. Figure 5.16a's main panel presents XMCD spectra around the Ir L_3 edge normalized to the XAS edge jump intensity

for various samples. The XMCD peak intensity reached its maximum for the sample with d_S= 1.2 nm and diminished with increasing d_S. For d_S = 4 nm, there is only a weak decrease of the XMCD signal, while a strong suppression occurs for d_S= 7 nm, indicating that, since XMCD is normalized to the XAS signal, only part of the SIO layer possesses a magnetic moment.

We can estimate the thickness of the interfacial SIO layer d_I, which has a magnetic moment, by scaling the XMCD peak intensity to that measured for d_S= 1.2 nm, as depicted in Figure 5.16b. The sigmoidal-like dotted line serves as a visual guide, demonstrating the exponential decrease of the intensity from which we estimate d_I = 2 nm.

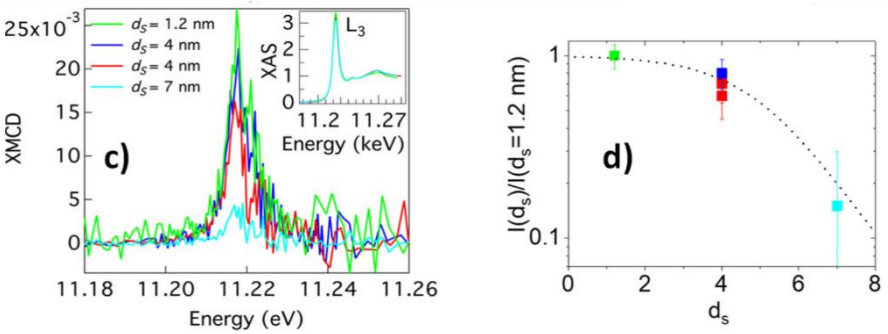

Figure 5.16 (a) XMCD intensities for samples STO//SIO(dS)/LSMO(5 nm) at the Ir L3 edge. For d_S =1.2 nm and 7 nm, T = 10 K and μ_{0H} = 60 mT. For d_S = 4 nm, two nominally identical samples were measured, at various temperatures (20 K and 2 K) and magnetic fields (55.6 mT, 0.5 T). The intensity was independent of the magnetic field applied. The peak intensity at 2 K is higher than those at 20 K. Inset: Normalized XAS intensity. **(b)** The ratio between measured XMCD peak intensities of samples with larger SIO thicknesses and the peak intensity of the sample with the thinnest SIO d_S= 1.2 nm as a function of SIO thickness.

To elucidate the origin of the induced ferromagnetism in the SIO layer, which is separated from LSMO by a double SrO layer, we initiated density functional theory (DFT) calculations on bulk SIO. Our findings revealed that canted antiferromagnetic (AFM) ordering, driven by the Dzyaloshinskii-Moriya interaction [17]–[20], is stable when the local U on

Ir d states exceeds ~1 eV [21]. Consequently, the SIO is in proximity to a canted antiferromagnetic state, induced by enhanced electron correlation. Given the small energy difference between various canted AFM states (less than ~10 meV/Ir), the weak superexchange interaction [13], [22]–[26] across the double SrO layers, as evidenced by the antiferromagnetic alignment of the Mn and Ir moments, is sufficient to produce the observed magnetic state. It is noteworthy that this superexchange interaction across double SrO layers has been observed in La1.85Sr0.15CuO4 (LSCO-214) cuprate/manganite interfaces [13], where it also results in an antiferromagnetic (Cu-Mn) state.

5. Discussion

The discovery of induced magnetism in SIO at the interface with LSMO on a nanometric scale suggests that the unexpected decrease in AHE conductivity (Figure 5.10) with increasing SIO thickness at the LSMO/SIO interface results from the emergence of AHE in SIO. Based on this notion, we examined the AHE data using a trilayer model that incorporates an interface layer, as depicted in Figure 5.17.

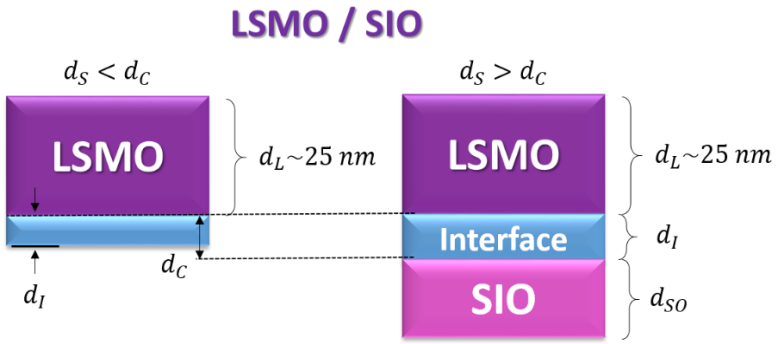

Figure 5.17. Sketch illustrating the trilayer model of the LSMO/SIO samples used to fit the conductivity results

Essentially, we divide the SIO layer into two sublayers: an interface layer "I" with thickness d_I, which exhibits induced magnetism and AHE, and a second layer "S0" with thickness d_{S0} that retains the intrinsic properties of

SIO (specifically, the absence of AHE), as observed in SIO/LSMO bilayers. We thus assume a characteristic length scale, dc, over which the magnetic and AHE properties of SIO are influenced by proximity to LSMO. In heterostructures where the SIO thickness is less than dc, the entire SIO layer displays altered properties ($d_I = d_S$). For heterostructures with SIO thickness exceeding dc, the entire interface thickness is impacted by the proximity effect ($d_I = d_C$), and the SIO thickness retaining its intrinsic properties will be the remainder of the SIO layer ($d_{S0} = d_S - d_C$). To simplify calculations, we assume the magnetic and electronic properties are uniform within each of the three layers: d_L, d_I, and d_{S0}. We can now apply Eq. 2 to the three-layer system using n = 3, with $\sigma_{xy,S0}^{AHE} = 0$, as the intrinsic SIO properties are preserved within dS0. This results in Eq. 2 yielding:

$$\sigma_{xy}^{AHE} = \frac{d_L \sigma_{xy,L}^{AHE} + d_I \sigma_{xy,I}^{AHE}}{d_L + d_S} \qquad (4)$$

Given that d_L, d_S, σ_{xy}^{AHE}, and $\sigma_{xy,L}^{AHE}$ are known parameters, and d_C (the upper limit of the interfacial layer thickness d_I) can be estimated from the thickness of the layer with an induced magnetic moment at the SIO interface (d_C = 2 nm), we can calculate the contribution to the anomalous Hall conductivity of the interfacial SIO layer with induced magnetism and plot it as a function of the SIO thickness d_S in Figure 5.18.

$$\sigma_{xy,I}^{AHE} = \frac{(d_L + d_S)\sigma_{xy}^{AHE} - d_L \sigma_{xy,L}^{AHE}}{d_I} \qquad (5)$$

Our analysis using the three-layer model identifies an intrinsic contribution to the AHE conductivity, $\sigma_{xy,I}^{AHE}$, which is negative and nearly independent of dS. In the following, we discuss the topological origin of

this contribution and its relationship to the induced magnetism in the SIO layer.

It is noteworthy that we did not observe the topological Hall effect (THE), which has been both theoretically predicted [27] and experimentally observed [28] in similar LSMO/SIO interfaces. THE arises from topological spin textures, such as skyrmions, and displays a characteristic signature in Hall resistivity as (antisymmetric) "humps" superimposed on the AHE and OHA signals. Generally, THE appears at the interface between ferromagnets with perpendicular magnetic anisotropy and spin-orbit materials, driven by the interfacial Dzyaloshinskii-Moriya interaction (DMI). As we will describe in the next chapter, THE can be observed but it requires careful choosing the thickness of both SIO and manganite. It is crucial to note that THE is a transport measurement and, as such, an indirect measurement of magnetic textures. As evident in the resistivity equations, the Hall measurement encompasses the sum of all different Hall contributions. The dominance of some Hall contributions could mask the presence of a weak THE contribution. Consequently, the absence of THE does not necessarily imply the nonexistence of any magnetic textures at the interface.

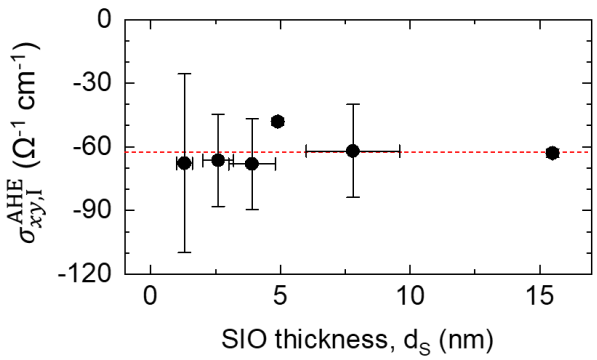

Figure 5.18. Calculated AHE conductivity of the interface layer, $\sigma_{xy,I}^{AHE}$, as a function of dS using Eq. 5. For the calculation, we used dc = 2 nm based on the XMCD measurements.

Lastly, it is worth noting that the strong negative contribution to the anomalous conductivity at the LSMO/SIO interface (not observed in the SIO/LSMO interface) is likely connected to the presence of magnetism in the interfacial LSMO, and consequently, the induced magnetism in the first 2 nm of SIO. This induced magnetism at the SIO interface offers an artificial realization of the necessary conditions for the AHE. Its temperature independence (scattering rate) signifies its intrinsic nature, which is related to the topological properties of Bloch states, specifically the Berry curvature of the occupied states [29].

While LSMO is generally considered to have topologically trivial bands, carriers have been proposed to acquire a real space Berry phase due to non-collinear spin structures, predominantly near T_C [30], [31], with small values of the anomalous Hall conductivity expected. In contrast, for SIO, $\sigma_{xy,I}^{AHE}$ = -63 $(\Omega cm)^{-1}$ is considerably larger, resulting in $\sigma_{xy,I}^{AHE}/\sigma_{xx}$ values between 6-13% when considering $\sigma_{xx}\approx$ 500-1000 $(\Omega cm)^{-1}$. These values are comparable, albeit larger, than those for $SrRuO_3$ [4] or MnSi [32], [33], or non-collinear antiferromagnet Mn_3Sn [34] or $CoNb_3S_6$ [35] with topologically non-trivial bands. Importantly, this is despite the small values of the magnetic moment induced by the interfacial proximity interaction (σ_{xy}^{AHE}, which is proportional to magnetization). The large absolute value of $\sigma_{xy,I}^{AHE}$, along with its scattering rate independence, strongly suggests its intrinsic origin—namely, the topological nature of the Bloch states in SIO.

To assess the presence of topological states, we conducted theoretical analyses based on density functional theory (DFT) calculations. These calculations were performed by Drs. Ling-Fang Lin, Narayan Mohanta Satoshi Okamoto and Elbio Daggotto at Oak Ridge National Laboratory. In order to simplify the system and minimize complications arising from the LSMO interface, we focused on studying bulk SIO with specific lattice constants: a=5.5617 Å, b=5.5909 Å, and c=7.8821 Å. To simulate the proximity coupling between SIO and LSMO, we performed constrained magnetic moment calculations where the spin polarization direction (S_{Ir}) of Ir atoms was fixed along the z-axis while its magnitude was varied.

By investigating the "proximity-induced" magnetism, we calculated the AHE conductivity (σ_{xy}) of SIO. The resulting values of σ_{xy} are presented in Figure 5.19a, illustrating its dependence on the Fermi level (E_F) for different S_{Ir} values; and in Fig. 5.19b, illustrating its variation with S_{Ir} for different E_F values. It is important to note that, according to the definition, positive SIO spin polarization corresponds to the experimental scenario where Ir moments are antialigned with Mn moments at the interface. In agreement with experimental findings, our calculations yielded a negative value for σ_{xy}, confirming consistency. Remarkably, under certain conditions, we observed a significant and non-monotonic behaviour of σ_{xy}, reaching an exceptionally large value of -1000 $(\Omega \cdot \mathrm{cm})^{-1}$. This behaviour, including the sign change, closely resembles the findings reported for $SrRuO_3$ [4], suggesting a shared origin involving magnetic monopoles in momentum space.

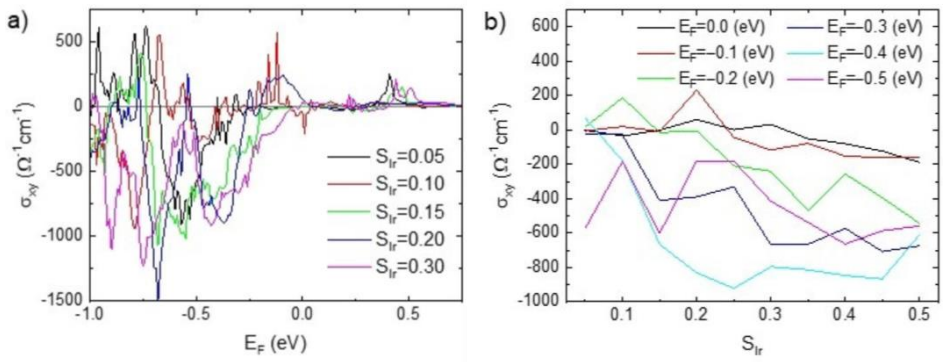

Figure 5.19. Intrinsic AH conductivity (a) as a function of the Fermi level E_F with several values of spin polarization $S_{Ir}= (n_{up}- n_{down})/2$ and (b) as a function of S_{Ir} with several values of E_F.

To investigate this proposed scenario, we examined the Berry curvature using different parameter sets, as illustrated in Figure 5.20. One potential explanation for the observed large σ_{xy} values is the presence of a Dirac nodal line in the U-R-X plane within the momentum space [33], [36]. This nodal line could give rise to magnetic monopoles, contributing to the anomalous Hall conductivity when the Fermi level (E_F) is close to zero, corresponding to stoichiometric SIO. At E_F=0 with S_{Ir}=0.05, the Berry

curvature exhibits a moderate enhancement only at (k_x, k_y, k_z)≈(π/a, 0, π/c) and (π/a, 2π/b, π/c), as shown in Figure 5.20c. This occurs because the line node is located away from E_F=0. However, a slight increase in S_{Ir} brings the line node closer to E_F=0, resulting in sharp peaks in the Berry curvature at (k_x, k_y, k_z)≈(π/a, 0.25π/b, π/c), as depicted in Figure 5.20d. By adjusting the values of S_{Ir} at E_F=0, the theoretical σ_{xy} values can become comparable to the experimental estimation for SIO, approximately -40 $(\Omega \cdot \mathrm{cm})^{-1}$, as indicated in Figures 5.19a and 5.19b. Furthermore, at negative E_F values, corresponding to hole doping, an additional enhancement occurs, leading to a σ_{xy} value of -1000 $(\Omega \cdot \mathrm{cm})^{-1}$, as observed in Figures 5.19a and 5.19b. This enhancement is attributed to magnetic monopoles induced at avoided band crossings in the presence of spin-orbit coupling (SOC) and magnetic ordering. Figures 5.19e and 5.19f demonstrate that the Berry curvature exhibits multiple peaks with varying magnitudes, providing strong support for this scenario.

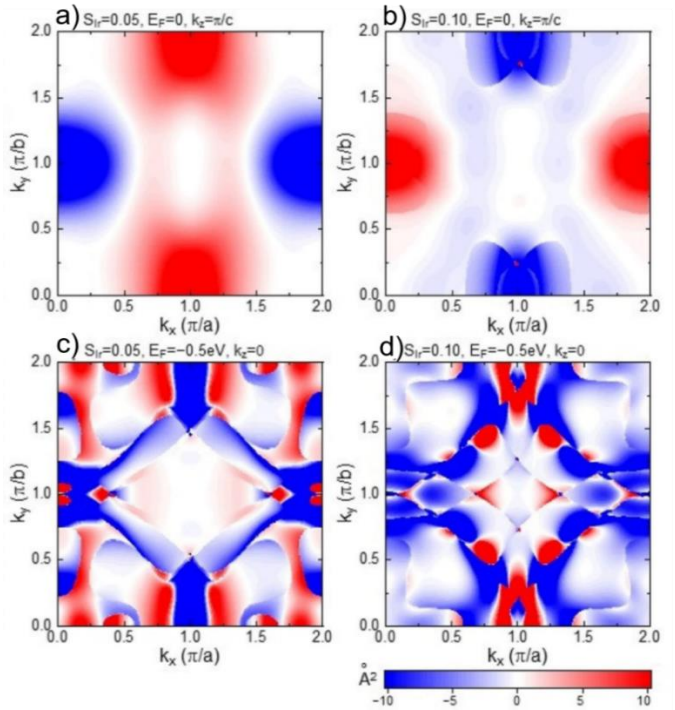

Figure 5.20. Plot in two dimensions of the Berry curvature for (a) S_{Ir}=0.05 at E_F=0 and k_z=π/c, (b) S_{Ir}=0.10 at E_F=0 and k_z=π/c, (c) S_{Ir}=0.05 at E_F=-0.5 eV and k_z=0, (d) S_{Ir}=0.10 at E_F=-0.5 eV and k_z=0. $n_{up(down)}$ is the spin-up (down) electron density per Ir site.

In order to gain a deeper understanding of the specific momentum and energy regimes contributing to the observed large σ_{xy} values, which involve a Dirac nodal line near the U point and the stoichiometric Fermi level, or avoided band crossings in the hole-doped regime, or possibly both, we conducted an analysis of the band dispersion near the Fermi level and the corresponding Berry curvature. It is worth noting that nodal lines present in the non-magnetic $SrIrO_3$ structure become unstable in the presence of magnetism, where a nonzero magnetic moment eliminates the nodal line and opens a gap. As the magnetic moment increases, different bands undergo upward or downward shifts, resulting in various types of band crossings. The semi-quantitative agreement observed between our experimental estimations and the theoretical calculations strongly supports the notion that the anomalous Hall effect in SIO/LSMO heterostructures originates from a topological mechanism, specifically involving magnetic monopoles in momentum space. This insight provides valuable evidence and corroborate the presence of topological characteristics within the system.

6. Conclusion

In summary, in this chapter we have explore the electronic reconstructions at SIO/LSMO and the LSMO/SIO interfaces by examining their transport and magnetic properties. Structurally, these two types of bilayers differ in the number of SrO planes present at the interface (LSMO/SIO has two SrO planes, while SIO/LSMO has three). Magnetically, both interfaces also differ. While LSMO/SIO displays robust LSMO magnetism at the interface, SIO/LSMO show substantially depressed LSMO magnetism at its interface. As a result, LSMO/SIO interface features an anomalous magnetic proximity induced SIO magnetism driven by superexchange, which is absent in SIO/LSMO samples.

We observe the emergence of an intrinsic AHE in the bilayers LSMO/SIO, in contrast with the absence of the effect in the bilayers SIO/LSMO. This emergent AHE is connected with the presence of magnetization in the

interfacial LSMO and the emergence of magnetism in the first SIO 2 nm by proximity effect; these two aspects differentiate both interfaces.

The induced intrinsic AHE uncovers an exciting scenario of the interplay between topology and correlations at the 3d/5d interface. The symmetry breaking by the proximity-induced magnetism at the interface conspires with the strong spin-orbit interaction of the iridate to yield the hot spots of the integrated Berry curvature at nodal lines and band anticrossings, providing an artificial realization of the minimal model of the AHE [29]. It is very important that, despite the small values of the magnetic moment induced in the iridate by proximity to the manganite, the amplification by the topological properties of the iridate is so large that the anomalous Hall angle reaches values among the largest reported in the literature.

7. References

[1] W. Witczak-Krempa, G. Chen, Y. B. Kim, y L. Balents, «Correlated quantum phenomena in the strong spin-orbit regime», *Annu. Rev. Condens. Matter Phys.*, vol. 5, n.º 1, pp. 57-82, mar. 2014, doi: 10.1146/annurev-conmatphys-020911-125138.

[2] Y. Tokura, M. Kawasaki, y N. Nagaosa, «Emergent functions of quantum materials», *Nat. Phys.*, vol. 13, n.º 11, pp. 1056-1068, nov. 2017, doi: 10.1038/nphys4274.

[3] B. Keimer y J. E. Moore, «The physics of quantum materials», *Nat. Phys.*, vol. 13, n.º 11, pp. 1045-1055, 2017.

[4] Z. Fang *et al.*, «The anomalous Hall effect and magnetic monopoles in momentum space», *Science*, vol. 302, n.º 5642, pp. 92-95, oct. 2003, doi: 10.1126/science.1089408.

[5] J. Matsuno *et al.*, «Interface-driven topological Hall effect in SrRuO3-SrIrO3 bilayer», *Sci. Adv.*, vol. 2, n.º 7, p. e1600304, jul. 2016, doi: 10.1126/sciadv.1600304.

[6] P. Bruno, V. K. Dugaev, y M. Taillefumier, «Topological Hall Effect and Berry Phase in Magnetic Nanostructures», *Phys. Rev. Lett.*, vol. 93, n.º 9, p. 096806, ago. 2004, doi: 10.1103/PhysRevLett.93.096806.

[7] T. Nagai, M. Nagao, K. Kurashima, T. Asaka, W. Zhang, y K. Kimoto, «Formation of nanoscale magnetic bubbles in ferromagnetic insulating manganite La7/8Sr1/8MnO3», *Appl. Phys. Lett.*, vol. 101, oct. 2012, doi: 10.1063/1.4760266.

[8] D. Yi *et al.*, «Atomic-scale control of magnetic anisotropy via novel spin–orbit coupling effect in La2/3Sr1/3MnO_3/$SrIrO_3$ superlattices», *Proc. Natl. Acad. Sci. U. S. A.*, vol. 113, n.º 23, pp. 6397-6402, 2016.

[9] J. Nichols *et al.*, «Emerging magnetism and anomalous Hall effect in iridate–manganite heterostructures», *Nat. Commun.*, vol. 7, n.º 1, Art. n.º 1, sep. 2016, doi: 10.1038/ncomms12721.

[10] D. Yi *et al.*, «Tuning Perpendicular Magnetic Anisotropy by Oxygen Octahedral Rotations in La1-xSrxMnO3/SrIrO3 Superlattices», *Phys. Rev. Lett.*, vol. 119, n.º 7, p. 077201, ago. 2017, doi: 10.1103/PhysRevLett.119.077201.

[11] M. Matvejeff, T. Chikyow, y M. Lippmaa, «Interface growth of La1.2Sr1.8Mn1.7Ru0.3O7 Ruddlesden–Popper films on SrTiO3», *J. Cryst. Growth*, vol. 311, n.º 4, pp. 1201-1205, feb. 2009, doi: 10.1016/j.jcrysgro.2008.11.057.

[12] Y. F. Nie *et al.*, «Atomically precise interfaces from non-stoichiometric deposition», *Nat. Commun.*, vol. 5, n.º 1, Art. n.º 1, ago. 2014, doi: 10.1038/ncomms5530.

[13] G. M. De Luca *et al.*, «Ubiquitous long-range antiferromagnetic coupling across the interface between superconducting and ferromagnetic oxides», *Nat. Commun.*, vol. 5, n.º 1, Art. n.º 1, nov. 2014, doi: 10.1038/ncomms6626.

[14] Y. Zhu, *Modern techniques for characterizing magnetic materials*. Springer, 2005.

[15] L. G. Parratt, «Surface studies of solids by total reflection of X-rays», *Phys. Rev.*, vol. 95, n.º 2, p. 359, 1954.

[16] S. Okamoto, J. Nichols, C. Sohn, S. Y. Kim, T. W. Noh, y H. N. Lee, «Charge Transfer in Iridate-Manganite Superlattices», *Nano Lett.*, vol. 17, n.º 4, pp. 2126-2130, abr. 2017, doi: 10.1021/acs.nanolett.6b04107.

[17] B. J. Kim *et al.*, «Phase-Sensitive Observation of a Spin-Orbital Mott State in Sr2IrO4», *Science*, vol. 323, n.º 5919, pp. 1329-1332, mar. 2009, doi: 10.1126/science.1167106.

[18] J. Matsuno *et al.*, «Engineering a Spin-Orbital Magnetic Insulator by Tailoring Superlattices», *Phys. Rev. Lett.*, vol. 114, n.º 24, p. 247209, jun. 2015, doi: 10.1103/PhysRevLett.114.247209.

[19] L. Hao *et al.*, «Two-Dimensional Jeff=1/2 Antiferromagnetic Insulator Unraveled from Interlayer Exchange Coupling in Artificial Perovskite Iridate Superlattices», *Phys. Rev. Lett.*, vol. 119, n.º 2, p. 027204, jul. 2017, doi: 10.1103/PhysRevLett.119.027204.

[20] L. Hao *et al.*, «Giant magnetic response of a two-dimensional antiferromagnet», *Nat. Phys.*, vol. 14, n.º 8, pp. 806-810, ago. 2018, doi: 10.1038/s41567-018-0152-6.

[21] M.-W. Yoo *et al.*, «Large intrinsic anomalous Hall effect in SrIrO3 induced by magnetic proximity effect», *Nat. Commun.*, vol. 12, n.º 1, Art. n.º 1, jun. 2021, doi: 10.1038/s41467-021-23489-y.

[22] J. Garcia-Barriocanal *et al.*, «Spin and orbital Ti magnetism at LaMnO3/SrTiO3 interfaces», *Nat. Commun.*, vol. 1, n.º 1, Art. n.º 1, sep. 2010, doi: 10.1038/ncomms1080.

[23] F. A. Cuellar *et al.*, «Reversible electric-field control of magnetization at oxide interfaces», *Nat. Commun.*, vol. 5, n.º 1, Art. n.º 1, jun. 2014, doi: 10.1038/ncomms5215.

[24] F. Y. Bruno *et al.*, «Insight into spin transport in oxide heterostructures from interface-resolved magnetic mapping», *Nat. Commun.*, vol. 6, n.º 1, Art. n.º 1, feb. 2015, doi: 10.1038/ncomms7306.

[25] S. Okamoto, «Magnetic interaction at an interface between manganite and other transition metal oxides», *Phys. Rev. B*, vol. 82, n.º 2, p. 024427, jul. 2010, doi: 10.1103/PhysRevB.82.024427.

[26] J. Salafranca y S. Okamoto, «Unconventional Proximity Effect and Inverse Spin-Switch Behavior in a Model Manganite-Cuprate-Manganite Trilayer System», *Phys. Rev. Lett.*, vol. 105, n.º 25, p. 256804, dic. 2010, doi: 10.1103/PhysRevLett.105.256804.

[27] N. Mohanta, E. Dagotto, y S. Okamoto, «Topological Hall effect and emergent skyrmion crystal at manganite-iridate oxide interfaces», *Phys. Rev. B*, vol. 100, n.º 6, p. 064429, ago. 2019, doi: 10.1103/PhysRevB.100.064429.

[28] Y. Li *et al.*, «Emergent Topological Hall Effect in La0.7Sr0.3MnO3/SrIrO3 Heterostructures», *ACS Appl. Mater.*

Interfaces, vol. 11, n.º 23, pp. 21268-21274, jun. 2019, doi: 10.1021/acsami.9b05562.

[29] S. Onoda, N. Sugimoto, y N. Nagaosa, «Intrinsic Versus Extrinsic Anomalous Hall Effect in Ferromagnets», *Phys. Rev. Lett.*, vol. 97, n.º 12, p. 126602, sep. 2006, doi: 10.1103/PhysRevLett.97.126602.

[30] Y. Lyanda-Geller *et al.*, «Charge transport in manganites: Hopping conduction, the anomalous Hall effect, and universal scaling», *Phys. Rev. B*, vol. 63, n.º 18, p. 184426, abr. 2001, doi: 10.1103/PhysRevB.63.184426.

[31] J. Ye, Y. B. Kim, A. J. Millis, B. I. Shraiman, P. Majumdar, y Z. Tešanović, «Berry Phase Theory of the Anomalous Hall Effect: Application to Colossal Magnetoresistance Manganites», *Phys. Rev. Lett.*, vol. 83, n.º 18, pp. 3737-3740, nov. 1999, doi: 10.1103/PhysRevLett.83.3737.

[32] M. Lee, Y. Onose, Y. Tokura, y N. P. Ong, «Hidden constant in the anomalous Hall effect of high-purity magnet MnSi», *Phys. Rev. B*, vol. 75, n.º 17, p. 172403, may 2007, doi: 10.1103/PhysRevB.75.172403.

[33] A. Neubauer *et al.*, «Topological Hall Effect in the A Phase of MnSi», *Phys. Rev. Lett.*, vol. 102, n.º 18, p. 186602, may 2009, doi: 10.1103/PhysRevLett.102.186602.

[34] S. Nakatsuji, N. Kiyohara, y T. Higo, «Large anomalous Hall effect in a non-collinear antiferromagnet at room temperature», *Nature*, vol. 527, n.º 7577, pp. 212-215, nov. 2015, doi: 10.1038/nature15723.

[35] N. J. Ghimire, A. S. Botana, J. S. Jiang, J. Zhang, Y.-S. Chen, y J. F. Mitchell, «Large anomalous Hall effect in the chiral-lattice antiferromagnet CoNb3S6», *Nat. Commun.*, vol. 9, n.º 1, Art. n.º 1, ago. 2018, doi: 10.1038/s41467-018-05756-7.

[36] M. A. Zeb y H.-Y. Kee, «Interplay between spin-orbit coupling and Hubbard interaction in SrIrO3 and related Pbnm perovskite oxides», *Phys. Rev. B*, vol. 86, n.º 8, p. 085149, ago. 2012, doi: 10.1103/PhysRevB.86.085149.

Chapter 6

Magnetic textures and its relationship with the topological Hall effect

1. Introduction

In the previous chapter, we discussed the growing research interest raised by oxide interfaces, which hold immense potential for uncovering new electronic phases with exciting magnetic properties. At the heart of this research are interfaces between 5d heavy metal- and 3d transition metal oxide ferromagnets, where chiral magnetic textures emerge through the interplay between Dzyaloshinskii-Moriya interaction (DMI) and Heisenberg exchange [1]–[3]. These interplay give rise to non-collinear spin textures, such as spin spirals or skyrmions [4]–[6], which are closely associated with the Topological Hall Effect (THE), an antisymmetric contribution to transverse resistivity. Dipolar interaction can also stabilize chiral spin structures, creating chiral magnetic bubbles [7], [8]. These structures have topological features similar to skyrmions, such as having the same skyrmion number and exhibiting a similar topological Hall effect [9]. Interfaces between correlated oxides, specifically involving 3d or 4d and 5d oxides magnets [10]–[17], present a particularly fascinating opportunity to investigate the interplay between topology and correlation, which may potentially lead to pronounced THE values [18].

In this chapter, we focus on the observation of a remarkably large THE in LSMO/SIO ultrathin bilayers. These findings exhibit unique characteristics, as the THE is detected across a broad range of

temperatures and magnetic fields in zero-field-cooled (ZFC) transport experiments but disappears when the sample is cooled in the presence of a perpendicular magnetic field. We will explore the connection between this controllable THE and the emergence of magnetic textures by employing x-ray absorption and magnetic force microscopy (MFM) measurements.

2. Structural characterization

For this experiment, we grew the LSMO/SIO bilayer using a $SrTiO_3$ (100) substrate. The bilayers were grown at the Complutense University of Madrid, utilising the high-pressure sputtering process detailed in the introductory chapter, employing high (pure oxygen) pressures (2.8 mbar) and high temperatures (650 °C for SIO and 900°C for LSMO).

When combining the LSMO with the SIO, there are two possibilities: either putting the SIO on the bottom or on the top which as we have shown previously, yields very different interface structures. In order to choose the most suitable interface, we have carried out a microscopy study of the different interfaces formed between the two materials. Figure 6.1 displays the high angle annular dark-field (HAADF) and electron energy loss spectroscopy (EELS) results pertaining to a trilayer of LSMO (15 nm)/SIO (4.4 nm)/LSMO (15 nm). These measurements were acquired at the "Centro Nacional de Microscopía Electronica" (CNME) using a JEOL JEM ARM200cF operated at 200 kV with a 1 mm condenser lens aperture. As we can see in Figure 6.1a, both interfaces are epitaxial and perfectly crystalline. However, the LSMO interface with the SIO below has two SrO planes, while the interface with the SIO above has three planes. This difference in the interfaces appears in both in situ and ex situ samples. We do not know the origin of this interface difference. One possible origin could be the growth temperature, since the interface with the SIO below has been grown at 900°C while the interface with the SIO above has been grown at 650°C.

It has been reported that extra SrO planes can decrease the superexchange interactions between LSMO and SIO [16]. In order to maximise the coupling between the two materials for this experiment, we have chosen the interface with the SIO below, which has fewer SrO planes.

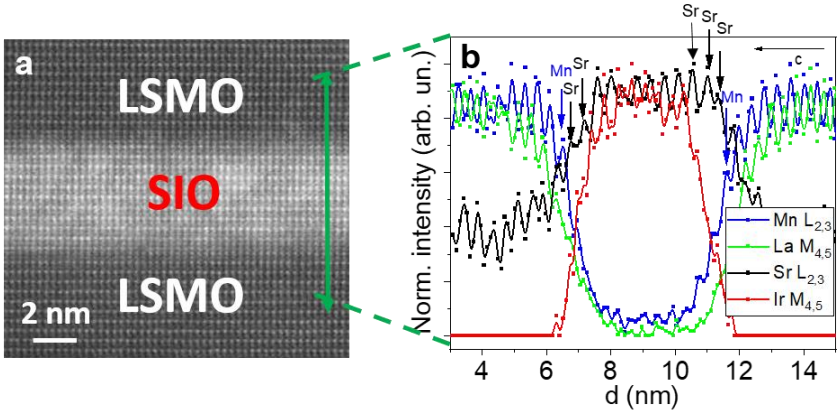

Figure 6.1. Characterization of interfaces by STEM microscopy (Re-adapted from previous chapter) (a) High resolution microscopy image; the green line indicates the profile taken for compositional analysis. (b) compositional analysis, where the different components of each atomic plane can be observed.

3. Transport characterization

The longitudinal and transverse resistances, R_{xx} and R_{xy}, were measured as a function of the magnetic field H (applied perpendicular to the film plane) for different temperatures in the range 5–300 K. We used a Quantum Design PPMS apparatus equipped with a He flow refrigerator (see Methods chapter) and a superconducting magnet. Samples were measured at the "Instituto de Ciencia de Materiales de Madrid" (ICMM).

The resistances are defined as $R_{xx} = V_{xx}/I_{xx}$ (longitudinal resistance) and $R_{xy} = V_{xy}/I_{xx}$ (transverse resistance), with I_{xx} the injected dc current and V_{xx} and V_{xy} the voltages measured parallel and perpendicular to the injected current. Samples were measured using the 4-point technique.

Based on the longitudinal resistance measurements R_{xx} as a function of the magnetic field H, we have calculated the magnetoresistance MR as:

$$MR(\%) = \frac{R(H) - R_0}{R_0} \cdot 100$$

where R_0 is the resistance at 0 T.

The pure Hall signal, which is "odd" with respect to the applied field, was calculated antisymmetrizing the transverse resistance as $\langle R_{xy}(H) \rangle = (R_{xy}(+H) - R_{xy}(-H))/2$. This allows removing any spurious contribution to R_{xy} resulting from the misalignment between voltage electrodes and the strong magnetoresistance of LSMO (which is "even" with respect to the applied field). We calculated the resistivity ρ_{xx} and ρ_{xy} via the Van der Pauw method from the resistances obtained as described above, by considering the films dimensions and thickness.

3.1. Thickness and monolayers characterization

In the LSMO/SIO heterostructure, the thickness of each component is of critical importance. For our investigation, an LSMO layer with a thickness of 3.5 nm was selected, corresponding to 8 unit cells (u.c.). This thickness is just above the critical thickness for dead layer, and, as discussed below, is adequate to ensure a "weak" ferromagnetism in the LSMO layer while still allowing it to be influenced by the adjacent SIO layer yielding chiral magnetization textures.

As demonstrated in Figure 6.2, the 3.5 nm LSMO layer exhibits metallic behavior across the entire temperature range studied (Figure 6.2a). It is worth noting that at elevated temperatures, the material approaches a metal-insulator transition, though, being above room temperature, it is not clearly observable in the data. The LSMO layer also displays colossal magneto-resistance (Figure 6.2b) which increases with temperature. This behaviour in magnetic manganites has been widely reported [19]–[21] and is thoroughly explained in the Introduction chapter.

In the Hall effect measurements (Figure 6.2c), a positive slope is observed, which aligns with the hole transport of manganite. Upon subtraction of the ordinary Hall effect component (Figure 6.2d), the LSMO layer exhibits an anomalous Hall effect (AHE) with a negative sign that becomes more pronounced as temperature increases. The AHE arises from non-coplanar spin configurations of the localised t_{2g} manifolds, which acquire a scalar spin chirality (real space Berry phase) and operate as a virtual magnetic field in real space, resulting in an intrinsic (real space) contribution to the AHE [22], [23].

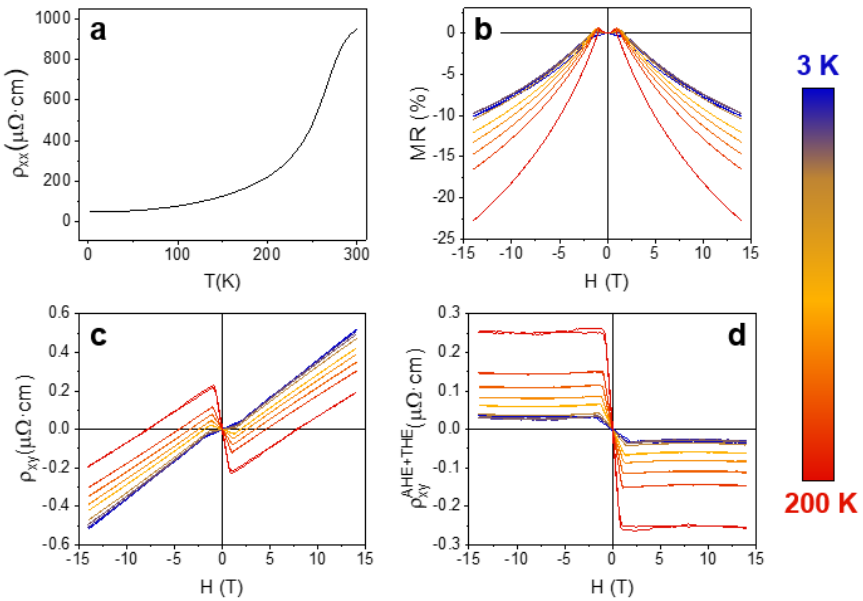

Figure 6.2. Transport characterisation of the LSMO. (a) Resistance as a function of temperature. (b) Magnetoresistance at 3, 10, 30, 60, 100, 120, 140, 160 and 200 K. (c) Hall effect at the same temperatures. (d) Hall effect after subtraction of the ordinary component.

For the SIO layer, we have opted for a thickness of 2.4 nm, with the electrical characterization depicted in Figure 6.3. At this thickness, the material exhibits low resistance (Figure 6.3a). Although a metal-insulator transition is observed at 160 K, the temperature dependence is very weak as typically observed in compensated semi-metals (see inset of Figure

6.3a). The SIO layer displays a positive magneto-resistance that decreases with increasing temperature (Figure 6.3b). In the Hall effect measurements (Figure 6.3c), a negative slope is present, which is characteristic of electron transport. As we saw in the last chapter, an anomalous Hall effect (AHE) is not observed in SIO.

The choice of SIO thickness has been carefully considered. The 2.4 nm thickness is sufficient to confer strong spin-orbit interaction to the system, as it has been reported that the Dzyaloshinskii-Moriya interaction can be modulated by the thickness of the SIO layer [24]. Simultaneously, the thickness is not so large as to dominate the electronic transport, ensuring a balanced contribution from both the LSMO and SIO layers.

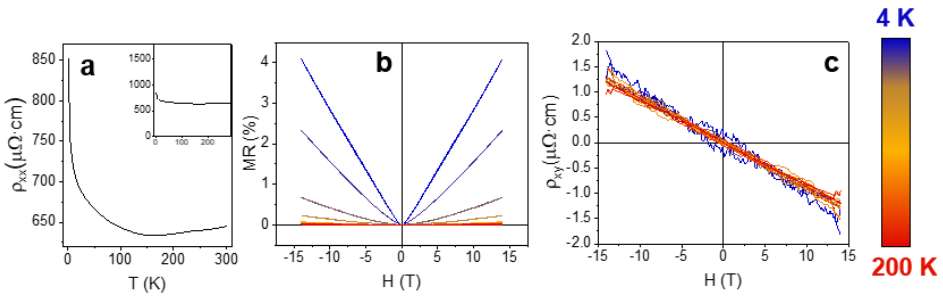

Figure 6.3. Transport characterisation of the SIO. (a) Resistance as a function of temperature. (b) Magnetoresistance at 4, 10, 30, 60, 100, 120, 140, 160 and 200 K. (c) Hall effect at the same temperatures.

3.2. THE in bilayer LSMO (3.5 nm)/ SIO (2.4 nm)

Upon combining the LSMO and SIO layers, we obtain a bilayer system with transport characteristics illustrated in Figure 6.4. The bilayer exhibits low resistivity (Figure 6.4a) and undergoes a metal-insulator transition (MIT) at 40 K. At elevated temperatures, the system approaches another MIT, likely originating from the manganite, although it is not distinctly observed. The magnetoresistance (MR) displays unexpected behavior, as depicted in Figure 6.4b. Contrary to the manganite, the MR is negative across all temperatures and increases at

lower temperatures. Furthermore, the magneto-resistance value is significantly larger at all temperatures compared to that in single manganite. The origin of this increase of the negative MR is not completely clear although it seems to be related to the LSMO in proximity with SIO.

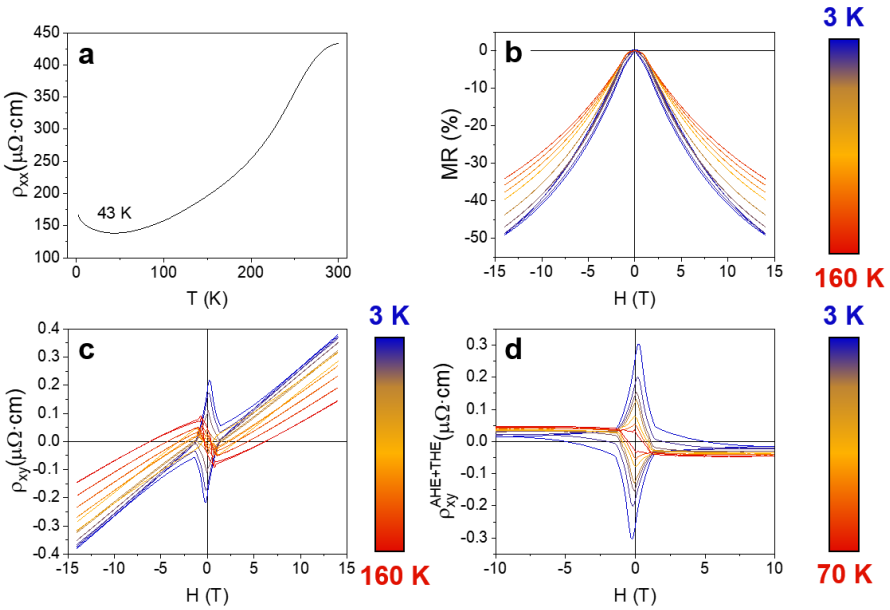

Figure 6.4. Transport characterisation of the bilayer. (a) Resistivity as a function of temperature. (b) Magnetoresistance at 3, 10, 30, 60, 100, 120, 140 and 160 K. (c) Hall effect measurements at the same temperatures. (d) Hall effect after subtraction of the ordinary component for 3, 6, 15, 20, 40, 50, 70 K.

In the Hall effect measurements (Figure 6.4c), a positive slope is observed, similar to that for manganite, and follows the same trend. However, a prominent topological peak emerges at low temperatures. Upon subtracting the ordinary Hall component (Figure 6.4d), it becomes evident that a very large topological Hall effect (THE) signal is superimposed on the manganite's AHE. The topological peak is an order of magnitude larger than the AHE at 3 K and diminishes with increasing temperature until it nearly vanishes at 70 K.

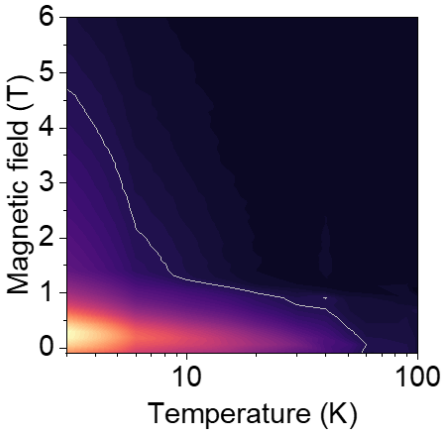

Figure 6.5. Phase diagram of the appearance of the topological Hall effect as a function of temperature and magnetic field.

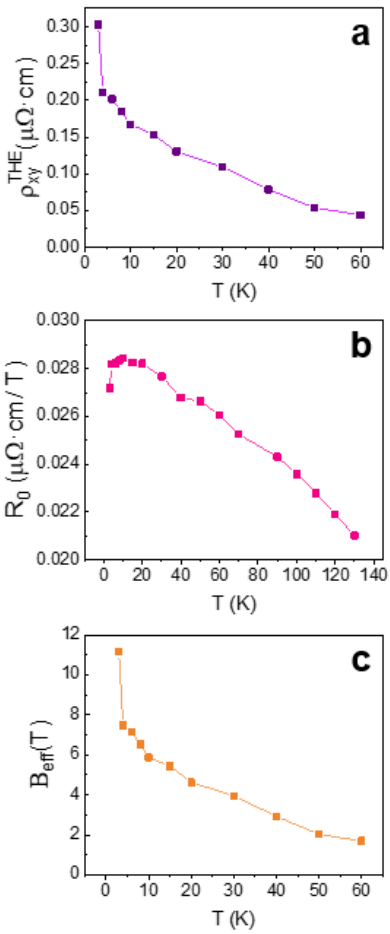

The evolution of the THE signal with temperature and magnetic field is best illustrated in the contour plot in Figure 6.5, where we can see that the topological peak narrows as temperature increases.

In our investigation of the LSMO/SIO system, we expected the presence of the topological Hall effect (THE). However, we encountered some unexpected findings, as shown in Figure 6.6, which illustrates the temperature dependence of the topological peak, Hall coefficient, and effective field as calculated using Bruno's formula [25]:

Figure 6.6. Temperature dependence of the topological parameters. Temperature dependence of (a) the topological peak ρ_{xy}^{THE}, (b) the R_0 Hall coefficient and (c) the effective magnetic field $B_{eff} = \rho_{xy}^{THE} / R_0$.

$$\rho_{xy}^{T} = PR_0\Phi_0\Phi \;\rightarrow\; \rho_{xy}^{T} = PR_0B_{eff}$$

The effective magnetic field B_{eff} represents the influence of magnetic skyrmions in the system. We observe that the topological peak diminishes with increasing temperature. This reduction is particularly pronounced at lower temperatures, where approximately one-third of the topological signal is lost within just a few degrees. Such a strong temperature dependence is atypical for magnetic textures like skyrmions, which are expected to exhibit temperature-independent behavior. Moreover, the effective magnetic fields are considerably weaker compared to values reported in the literature, suggesting that additional, unaccounted-for factors may be at play within this system.

We can determine the system's skyrmion densities and diameters using the effective magnetic field.

$$\rho_{xy}^{T} = PR_0B_{eff} = PR_0n_{sk}\Phi_0 \rightarrow B_{eff} = n_{sk}\Phi_0$$

$$n_{sk} = \sqrt{1/d}$$

The mathematical calculations have yielded the diameters of skyrmions, as presented in Table 6.1, falling within the range of 20 to 50 nm.

Temperature (K)	Diameter (nm)
3	18
4	22
6	23
8	24
10	25
15	26
20	28
30	31
40	36
50	43
60	47

Table 6.1. Skyrmion diameters at different temperatures.

A striking result is that the THE depends on magnetic history (see Figure 6.7). Figure 6.7a displays the Hall measurements, excluding the ordinary component, which were conducted after a zero-field cooling (ZFC) process. This entails cooling the system to 2 K without applying any external magnetic field. However, when the same measurements are performed following a field-cooling (FC) protocol – cooling the system to 2 K while applying a 14 T out-of-plane magnetic field – the THE nearly vanishes at all temperatures (Figure 6.7b), leaving only the expected AHE for the manganite. Consequently, we have identified a mechanism to control the emergence of THE based on the system's magnetic history.

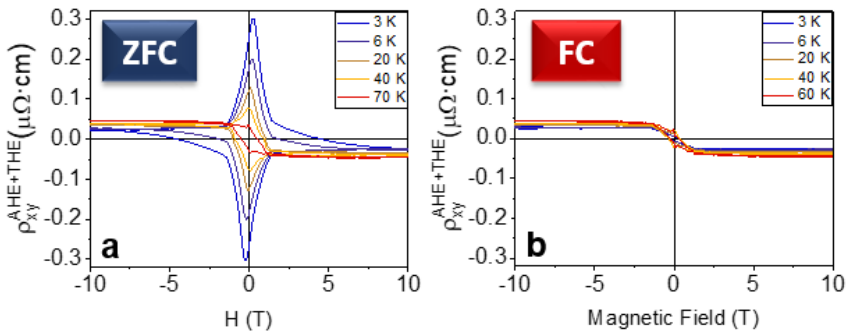

Figure 6.7. Topological Hall effect at ZFC y FC. Hall effect after subtraction of the ordinary component for temperatures between 3 and 70 K at (a) Zero field cool, ZFC (b) Field cool, FC.

To more effectively visualize the impact of the FC process on the Hall measurements, Figure 6.8 presents a comparison between ZFC (red lines) and FC (black lines) measurements at each temperature. To verify whether the THE could be recovered, we conducted another ZFC process and repeated the measurements at 3, 10, and 20 K (blue lines). These measurements confirm that we can recover THE after FC suppressing it. Moreover, we observe an increased intensity of THE, with its value at 3 K rising by 40%. It is important to note that the AHE values at high field are consistent between the FC and ZFC cases. This demonstrates that we have achieved control over the topological Hall effect exclusively without affecting the anomalous Hall effect of the system.

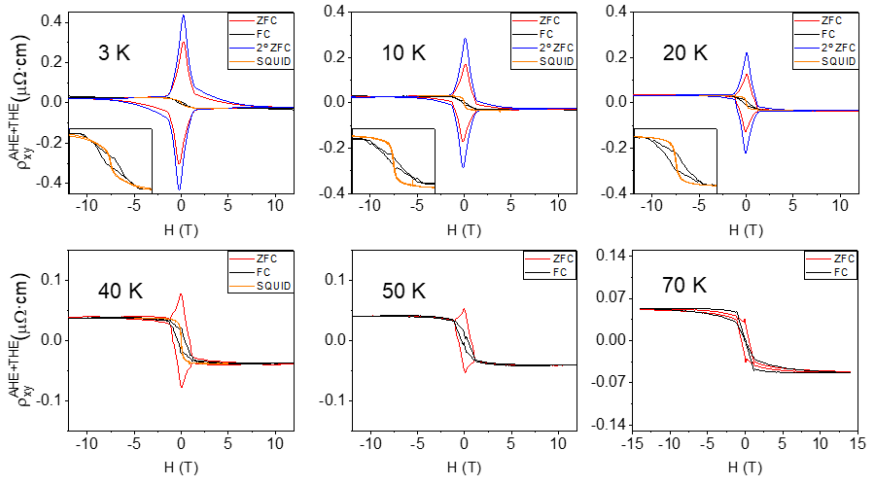

Figure 6.8. Comparison of Hall effect after ZFC and FC at each temperature. Hall Effect without the ordinary component at 3, 10, 20, 40, 50, and 70 K. Red and blue lines represent the first and second measurements taken at zero field cooling (ZFC), going from 300 K to 2 K at 0 T. Black lines represent the measurements taken at field cooling (FC) going from 320 K to 2 K at 14T. Orange lines correspond to normalized SQUID signal.

In order to determine the magnitude of the FC magnetic field necessary for the suppression of the THE, a series of field cooling (FC) experiments were conducted at varying magnetic fields, as depicted in Figure 6.9. Our observation indicates that a magnetic field strength of 1 Tesla is insufficient to suppress the THE. Nevertheless, it is noteworthy that a magnetic field of 5 T can produce an effect equivalent to that of a 14 T field, as both fields are capable of suppressing the transverse relaxation time of THE. The significance of this will be relevant in the context of magnetic force microscopy (MFM) measurements, as will be discussed below.

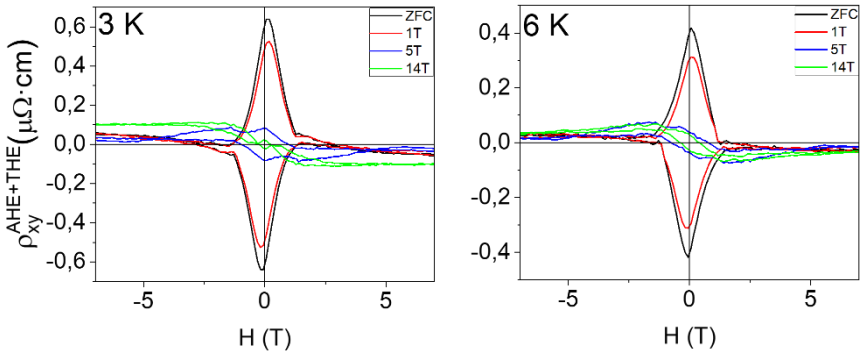

Figure 6.9. Comparison of Hall effect after ZFC and FC at different magnetic field. Hall Effect without the ordinary component at 3 and 6 K. Black lines represent measurements taken after a ZFC. Red, blue and green lines represent measurements taken after a FC at 1, 5 and 14 T respectively (going from 320 K to 2 K).

4. Magnetic characterization in bilayer LSMO (3.5 nm) / SIO (2.4 nm)

In the following sections, we will examine the relationship between the observed THE in the LSMO/SIO bilayer and the system's macroscopic magnetic properties under ZFC and FC conditions, utilizing a superconducting quantum interference device (SQUID). Additionally, we will investigate the microscopic magnetic characteristics of the LSMO/SIO bilayer employing magnetic force microscopy (MFM) and X-ray magnetic circular dichroism (XMCD).

4.1. SQUID characterization

For the SQUID measurements, we employed a Quantum Design PPMS apparatus outfitted with a He flow refrigerator (refer to the Methods chapter) and a superconducting magnet. The samples were measured at the "Instituto de Ciencia de Materiales de Madrid" (ICMM).

To gain a better understanding of the effects of zero-field cooling (ZFC) and field cooling (FC) on the system, we conducted measurements of magnetization as a function of temperature for both ZFC and FC cases. These measurements were taken with magnetization both in-plane and

out-of-plane, as presented in Figure 6.10a and 6.10b, respectively. The measuring field was 1000 Oe. While there are no significant differences between ZFC and FC for in-plane magnetization, distinct differences are observed for out-of-plane magnetization. In the ZFC case, out-of-plane magnetization is suppressed at low temperatures indicating the nucleation of small magnetic domains, whereas it exhibits rather standard values in the FC case. The relationship between these observations and the potential presence or absence of skyrmions in the system will be discussed later.

Furthermore, we measured the magnetization versus magnetic field at various temperatures, obtaining the hysteresis loops displayed in Figure 6.10c for in-plane magnetization and Figure 6.10d for out-of-plane magnetization. The out-of-plane coercive field values range from 200 to 80 Oe, which do not appear to be correlated with the fields at which the topological peak manifests; the topological peak ranges from 1820 to 0 Oe.

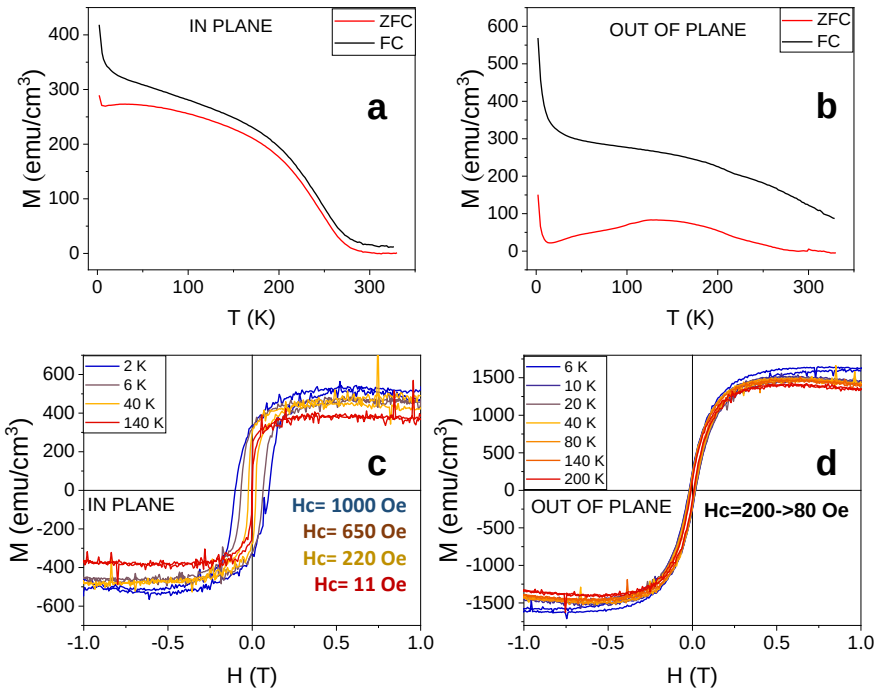

Figure 6.10 SQUID measurements. Magnetisation as a function of temperature for ZFC and FC (a) in-plane and (b) out-of-plane. Hysteresis cycles at different temperatures (c) in-plane (d) out-of-plane.

A striking result is that the shape of the SQUID hysteresis loop departs strongly from the AHE and THE plots in the high field region. I.e., above the main peak of the THE. See Figure 6.8 for a compartison. This suggest that there may be in fact two contributions to the THE, one strongly peaked at low fields and another yielding a broad peak which extends up to fields of 7 T (see Fig. 6.8).

4.2. XMCD and MFM characterization

In an effort to gain a deeper understanding of the origin of THE and the impact of FC on the system, we have conducted microscopy studies employing both x-ray magnetic circular dichroism (XMCD) contrast and magnetic force microscopy (MFM).

The XMCD measurements were performed at the Mn $L_{2,3}$ edge using photoemission electron microscopy (PEEM). Two samples were examined: LSMO (3.5 nm) and LSMO (3.5 nm) / SIO (5 nm). In the PEEM image of the LSMO 3.5 nm sample (Figure 6.11a), a domain structure oriented in the [110] direction is observed, which is anticipated in manganite. In contrast, the PEEM image of the bilayer composed of LSMO 3.5 nm and SIO 5 nm (Figure 6.11c) reveals the emergence of circular and ellipsoidal domains dispersed throughout the material. It is important to note that these textures were generated with 5 nm SIO, a thickness greater than the SIO utilized for Hall measurements. As discussed at the beginning of this chapter, the thickness of the iridate can influence Hall effect measurements as it introduces an additional conduction channel. However, a thicker iridate layer does not hinder the formation of magnetic textures in the system.

The MFM measurements were conducted at the Instituto de Ciencia de Materiales de Madrid. The MFM images show similar patterns to those in the XMCD images: domains in the 3.5 nm LSMO (Figure 6.11b) and magnetic textures in the bilayer of LSMO 3.5 nm and SIO 2.4 nm (Figure 6.11d). Although the PEEM and MFM images exhibit similarities, it is essential to emphasize that they are not depicting exactly the same

magnetic contrast. The MFM image displays out-of-plane magnetization in red and blue, whereas in the PEEM image, red and blue represent the summation of out-of-plane and in-plane magnetization components. This discrepancy arises because the PEEM images were obtained using synchrotron X-rays at a 20-degree orientation. A detailed explanation of this procedure can be found in the methods section. These findings align well with prior research on LSMO/SIO [13], [14] and various doped manganites [18], [26], where the observed THE is linked to the magnetic textures identified by MFM and PEEM.

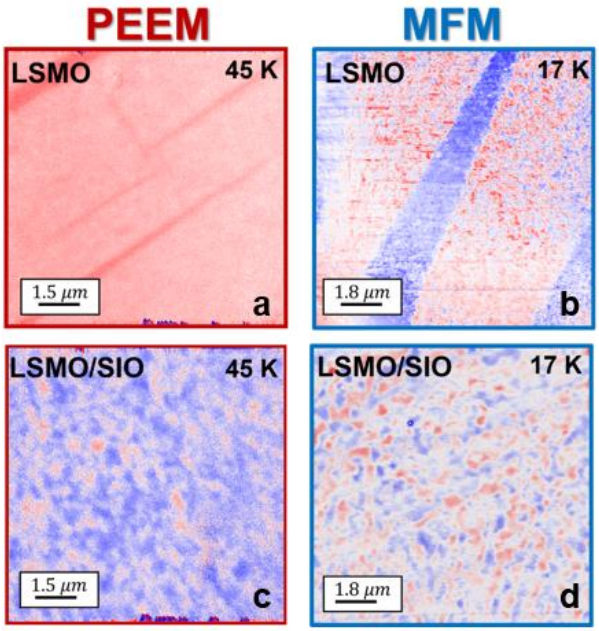

Figure 6.11. Change of the magnetic structure from the monolayer of LSMO to the bilayer of LSMO/SIO. (a)-(c) Photoemission electron microscopy (PEEM) images of LSMO (3.5 nm) and a bilayer of LSMO (3.5 nm)/SIO (5 nm). (b)-(d) Magnetic force microscopy (MFM) images of LSMO (3.5 nm) and a bilayer of SIO (2.4 nm)/LSMO (3.5 nm).

In an effort to further elucidate the relationship between THE and the observed magnetic textures, we carried out an MFM study involving the application of magnetic fields. In this investigation, magnetization images were obtained using the same method as for electrical measurements. This process entailed performing both ZFC and FC down to 17 K, the lowest

temperature our MFM could measure. At this temperature, the magnetic field was swept from 5 T to -5 T and then back to 5 T.

A noteworthy observation can be seen at 5 T, as illustrated in Figure 6.12, where there are magnetization discrepancies between the ZFC and FC cases. Although the sample appears saturated in the MFM image of the ZFC case (Figure 6.12b), faint white bands can still be detected. As depicted in Figure 6.12a, these white bands do not correspond to any topographic defects. To mitigate the saturation effect, we adjusted the color scale, yielding Figure 6.12c. The adjustment reveals that the white bands evolve into spin spirals. The absence of spirals in the FC case, as demonstrated in Figures 6.12e-f, marks the first distinction between ZFC and FC conditions. In future analyses, a more suitable contrast will be employed to provide clearer visualizations of the magnetic contrast, independent of the sample's saturation level.

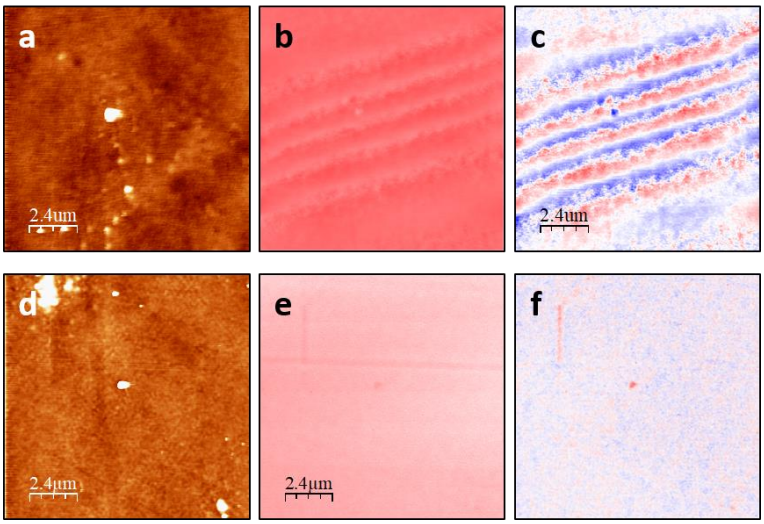

Figure 6.12. MFM images of the bilayer LSMO (3.5 nm)/SIO (2.4 nm) at 17 K and 5 T. At ZFC (a) Topography. (b)-(c) Magnetization of the sample with different colour scales. At FC (d) Topography. (e)-(f) Magnetization of the sample with different colour scales.

In examining the evolution of magnetic textures from -5 to 5 T in both ZFC and FC cases (Figure 6.13), it becomes apparent that the spin spirals observed at high magnetic fields transition into magnetic textures at lower

fields, where the THE is more pronounced. Surprisingly, magnetic textures are also present in the FC case, despite the disappearance of the topological Hall effect. At low fields, there seems to be no substantial difference between the ZFC and FC images. The only discernible distinction between the ZFC and FC sequences is found at high fields, where the THE is weaker (non-zero high field component described above) and only spin spirals are visible in the ZFC images.

Given the presence of magnetic textures in both the ZFC and FC cases, it can be deduced that magnetic textures alone are not solely responsible for the emergence of THE. We propose that the magnetic textures observed in the ZFC case at low fields are the result of disrupted spin spirals. These spin spirals may induce chirality at the boundaries of the magnetic textures, consequently giving rise to THE. However, in the FC case, where no spirals are observed, the boundaries of the magnetic textures are not chiral and, thus, THE is not observed.

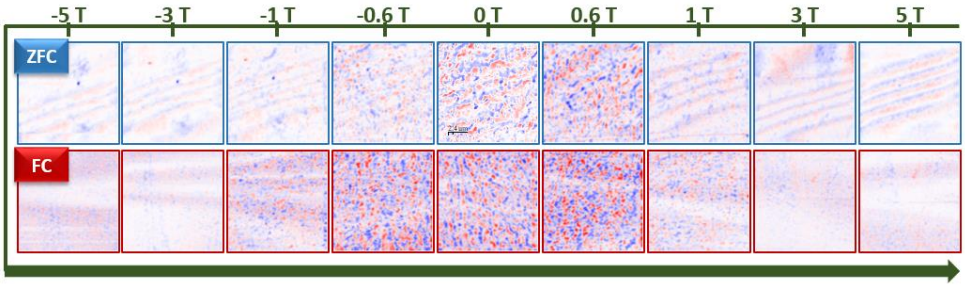

Figure 6.13. Evolution the magnetic textures with the magnetic field. MFM images after a ZFC (blue border) and after a FC (red border) going from -5T to 5 T.

5. Control experiments. Transport characterization in bilayer LSMO (3.5 nm)/SIO (5 nm)

As demonstrated earlier, the observation of the large THE is contingent upon the appropriate selection of iridate and manganite thicknesses. In the following section, we will examine bilayers with varying manganite

and iridate thicknesses, in which a significant THE was not observed, to better understand the interplay between these two materials.

PEEM measurements (Figure 6.11) indicate that a bilayer with increased SIO thickness (from 2.4 nm to 5 nm) continues to exhibit magnetic textures. Nonetheless, the electrical characterization of the LSMO 3.5 nm/SIO 5 nm bilayer (Figure 6.14) reveals both similarities and noteworthy differences compared to the SIO 2.4 nm bilayer.

On one hand, the resistivity as a function of temperature displays a behavior strikingly similar to that of the first bilayer, with a metal-insulator transition (MIT) at 50 K and a near occurrence of another MIT at 300 K (Figure 6.14a). Likewise, the magnetoresistance (MR) of this bilayer exhibits the same anomalous behavior as the previous bilayer, with high negative MR values increasing as the temperature decreases, contrary to the tendency observed in manganite (Figure 6.14b).

Conversely, the Hall effect slope exhibits a strong temperature dependence. While the initial bilayer exhibited a positive slope across the entire temperature range, the slope in this second bilayer changes. At low temperatures, the positive slope suggests that LSMO governs the transport, whereas at high temperatures, the negative slope indicates SIO dominance in transport.

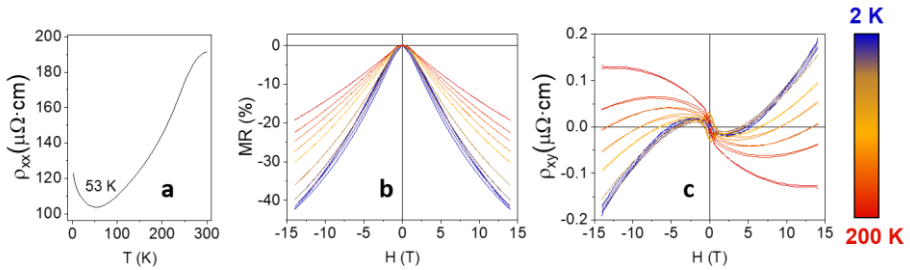

Figure 6.14. Transport characterisation of bilayer LSMO 3.5 nm /SIO 5 nm. (a) Resistance as a function of temperature. (b) Magnetoresistance at 2, 10, 30, 60, 100, 120, 140, 160 and 200 K. (c) Hall effect at the same temperatures.

The curvature in the Hall signal complicates the subtraction of the ordinary component of the Hall effect. As illustrated in Figure 6.15a, if the ordinary component is subtracted using the linear fit at high fields,

the remaining AHE exhibits exceedingly large negative values. Conversely, if the ordinary component is subtracted at lower fields (Figure 6.15b), the anomalous Hall effect values become more reasonable, although the Hall effect diverges at high fields.

In both instances, it is evident that the Hall effect displays an hysteretic peak at low fields. This hysteresis is substantially smaller than that observed in the first bilayer and occurs within a different temperature range, primarily between 20 and 120 K. This bilayer illustrates the impact of increased SIO thickness on THE. Despite the presence of magnetic textures comparable to those of the previous bilayer, the contribution of a secondary conduction channel significantly diminishes THE.

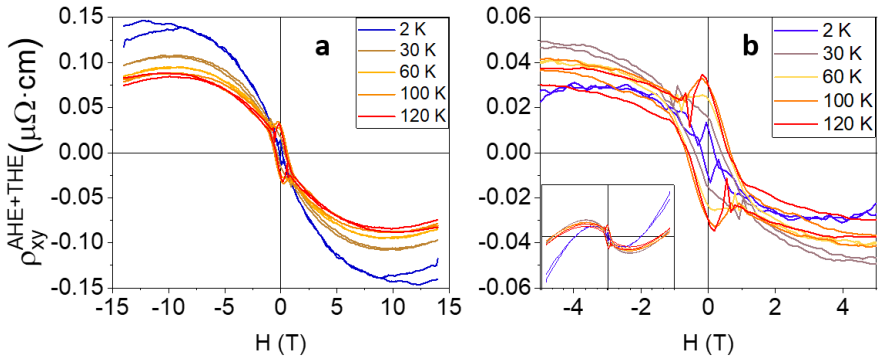

Figure 6.15. Hall effect comparison based on linear adjustment of bilayer LSMO 3.5 nm /SIO 5 nm. Hall effect without the ordinary component, subtracting the slope at high fields (a) and at low fields (b).

6. Control experiments. Transport characterization in trilayer SIO (2.4 nm) / LSMO (3.5 nm) / SIO (2.4 nm)

The difficulties of transport measurements to assess the presence of magnetic textures in a system comes here to the front. This is evident in the transport measurements depicted in Figure 6.16, which correspond to a trilayer with the following structure: SIO (2.4 nm)/LSMO (3.5 nm)/SIO

(2.4 nm). The objective of this layer sequence was to reduce the symmetry breaking within the system. Our hypothesis postulated that if magnetic textures arise due to the Dzyaloshinskii-Moriya interaction, which involves symmetry breaking, minimizing the asymmetry of the system would preclude the formation of magnetic textures.

The trilayer exhibits behavior similar to the previous LSMO 3.5 nm / SIO 5 nm bilayer: it undergoes a metal-insulator transition (MIT) at low temperatures and appears to approach another MIT at room temperature (Figure 6.16a); it demonstrates a large negative MR with an opposite trend to that of manganite, as observed previously in LSMO 3.5 nm / SIO 2.4 nm bilayer (Figure 6.16b); and it exhibits a curved Hall effect at high fields with a slope that varies significantly with temperature (Figure 6.16c).

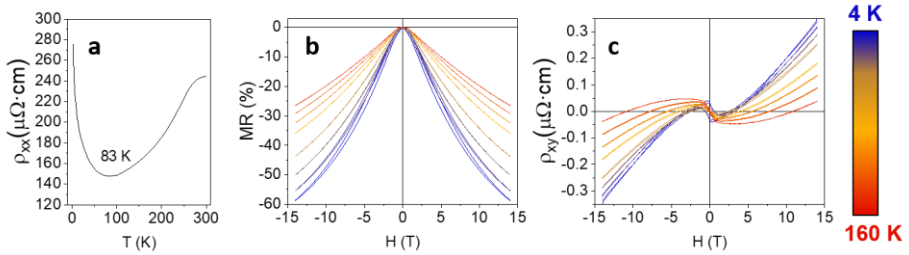

Figure 6.16. Transport characterisation of trilayer SIO 2.4 /LSMO 3.5 nm /SIO 2.4 nm. (a) Resistance as a function of temperature. (b) Magnetoresistance at 4, 10, 30, 60, 100, 120, 140, 160 and 200 K. (c) Hall effect at the same temperatures.

Since the Hall effect is curved at high fields, we have the same problem as in the previous 5nm SIO bilayer. As shown in Figure 6.17, the linear component can be rectified at high fields (Figure 6.17a) or intermediate fields (Figure 6.17b). This trilayer exhibits a slight hysteresis at low fields, which decreases with increasing temperature.

This weak hysteresis could indicate that we have eliminated or reduced the magnetic textures of the system. But, one has to keep in mind that the reduced THE may both result of textures getting suppressed or because the system is getting more conduction channels (notice the small

values of the transverse resistivity compared to those found at the large THE peak in the LSMO 3.5 nm / SIO 2.4 nm bilayer .

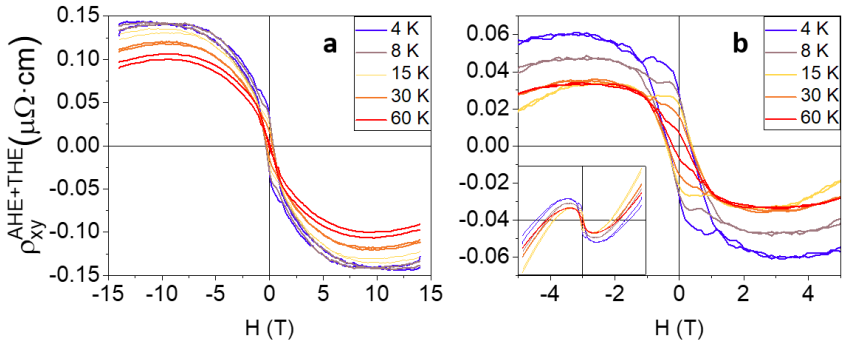

Figure 6.17. Hall effect comparison based on linear adjustment of trilayer SIO 2.4 /LSMO 3.5 nm /SIO 2.4 nm. Hall effect without the ordinary component, subtracting the slope at high fields (a) and at low fields (b).

7. Control experiments. Transport characterization in bilayer LSMO (8 nm) /SIO (2.4 nm)

In light of the findings from the previous two bilayers, we conclude that it is necessary for the transport to be dominated by LSMO in order to circumvent the curved Hall effect. However, if the thickness of the LSMO is too large, the topological Hall effect (THE) will not emerge, as demonstrated in LSMO/SIO bilayers with LSMO 25 nm in the previous chapter. One plausible explanation is that when the LSMO is sufficiently thick, the Dzyaloshinskii-Moriya interaction (DMI) does not influence its magnetism, since the DMI takes place at the interface and has a short (nanometer scale) effective range. In response to this situation, we opted to characterize the transport properties of a bilayer with an intermediate LSMO thickness: LSMO 8 nm / SIO 2.4 nm (Figure 6.18).

In this bilayer, a clear LSMO dominance in transport is evident: the resistivity is low, with a barely discernible metal-insulator transition (MIT) at 20 K (Figure 6.18a); the magnetoresistance (MR) is negative,

and takes roughly the same values in the whole temperature range (Figure 6.18b); and the Hall effect demonstrates a positive slope that scarcely varies across the temperature range (Figure 6.18c).

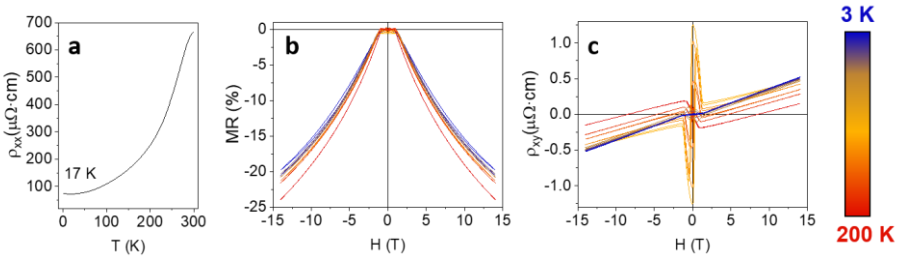

Figure 6.18 Transport characterisation of bilayer LSMO 8 nm /SIO 2.4 nm. (a) Resistance as a function of temperature. (b) Magnetoresistance at 3, 10, 30, 60, 100, 120, 140, 160 and 200 K. (c) Hall effect at the same temperatures.

In this system, we uncover a highly unanticipated behavior of the topological Hall effect (THE). At low temperatures (Figure 6.19a), the THE observed in the LSMO 3.5 nm / SIO 2.4 nm bilayer is absent. Rather a THE peak starts to emerge at 60 K, a temperature where the large THE of the LSMO 3.5 nm / SIO 2,4 nm bilayer had disappeared. This already shows that the large THE contribution is not observed when the thickness of the LSMO is increased. Moreover, at higher temperatures, an entirely distinct phenomenon occurs. Firstly, at 100 K, the anomalous Hall effect (AHE) changes sign (from negative to positive) and undergoes another change at 140 K. This temperature range could correspond to the Curie temperature of the LSMO at the interface and could thus potentially be attributed to the non-coplanar spin triads present in manganite, which have been demonstrated to generate an unexpected AHE through skew scattering effects [27], [28] close to Tc.

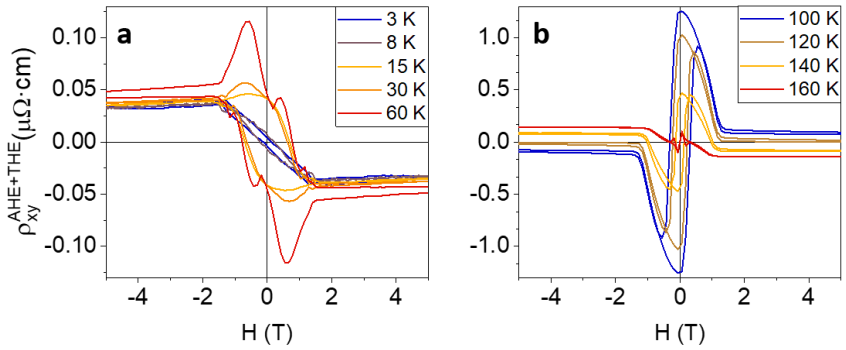

Figure 6.19. Differences in the Hall effect at low and high temperature of bilayer LSMO 8 nm /SIO 2.4 nm. Hall effect without the ordinary component at temperatures between (a) 3-60 K and (b) 100-160 K.

8. Control experiments. Transport characterization in bilayer SIO (2.4 nm) /LSMO(3.5 nm) with inverted layer sequence

Finally, we aimed to examine the transport characteristics of a 2.4 nm SIO/3.5 nm LSMO bilayer, with the same thickness as the initial bilayer but with the opposite layer sequence. Our objective was to get a deeper understanding of the interface's impact on the system since, as mentioned at the beginning of the chapter, this interface features an additional SrO plane which is expected to weaken superexchange interaction across the interface.

As displayed in Figure 6.20a, the resistivity of the bilayer is similar to the previous one: low resistance, metal-insulator transition (MIT) at room temperature, and an indication insulating state at low temperature suggesting localization. However, the magnetoresistance (MR) is in stark contrast (Figure 6.20b) with the behaviour observed in the LSMO 3.5 nm / SIO 2.4 nm bilayer: negative MR values increasing with temperature, as it is typically observed in manganites. This suggests conventional

LSMO behavior. This is also evident from the Hall effect measurements, where the slope remains consistently positive and exhibits typical manganite bahvior (Figure 6.20c).

Aside from the typical LSMO anomalous Hall effect (AHE), no indication of topological Hall effect (THE) is observed in this sample. This could be rationalized in view of the observed interface structure with depressed LSMO magnetism and with an additional SrO plane which weakens superexchange interaction across the interface.

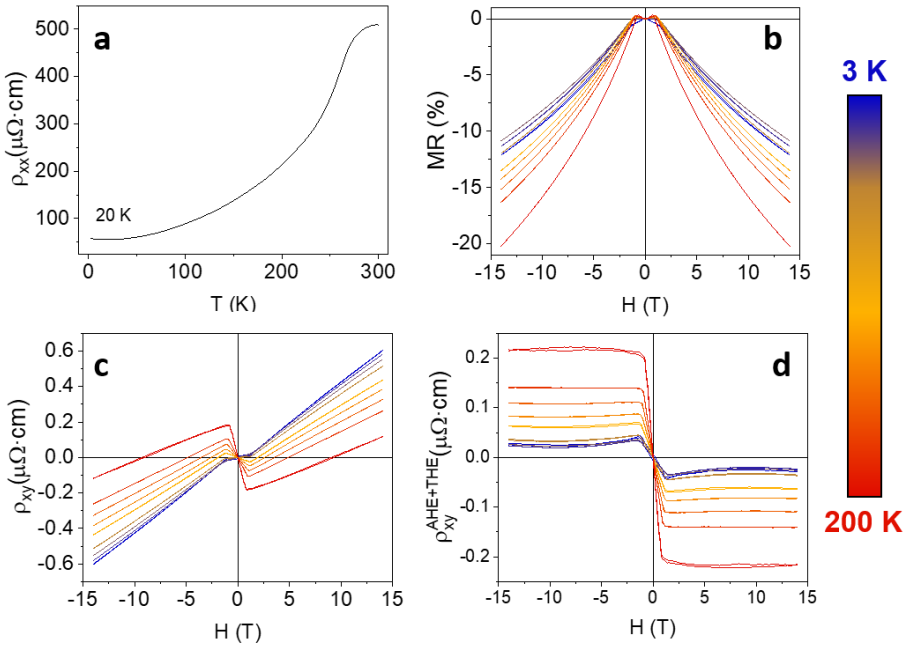

Figure 6.20. Transport characterisation of bilayer SIO 2.4 nm / LSMO 3.5 nm. (a) Resistance as a function of temperature. (b) Magnetoresistance at 3, 10, 30, 60, 100, 120, 140, 160 and 200 K. (c) Hall effect at the same temperatures. (d) Hall effect without the ordinary component at the same temperatures.

By collecting the magnetoresistance (MR) values at 10 T at various temperatures for all the samples discussed earlier, we can discern the relationship between MR and temperature, as illustrated in Figure 6.21. Among these measurements, only three of the samples exhibit MR trends that depart from the typical manganite behaviour. Notably, only the

bilayer LSMO (3.5 nm)/SIO(2.4 nm), which shows the most pronounced topological Hall effect (THE), displays a linear Hall effect at high fields. Conversely, the Hall effect in the other two samples exhibits curvature. This finding suggests that the observation of the large topological Hall effect results from a delicate balance between the contributions of SIO and LSMO to the transverse resistivity.

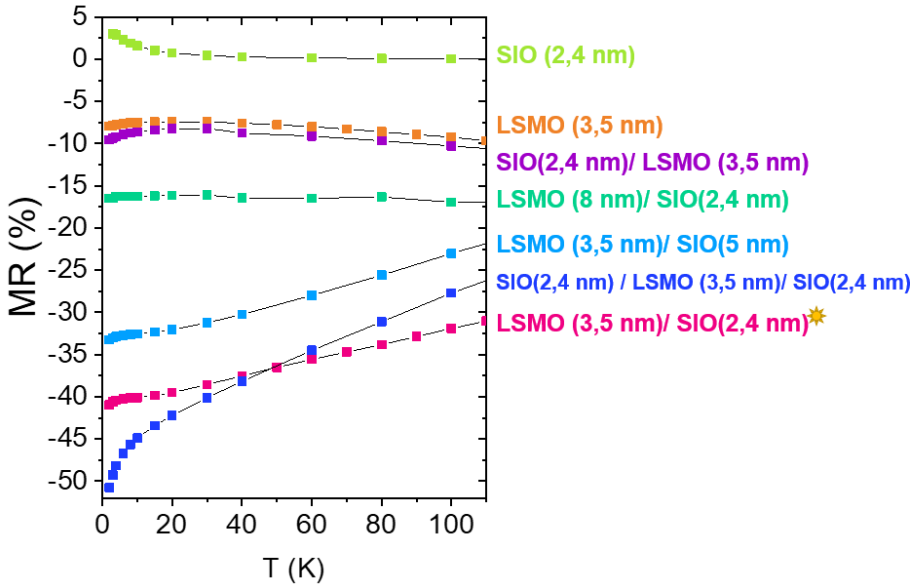

Figure 6.21. Magnetoresistance tendency with the temperature. Value of the MR at 10 T, at temperatures from 2 to 100 K in all the bilayer.

9. Discussion

In summary, we have observed a large topological Hall effect (THE) in SIO/LSMO bilayers, confirming the theoretical prediction of THE in this system [29]. Yet, the appearance of the THE contribution to the transverse resistivity depends on magnetic history, what, compared to previous reports of THE, is a very anomalous result. In the following we discuss the possible origin of this behaviour.

The Dzyaloshinskii-Moriya interaction (DMI) is an antisymmetric exchange interaction [1], [3] induced by the interplay between spin-orbit

coupling and superexchange interaction. It was initially used to explain the weak ferromagnetism in antiferromagnetic oxides and anisotropy fields in spin glasses [30] and magnetoelectric coupling in multiferroic perovskite oxides [31]. Later, it was found to be responsible for understanding a variety of physical phenomena including noncollinear spin textures in chiral magnets (e.g., spin spirals [32], magnetic skyrmions [8], [33], and chiral domain walls [34]), etc.

Under the Dzyaloshinskii-Moriya interaction (DMI) real-space noncollinear magnetic textures nucleate with a finite scalar spin chirality $S_i \bullet (S_j \times S_k)$ [35], [36]. This spin chirality generates an effective electromagnetic field for electrons through the spin Berry phase mechanism giving rise to the topological Hall effect (THE), an antisymmetric contribution to the transverse resistivity governed by the Berry phase acquired by conduction electrons when their spin couple to the non collinear local spins of the magnetic texture [25]. THE has been observed chiral magnets [27], [37], frustrated magnets [38], and Heusler alloys [39]–[41], and also in perovskite oxides [18], [26], [42].

In addition to the noncentrosymmetric magnetic single crystals [43], DMI has been demonstrated in multilayers combining materials with heavy elements and ferromagnets. In multilayers DMI competes with the Heisenberg exchange over atomically short length scales from the interface to twist spins and nucleate non-collinear spin textures, such as a spin spirals or skyrmions [4]–[6]. A resultant net interfacial requires thin films with asymmetric interfaces [6], [44], [45], where the asymmetry may be controlled by the layer sequence or induced chemically [46], [47] or structurally through strain engineering [48], [49].

Interfaces between correlated oxides are an interesting scenario to explore chiral magnetic textures. In particular, interfaces between 3d (LSMO) or 4d (SRO) magnets and 5d (SIO) oxides [10]–[17] with strong spin orbit interaction are acclaimed benchmarks to explore the interplay between topology and correlations, which has been proposed to be the source of

large (giant) values of the THE [18]. At oxides interfaces there are typically charge transfer processes and polar discontinuities which conspire with correlation broken orbital degeneracy to promote non collinear spin textures [50], [51]. Moreover, the atomic control of interface termination enabled by modern oxide epitaxy allows controlling symmetry breaking [17] what has been recently shown to play a decisive role in the appearance of THE in LMO/SIO superlattices.

However, there is a growing debate on the connection between electronic transport phenomena and chiral magnetism [9], [25], [52]. While in some cases THE has been found to scale with the skyrmion density [10], [11], [27], [53], this is not the case in magnetic multilayers where large discrepancies between the skyrmion densities obtained from THE and MFM observations have been reported. Moreover, chiral spin structures can be also stabilized by the dipolar interaction in what are called chiral magnetic bubbles [7], [8] with topological properties akin to skyrmions (they possess the same skyrmion number), and displaying similar THE [9]. The interpretation of THE as the transport signature of chiral spin textures has been recently challenged [54]–[58] mostly in connection to experiments on SRO oxide interfaces showing that, in addition, intrinsic (momentum space) electronic mechanisms and/or inhomogeneities may yield inhomogeneous multicomponent anomalous Hall effect which can be mistaken with THE [58].

Here we report a very large THE in LSMO/SIO ultrathin bilayers. It displays highly anomalous features which may provide useful insights into the connection between THE and spin textures. The main experimental evidences can be summarized as follows:

1- While the THE is observed in a wide temperature and magnetic field range in ZFC transport experiments, it is suppressed when the sample is (FC) cooled in a perpendicular magnetic field. Systematic MFM and x ray absorption spectroscopy on these samples has evidenced that the appearance a coarse granular magnetic texture with small magnetic domains of a (roughly) 400 nm average diameter. Although this magnetic texture is the

dominant feature in the magnetic field and temperature range where the THE signal is observed it appears both after ZFC (maximal THE) and FC (no THE) sequences. Yet, the large THE signal correlates with the presence of spin spirals detected in MFM experiments and high fields, which evolve into a coarse granular domain structure when magnetic field is reduced towards the values where the THE signal is observed. This suggest that spirals may introduce chiral features in the small magnetic domains causing the large THE signals.

2- The evolution of the THE signal with temperature is also anomalous. The magnitude of the THE (rhoxy (THE)) decreases strongly when temperature is increased which in principle rules out the connection with fluctuating non collinear spins, known to be present in manganites at the metal to insulator transition (MIT). On the other hand, and if the THE is interpreted to result from skyrmions, one expect the THE resistivity to be to large extent temperature independent. Yet, its temperature dependence [25] indicates skyrmions sizes evolving with temperature which is in principle unexpected. Following Bruno, the THE results from the Berry phase acquired by the electron when it moves in the spatially varying spin texture. Its effect can described by an effective (emergent) perpendicular magnetic field $\boldsymbol{b}$ that produces a Hall effect, the THE, just as an external magnetic field. The amplitude of $\boldsymbol{b}$ depends on the topology of the spin textures through skyrmion density $\langle b \rangle = \Phi_0 n_{sk}$ where Φ_0 is the flux quantum and n_{sk} the average skyrmion density carrying a topological charge $Q = 1$. In this simple model for strong ferromagnetic exchange coupling, the THE then writes

$$\rho_{THE} = \frac{P\langle b \rangle}{en} = \frac{\Phi_0 n_{sk} P}{en} = \Phi_0 n_{sk} P R_0$$

with P the spin polarization and e the electron charge, n is the charge density and R_0 is the Hall resistivity. Plugging into this expression the experimental values of the THE and Hall resistivity (see Figure 6.6), skyrmion diameters in the range 20 – 50 nm are obtained, much larger than the values obtained from the analysis of the experimental images where an average size of 400 nm is found for the granular small features.

The presence of spin spirals and eventually also of skyrmions can be understood on theoretical grounds [24] in terms of the strong DM interaction expected at the interface between the ferromagnetic manganites of the $La_{1-x}Sr_xMnO3$ (LSMO) family with 3d orbitals and the 5d paramagnetic semimetal $SrIrO_3$ (SIO), arising from the spin-orbit coupling in SIO and broken inversion symmetry at the interface. Moreover, this scenario is favored by the high structural and chemical compatibility of both materials allowing for the growth of the highly ordered interfaces shown previously.

The competition between the Dzyaloshinskii-Moriya (DM) interaction with a ferromagnetic (FM) exchange, favors a spin-spiral phase [50], [59] which evolves into a skyrmion crystal in presence of magnetic fields [33], [60]–[63]. I.e., the DMI acting on the magnetic moments of the ferromagnet with out of plane magnetic anisotropy will give rise to the helix (spiral) phase at low magnetic fields, and will evolve into the skyrmion phase when magnetic field is increased and finally into the homogeneous ferromagnet. On the other hand for a given magnetic field, the spiral state will be favoured by an increased strength of the DMI, or alternatively by a decrease of the strength of the ferromagnetic interaction [24].

Yet, with this theoretical scenario at hand, it appears puzzling that the coarse granular domain structure apparently responsible for the presence of the THE is also observed in FC magnetic sequences where the THE is not detected. Furthermore, it is also intriguing that the spiral features (expected to result from the largest values of the DMI) are observed in strong out of plane magnetic fields, stronger than those where THE is

measured. Moreover, the dependence of the THE on the magnetic history and the large size (compared to expected skyrmion size) of the granular magnetic features observed in MFM and PEEM images suggests that, rather than conventional skyrmions, the THE may be caused by some chiral magnetic domains.

We discuss next that this phenomenology results from the modulation of the strength of the ferromagnetic interaction of the ultrathin manganite layer by the external magnetic field. This is meant in the following sense. Metastable individual skyrmions and chiral magnetic domains can exist in zero magnetic field if the effective DMI constant [52]) becomes smaller than a critical value $D_c = \frac{4}{\pi}(AK)^{1/2}$ (A and K are the exchange stiffness and the effective out-of-plane anisotropy, respectively). Although the exchange stiffness, as it is determined by the local electronic structure, its value is rather immobile, magnetic anisotropy in ultrathin manganites, on the other hand, depends on magnetic history. Ultrathin manganites are known to show depressed ferromagnetism (and dead layers) with small magnetic domains with weakened (in plane) anisotropy. The fingerprint of this inhomogeneous magnetic state can be found in the strong domain blocking observed in ZFC SQUID measurements of figure 6.10. Notice that apart of the significant blocking of domains pointed by the temperature dependence of the ZFC magnetization, hysteresis loops of Figure 6.10 measured with in plane fields have rounded shapes at remanence indicating weakened in plane anisotropy with significant rotation of the magnetization at switching. In addition, the strong low temperature magnetoresistance observed in bilayers displaying the THE (see Figures 6.4 and 6.14) is further indication of an inhomogeneous ferromagnetic state. It is important to notice that the strong low temperature magnetoresistance in excess of 50% decreasing when temperature is increased is highly anomalous. Single manganite layers (see Figure 6.2), although they display sizeable low temperature MR of 10% it increases as the temperature is increased. Within the double exchange transport scenario, this large MR denounces a granular magnetic structure with spin disorder at boundaries which yields depressed in plane anisotropy and out of plane moments sensing the DMI interaction. The

magnetically granular structure, thus, reduces the relative strength of the dipolar in plane anisotropy field, and allows for an out of plane magnetization component necessary for the DMI to develop the chiral magnetization. Notice that increasing the out of plane field has an effect of rotating the magnetic moments in the individual domains out of plane, what promotes the action of the DMI driving the formation of spirals. The weak ferromagnetic state occurring at ZFC at low temperatures is an essential ingredient for the DMI to drive the chiral magnetization state. On the other hand, the FC sequence produces a much homogeneous ferromagnetic state which is not modified by the interfacial DMI and thus THE is not observed. It is important to remark that this homogeneous ferromagnetic state is also attained in FC experiments if the cooling field is increased above 5 -7 T magnetic fields.

This scenario also explains the reduction of the THE when the thickness of the ferromagnetic layer is increased. Increasing the thickness of the ferromagnet is expected to enhance the relative strength of the ferromagnetic interaction eventually yielding a homogeneous ferromagnetic state with in plane (biaxial) magnetic anisotropy with suppressed effect of the interfacial DMI, and thus not showing THE. On the other hand, increasing the thickness of the SIO is expected to promote the SO groundstate at the interface, thus favoring the topological magnetization state. However, THE will be observed only if significant fraction of the current flows through the LSMO layer.

A final comment regards the absence of THE in the SIO/LSMO bilayer with the inverted layer sequence (SIO layer on top). The interface structure of this inverted bilayer with an increased number of SrO blocks and depressed LSMO magnetism results in a suppression the exchange interaction across the interface (as evidenced by the absence of interfacially induced magnetism mediated by Mn-O-Ir superexchange interaction). DMI is itself a form of superexchange interaction across the interface which will be also suppressed by the thick SrO interfacial block and, accordingly, the THE will be also absent. The nearly vanishing THE in the case of the SIO/LSMO/SIO trilayer probably results from the

geometry of the current distribution with dominant effect of the top interface.

Hall effect measurements of ultrathin manganites yielded in all cases AHE with negative Hall conductivity. Thus extrinsic factors due to interfacial layers with negative values of the anomalous Hall conductivity yielding (by superposition) THE-like contributions to the transverse resistivity as those described in references [54]–[58] for SRO based multilayers, can be ruled out in our system. We conclude that the observed THE is an intrinsic effect. Yet, since the estimates of the size magnetic textures from the THE peaks yields sizes much smaller (20- 50 nm) than those observed from MFM image analysis (300- 400 nm). This may be taken as an indication that, rather than from skyrmions, the observed THE feature results from chiral magnetic domains. The onset of the THE irreversibility, observed for magnetic fields in the 5 T range, is due to the formation of magnetic spirals. The strong THE peak at smaller fields (below 1 T) is attributed to small domains with chiral boundaries originating at the spiral state. It becomes clear, that having found THE peaks in the transverse resistivity, the observation of granular magnetic textures is not sufficient to attribute THE to skyrmions and chiral magnetization states have to be further assessed.

10. Conclusion

In summary, we have found a large THE in LSMO/SIO bilayers which results from the interfacial DMI across the interface between the strong spin orbit SIO iridate and the LSMO. The in plane DMI acts on the fraction of out of plane moments of the manganite which occur at the interface resulting from weakened in plane anisotropy of a granular magnetic structure. Thus, DM exchange interaction and granular domain structure (typically observed in ZFC cooling protocols), are necessary ingredients for the observation of the THE. Increasing magnetic field in samples cooled in zero magnetic field promoted out of plane magnetic moments and the DMI becomes stronger eventually yielding a spiral state. At low fields (one T range) this spirals evolve into granular domains with

chiral boundaries responsible for the large THE signals. Our experiment not only provides evidence for the role of chiral magnetic domains in the topological Hall effect (THE), which goes beyond skyrmions and bubbles, but also improves our knowledge of the underlying mechanisms that might give rise to the topological Hall effect (THE).

11. References

[1] I. Dzyaloshinsky, «A thermodynamic theory of "weak" ferromagnetism of antiferromagnetics», *J. Phys. Chem. Solids*, vol. 4, n.º 4, pp. 241-255, ene. 1958, doi: 10.1016/0022-3697(58)90076-3.

[2] I. Dzyaloshinskiĭ, «THEORY OF HELICOIDAL STRUCTURES IN ANTIFERROMAGNETS. I. NONMETALS», 1964.

[3] T. Moriya, «Anisotropic Superexchange Interaction and Weak Ferromagnetism», *Phys. Rev.*, vol. 120, n.º 1, pp. 91-98, oct. 1960, doi: 10.1103/PhysRev.120.91.

[4] C. Moreau-Luchaire *et al.*, «Additive interfacial chiral interaction in multilayers for stabilization of small individual skyrmions at room temperature», *Nat. Nanotechnol.*, vol. 11, n.º 5, Art. n.º 5, may 2016, doi: 10.1038/nnano.2015.313.

[5] B. Dupé, G. Bihlmayer, M. Böttcher, S. Blügel, y S. Heinze, «Engineering skyrmions in transition-metal multilayers for spintronics», *Nat. Commun.*, vol. 7, n.º 1, Art. n.º 1, jun. 2016, doi: 10.1038/ncomms11779.

[6] S. Heinze *et al.*, «Spontaneous atomic-scale magnetic skyrmion lattice in two dimensions», *Nat. Phys.*, vol. 7, n.º 9, Art. n.º 9, sep. 2011, doi: 10.1038/nphys2045.

[7] A. P. Malozemoff y J. C. Slonczewski, «Magnetic Domain Walls in Bubble Materials (Academic», *N. Y.*, 1979.

[8] W. Jiang *et al.*, «Blowing magnetic skyrmion bubbles», *Science*, vol. 349, n.º 6245, pp. 283-286, 2015.

[9] N. Nagaosa y Y. Tokura, «Topological properties and dynamics of magnetic skyrmions», *Nat. Nanotechnol.*, vol. 8, n.º 12, pp. 899-911, 2013.

[10] J. Matsuno *et al.*, «Interface-driven topological Hall effect in SrRuO3-SrIrO3 bilayer», *Sci. Adv.*, vol. 2, n.º 7, p. e1600304, jul. 2016, doi: 10.1126/sciadv.1600304.

[11] Y. Ohuchi *et al.*, «Electric-field control of anomalous and topological Hall effects in oxide bilayer thin films», *Nat. Commun.*, vol. 9, n.º 1, Art. n.º 1, ene. 2018, doi: 10.1038/s41467-017-02629-3.

[12] J. Nichols *et al.*, «Emerging magnetism and anomalous Hall effect in iridate–manganite heterostructures», *Nat. Commun.*, vol. 7, n.º 1, Art. n.º 1, sep. 2016, doi: 10.1038/ncomms12721.

[13] Y. Li *et al.*, «Emergent Topological Hall Effect in La0.7Sr0.3MnO3/SrIrO3 Heterostructures», *ACS Appl. Mater. Interfaces*, vol. 11, n.º 23, pp. 21268-21274, jun. 2019, doi: 10.1021/acsami.9b05562.

[14] D. Yi *et al.*, «Atomic-scale control of magnetic anisotropy via novel spin–orbit coupling effect in La2/3Sr1/3MnO_3/$SrIrO_3$ superlattices», *Proc. Natl. Acad. Sci. U. S. A.*, vol. 113, n.º 23, pp. 6397-6402, 2016.

[15] S. Okamoto, J. Nichols, C. Sohn, S. Y. Kim, T. W. Noh, y H. N. Lee, «Charge Transfer in Iridate-Manganite Superlattices», *Nano Lett.*, vol. 17, n.º 4, pp. 2126-2130, abr. 2017, doi: 10.1021/acs.nanolett.6b04107.

[16] M.-W. Yoo *et al.*, «Large intrinsic anomalous Hall effect in SrIrO3 induced by magnetic proximity effect», *Nat. Commun.*, vol. 12, n.º 1, Art. n.º 1, jun. 2021, doi: 10.1038/s41467-021-23489-y.

[17] E. Skoropata *et al.*, «Interfacial tuning of chiral magnetic interactions for large topological Hall effects in LaMnO3/SrIrO3 heterostructures», *Sci. Adv.*, vol. 6, n.º 27, p. eaaz3902, 2020.

[18] L. Vistoli *et al.*, «Giant topological Hall effect in correlated oxide thin films», *Nat. Phys.*, vol. 15, n.º 1, pp. 67-72, 2019.

[19] Y. Tokura, «Correlated-Electron Physics in Transition-Metal Oxides», *Phys. Today*, vol. 56, n.º 7, pp. 50-55, jul. 2003, doi: 10.1063/1.1603080.

[20] E. Dagotto, «Open questions in CMR manganites, relevance of clustered states and analogies with other compounds including the cuprates», *New J. Phys.*, vol. 7, n.º 1, p. 67, feb. 2005, doi: 10.1088/1367-2630/7/1/067.

[21] S. Jin, T. H. Tiefel, M. McCormack, R. A. Fastnacht, R. Ramesh, y L. H. Chen, «Thousandfold change in resistivity in magnetoresistive

la-ca-mn-o films», *Science*, vol. 264, n.º 5157, pp. 413-415, abr. 1994, doi: 10.1126/science.264.5157.413.

[22] Y. Lyanda-Geller *et al.*, «Charge transport in manganites: Hopping conduction, the anomalous Hall effect, and universal scaling», *Phys. Rev. B*, vol. 63, n.º 18, p. 184426, abr. 2001, doi: 10.1103/PhysRevB.63.184426.

[23] J. Ye, Y. B. Kim, A. J. Millis, B. I. Shraiman, P. Majumdar, y Z. Tešanović, «Berry Phase Theory of the Anomalous Hall Effect: Application to Colossal Magnetoresistance Manganites», *Phys. Rev. Lett.*, vol. 83, n.º 18, pp. 3737-3740, nov. 1999, doi: 10.1103/PhysRevLett.83.3737.

[24] N. Mohanta, E. Dagotto, y S. Okamoto, «Topological Hall effect and emergent skyrmion crystal at manganite-iridate oxide interfaces», *Phys. Rev. B*, vol. 100, n.º 6, p. 064429, ago. 2019, doi: 10.1103/PhysRevB.100.064429.

[25] P. Bruno, V. K. Dugaev, y M. Taillefumier, «Topological Hall Effect and Berry Phase in Magnetic Nanostructures», *Phys. Rev. Lett.*, vol. 93, n.º 9, p. 096806, ago. 2004, doi: 10.1103/PhysRevLett.93.096806.

[26] M. Nakamura *et al.*, «Emergence of topological hall effect in half-metallic manganite thin films by tuning perpendicular magnetic anisotropy», *J. Phys. Soc. Jpn.*, vol. 87, n.º 7, 2018, doi: 10.7566/JPSJ.87.074704.

[27] A. Neubauer *et al.*, «Topological Hall Effect in the A Phase of MnSi», *Phys. Rev. Lett.*, vol. 102, n.º 18, p. 186602, may 2009, doi: 10.1103/PhysRevLett.102.186602.

[28] H. Ishizuka y N. Nagaosa, «Spin chirality induced skew scattering and anomalous Hall effect in chiral magnets», *Sci. Adv.*, vol. 4, n.º 2, p. eaap9962, 2018.

[29] S. Okamoto, «Magnetic interaction at an interface between manganite and other transition metal oxides», *Phys. Rev. B*, vol. 82, n.º 2, p. 024427, jul. 2010, doi: 10.1103/PhysRevB.82.024427.

[30] A. Fert y P. M. Levy, «Role of anisotropic exchange interactions in determining the properties of spin-glasses», *Phys. Rev. Lett.*, vol. 44, n.º 23, p. 1538, 1980.

[31] I. A. Sergienko y E. Dagotto, «Role of the Dzyaloshinskii-Moriya interaction in multiferroic perovskites», *Phys. Rev. B*, vol. 73, n.º 9, p. 094434, 2006.

[32] M. Bode *et al.*, «Chiral magnetic order at surfaces driven by inversion asymmetry», *Nature*, vol. 447, n.º 7141, pp. 190-193, 2007.

[33] S. Mühlbauer *et al.*, «Skyrmion lattice in a chiral magnet», *Science*, vol. 323, n.º 5916, pp. 915-919, 2009.

[34] K.-S. Ryu, L. Thomas, S.-H. Yang, y S. Parkin, «Chiral spin torque at magnetic domain walls», *Nat. Nanotechnol.*, vol. 8, n.º 7, pp. 527-533, 2013.

[35] M. Onoda, G. Tatara, y N. Nagaosa, «Anomalous Hall effect and skyrmion number in real and momentum spaces», *J. Phys. Soc. Jpn.*, vol. 73, n.º 10, pp. 2624-2627, 2004.

[36] S. Do Yi, S. Onoda, N. Nagaosa, y J. H. Han, «Skyrmions and anomalous Hall effect in a Dzyaloshinskii-Moriya spiral magnet», *Phys. Rev. B*, vol. 80, n.º 5, p. 054416, 2009.

[37] N. Kanazawa *et al.*, «Large topological Hall effect in a short-period helimagnet MnGe», *Phys. Rev. Lett.*, vol. 106, n.º 15, p. 156603, 2011.

[38] Y. Taguchi, Y. Oohara, H. Yoshizawa, N. Nagaosa, y Y. Tokura, «Spin chirality, Berry phase, and anomalous Hall effect in a frustrated ferromagnet», *Science*, vol. 291, n.º 5513, pp. 2573-2576, 2001.

[39] K. G. Rana *et al.*, «Observation of topological Hall effect in Mn2RhSn films», *New J. Phys.*, vol. 18, n.º 8, p. 085007, 2016.

[40] P. Swekis *et al.*, «Topological Hall effect in thin films of Mn 1.5 PtSn», *Phys. Rev. Mater.*, vol. 3, n.º 1, p. 013001, 2019.

[41] P. Vir *et al.*, «Anisotropic topological Hall effect with real and momentum space Berry curvature in the antiskrymion-hosting Heusler compound Mn 1.4 PtSn», *Phys. Rev. B*, vol. 99, n.º 14, p. 140406, 2019.

[42] W. Wang *et al.*, «Spin chirality fluctuation in two-dimensional ferromagnets with perpendicular magnetic anisotropy», *Nat. Mater.*, vol. 18, n.º 10, pp. 1054-1059, 2019.

[43] K. Shibata *et al.*, «Large anisotropic deformation of skyrmions in strained crystal», *Nat. Nanotechnol.*, vol. 10, n.º 7, pp. 589-592, 2015.

[44] A. R. Fert, «Magnetic and transport properties of metallic multilayers», en *Materials science forum*, Trans Tech Publ, 1990, pp. 439-480.

[45] N. Romming *et al.*, «Writing and deleting single magnetic skyrmions», *Science*, vol. 341, n.º 6146, pp. 636-639, 2013.

[46] G. Chen *et al.*, «Large Dzyaloshinskii-Moriya interaction induced by chemisorbed oxygen on a ferromagnet surface», *Sci. Adv.*, vol. 6, n.º 33, p. eaba4924, 2020.

[47] D.-H. Kim *et al.*, «Bulk Dzyaloshinskii–Moriya interaction in amorphous ferrimagnetic alloys», *Nat. Mater.*, vol. 18, n.º 7, pp. 685-690, 2019.

[48] A. V. Davydenko *et al.*, «Dzyaloshinskii-Moriya interaction in symmetric epitaxial [Co/Pd (111)] N superlattices with different numbers of Co/Pd bilayers», *Phys. Rev. B*, vol. 99, n.º 1, p. 014433, 2019.

[49] W. Zhang *et al.*, «Tunable interfacial Dzyaloshinskii–Moriya interaction in symmetrical Au/[Fe/Au] n multilayers», *Nanoscale*, vol. 13, n.º 4, pp. 2665-2672, 2021.

[50] S. Banerjee, O. Erten, y M. Randeria, «Ferromagnetic exchange, spin–orbit coupling and spiral magnetism at the LaAlO3/SrTiO3 interface», *Nat. Phys.*, vol. 9, n.º 10, pp. 626-630, 2013.

[51] A. K. Nandy, N. S. Kiselev, y S. Blügel, «Interlayer exchange coupling: a general scheme turning chiral magnets into magnetic multilayers carrying atomic-scale skyrmions», *Phys. Rev. Lett.*, vol. 116, n.º 17, p. 177202, 2016.

[52] A. Fert, N. Reyren, y V. Cros, «Magnetic skyrmions: advances in physics and potential applications», *Nat. Rev. Mater.*, vol. 2, n.º 7, pp. 1-15, 2017.

[53] M. Raju *et al.*, «The evolution of skyrmions in Ir/Fe/Co/Pt multilayers and their topological Hall signature», *Nat. Commun.*, vol. 10, n.º 1, p. 696, 2019.

[54] A. Gerber, «Interpretation of experimental evidence of the topological Hall effect», *Phys. Rev. B*, vol. 98, n.º 21, p. 214440, 2018.

[55] G. Kimbell *et al.*, «Two-channel anomalous Hall effect in SrRuO 3», *Phys. Rev. Mater.*, vol. 4, n.º 5, p. 054414, 2020.

[56] L. Wang, Q. Feng, H. G. Lee, E. K. Ko, Q. Lu, y T. W. Noh, «Controllable thickness inhomogeneity and Berry curvature engineering of anomalous Hall effect in SrRuO3 ultrathin films», *Nano Lett.*, vol. 20, n.º 4, pp. 2468-2477, 2020.

[57] D. J. Groenendijk *et al.*, «Berry phase engineering at oxide interfaces», *Phys. Rev. Res.*, vol. 2, n.º 2, p. 023404, 2020.

[58] G. Kimbell, C. Kim, W. Wu, M. Cuoco, y J. W. Robinson, «Challenges in identifying chiral spin textures via the topological Hall effect», *Commun. Mater.*, vol. 3, n.º 1, p. 19, 2022.

[59] X. Li, W. V. Liu, y L. Balents, «Spirals and skyrmions in two dimensional oxide heterostructures», *Phys. Rev. Lett.*, vol. 112, n.º 6, p. 067202, 2014.

[60] M. Ezawa, «Compact merons and skyrmions in thin chiral magnetic films», *Phys. Rev. B*, vol. 83, n.º 10, p. 100408, 2011.

[61] S. X. Huang y C. L. Chien, «Extended skyrmion phase in epitaxial FeGe (111) thin films», *Phys. Rev. Lett.*, vol. 108, n.º 26, p. 267201, 2012.

[62] X. Z. Yu *et al.*, «Biskyrmion states and their current-driven motion in a layered manganite», *Nat. Commun.*, vol. 5, n.º 1, p. 3198, 2014.

[63] A. Bogdanov y A. Hubert, «Thermodynamically stable magnetic vortex states in magnetic crystals», *J. Magn. Magn. Mater.*, vol. 138, n.º 3, pp. 255-269, 1994.

Chapter 7

Conclusions

The experiments conducted along this thesis were aimed to explore the quantum matter and electronic phases of $SrIrO_3$, a 5d transition metal oxide featuring a unique combination of electronic correlations and strong spin-orbit coupling. We have shown that the delicate balance between band width (kinetic energy), Coulomb repulsion and spin orbit interaction, all three with similar energy scales (0.4 eV) confers the large tunability to this system where small external perturbations may yield large modifications of the electronic structure. Moreover, the strong spin-orbit coupling exhibited by this material opens the door to a wide range of novel phenomena, from unconventional magnetic behaviours to exotic electronic phases driven by topological properties.

In this thesis, we have explored routes to manipulate the electronic structure of $SrIrO_3$ using epitaxial strain and electric field effects as external perturbations.

We have employed epitaxial strain as a practical tool to modify the structural properties of $SrIrO_3$ thin films. $SrIrO_3$ electronic structure demonstrates a high sensitivity to small perturbations in bond lengths and angles. This sensitivity is to large extent due to the influence of its pronounced spin-orbit interaction, which links the lattice details to the electronic structure. For this reason, the epitaxial engineering has provided excellent opportunities to highlight the interrelation between structure and electrical properties.

We found a strong tunability of the MIT (metal to insulator transition) of this oxide with the substrate chosen; compressive strain generates an increase in conductivity and a more metallic behaviour while expansive strain induces an insulating state in the material. This study demonstrates that bond reconstruction has an effect in modifying the connectivity of IrO_6 octahedra and thus the dimensionality of the electronic system. This behaviour illustrates the role of out-of-plane orbitals in the electronic transport properties.

Furthermore, we have shown that in addition to strain the symmetries imposed by the substrate trigger profound modifications of the electronic structure. This is the case of $DyScO_3$, a material with a non-symorphic pattern of octahedral rotations, which triggers the nucleation of a $SrIrO_3$ monoclinic phase. This reconstruction is visible only in a thickness window between 5 and 8 nm and exhibits exotic electronic properties. We have found that the resistivity becomes independent of temperature in a wide temperature interval (300 – 2 K) suggesting that the system is in the vicinity of a quantum phase transition. At the same time, a Dirac cone is formed 30 mV above the Fermi level. These findings illustrate the profound influence of strain and thickness on the electronic properties of $SrIrO_3$ thin films, providing valuable insights into the modulation of the electronic structure enabled by its coupling to structural details enabled by spin orbit interaction.

Ionic liquid gating technique is a complementary route to explore novel electronic phases of $SrIrO_3$. This approach encompasses the generation of strong electric fields, which, in ultrathin layers, couple to the electronic structure through the strong spin-orbit coupling. Spin-orbit interaction splits t_{2g} bands according to different spin and orbital symmetry, resulting in narrow bands susceptible to Coulomb interactions. Inversion symmetry breaking at surfaces or interfaces introduces additional hopping channels, affects orbital mixing, band width, and spin splitting. The large electric fields developing in field effect experiments using ionic liquids modify symmetry-breaking fields of ultrathin layers. As a result, the electronic structure, which is strongly coupled to the electric field via strong spin-orbit coupling, may be significantly modified.

We have demonstrated that the large electric fields generated in field effect experiments with ionic liquids have a leading influence on the electronic structure of ultrathin $SrIrO_3$ films, inducing modifications beyond those expected from doping. The emergent anomalous Hall effect, linked to the out-of-plane canted antiferromagnetic state identified in the insulating phase, provides evidence for the pivotal role of electron correlations in driving the transition. The unusual band splitting and gap opening, which underpins the metal-to-insulator transition, can be traced back to the opening of new inter-orbital hopping channels driven by the electric field and broken inversion symmetry. It becomes evident that the breaking of inversion symmetry, under the control of an electric field, is an effective ´knob´ to modulate the effective strength of the correlations giving rise to the metal-to-insulator transition.

Once again the possibility of turning on and off the metal-to-insulator transition and ensuing emergent magnetism, could be exploited to engineer next-generation spintronic devices.

With regard to $La_{0.7}Sr_{0.3}MnO_3$/ $SrIrO_3$ heterostructures, we have found that the 3d/5d oxide interface is a highly promising area of research to examine the interplay between strong spin-orbit coupling of the 5d oxides with the strong electron correlations and magnetism of the 3d oxides. In particular, this system open the way to an exciting new scenario to study the interplay between correlations and topology. The anomalous Hall effect (AHE) is a very effective tool to analyse the topological electronic states nucleating at the interfaces between these two materials where magnetism and symmetry breaking occur naturally.

We explored the differences between the $SrIrO_3/La_{0.7}Sr_{0.3}MnO_3$ (SIO/LSMO) and $La_{0.7}Sr_{0.3}MnO_3$/ $SrIrO_3$ (LSMO/SIO) interfaces, which turn out to be structurally very different. The distinction relies on the different number of SrO planes with rock salt structure occurring at the interface; the LSMO/SIO interface has two planes, while the SIO/LSMO interface has three. The emergent intrinsic anomalous Hall effect (AHE) in the LSMO/SIO bilayers contrast with the absence of this effect in the SIO/LSMO bilayers. We were able to correlate this AHE in the

LSMO/SIO bilayer with the magnetic state of the interfacial $La_{0.7}Sr_{0.3}MnO_3$ and the proximity-induced magnetism in the first 2 nm of $SrIrO_3$.

The intrinsic AHE induced in the LSMO/SIO bilayers brings to light an intriguing interplay between topology (in momentum space) and electron correlations at the 3d/5d interface. The proximity-induced magnetism and broken symmetry at the interface combined with the robust spin-orbit interaction in $SrIrO_3$, generates 'hot spots' of integrated Berry curvature at nodal lines and band (avoided) anticrossings, thus providing an artificial realization of the minimal model of the AHE. Despite the small values of the magnetic moment induced in $SrIrO_3$ due to its proximity to $La_{0.7}Sr_{0.3}MnO_3$, it is noticeable that the topological properties of $SrIrO_3$ greatly amplify this effect on the AHE, and consequently, the anomalous Hall angle achieves some of the highest values reported in the literature.

This finding holds significant importance, enriching our understanding of the intricate interplay between topology, electron correlations, and magnetism in these materials. The possibility of tuning the anomalous Hall effect in these heterostructures could signal novel device concepts for next generation of spin orbitronics.

Finally, regarding spin textures in the $La_{0.7}Sr_{0.3}MnO_3/SrIrO_3$ bilayer systems, we have shown that the competition between spin-orbit coupling and superexchange interaction furnishes an optimal milieu to lodge the Dzyaloshinskii-Moriya interaction (DMI). This antisymmetric exchange interaction, when combined with the Heisenberg exchange, can prompt the nucleation of noncollinear spin textures in chiral magnets such as spin spirals, magnetic skyrmions, and chiral domain walls. The emergence of spin chirality generates an effective electromagnetic field for electrons in real space via the spin Berry phase process, leading to the occurrence of the topological Hall effect (THE).

We have observed a very large THE in SIO/LSMO bilayers, corroborating the theoretical anticipation of THE in this structure. However, it exhibits unique features that might offer valuable insights into the association between THE and spin configurations.

We have found that the appearance of the THE is determined by magnetic history. THE shows up in zero field cooling (ZFC) transport experiments in a wide range of temperatures and magnetic fields. However, when the sample is field cooled (FC) in a perpendicular magnetic field, THE is quenched. Systematic MFM and x-ray absorption spectroscopy and imaging conducted on these samples have shown a granular magnetic texture characterized by magnetic domains with an approximate 400 nm average diameter. Yet, the occurrence of THE is linked to the observation of spin spirals which transmute into a rough, granular domain structure when the magnetic field is diminished to the values where THE signal is observed. This implies that spirals may imprint chiral attributes in the small magnetic domains, triggering the large THE signals.

The dependence of the THE signal with temperature is also anomalous. The amplitude of THE diminishes notably as temperature is increased, which fundamentally dismisses the association with fluctuating non-collinear spins, known to be present in manganites at the metal to insulator transition (MIT). Conversely, if THE is interpreted to arise from skyrmions, one anticipates the THE resistivity to be largely temperature-independent. However, its temperature dependence suggests skyrmion dimensions evolving with temperature, which is typically unforeseen. Moreover, according to theoretical estimates, anticipated skyrmion diameters lie within the 20-70 nm range in this system. These values are significantly smaller than practical domain sizes (400 nm) found from the experimental images.

It is worth mentioning that these discrepancies have fuelled an escalating debate regarding the connection between electronic transport phenomena and chiral magnetism, particularly in magnetic multilayers, where significant discrepancies between the skyrmion densities derived from THE and MFM observations are reported. The interpretation of THE as the transport signature of chiral spin configurations has been recently contested, in relation to experiments on $SrRuO_3$ oxide interfaces. It was suggested that intrinsic electronic mechanisms and/or inhomogeneities could contribute to the generation of multiple components of anomalous Hall effect, which could be erroneously identified as THE. Yet, these

artefacts require that at least 2 AHE components have different signs, what occurs frequently in $SrRuO_3$ but it has never been observed in manganites. We conclude that our large THE is an intrinsic effect.

The manifestation of spin spirals and potentially skyrmions can be theoretically rationalized through the interfacial Dzyaloshinskii-Moriya interaction (DMI) resulting from spin-orbit coupling and the broken inversion symmetry expected to occur naturally at the interface between the ferromagnetic manganites of the $La_{1-x}Sr_xMnO_3$ family and the paramagnetic semimetal $SrIrO_3$. Additionally, this scenario is enabled by the remarkable structural and chemical compatibility of both materials, allowing for the fabrication of highly organized interfaces. The DMI, acting on the magnetic moments of the ferromagnet with out-of-plane magnetic anisotropy, will induce the helix (spiral) phase at low magnetic fields, evolving into the skyrmion phase as the magnetic field is high enough, and ultimately transitioning into the uniform ferromagnet. Conversely, for a set magnetic field, the spiral state will be promoted by an enhanced strength of the DMI, or alternatively by a reduction in the strength of the ferromagnetic interaction.

The observed behavior stems from the modulation of the ferromagnetic interaction strength within the ultrathin manganite layer by the external magnetic field. In the absence of a magnetic field, metastable individual skyrmions and chiral magnetic domains can persist if the effective DMI constant diminishes below a critical value Dc, which is proportional to the exchange stiffness and the effective out-of-plane anisotropy. While the exchange stiffness, determined by the local electronic structure, remains relatively immobile, the magnetic anisotropy in ultrathin manganites is dependent upon the magnetic history. Ultrathin manganites are recognized for exhibiting suppressed ferromagnetism (alongside dead layers), characterized by small magnetic domains with weakened (in-plane) anisotropy (as observed from the substantial domain blocking observed in SQUID measurements following a ZFC). In addition, the significant low-temperature MR reveals the presence of a granular magnetic structure with spin disorder at boundaries, leading to attenuated in-plane anisotropy and to the manifestation of out-of-plane moments, thus engaging with the DMI interaction. Consequently, the magnetically

granular structure diminishes the relative strength of the dipolar in-plane anisotropy field, allowing for the development of an out-of-plane magnetization component crucial for the development of chiral magnetization through the DMI. It is noteworthy that increasing the out-of-plane field induces a rotation of the magnetic moments within individual domains out of the plane, further facilitating the operation of the DMI and promoting the formation of spirals. The presence of the weak ferromagnetic state during ZFC at low temperatures serves as a crucial element for the DMI to induce the chiral magnetization state. Conversely, the FC sequence yields a more uniform ferromagnetic state that remains unaltered by the interfacial DMI, consequently resulting in the absence of THE.

Finally, the observed discrepancy between theoretical and experimental skyrmion size may suggest that the observed THE feature, rather than originating from skyrmions, results from chiral magnetic domains. The emergence of irreversibility in THE, detected at magnetic fields in the range of 5 T, can be attributed to the formation of magnetic spirals. Furthermore, the prominent THE peak at lower fields (below 1 T) is ascribed to small domains characterized by chiral boundaries originating from the spiral state. It becomes evident that, despite the observation of granular magnetic textures, the presence of THE alone is insufficient to attribute it to skyrmions, thus necessitating further assessment of chiral magnetization states.

Our experiment not only provides evidence for the role of chiral magnetic domains in the topological Hall effect (THE), which goes beyond skyrmions and bubbles, but also improves our knowledge of the underlying mechanisms that might give rise to the topological Hall effect (THE).

Our research on $SrIrO_3$ thin films signals fascinating new avenues for future research. Given our understanding of how strain and film thickness conspire to modulate the electronic properties of $SrIrO_3$, it will be intriguing to see if other materials families (ruthenates, osmiates, etc) behave similarly under different conditions of strain and film thickness. Another exciting facet is to investigate how the novel electronic phases can be manipulated to create tailored material functionalities for specific

applications, such as spintronics or quantum computing. It is our hope that these results will inspire future research to further elucidate the complex interplay between structural properties and electronic behaviours, ultimately leading to innovative material designs and applications.

Publications[1–4]

(1) Yoo, M.-W.; Tornos, J.; Sander, A.; Lin, L.-F.; Mohanta, N.; **Peralta, A.**; Sanchez-Manzano, D.; Gallego, F.; Haskel, D.; Freeland, J. W.; Keavney, D. J.; Choi, Y.; Strempfer, J.; Wang, X.; Cabero, M.; Vasili, H. B.; Valvidares, M.; Sanchez-Santolino, G.; Gonzalez-Calbet, J. M.; Rivera, A.; Leon, C.; Rosenkranz, S.; Bibes, M.; Barthelemy, A.; Anane, A.; Dagotto, E.; Okamoto, S.; te Velthuis, S. G. E.; Santamaria, J.; Villegas, J. E. Large Intrinsic Anomalous Hall Effect in SrIrO3 Induced by Magnetic Proximity Effect. *Nat. Commun.* **2021**, *12* (1), 3283. https://doi.org/10.1038/s41467-021-23489-y.

(2) Gallego, F.; Tornos, J.; Beltran, J. I.; **Peralta, A.**; Garcia-Barriocanal, J.; Yu, G.; Rojas, G.; Munuera, C.; Cabero, M.; Sanchez-Manzano, D.; Cuellar, F.; Sanchez-Santolino, G.; Sefrioui, Z.; Rivera-Calzada, A.; Mompean, F. J.; Garcia-Hernandez, M.; Leon, C.; del Carmen Muñoz, M.; Santamaria, J. Reversible Metal-Insulator Transition in SrIrO3 Ultrathin Layers by Field Effect Control of Inversion Symmetry Breaking. *Commun. Mater.* **2023**, *4* (1), 1–10. https://doi.org/10.1038/s43246-023-00362-7.

(3) López, A.; Tornos, J.; **Peralta, A.**; Barbero, I.; Fernandez-Canizares, F.; Sanchez-Santolino, G.; Varela, M.; Rivera, A.; Camarero, J.; León, C.; Santamaría, J.; Romera, M. Electrolyte Gated Synaptic Transistor Based on an Ultra-Thin Film of La0.7Sr0.3MnO3. *Adv. Electron. Mater.* **2023**, *n/a* (n/a), 2300007. https://doi.org/10.1002/aelm.202300007.

(4) Orfila, G.; Sanchez-Manzano, D.; Arora, A.; Cuellar, F.; Ruiz-Gómez, S.; Rodriguez-Corvillo, S.; López, S.; **Peralta, A.**; Carreira, S. J.; Gallego, F.; Tornos, J.; Rouco, V.; Riquelme, J. J.; Munuera, C.; Mompean, F. J.; Garcia-Hernandez, M.; Sefrioui, Z.; Villegas, J. E.; Perez, L.; Rivera-Calzada, A.; Leon, C.; Valencia, S.; Santamaria, J. Large Magnetoresistance of Isolated Domain Walls in

La2/3Sr1/3MnO3 Nanowires. *Adv. Mater. n/a* (n/a), 2211176. https://doi.org/10.1002/adma.202211176.

Contributions to Symposiums

-**Sandra Lopez** *et al.* Quantum Oxide Research Online Meeting 9, **QUOROM 9** (Online, 2023) – Poster – *Magnetic field effects on the amplitude of the Topological Hall Effect in La0.7Sr0.3MnO3 / SrIrO3 bilayers.*

-**Sandra Lopez** *et al.* Quantum Oxide Research Online Meeting 8, **QUOROM 8** (Online, 2023) – Poster – *Spin textures in La0.7Sr0.3MnO3 / SrIrO3 bilayers and the effect on superconducting YBa2Cu3O7.*

-**Andrea Peralta-Somoza** *et al.* XII Reunión del grupo de Física de la Materia Condensada de la RSEF, **GEFES2023** (Salamanca, Spain, 2023) – Poster – *Large topological Hall effect and spin textures in La0.7Sr0.3MnO3 / SrIrO3 bilayers.*

-**Andrea Peralta** *et al.* 28th International Workshop on Oxide Electronics, **IWOE28** (Portland, Maine, United States, 2022) – Oral – *Large topological Hall effect and spin textures in La0.7Sr0.3MnO3 / SrIrO3 bilayers.*

- **Andrea Peralta** *et al.* 2022 Joint European Magnetic Symposia, **JEMS2022** (Warsaw, Poland, 2022) – Poster – *Observation of spin textures in La0.7Sr0.3MnO3 /SrIrO3 bilayers.*

-**Andrea Peralta** *et al.* Quantum Oxide Research Online Meeting 6, **QUOROM 6** (Online, 2022) – Poster – *Observation of spin textures in La0.7Sr0.3MnO3 / SrIrO3 bilayers.*

-**Andrea Peralta** *et al.* Quantum Oxide Research Online Meeting 5, **QUOROM 5** (Online, 2021) – Poster – *Field effect control of symmetry breaking in SrIrO3 ultrathin layers.*

-**Andrea Peralta** *et al.* 27th International Workshop on Oxide Electronics, **IWOE27** (Genoa, Italy, 2021) – Oral – *Field effect control of symmetry breaking in SrIrO3 ultrathin layers.*

-**Andrea Peralta** *et al.* International School of Oxides Electronics 2019, **ISOE2019** (Corsica, France, 2019) – Poster – *Metal-insulator transition in SrIrO3 controlled by doping.*

Resumen en español

Recientemente, los materiales cuánticos han ganado relevancia en la física del estado sólido debido a su capacidad para mostrar fenómenos cuánticos emergentes. Muchos de estos fenómenos provienen del acoplamiento espín-órbita, una interacción cuántica relativista que vincula el movimiento orbital de los electrones con su espín, generando fases electrónicas inusuales y comportamientos magnéticos poco convencionales.

El $SrIrO_3$, un óxido metálico de transición 5d, es un destacado material cuántico debido a su equilibrio entre correlaciones electrónicas y acoplamiento espín-órbita. Este equilibrio le permite modular sus propiedades físicas ante perturbaciones externas, manifestando cambios significativos en sus características eléctricas y magnéticas, incluso ante estímulos leves. Esta notable sensibilidad hace del $SrIrO_3$ un modelo de estudio para entender el impacto de dichas perturbaciones en materiales cuánticos.

Un objetivo clave de esta tesis doctoral es emplear perturbaciones externas para manipular las propiedades del $SrIrO_3$. Nos centramos principalmente en dos métodos: tensión epitaxial y dispositivos de efecto campo con líquidos iónicos. Ambos métodos han probado ser efectivos para modificar propiedades electrónicas. A través de la tensión epitaxial, eligiendo el sustrato, podremos inducir una tensión compresiva o expansiva en el $SrIrO_3$ y así conseguir información crucial sobre el efecto de los cambios estructurales en los estados electrónicos. Por otro lado, la aplicación de voltajes de puerta mediante líquidos iónicos nos permite inducir fuertes campos eléctricos en el material. Esta herramienta nos permitirá estudiar la relación entre la estructura electrónica del $SrIrO_3$ y la ruptura de la simetría que experimente este sistema, interrelación posible gracias al acoplo espín-órbita. Con estos experimentos no sólo pretendemos entender el comportamiento del $SrIrO_3$ ante perturbaciones, sino también evidenciar el potencial de estas técnicas para para su aplicación en futuros dispositivos electrónicos.

La combinación de óxidos 5d como el $SrIrO_3$, con fuerte interacción espín-órbita, y óxidos 3d ferromagnéticos es también buena estrategia para estudiar la interacción entre topología y correlaciones. Esta combinación nos permite estudiar nuevos fenómenos emergentes como las texturas quirales de espín o fenómenos de proximidad exóticos en las interfaces. Como segundo objetivo de esta tesis, estudiaremos las propiedades de transporte de heteroestructuras combinando $SrIrO_3$ y $La_{0.7}Sr_{0.3}MnO_3$. Estas bicapas ofrecen un amplio campo de juego para investigar propiedades topológicas utilizando el efecto Hall anómalo (AHE) y el efecto Hall topológico (THE). La aparición del THE y su relación con la nucleación de texturas quirales de espín nos permitirán comprender los mecanismos fundamentales que subyacen al THE. Estas investigaciones no sólo pretenden ahondar en la comprensión fundamental de la interacción entre el acoplamiento espín-órbita y las correlaciones en los materiales cuánticos, sino también allanar el camino hacia el diseño de nuevos dispositivos espintrónicos.

Los objetivos de esta tesis se alcanzarán mediante el crecimiento de películas delgadas y heteroestructuras mediante la técnica de pulverización catódica de alta presión de oxígeno. Se explorarán las propiedades estructurales, eléctricas y magnéticas de estos sistemas mediante una amplia variedad de técnicas experimentales. Finalmente, los resultados se contrastarán mediante simulaciones de primeros principios.

Como resultado, esta tesis está estructurada en siete capítulos. Los capítulos 1 y 2 se corresponden con la introducción y los métodos experimentales de la tesis. A continuación, se suceden cuatro capítulos de resultados:

- El capítulo 3 está dedicado al efecto de la tensión epitaxial en el $SrIrO_3$. Estudiamos las propiedades estructurales y electrónicas del $SrIrO_3$ bajo diferentes tensiones epitaxiales. Observamos que ciertos sustratos pueden imponer restricciones de simetría que desencadenan modificaciones de las propiedades electrónicas. En particular, el $DyScO_3$, da lugar a una fase monoclínica altamente anómala.

- En el capítulo 4 hemos estudiado los efectos de campo eléctrico en el $SrIrO_3$. Usando campos eléctricos generados con un líquido iónico, estudiamos la estructura electrónica de una capa ultradelgada de $SrIrO_3$. Mediante medidas de magnetotransporte observamos una transición metal-aislante en función del campo eléctrico y un efecto Hall anómalo (AHE) en el estado aislante. A través de simulaciones de la teoría del funcional de la densidad observamos que el campo eléctrico produce un desdoblamiento de las bandas electrónicas, abriendo un gap que es el responsable de la transición metal-aislante. Demostramos que el efecto de la ruptura de simetría en el sistema puede ser modulado por un campo eléctrico gracias al acoplo espín-orbita.

- En el capítulo 5 examinamos el AHE que emerge en heteroestructuras $La_{0.7}Sr_{0.3}MnO_3/SrIrO_3$. Atribuimos este AHE a un estado magnético inducido en el $SrIrO_3$ por proximidad. Este efecto depende de la secuencia en la que se encuentren los materiales en la interfase. Correlacionamos este AHE con el estado magnético de la manganita en la interfase y el magnetismo inducido por proximidad en el $SrIrO_3$ en los 2 nm iniciales de la interfase.

- En el capítulo 6 estudiamos el efecto Hall topológico (THE) que emerge en heteroestructuras $La_{0.7}Sr_{0.3}MnO_3/SrIrO_3$. Este THE depende fuertemente de la temperatura y desaparece al enfriar el sistema con un campo magnético aplicado. Las imágenes obtenidas mediante microscopía de fuerza magnética muestran texturas magnéticas granulares similares a skyrmiones y espirales. Observamos que la aparición de espirales está ligada a la aparición del THE.

Finalmente, en el capítulo 7 se presentan las conclusiones de la tesis, donde se discuten los resultados mencionados anteriormente. Haremos hincapié en los resultados obtenidos en el último capítulo, al ser los más relevantes y difíciles de interpretar. Y es que actualmente existe un creciente debate entre la relación del THE con las texturas de espín. La correlación de las texturas magnéticas observadas con la aparición de THE aporta una información esencial a este debate, permitiendo comprender mejor el papel

de la interacción Dzyaloshinskii-Moriya y la anisotropía magnética como mecanismos subyacentes a THE.

En definitiva, nuestra investigación sobre las láminas delgadas de $SrIrO_3$ y $La_{0.7}Sr_{0.3}MnO_3/SrIrO_3$ abre nuevas y fascinantes vías de investigación. Considerando cómo la tensión epitaxial y el espesor de la película conspiran para modular las propiedades electrónicas del $SrIrO_3$, será interesante comprobar si otros materiales (rutenatos, osmiatos, etc.) se comportan de forma similar. A su vez, los fenómenos emergentes observados en bicapas $La_{0.7}Sr_{0.3}MnO_3/SrIrO_3$ aumentan nuestra comprensión de las interfases de óxidos 3d/5d, siendo extrapolable a sistemas similares.

Summary in English

Recently, quantum materials have gained relevance in solid-state physics because of their ability to manifest emergent quantum phenomena. Many of these phenomena arise from spin-orbit coupling, a relativistic quantum interaction that links the orbital motion of electrons to their spin, generating unusual electronic phases and unconventional magnetic behaviour.

$SrIrO_3$, a 5d transition metal oxide, is an exceptional quantum material due to the balance between electronic correlations and spin-orbit coupling. This balance allows the $SrIrO_3$ to modulate its physical properties in response to external perturbations, manifesting significant changes in its electrical and magnetic characteristics, even under small stimuli. This remarkable sensitivity makes $SrIrO_3$ a model for understanding the impact of these perturbations in quantum materials.

One of the key objectives of this thesis is to use external perturbations to manipulate the properties of $SrIrO_3$. We focus mainly on two methods: epitaxial strain and field effect devices with ionic liquids. Both methods have proven to be effective in modifying electronic properties. By epitaxial strain, choosing the substrate, we can induce a compressive or expansive strain in $SrIrO_3$ and thus obtain crucial information about the effect of structural changes on the electronic states. On the other hand, the application of gate voltages by using ionic liquids allows us to induce strong electric fields in the material. This tool will allow us to study the relationship between the electronic structure of $SrIrO_3$ and the symmetry breaking experienced by this system, an interrelation possible by spin-orbit coupling. With these experiments, we not only pretend to understand the behaviour of $SrIrO_3$ under perturbations, but also to demonstrate the potential of these techniques for future electronic devices.

The combination of 5d oxides such as $SrIrO_3$, with strong spin-orbit interaction, and ferromagnetic 3d oxides is also a good strategy to study the interplay between topology and correlations. This combination allows us to study new emerging phenomena such as chiral spin textures or exotic

proximity phenomena at interfaces. As a second objective of this thesis, we will study the transport properties of heterostructures combining $SrIrO_3$ and $La_{0.7}Sr_{0.3}MnO_3$. These bilayers offer a wide playing field to investigate topological properties using the anomalous Hall effect (AHE) and the topological Hall effect (THE). The emergence of THE and its relation to the nucleation of chiral spin textures will allow us to understand the fundamental mechanisms underlying THE. These investigations are not only intended to provide a fundamental understanding of the interplay between spin-orbit coupling and correlations in quantum materials, but also to pave the way towards the design of new spintronic devices.

The objectives of this thesis will be achieved by growing thin films and heterostructures using the high-pressure sputtering technique. The structural, electrical, and magnetic properties of these systems will be explored using a wide variety of experimental techniques. Finally, the results will be contrasted by first-principles simulations.

As a result, this thesis is structured into seven chapters. Chapters 1 and 2 correspond to the introduction and experimental methods of the thesis. This is followed by four chapters of results:

- Chapter 3 is devoted to the effect of epitaxial stress on $SrIrO_3$. We study the structural and electronic properties of $SrIrO_3$ under different epitaxial stresses. We observe that certain substrates can impose symmetry constraints that trigger modifications of the electronic properties. In particular, $DyScO_3$ gives rise to a highly anomalous monoclinic phase.

- In chapter 4, we studied the effects of electric fields on $SrIrO_3$. Using electric fields generated by an ionic liquid, we studied the electronic structure of an ultrathin $SrIrO_3$ film. Through magnetotransport measurements, we observe a metal-insulator transition as a function of the electric field and an anomalous Hall effect (AHE) at the insulating state. Using density functional theory simulations, we observe that the electric field produces a splitting of the electronic bands, opening a gap that is responsible for the metal-insulator transition. We show that the

effect of symmetry breaking in the system can be modulated by an electric field thanks to spin-orbit coupling.

- In chapter 5, we examined the emergence of an AHE in $La_{0.7}Sr_{0.3}MnO_3/SrIrO_3$ heterostructures. We attribute this AHE to a magnetic state induced in $SrIrO_3$ by proximity. This effect depends on the sequence of materials at the interface. We correlate this AHE with the magnetic state of manganite at the interface and the proximity-induced magnetism in $SrIrO_3$ in the initial 2 nm of the interface.

- In chapter 6, we studied the topological Hall effect (THE) that emerges in $La_{0.7}Sr_{0.3}MnO_3/SrIrO_3$ heterostructures. This THE is strongly temperature-dependent and disappears upon cooling the system with an applied magnetic field. Magnetic force microscopy images show granular magnetic textures similar to skyrmions and spirals. We observe that the emergence of spirals is linked to the emergence of THE.

Finally, chapter 7 presents the conclusions of the thesis, where the results mentioned above are discussed. We will focus on the results obtained in the last chapter, as they are the most relevant and difficult to interpret. Nowadays, there is a growing debate about the relationship between THE and spin textures. The correlation of the observed magnetic textures with the emergence of THE provides essential information for this debate, allowing us to better understand the role of the Dzyaloshinskii-Moriya interaction and magnetic anisotropy underlying THE.

In conclusion, our research on $SrIrO_3$ and $La_{0.7}Sr_{0.3}MnO_3/SrIrO_3$ thin films provides fascinating new avenues of investigation. Considering how epitaxial strain and film thickness conspire to modulate the electronic properties of $SrIrO_3$, it will be interesting to see whether other materials (ruthenates, osmiates, etc.) behave similarly. In turn, the emerging phenomena observed in $La_{0.7}Sr_{0.3}MnO_3/SrIrO_3$ bilayers increase our understanding of 3d/5d oxide interfaces, making them transferable to similar systems.